

This item was submitted to Loughborough's Institutional Repository (<https://dspace.lboro.ac.uk/>) by the author and is made available under the following Creative Commons Licence conditions.



For the full text of this licence, please go to:
<http://creativecommons.org/licenses/by-nc-nd/2.5/>

Uncertainty due to speckle noise in laser vibrometry

by

Peter Martin

A Doctoral Thesis

Submitted in partial fulfillment of the requirements for the award of
Doctor of Philosophy

Loughborough University

Wolfson School of Mechanical & Manufacturing Engineering

August 2010

© **Peter Martin 2010**

Abstract

This thesis presents fundamental research in the field of laser vibrometry for the application to vibration measurements. A key concern for laser vibrometry is the effect of laser speckle which appears when a coherent laser beam scatters from an optically rough surface. The laser vibrometer is sensitive to changes in laser speckle which result from surface motions not in the direction of the incident beam. This adds speckle noise to the vibrometer output which can be indistinguishable from the genuine surface vibrations. This has been termed ‘pseudo-vibration’ and requires careful data interpretation by the vibration engineer. This research has discovered that measurements from smooth surfaces, even when no identifiable speckle pattern is generated, can produce noise and therefore reference to speckle noise, in such circumstances, is inappropriate. This thesis has, therefore, adopted the more general term of pseudo-vibration to include noise generated from any surface roughness or treatment, i.e. including but not limited to speckle noise.

This thesis develops and implements novel experimental methods to quantify pseudo-vibration sensitivities (transverse, tilt and rotation sensitivity) with attention focussed on commercially available laser vibrometers and consideration is given to a range of surface roughnesses and treatments. It investigates, experimentally, the fundamental behaviour of speckles and attempts to formulate, for the first time, a relationship between changes in intensity to pseudo-vibration sensitivity levels. The thesis also develops and implements models for computational simulation of pseudo-vibrations using the fundamental behaviour of speckles. The combination of experimentation and simulation improves current understanding of the pseudo-vibration mechanisms and provides the vibration engineer with a valuable resource to improve data interpretation.

Two experimental methods of quantifying pseudo-vibration sensitivity are developed and successfully applied in the evaluation of transverse, tilt and rotation sensitivity for two models of commercial laser vibrometer. These evaluations cover both single beam (translational vibration measurement) and parallel beam (for angular vibration measurement) modes. The first method presented requires correction of the vibrometer measurement with an independent measurement of genuine velocity to produce an

apparent velocity dominated by the required noise components. The second method requires a differential measurement using two vibrometers to cancel common components such as genuine velocity, leaving only uncorrelated noise from each measurement in the resulting apparent velocity. In each case, a third measurement is required of the surface motion component causing pseudo-vibration and this is used to normalise the apparent velocity. Pseudo-vibration sensitivity is then presented as a map showing the spectral shape of the noise, as a mean and standard deviation of harmonic peaks in the map and as a total rms level across a defined bandwidth.

The simulations employ a novel and effective approach to modelling speckle evolution. Transverse and tilt sensitivity are predicted for the first time and are verified by the experimental study. They provide the vibration engineer with the potential to estimate pseudo-vibrations using a simple piece of software.

The laser beam spot diameter has a large influence on the pseudo-vibration sensitivity. Transverse sensitivity has been quantified as around 0.03% and 0.01% (per order) of the transverse velocity of the surface for beam spot diameters of 100 μm and 600 μm respectively. Larger beam spots have been shown to significantly reduce transverse sensitivity and measurements from smoother surfaces have also shown a reduced level of transverse sensitivity. Tilt sensitivity has been quantified at about 0.1 $\mu\text{ms}^{-1}/\text{degs}^{-1}$ and 0.3 $\mu\text{ms}^{-1}/\text{degs}^{-1}$ (per order) of angular velocity of the surface for beam spot diameters of 100 μm and 600 μm respectively. Smaller beam spot diameters significantly reduce tilt sensitivity. The surface roughness or treatment has been shown to have little effect on the level of tilt sensitivity. Rotation sensitivity has been quantified at approximately 0.6 $\mu\text{ms}^{-1}/\text{rads}^{-1}$ and 1.9 $\mu\text{ms}^{-1}/\text{rads}^{-1}$ (per order) of rotation velocity of the rotor for 90 μm and 520 μm . Smaller beam spot diameters have shown a significant reduction in rotation sensitivity and measurements on smoother surfaces have shown a reduced rotation sensitivity. Focussing the laser beam approximately on the rotation axis has also shown a significant reduction in rotation sensitivity. Parallel beam rotation sensitivity has been quantified at 0.016 $\text{degs}^{-1}/\text{rads}^{-1}$ and it is demonstrated that this can adequately be estimated using the single beam rotation sensitivity.

KEYWORDS: Laser Vibrometer, Laser Doppler Vibrometry, laser speckle, vibration measurement, speckle noise, pseudo-vibration, transverse sensitivity, tilt sensitivity, rotation sensitivity.

Acknowledgements

I would like to thank the ESPRC and Loughborough University for their financial support during the preparation of this thesis.

A special thanks goes to my supervisor Steve Rothberg who's patience, support, encouragement, understanding and enthusiasm has been an inspiration and without his guidance this thesis would not have been possible.

I am very grateful to the friends around me who supported and encouraged me throughout. Without them the time would not have been as interesting or as bearable.

My deepest thanks go to my family and especially my parents who have continuously encouraged, supported and loved me, I couldn't ask for more. I dedicate this thesis to my parents.

Mum and Dad

Contents

Certificate of originality	i
Abstract.....	ii
Acknowledgements.....	iv
Contents	vi
List of figures.....	x
List of tables	xx
Nomenclature.....	xxii
1 Introduction.....	1
1.1 Principles of the laser vibrometer	3
1.1.1 Derivation of the photodetector output.....	4
1.1.2 Doppler shift and target velocity	6
1.1.3 Commercial laser vibrometers.....	7
1.1.4 Gaussian beams	10
1.2 Laser Speckle.....	12
1.2.1 History of laser speckle	12
1.2.2 Laser speckle generation.....	12
1.3 Laser vibrometry.....	14
2 Laser speckle in laser vibrometry	16
2.1 Laser speckle	16
2.1.1 Diffuse scatter	16
2.1.2 Speckle noise	17
2.2 Pseudo-vibration	20
2.2.1 A surface translating transverse to the optical axis	20
2.2.2 A tilting surface	21
2.2.3 A rotating surface	23
2.2.4 Parallel beam laser vibrometer configuration.....	25
2.2.5 Differential measurements.....	26

2.3	Pseudo-vibration in differential measurements: dynamic backlash .	28
2.3.1	Experimental Configuration	28
2.3.2	Verification using high speed digital camera	31
2.3.3	Dynamic backlash using two laser rotational vibrometers	32
2.3.4	Simulation of dynamic backlash.....	36
3	Properties of a stationary speckle	43
3.1	Formation of a speckle.....	43
3.2	Speckle intensity and phase	48
3.3	Contrast.....	51
3.4	Speckle Size.....	52
3.4.1Autocorrelation from the power spectral density (Wiener-Khinchin Theorem).....	54
4	Properties of a dynamic speckle	56
4.1	Space-Time Correlation Function.....	57
4.1.1Properties of dynamic speckles when a surface moves transverse to the optical axis.....	60
4.1.2Properties of dynamic speckles when a surface tilts on the optical axis	63
4.1.3Properties of dynamic speckles when a cylindrical surface rotates.....	65
4.2	Speckle motions.....	69
4.2.1Speckle translation.....	69
4.2.2Speckle evolution.....	70
4.2.3Dominant speckle motion	70
5	Quantifying pseudo-vibration sensitivity by experimentation	77
5.1	Vibrometer signal features.....	78
5.1.1Signal Dropouts	79
5.1.2Speckle noise	81
5.2	Processing and capturing speckle noise.....	84

5.2.1Processing speckle noise.....	86
5.2.2Periodic transverse surface motion.....	89
5.2.3Periodic tilt surface motion.....	92
5.2.4Rotating surface.....	94
5.3	Pseudo-vibration sensitivities to surface motions.....	100
5.3.1Transverse sensitivity.....	100
5.3.2Tilt sensitivity.....	114
5.3.3Rotation sensitivity.....	119
5.3.4Parallel beam rotation sensitivity.....	133
6	Observation of dynamic speckle.....	138
6.1	Speckle patterns.....	138
6.1.1	Speckle size.....	141
6.2	Qualitative observation of speckle behaviour.....	142
6.2.1	Speckle translation during surface tilt.....	143
6.2.2	Speckle evolution during surface translation.....	145
6.3	Quantitative analysis of speckle behaviour.....	148
6.3.1	Cross-correlation analysis.....	149
6.3.2	Transverse surface motion.....	152
6.3.3	Tilt surface motion.....	158
6.3.4	Rotating surface.....	161
6.4	Summary of dynamic speckle.....	167
7	Estimating pseudo-vibration sensitivity by simulation.....	168
7.1	Transverse sensitivity simulator.....	169
7.1.1	Formation of a simulated speckle.....	170
7.1.2	Modelling a speckle pattern.....	172
7.1.3	Simulating speckle dynamics.....	180
7.1.4	Transverse sensitivity using the simulator.....	186
7.2	Tilt sensitivity simulator.....	202
7.2.1	Formation of a simulated speckle.....	203

7.2.2	Modelling a speckle pattern.....	204
7.2.3	Simulating speckle dynamics	207
7.2.4	Tilt sensitivity using the simulator	207
7.3	Understanding gained from the simulations.....	212
8	Conclusions and recommendations for further work.....	215
8.1	Introduction.....	215
8.2	Transverse surface motion and transverse sensitivity	218
8.3	Tilt surface motion and tilt sensitivity.....	220
8.4	Rotation and rotation sensitivity.....	220
8.5	Recommendations for further work.....	223
8.5.1	Wavefront analysis of dynamic speckle	224
8.5.2	Pseudo-vibration sensitivities for parallel beam vibrometers.	224
8.5.3	Continuous scanning laser vibrometers	226
8.5.4	In-situ estimate of noise.....	228
8.5.5	Standardising pseudo-vibration sensitivity for commercial laser vibrometers.....	229
Appendix A.....		231
Algorithm overview.....		231
References.....		233

List of figures

Figure 1.1 - Typical vibrometer Configuration	4
Figure 1.2 - Doppler shift arrangement	6
Figure 1.3 - Polytec OFV-302 vibrometer Optical configuration	8
Figure 1.4 - Typical use of a parallel beam laser vibrometer	9
Figure 1.5 - Gaussian beam profile	10
Figure 1.6 - Example of measured diameters of the propagation of a laser beam emitted from commercial laser vibrometer (Polytec OFV302)	10
Figure 1.7 - Typical fully developed speckle pattern	13
Figure 1.8 - Typical partially developed speckle pattern	14
Figure 2.1 - Electron Micrograph of the surface of retro-reflective tape	17
Figure 2.2 - Speckle pattern produced from retro-reflective tape	17
Figure 2.3 - Typical spectrum showing speckle harmonics. Speckle noise from target vibrating in-plane	19
Figure 2.4 - Typical data of the apparent and transverse velocity using a beam spot diameter of $D=600\mu\text{m}$ on a surface with $R_a 1.0\mu\text{m}$.	21
Figure 2.5 – A typical spectrum of apparent velocity dominated by speckle noise from a tilting target.	22
Figure 2.6 – Radial vibration of 4-stroke, 4-cylinder, 2-litre diesel engine (a) time and (b) frequency domain [2.7]	24
Figure 2.7 – Rotation velocity of 4-stroke, 4-cylinder, 2-litre diesel engine (a) time and (b) frequency domain using parallel beam vibrometer [2.7]	26
Figure 2.8 – Differential velocity measurement across an alternator belt of a diesel engine [2.8] (n is rotation order)	27
Figure 2.9- Experimental set-up of dynamic backlash measurement	29

Figure 2.10 - Backlash measurement on consecutive tooth face impacts.	32
Figure 2.11–Video footage showing gear motion with 60Hz sinusoidal excitation (no whole body rotation). Bottom gear is the drive gear and top gear is the driven gear.....	33
Figure 2.12 - Backlash with sinusoidal excitation at 60Hz, with whole body rotation of the drive gear at 217rpm	34
Figure 2.13 - Backlash with sinusoidal excitation at 60Hz, without whole body rotation.....	35
Figure 2.14 – Backlash, drive gear rotating at 1800rpm and oscillating with 50Hz fundamental frequency.....	36
Figure 2.15 - Simulated signals of vibrometer output without the addition of speckle noise.....	37
Figure 2.16 – Calculated dynamic backlash from simulated vibrometer outputs before and after the addition of noise.	38
Figure 2.17 - Backlash calculated with integration in time domain (black) and frequency domain (green, hanning windowed to reduce leakage). Drive gear rotating 1000rpm, oscillation at 60Hz.....	39
Figure 2.18 – Pseudo-random signal harmonics (speckle harmonics) on backlash spectrum.....	39
Figure 2.19 – Experimental (blue) and Simulated (red) backlash using frequency domain integration, drive gear rotating at 1300rpm with 50Hz oscillation.....	41
Figure 3.1 - Schematic of the coordinate system used in the statistical properties	44
Figure 3.2 - Random walk in a complex plane.....	45
Figure 3.3 - Probability density function of intensity for a speckle pattern with unit mean	50

Figure 3.4 - McKechnie's histogram based on 23,000 intensity measurements taken from a speckle pattern [3.10].	51
Figure 4.1 – Schematic of coordinate system for time varying speckles	57
Figure 4.2 - Schematic of configuration for the autocorrelation for a surface which tilts.....	63
Figure 4.3 – Schematic of configuration for autocorrelation function from a rotating cylindrical surface	66
Figure 4.4 – Effective wavefront curvature from a cylindrical object surface.	66
Figure 4.5 – Example of an indication of dominant speckle motion regime for a surface translating transverse to the optical axis. Beam waist diameter, $D_0=100\mu\text{m}$	73
Figure 5.1 - Vibrometer outputs showing (a) periodic dropouts (b) unusable signal. Tilting surface with roughness $Ra2.39\ \mu\text{m}$ oscillating at 10Hz.....	80
Figure 5.2 - Doppler signal (top) synchronised with the vibrometer output signal (bottom) showing a typical signal dropout from a tilting surface treated with retro-reflective tape oscillating at 30Hz on 200 μs timescale.....	80
Figure 5.3 – Apparent velocity (nominally speckle noise) in mm/s and phase in radians from two measurements sampling similar speckle patterns from a tilting target surface treated with retro-reflective tape oscillating at (a) 10Hz and (b)30Hz.....	82
Figure 5.4 - Doppler Signal (top) synchronised with the vibrometer output (bottom) showing typical speckle noise peak. Tilting surface treated with retro-reflective tape oscillating at 30Hz on a 200 μs timescale.	83

Figure 5.5 – (a) typical spectrum of apparent velocity dominated by speckle noise. (b) influence of speckle noise on the measured velocity	87
Figure 5.6 – Example of tilt sensitivity in units of $\mu\text{ms}^{-1} / \text{degs}^{-1}$ for a tilting surface with roughness Ra 190nm over a range of vibration frequencies from 10Hz to 30Hz.....	88
Figure 5.7 - Schematic of transverse sensitivity measurement.....	90
Figure 5.8 - Schematic of tilt experimental configuration.....	93
Figure 5.9 – Radial vibration measurement from a rotating shaft.....	94
Figure 5.10 – Effect of shaft out-of-roundness on a measurement using beam diameters of 520 μm	96
Figure 5.11 – Roundness measurement from the surface with Ra11nm	97
Figure 5.12 - Schematic of rotation sensitivity measurement	98
Figure 5.13 – Rotation sensitivity from a surface treated with retro-reflective tape using a single beam and two beams (with $\sqrt{2}$ correction) indicating the statistical relationship between the two approaches. Beam diameters are 90 μm	99
Figure 5.14 - Typical data of measured velocity, genuine velocity and transverse velocity. Beam diameter, $D=600\mu\text{m}$. Surface roughness, Ra 1.0 μm	101
Figure 5.15 - Typical data of the apparent and transverse velocity using a beam spot diameter of $D=600\mu\text{m}$ on a surface with Ra 1.0 μm	101
Figure 5.16 – Transverse sensitivity map for a surface with a displacement of 420 μm rms. (a) transverse sensitivity using 600 μm beam spot diameter. (b) transverse sensitivity using 100 μm beam spot diameter.	103
Figure 5.17 – Transverse sensitivity while varying the vibration displacement amplitude using a beam diameter of 100 μm and a surface Ra 1.0 μm	108

Figure 5.18 – Comparison of transverse sensitivity for 100 μ m beam spot diameter and 600 μ m beam spot diameter	111
Figure 5.19 – (a) beam spot on surface with no additional aperture in the laser beam path, (b) beam spot with an additional vertical 1mm wide aperture in the laser beam path. ((a) and (b) not to the same scale).....	112
Figure 5.20 – The effect of introducing an additional vertical 1mm wide aperture into the vibrometer beam path, using an undisturbed beam spot diameter of 100 μ m on a surface treated with retro-reflective tape, vibration displacement 420 μ m.....	113
Figure 5.21 - Typical data of speckle noise and angular velocity from tilting target surface. Beam diameter, $D=100\mu$ m. Surface roughness, R_a 1.0 μ m.	114
Figure 5.22 –Tilt sensitivity map for a surface with angular displacement 0.78° rms. (a) tilt sensitivity using 600 μ m beam spot diameter. (b) tilt sensitivity using 100 μ m beam spot diameter.	116
Figure 5.23 - Typical data of the apparent velocity from tilting target surface with roughness of (a) R_a 1.0 μ m and (b) R_a 11nm. Beam diameter, $D=600\mu$ m.....	118
Figure 5.24 – Typical measured velocities from (a) vibrometer A (b) vibrometer B and (c) the calculated differential velocity from a rotor with surface roughness R_a 1.0 μ m using beam spot diameters of 90 μ m.....	120
Figure 5.25 – Rotation sensitivity map for a shaft 15mm in diameter (a) rotation sensitivity using a 520 μ m beam spot diameter (b) rotation sensitivity using a 90 μ m beam spot diameter. BL= Baseline.....	122
Figure 5.26– Typical measured velocities from (a) vibrometer A & vibrometer B and (b) the calculated difference velocity from a	

rotor with surface roughness Ra 65nm using beam spot diameters of 90 μ m.....	125
Figure 5.27 – Spectra of measured velocities A and B and calculated difference velocity from surface with Ra 65nm, $D=90\mu$ m.....	126
Figure 5.28 – Rotation sensitivity showing (a) the effect of an increased shaft diameter and (b) changing the focal point. (§ - focussed on the rotation axis)	130
Figure 5.29 – Expected correlation times for a shaft rotating at 35Hz when using a 90 μ m beam, either focussing on the shaft surface or focussing on the rotation axis. The three shafts used in this study are identified by the data points presented in the plot.	131
Figure 5.30 - Parallel beam rotation sensitivity arrangement.....	134
Figure 5.31 - Parallel beam rotation sensitivity for a shaft 15mm in diameter, $D=520\mu$ m. RRT – Retro-reflective tape	135
Figure 6.1 - Speckle patterns from a variety of surfaces using beam spot diameters of 520 μ m and 90 μ m	139
Figure 6.2 – Speckle pattern sectional profiles as the surface tilts at incremental displacements of 0.1°	144
Figure 6.3 – Speckle patterns and sectional profiles from a Ra 1.0 μ m surface using $D=90\mu$ m showing speckle evolution.....	146
Figure 6.4 – Speckle patterns and a region of a speckle pattern from a Ra 1.0 μ m surface using $D=520\mu$ m showing speckle evolution.....	147
Figure 6.5 - Normalised auto-correlation of surface treated with retro-reflective tape (0.0°)	150
Figure 6.6 - Normalised cross-correlations for (a) 0.1° and (b) 0.2°.....	151
Figure 6.7 - Normalised cross-correlation for tilting surface treated with Retro-Reflective Tape using a beam spot diameter of 520 μ m	152

Figure 6.8 – Normalised cross-correlation peaks of speckle motions from a surface moving transverse to the optical axis, using a beam diameter of 520 μm	153
Figure 6.9 – Example normalised cross-correlation from a surface with Ra 75nm moving transverse to the optical axis ($D=520\mu\text{m}$)	154
Figure 6.10 – Normalised cross-correlation amplitude from a surface moving transverse to the optical axis using a beam spot diameter of 90 μm	155
Figure 6.11 – Estimated gearing term using the measured spatial delays and the expected spatial delays using data from Ra 1.0 μm surface located at the camera	156
Figure 6.12 - Example normalised cross-correlation from a surface with Ra 1.0 μm moving transverse to the optical axis. $D=90\mu\text{m}$	157
Figure 6.13 – Normalised cross-correlation of the speckle motions from a tilting target using (a) $D=520\mu\text{m}$ and (b) $D=90\mu\text{m}$	159
Figure 6.14 – Normalised cross-correlation of speckle motions from a rotating cylindrical surface using a beam spot diameter of 520 μm . ..	161
Figure 6.15– Example normalised cross-correlation from a surface treated with retro-reflective tape.....	163
Figure 6.16 – Example normalised cross-correlation from a surface with Ra11nm.....	164
Figure 6.17 - Normalised cross-correlation of speckle motions from a rotating cylindrical surface using a beam spot diameter of 90 μm	165
Figure 7.1 – Statistical distribution of 25,000 simulated speckles (black) together with the expected probability density functions (red). Summing 2 phasors per speckle (a) Intensity distribution; (b) Phase distribution; (c) Amplitude distribution. When summing 15	

phasors per speckle (d) Intensity distribution; (e) Phase distribution; (f) Amplitude distribution.	171
Figure 7.2 – Profile of a speckle pattern and a model of a simulated speckle pattern	173
Figure 7.3 – (a) portion of an image of a ‘real’ speckle pattern (b) example of a simulated speckle pattern	174
Figure 7.4 – Schematic of returning beam components for a vibrometer without a lens	176
Figure 7.5 - Schematic of returning beam components for a vibrometer with a lens	176
Figure 7.6 – Speckle pattern matrix and an example of the detecting aperture positioning	177
Figure 7.7 - Example Argand diagram of total light amplitude on a simulated detector	178
Figure 7.8 – Surface displacement and convolution routine	181
Figure 7.9 – Cross correlation of patterns of 40x40 speckles, purely evolving with speckles at surface displacement = 0. Simulated speckles - black, real speckles – blue and limit of correlation at $\exp[-2]$ - red.	183
Figure 7.10 – Speckle translation	184
Figure 7.11 - An example of the area of a speckle incident on the receiving aperture showing the appropriate dimension parameters	186
Figure 7.12 - Speckles incident on the receiving aperture	187
Figure 7.13 – (a) Doppler signal amplitude and the average intensity for one whole cycle, (b) Unwrapped phase of the Doppler signal for one whole cycle, (c) Apparent velocity for one whole cycle, (d) In-plane surface velocity for one whole cycle	189
Figure 7.14 - Polar plot of the path (locus) of the resultant from the target speckle pattern. Green phasor (time step 43) to red phasor (time	

step 129) is the same duration as the peak to peak range of the surface displacement	190
Figure 7.15 – Comparison of simulated and experimental transverse sensitivity	192
Figure 7.16 – Simulated and experimental estimates of transverse sensitivity. Surface vibration displacement amplitude is $52.5\mu\text{m}$ and $D=100\mu\text{m}$	195
Figure 7.17 – Simulated and experimental estimates of transverse sensitivity. Surface vibration displacement amplitude is $210\mu\text{m}$ and $D=100\mu\text{m}$	195
Figure 7.18 – Transverse sensitivity when altering the aperture to speckle size ratio, M	197
Figure 7.19 – Transverse sensitivity estimations for various speckle translation distances, varying T while M remains constant at 0.26	199
Figure 7.20 – Transverse sensitivity estimations for various speckle translation distances, varying T while M remains constant at 3.19	201
Figure 7.21- Statistical distribution of 25,000 simulated speckles (black) together with the expected probability density functions (red). (a) Intensity distribution; (b) Phase distribution; (c) Amplitude distribution	204
Figure 7.22 – Modelling the speckle pattern	205
Figure 7.23 – (a) Doppler signal amplitude and the average intensity for one whole cycle, (b) Unwrapped phase of the Doppler signal for one whole cycle, (c) Apparent velocity for one whole cycle, (d) Tilt surface velocity for one whole cycle	209
Figure 7.24 – Comparison of simulated estimates to experimental estimates of speckle noise	210

Figure 8.1 – Set-up for measurement of in-plane rotation sensitivity using
parallel beam laser vibrometer 225

Figure 8.2 – Set-up for measurement of tilt sensitivity using parallel beam
laser vibrometer 226

List of tables

Table 4.1 - Indication of dominant speckle motion regime.....	72
Table 5.1 - Transverse sensitivity for a target with a displacement of 420 μm rms using beam diameter of 600 μm	104
Table 5.2 - Transverse sensitivity for a target with a displacement of 420 μm rms using beam diameter of 100 μm	105
Table 5.3 – ANOVA test results for the significance in the mean sensitivities from the various surface finishes when using beam spot diameters of 600 μm and 100 μm . Vibration displacement 420 μm	106
Table 5.4 – Results of Tukey’s test for beam diameter of 100 μm configurations identifying which surfaces are significantly different. Vibration displacement 420 μm rms.	107
Table 5.5 - Transverse sensitivity while varying the vibration displacement amplitude using a beam diameter of 100 μm and a surface Ra 1.0 μm	109
Table 5.6 –Tukey’s test for beam diameter of 100 μm configurations.....	110
Table 5.7 – Transverse sensitivities showing the effect of introducing an aperture into the laser beam path. Vibration displacement 420 μm . ..	113
Table 5.8 - Tilt sensitivity (μms^{-1} / degs^{-1}) for a target with an angular displacement of 0.78° rms.....	117
Table 5.9 - Rotation sensitivity (μms^{-1} / rads^{-1}) using a beam diameter of 520 μm . Shaft diameter = 15mm	123
Table 5.10 - Rotation sensitivity (μms^{-1} / rads^{-1}) using a beam diameter of 90 μm . Shaft diameter = 15mm	124
Table 5.11 – Results of Tukey’s test for the surfaces when using a beam diameter of 520 μm using orders 41-50. Shaft diameter = 15mm....	128

Table 5.12 – Results of Tukey’s test for the surfaces when using a beam diameter of 90µm using orders 41-50. Shaft diameter = 15mm.....	128
Table 5.13 – Rotation sensitivity of orders 41-50 with various shaft diameters treated with retro-reflective tape and also showing the effect of focussing on the rotation axis of the shaft. (§ - focussed on the rotation axis)	130
Table 5.14 – Tukey’s test for various shaft diameters. (§ - focussed on the rotation axis)	132
Table 5.15 - Rotation sensitivity (degs ⁻¹ / rads ⁻¹) using beam diameters of 520µm. Shaft diameter = 15mm, D=520µm. Surface is treated with retro-reflective tape.....	136
Table 6.1- Expected speckle sizes, measured speckle sizes and contrasts of speckle patterns.....	141
Table 7.1 – Comparison of simulated estimates to experimental estimates of speckle noise. Experimental transverse sensitivity is taken from Ra 1.0 µm surface, as shown in Tables 5.1 and 5.2.	193
Table 7.2 - Simulated and experimental (Ra 1.0 µm) transverse sensitivities for various vibration amplitudes	196
Table 7.3 – Transverse sensitivity estimations for various aperture dimensions for the laser vibrometer with a 100µm beam diameter. The speckle translation distance is maintained at T=0.02	198
Table 7.4 –Speckle noise estimations for various speckle translation distances while maintaining the aperture size at M=0.26	200
Table 7.5 - Speckle noise estimations for various speckle translation distances while maintaining the aperture size at M=3.19	201
Table 7.6 – Speckle noise estimations, comparing those produced by the simulation with those produced through experimentation	211

Table 7.1 – Comparison of simulated estimates to experimental estimates of speckle noise. Experimental transverse sensitivity is taken from Ra 1.0 μm surface, as shown in Tables 5.1 and 5.2.	192
Table 7.2 - Simulated and experimental (Ra 1.0 μm) transverse sensitivities for various vibration amplitudes.....	195
Table 7.3 – Transverse sensitivity estimations for various aperture dimensions for the laser vibrometer with a 100 μm beam diameter. The speckle translation distance is maintained at $T=0.02$	197
Table 7.4 –Speckle noise estimations for various speckle translation distances while maintaining the aperture size at $M=0.26$	199
Table 7.5 - Speckle noise estimations for various speckle translation distances while maintaining the aperture size at $M=3.19$	200
Table 7.6 – Speckle noise estimations, comparing those produced by the simulation with those produced through experimentation.....	211
Table 8.1 - Quick reference for pseudo-vibration sensitivities	223

Nomenclature

Symbol	Description
a	- Target vibration displacement
a_0	- Amplitude of target vibration displacement
a_y	- Surface vibration displacement in y direction
a_C	- Surface displacement required to decorrelate speckle intensity
\tilde{a}_y	- Pseudo y displacement amplitude
A_s	- Fraction of area of speckle s
C	- Contrast of speckle pattern
D	- Exp[-2] diameter by intensity of Gaussian laser beam
D_0	- Exp[-2] diameter by intensity at beam waist of Gaussian laser beam
D_c	- Uniform circular beam diameter
D_{OPT}	- Optimum beam diameter for a fixed z
d	- Beam separation distance
e	- Average phasor amplitude
e_p	- Amplitude of p^{th} elementary phasor
E	- Total electromagnetic complex field
E_0	- Total electromagnetic field amplitude
E_{0R}	- Amplitude of E-field contribution from reference beam
E_{0T}	- Amplitude of E-field contribution from target beam
$E_R(t)$	- Electromagnetic field contribution from reference beam
$E_T(t)$	- Electromagnetic field contribution from target beam
E_s	- Amplitude of speckle s
f	- Light frequency (Hz)
f_a	- Target vibration frequency (Hz)
f_B	- Beat frequency (Hz)
f_D	- Doppler frequency
f_R	- Frequency pre-shift of reference beam (Hz)
$FT^{-1}[m]$	- Inverse Fourier Transform function of $[m]$
$h_{s,0}$	- Factor of speckles s off of the aperture in a vertical direction from the top edge of the speckle
$h_{s,1}$	- Factor of speckles s off of the aperture in a vertical direction from the bottom edge of the speckle
I	- Intensity
I_R	- Reference beam intensity
I_{res}	- Doppler signal amplitude
I_T	- Target beam intensity
j	- $\sqrt{-1}$

$J_1[m]$	-	First order Bessel Function of the first kind of $[m]$
k	-	Wavenumber
L_B	-	Width of square illuminating beam
L_d	-	Exp[-2] Diameter of Gaussian ‘soft aperture’
M	-	Number of speckles in the receiving aperture
N_A	-	Number of teeth on gear A
N_B	-	Number of teeth on gear B
p	-	p^{th} elementary phasor
P	-	Number of elementary phasors
$P(m)$	-	Probability density function of (m)
r	-	Radius of wavefront curvature
r_A	-	Contact radius of gear A
r_{APCR}	-	Pitch circle radius of gear A
r_B	-	Contact radius of gear B
r_{BPCR}	-	Pitch circle radius of gear B
r'	-	Effective radius of wavefront curvature
R	-	Radius of rotor
s	-	Relative tangential separation
S	-	Number of speckles
$S(m)$	-	Power spectral density of (m)
t	-	Time
T	-	Speckle translation distance in number of speckles
T_e	-	Speckle translation distance in number of speckles for a rotating target
U_m	-	Sensed genuine velocity/measured velocity
v	-	Target velocity
$w_{s,0}$	-	Factor of speckles s off of the aperture in a horizontal direction from the left edge of the speckle
$w_{s,1}$	-	Factor of speckles s off of the aperture in a horizontal direction from the right edge of the speckle
x	-	Coordinate axis
\dot{x}	-	Surface vibration velocity in x direction
X	-	Spatial delay
X_T	-	Speckle translation distance
\mathbf{X}	-	Total spatial duration
y	-	Coordinate axis
y_0	-	Initial displacement in y direction from measurements axes origin
z	-	Coordinate axis
z_0	-	Displacement from beam waist
z_S	-	Orthogonal separation target to observation plane/photodetector
β	-	Angle between beam direction and x,y plane

γ_S	-	Scattering angle relative to the target beam incidence
$\gamma_{\Delta I}$	-	Normalised autocorrelation function of fluctuating component of intensity
$\Gamma_{\Delta I}$	-	Autocorrelation function of fluctuating component of speckle intensity
ΔD	-	Target displacement corresponding to one phasor exchange
Δr_A	-	Radial distance from pitch circle radius of gear A to contact radius of gear A
Δr_B	-	Radial distance from pitch circle radius of gear B to contact radius of gear B
ΔU_m	-	Difference in measured velocity
$\Delta \Phi_A$	-	Change in Doppler signal phase from vibrometer A
$\Delta \Phi_B$	-	Change in Doppler signal phase from vibrometer B
$\Delta \Omega_A$	-	Alternating component of angular velocity of gear A
$\Delta \Omega_B$	-	Alternating component of angular velocity of gear B
η	-	Coordinate axis
θ_A	-	Angular position of gear A
θ_B	-	Angular position of gear B
θ_C	-	Angular displacement of the surface required to decorrelate speckle intensity
$\dot{\theta}_y$	-	Angular vibration velocity around y axis
$\dot{\theta}_z$	-	Angular vibration velocity around z axis
λ	-	Wavelength of light
μ	-	Refractive index
ζ	-	Coordinate axis
σ	-	Speckle translation gearing term
$\langle \sigma_0 \rangle$	-	Average speckle width
σ_x	-	Speckle size in x direction
σ_y	-	Speckle size in y direction
σ_ε	-	Speckle translation gearing term for rotating target
τ	-	Time separation $t_2 - t_1$
τ_C	-	Correlation time
φ_p	-	Phase of pth elementary phasor
Φ	-	Total electromagnetic field phase
Φ_{res}	-	Doppler signal phase
Φ_s	-	Phase of speckle s
Φ_R	-	Phase of E-field contribution from reference beam
Φ_T	-	Phase of E-field contribution from target beam
ω_R	-	Frequency pre-shift of reference beam (rad.s^{-1})
Ω	-	Angular velocity
Ω_A	-	Angular velocity of gear A
Ω_B	-	Angular velocity of gear B

- $\overline{\Omega}_A$ - Mean angular velocity of gear A
- $\overline{\Omega}_B$ - Mean angular velocity of gear B
- $\langle \rangle$ - Denotes ensemble average
- $\Re[m]$ - Real component of $[m]$
- $\Im[m]$ - Imaginary component of $[m]$

1 Introduction

The laser vibrometer is now well established as an effective, non-contact alternative to the use of a traditional contacting vibration transducer. Laser vibrometers are technically well suited to general application but offer special benefits where certain measurement constraints are imposed, for example by the context, which may demand high frequency operation, high spatial resolution or remote transducer operation, or by the structure itself, which may be hot, sensitive to mass loading or rotating. Despite all the capabilities laser vibrometry can offer, unresolved issues remain which cause uncertainty in a measurement and this thesis presents the study of a key concern associated with the laser speckle effect known as “speckle noise”.

This introductory chapter opens with the principles of operation of the laser vibrometer, introducing the typical configurations commercially available and relevant to this thesis. This is followed by a description of the generation of laser speckle. Chapter 2 explains how laser speckle can cause significant levels of noise in a measurement with a laser vibrometer. It gives examples of situations where speckle noise can become a significant source of uncertainty (pseudo-vibration). This is the core motivation for the research examined in this thesis. It presents an experimental study of differential measurements, focussing on the novel measurement of dynamic backlash using two laser vibrometers. Attention is given to the significance of speckle noise which is always increased when differential measurements are required.

Chapter 3 examines literature, using the fundamental statistics of speckle intensity, to investigate the parameters used to describe laser speckle. Chapter 4 continues the examination of the literature, using laser speckle statistics on the fluctuations of intensity, to study the relationship between particular surface motions and the resulting behaviour of the speckles. This proposes to analyse, statistically, the mechanisms which govern the generation of speckle noise in laser vibrometry.

Using commercially available laser vibrometers, Chapter 5 presents detailed quantification of pseudo-vibration sensitivity produced from experimental analysis. This is a key novelty in this thesis. Pseudo-vibration sensitivity is the collective term (developed by this thesis) for the sensitivity to noise of a laser vibrometer from periodic surface motions which are not parallel with the optical axis. This is an important resource for data interpretation to the vibration engineer never before available to them. The chapter focuses on the most important sources of pseudo-vibration sensitivity: transverse sensitivity, tilt sensitivity and rotation sensitivity. The experimental study also examines the effect of surface roughness and treatment on the pseudo-vibration sensitivity.

Chapter 6 uses the statistical tools, described in Chapter 3 and 4, to examine speckle behaviour using sequential images of speckle patterns in motion (using the actual speckle patterns generated). It presents the motion of the speckle pattern when the surface moves with the non-normal motions examined in Chapter 5. The chapter proposes to provide a relationship between the speckle motions and the pseudo-vibration sensitivity. The study of this association has never been examined before in laser vibrometry.

Pseudo-vibration sensitivities are estimated in Chapter 7 using numerical simulations, modelling speckles and their motions described in Chapters 3, 4 and 6. The simulations verify the pseudo-vibration sensitivities measured experimentally in Chapter 5. The chapter concentrates on the simulation of pseudo-vibration sensitivities (transverse sensitivity and tilt sensitivity) never before studied numerically in laser vibrometry.

Concluding remarks, summarising pseudo-vibration sensitivity in laser vibrometry together with practical means to minimise the effects of speckle noise, are made with recommendations for further research in Chapter 8.

1.1 Principles of the laser vibrometer

Laser vibrometry relies on the detection of a Doppler shift in the frequency of coherent light scattered from a moving surface. Light incident on a moving target undergoes a frequency shift proportional to the component of velocity in the direction of the laser beam. The scattered light is collected and the intensity is measured using a photodetector. Typically the electromagnetic wave, operating in the visible range in the spectrum, oscillates at 10^{14} Hz. The photodetector cannot respond fast enough to detect the Doppler shift in the target beam directly and therefore a reference beam is typically used to provide a carrier signal. Additionally, the reference beam is usually frequency pre-shifted to avoid ambiguity of direction in the measured velocity. The scattered target beam is heterodyned with the reference beam on the photodetector, modulating the frequency. The fluctuating component of the intensity measured by the photodetector is usually referred to as the Doppler signal. Frequency demodulation of the Doppler signal yields a beat frequency which is the difference between the reference beam pre-shift frequency and the target beam Doppler shift frequency. A typical schematic arrangement is shown in

Figure 1.1. In this arrangement, the laser beam is amplitude divided into a reference and target beam by a beamsplitter. The target beam, Doppler shifted by f_D , and the reference beam, frequency pre-shifted by f_R , are mixed on the photodetector surface resulting in the beat frequency $|f_R - f_D|$. The signal is demodulated using an appropriate Doppler signal processor which produces a time-resolved signal analogue of the target vibration in the direction of the laser beam.

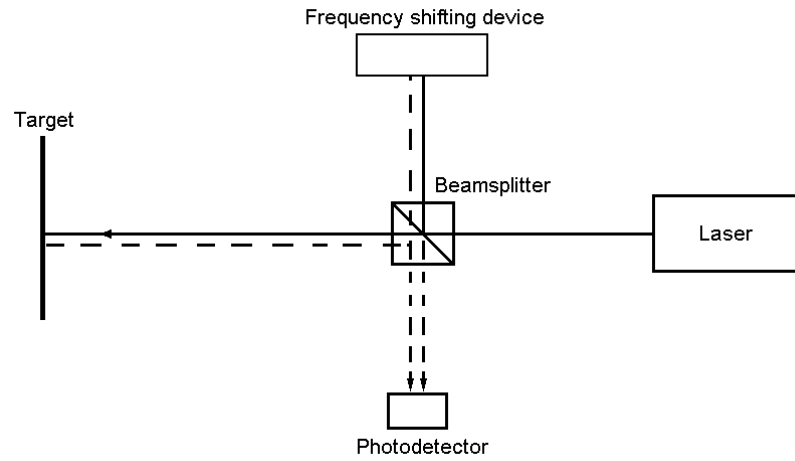


Figure 1.1 - Typical vibrometer Configuration

1.1.1 Derivation of the photodetector output

The photodetector detects the intensity, I , of the target and reference beam mixed on the photodetector surface. The intensity is related to the time-average of the square of the total light amplitude and is given by

$$I = \langle |E(t)|^2 \rangle = \langle |E_R(t) + E_T(t)|^2 \rangle \quad (1.1)$$

The reference beam contribution, $E_R(t)$, has amplitude, E_{0R} , optical frequency, f , and phase, Φ_R , which has undergone a frequency pre-shift, f_R . The target beam contribution, $E_T(t)$, has amplitude, E_{0T} , optical frequency, f , and phase, Φ_T , for a stationary target. The reference and target beam contributions, respectively, are as follows

$$E_R(t) = E_{0R} \exp\left[j\left(2\pi(f + f_R)t + \Phi_R\right)\right] \quad (1.2)$$

$$E_T(t) = E_{0T} \exp\left[j\left(2\pi ft + \int 2\pi f_D(t) dt + \Phi_T\right)\right] \quad (1.3)$$

When mixed on the photodetector surface the intensity is

$$I = I_R + I_T + 2\sqrt{I_R I_T} \cos\left[2\pi f_R t - \int 2\pi f_D(t) dt + (\Phi_R - \Phi_T)\right] \quad (1.4)$$

where

$$I_R = |E_R(t)|^2 \quad (1.5a)$$

and

$$I_T = |E_T(t)|^2 \quad (1.5b)$$

In this analysis $I_R + I_T$ is constant. These terms are usually filtered either electronically or optically [1.1]. The higher frequency cosine term is the Doppler signal. Demodulation of this signal reveals the time derivative of the cosine argument which is related to the vibration velocity of the target as described in the next sub-section.

1.1.2 Doppler shift and target velocity

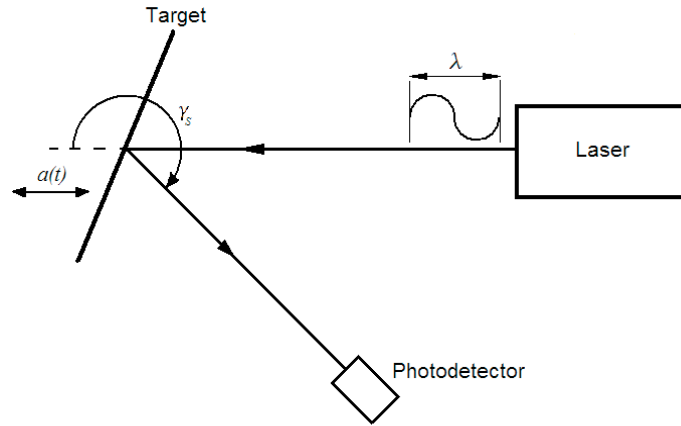


Figure 1.2 - Doppler shift arrangement

Figure 1.2 shows the arrangement of the laser beam and target by which the Doppler shift is calculated. If a beam of wavelength, λ , propagating through a medium of refractive index, μ , is incident on a solid surface which is vibrating with displacement in the direction of the beam of $a(t)$, and the scattered beam is sensed at an angle, γ_s , then the Doppler shift frequency, f_D , is given by [1.1]

$$f_D = \frac{2\mu}{\lambda} \frac{da(t)}{dt} \sin \frac{\gamma_s}{2} \quad (1.6)$$

The refractive index of air is usually considered as unity and the angle of the scattering direction is π for direct backscatter. Therefore the Doppler shift becomes

$$f_D = \frac{2}{\lambda} \frac{da(t)}{dt} \quad (1.7)$$

Equation (1.4) can therefore be re-written as

$$I = I_R + I_T + 2\sqrt{I_R I_T} \cos[2\pi f_R t - 2ka(t) + (\Phi_R - \Phi_T)] \quad (1.8)$$

where k is the wavenumber. Frequency demodulation of the cosine term yields the beat frequency, f_B , and it follows that

$$f_B = \left| f_R - \frac{2}{\lambda} \frac{da(t)}{dt} \right| = |f_R - f_D| \quad (1.9)$$

1.1.3 Commercial laser vibrometers

The principal operation is very similar for all laser vibrometers. This section describes a couple of optical configurations most commonly used, single beam and parallel beam configurations. Both these configurations are used in this thesis. Single beam laser vibrometers are suitable for measurements of surface translation. The optical configuration of a typical translational commercial laser vibrometer (Polytec OFV-302) is shown in Figure 1.3. A polarised laser beam is emitted from the laser. Beam splitter, BS1, transmits and reflects orthogonal polarisations of the beam which respectively become the target and reference beams. The target beam passes through beam splitter, BS2, quarter wave plate, QWP, and focusing lens before it is incident on the target. The QWP ensures the backscattered light is reflected at BS2 and directed towards beam splitter BS3. The reference beam is frequency pre-shifted by a Bragg cell (BC). The Doppler shifted target beam and frequency pre-shifted reference beam are combined at BS3. BS3 reflects and transmits the modulated signal directing the resulting two beams towards photodetectors PD1 and PD2. The reflected and transmitted signals are in anti-phase and the resulting two signals are combined using a differential pre-amp. The fundamental operation of this

vibrometer is the same as that shown in Figure 1.1 producing an output signal which is proportional to the velocity of the surface in the direction of the beam.

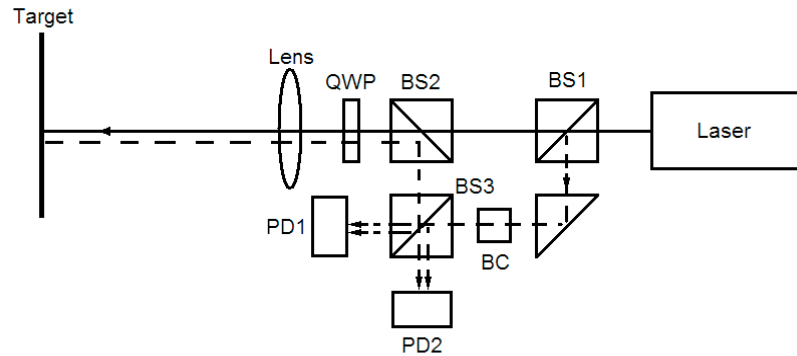


Figure 1.3 - Polytec OFV-302 vibrometer Optical configuration

Laser rotational vibrometers offer advantages for measuring angular vibrations on rotating targets by virtue of their capabilities for non-contact measurement, their insensitivities to whole body translational motions and also to target cross sectional profiles. Differential measurements, such as shaft torque, belt slip or backlash can be useful in the assessment of system and or component integrity. Difficulty in acquiring such measurements increases when the components under investigation are rotating. The laser rotational vibrometer is a prime candidate for acquiring such measurements. Often a measurement of the rotational velocity is required, whether it be the whole body angular velocity (DC component) or the torsional/angular vibration (AC component). Parallel beam vibrometers are suitable for measuring the angular velocity of a target surface. Figure 1.4 shows a typical application of a parallel beam vibrometer. The parallel beam arrangement offers an inherent insensitivity to the target shape and the translational motions of the target surface. The operation of the parallel beam vibrometer is in essence a differential measurement.

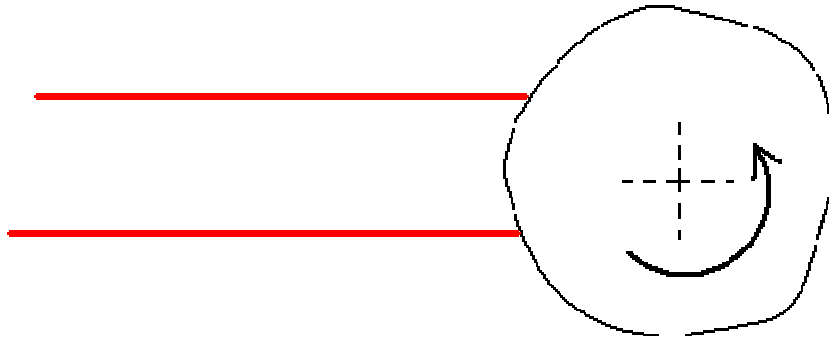


Figure 1.4 - Typical use of a parallel beam laser vibrometer

Each laser beam is Doppler shifted by the component of velocity in the direction of the beam. The Doppler shift in each beam will often be a combination of the whole body translational motion and a component of the tangential velocity of the surface in the direction of the beam. The whole body translational motion, Doppler shifting both beams, is identical and this information is cancelled in the beat signal (either optically or electronically). The beat frequency is the modulus of the difference in the Doppler shifted beams leaving a Doppler frequency, similar to equation (1.7), which can be expressed as

$$f_D = \frac{2}{\lambda} d \Omega(t) \quad (1.10)$$

where d is the perpendicular distance between beams and Ω is the angular velocity of the target. The vibrometer's output is proportional to the angular velocity of the target surface.

1.1.4 Gaussian beams

Typically a laser vibrometer will use a He-Ne laser operating in the fundamental mode TEM_{00} producing a Gaussian electric field in the transverse plane of the beam. The optical power is therefore concentrated circularly symmetrically around the optical axis.

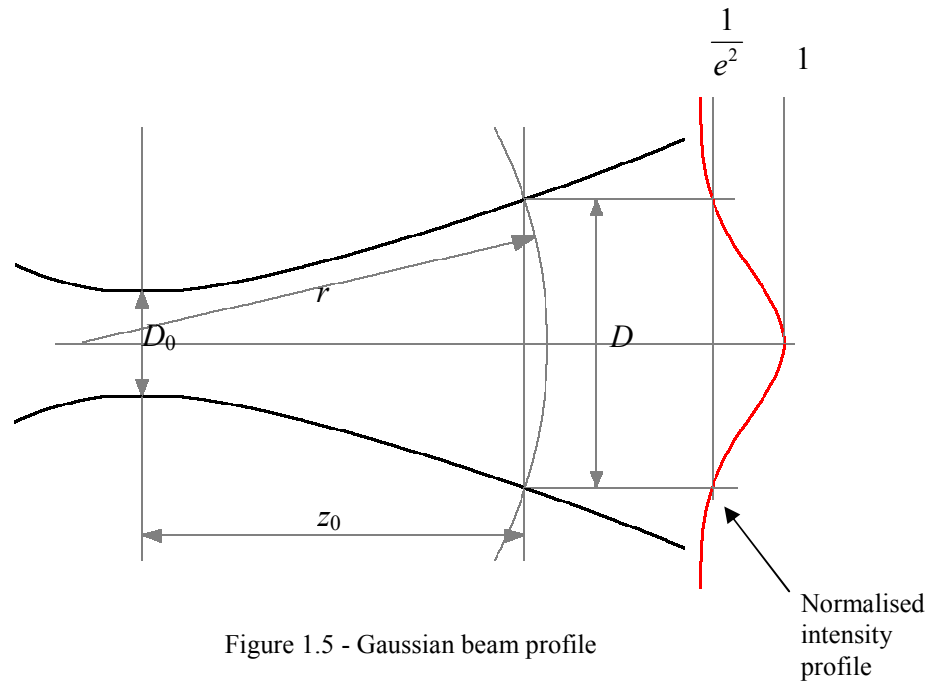


Figure 1.5 - Gaussian beam profile

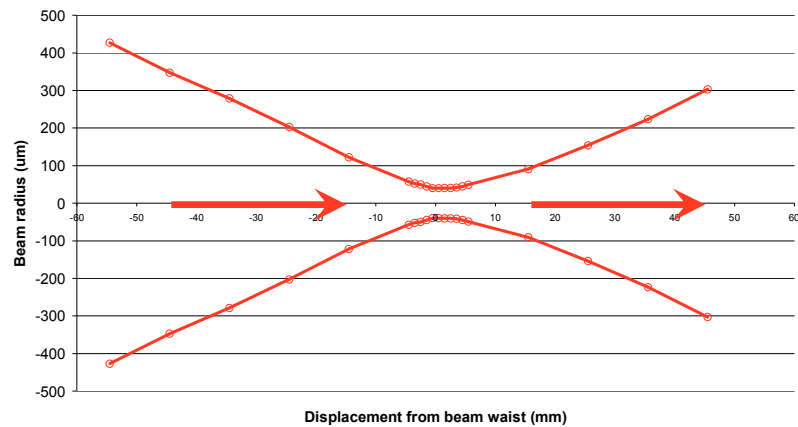


Figure 1.6 - Example of measured diameters of the propagation of a laser beam emitted from commercial laser vibrometer (Polytec OFV302)

As shown in Figure 1.5 and Figure 1.6, the beam diameter, D , is defined by the locus of intensity bound by $\exp[-2]$ of the value on the optical axis and is given as [1.2]

$$D = D_0 \left(1 + \left(\frac{4z_0\lambda}{\pi D_0^2} \right)^2 \right)^{1/2} \quad (1.11)$$

where D_0 is the beam diameter at the beam waist, z_0 is the propagation distance from the beam waist and λ is the wavelength of the beam. Figure 1.6 presents measurements of the diameter of a laser beam from a commercial laser vibrometer. The measurements are shown by the data points and are taken, using a beam profiler, at a range of displacements near the laser beam's waist and along its trajectory. The line shows a fit to the data points, which highlights the boundary of the laser beam, identified by the normalised intensity $\exp[-2]$ criteria. A Gaussian beam has wavefronts which are spherical and the radii of curvature reach a minimum and increase with advancing propagation towards the beam waist. The curvature becomes planar at the beam waist. The radius of curvature, r , can be expressed as follows

$$r = z_0 \left(1 + \left(\frac{\pi D_0^2}{4z_0\lambda} \right)^2 \right) \quad (1.12)$$

1.2 Laser Speckle

1.2.1 History of laser speckle

In the early 1960's, the development of the continuous wave laser resulted in the first observations of laser speckle. The appearance of laser speckle was described as “granular or peppery” [1.3] and “sparkling” in nature [1.4]. However this was not the first occurrence of such a phenomenon. During the late nineteenth century a great deal of interest arose around the phenomenon of interference in scattered light such as that encountered with Newton's diffraction rings [1.5] or Quételet's fringes. In 1877, Exner sketched the radially granular speckle pattern observed when shining candle light through a glass plate on which he had breathed. Later in 1914, von Laue produced a photograph of Fraunhofer rings clearly showing a radial granular pattern akin to that seen by Exner [1.6]. In early work, the laser speckle phenomenon was not held in the highest regard, described by Gabor as “Enemy Number One of Holography” [1.7]. However the reputation this foe has in holography has since been re-evaluated in such applications as the measurement of surface roughness [1.8], [1.9], [1.10], Electronic Speckle Pattern Interferometry (ESPI) [1.11], Stellar Speckle Interferometry [1.12] and shaft torque measurement [1.1], [1.13]. However, laser speckle remains a limiting factor in applications such as laser vibrometry with which this thesis is concerned.

1.2.2 Laser speckle generation

Typical target surfaces encountered by the vibration engineer are optically rough. The surfaces have sufficient roughness, which is comparable to the wavelength, and the lateral scale of the surface is exceeded by the laser beam. Illumination of a rough surface leads to diffuse reflection and the micro-scale

surface elements cause the coherent component wavelets to become de-phased. Propagation of these coherent but de-phased wavelets leads to interference and a chaotic distribution of intensity. This intensity distribution, full of light and dark regions caused by constructive and destructive interference respectively, is referred to as a speckle pattern. Diffuse scatter from an optically rough surface causes the phase distribution of the scattered component wavelets to occupy a 2π range resulting in a fully developed speckle pattern as shown in Figure 1.7.

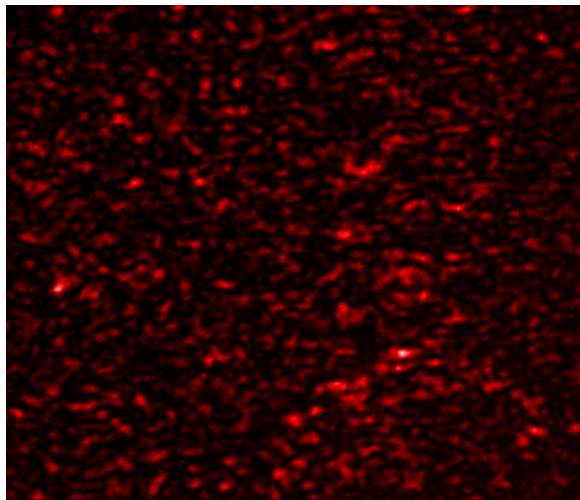


Figure 1.7 - Typical fully developed speckle pattern

Illumination of smoother surfaces, whereby the scattered wavelet phases do not occupy a full 2π range, produces partially developed speckle patterns together with elements of specular reflection such as that shown in Figure 1.8.

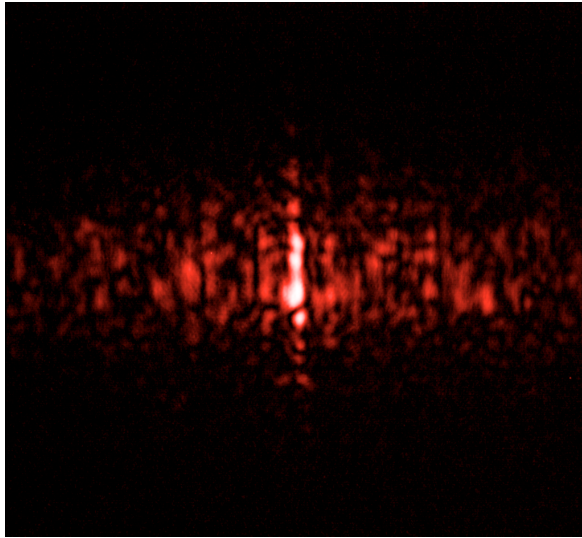


Figure 1.8 - Typical partially developed speckle pattern

Smooth, mirror-like surfaces cause specular reflection and no speckles are formed. A study of scatter from surfaces with different roughness is described in Chapter 6.

1.3 Laser vibrometry

The technique of laser vibrometry on solid surfaces was developed from non-intrusive fluid flow measurements [1.14] and is now well established as a reliable non-contact alternative to traditional contacting transducers such as accelerometers. The range of applications where laser vibrometry is employed is vast, a few of which are in areas of mechanical engineering [1.15]; automotive and aeronautical engineering [1.16]; MEMS [1.17]; artwork; archaeology; civil engineering; the military and defence[1.18]; Bioacoustics and Biological systems [1.19], [1.20]. Development of the laser vibrometer has brought about many variations of the product including single point translational; rotational; continuous scanning and tracking; In-plane; 3D scanning; multi-beam and differential laser vibrometers. Fundamentally these

vibrometers operate in the same way and the limitations and uncertainties are applicable throughout. Speckle noise is a main source of uncertainty in a measurement with a laser vibrometer [1.21]. Some effort has been made to try and understand speckle noise [1.1], [1.18], [1.22], [1.23]. Parameters such as beam diameter, standoff distance; surface roughness and the surface vibration are expected to influence speckle noise but as of yet little is understood about how much they effect the signal or the fundamental mechanisms which generate it. This thesis addresses this deficiency. The following chapter describes how laser speckle can affect a measurement, and why speckle noise is of concern in laser vibrometry.

2 Laser speckle in laser vibrometry

2.1 Laser speckle

2.1.1 Diffuse scatter

Laser vibrometers measure the component of target surface velocity in the direction of their incident beam. However it is not unusual in practical applications, due to limited space or access, for it to be impossible to measure the velocity component under scrutiny from a position normal to the surface. In these circumstances the inherent angular spread of the diffuse scatter can be used to benefit the technique and make an otherwise impossible measurement attainable. Diffuse scatter, inherent with speckle patterns, is typically required for measurements on rotors, where the surface normal can easily cause the reflected angles to deviate from the optical axis. Smooth surfaces producing principally specular reflection with little or no speckle can reflect the light away from the receiving aperture causing an unattainable vibration velocity.

When light levels are too low from the diffuse scatter or when the specular reflection misses the receiving aperture it is not uncommon to treat the surface in some way, with paint, developer powder or more commonly retro-reflective tape to increase the backscattered returning light intensity. Retro-reflective tape increases the backscattered light intensity by concentrating the scattered light back along the optical axis. Figure 2.1 shows the surface of retro-reflective tape

at a microscopic level. The tape consists of many nominally spherical glass beads, approximately $50\mu\text{m}$ in diameter, embedded into a substrate. The substrate reflects the light and the bead refracts the scatter back towards the source. The spherical shape of the beads introduces, in essence, small circular apertures which when the light scatters from the surface produces an Airy disc in backscatter with its peak intensity on the optical axis. However the backscattered light still consists of many de-phased wavelets and superimposed on the Airy disc is a speckle pattern. The following section describes how the laser speckle effect affects a measurement in laser vibrometry.

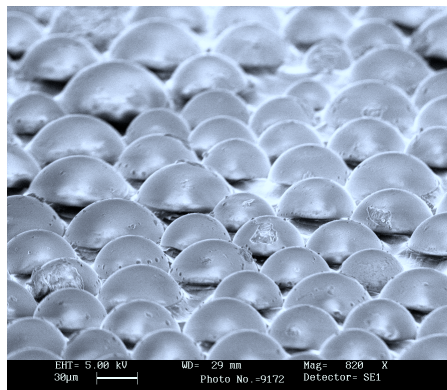


Figure 2.1 - Electron Micrograph of the surface of retro-reflective tape

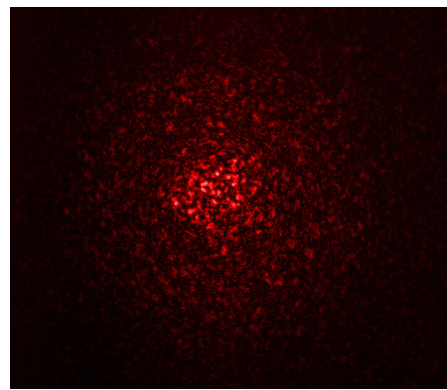


Figure 2.2 - Speckle pattern produced from retro-reflective tape

2.1.2 Speckle noise

Practical applications of laser vibrometry often encounter surfaces that are optically rough. More often than not a speckle pattern will form the target beam contribution to the Doppler signal. In certain circumstances the motion of the surface causes the speckle pattern to change over time and therefore modulation of the reference beam results in a Doppler signal which also has a time dependent amplitude, $I_{res}(t)$, and, importantly, phase $\Phi_{res}(t)$. Equation (1.8) can be rewritten

$$I = I_R + I_T(t) + I_{res}(t) \cos[\omega_R t - 2ka(t) + \Phi_{res}(t)] \quad (2.1)$$

where $I_{res}(t) = 2\sqrt{I_R} \sqrt{I_T(t)}$ and $\Phi_{res}(t) = \Phi_R - \Phi_T(t)$. Demodulation of the cosine argument results in a beat frequency

$$f_B = \left| f_R - \frac{2}{\lambda} \frac{da(t)}{dt} + \frac{1}{2\pi} \frac{d\Phi_{res}(t)}{dt} \right| \quad (2.2)$$

and with the Doppler signal phase now a function of time, uncertainty is added to the measurement of the surface vibration velocity. This modulation occurs irrespective of the amplitude of the signal and can be a significant source of broadband noise known as speckle noise.

The term ‘speckle noise’ is sometimes used to describe ‘drop outs’ in the output signal from the laser vibrometer [2.1], [2.2], [2.3]. This interpretation over-emphasises the importance of amplitude modulation in the generation of speckle noise. Speckle motions do cause amplitude and phase modulation and these will commonly occur in unison. Drop outs are attributed to low levels of Doppler signal amplitude which can be the result of low levels of returning light or an unfortunate summation of speckles. When the latter occurs, significant changes in phase also follow. Therefore, when the Doppler signal amplitude is low the likelihood of large phase changes is increased. However, phase changes can occur irrespective of the amplitude of the Doppler signal and speckle noise is present even when the amplitude is sufficient for accurate demodulation.

Speckle noise is of particular concern if surface motions are periodic. This causes the speckle noise itself to be periodic, with the same fundamental

frequency as the surface vibration frequency. In fact, for periodic motions, speckle noise is pseudo-random with energy at many harmonics of the fundamental frequency and importantly this occurs even when surfaces are vibrating with a single frequency [2.4], [2.5], [2.6] as shown in Figure 2.3.

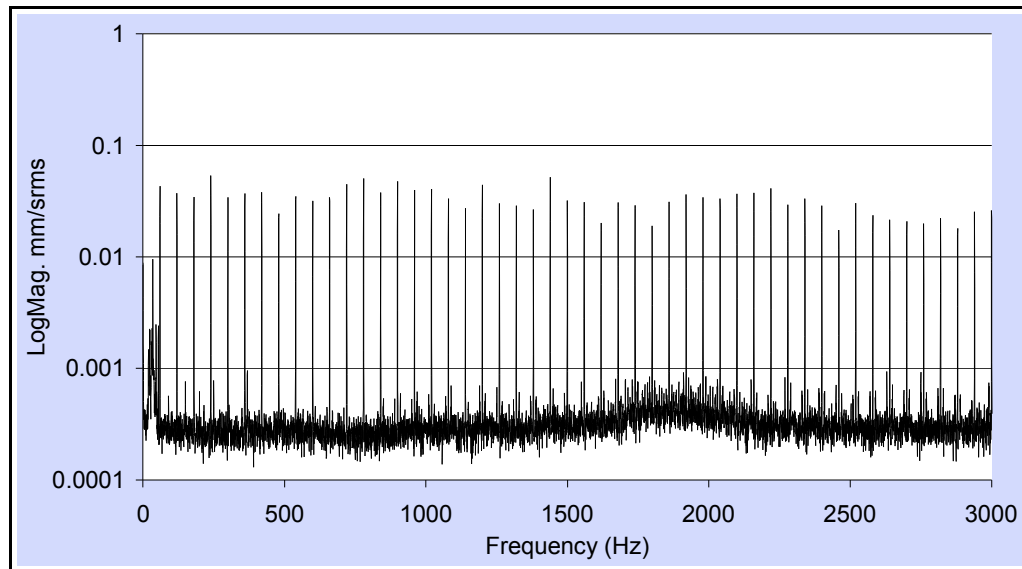


Figure 2.3 - Typical spectrum showing speckle harmonics.
Speckle noise from target vibrating in-plane

The concentration of energy at the frequencies likely to be of most interest to the vibration engineer is particularly problematic making speckle noise indistinguishable from the genuine vibration velocities. For this reason, the term “pseudo-vibration” [2.4] has been used. This noise is generally considered as low level but, as yet, it has not been adequately quantified. The implications of this are that a great deal of interpretation is required, particularly when low level genuine vibrations are concerned. Experimental data in Chapter 5 together with simulated data in Chapter 7 attempt to address this deficiency by quantifying speckle noise levels for the first time for fundamental surface motions of in-plane, tilt and rotation.

2.2 Pseudo-vibration

Pseudo-vibration is attributed to speckle motions on the photodetector. The terms ‘pseudo-vibration’ and ‘speckle noise’ have been used interchangeably but, as shown in Chapter 5, pseudo-vibration is apparent even when speckles are not such a prominent feature of the scatter, i.e. from smoother surfaces. This section looks at speckle noise in measurements from target surfaces moving transverse to the optical axis, tilting and rotating and shows why pseudo-vibration is of such concern.

2.2.1 A surface translating transverse to the optical axis

Figure 2.4 shows a measurement from a surface which is moving transversely to the optical axis of the beam, together with the transverse velocity of the target surface. The surface motion in the direction of the beam is nominally zero and yet the vibration engineer, assessing this data, sees the apparent velocity fluctuating with a distinctive repetition at the same period as the surface motion. The apparent velocity shown is collected under controlled experimental procedures and the data trace is, in this case, dominated by pseudo-vibration. Generally the vibration engineer will likely misinterpret the data. However, using knowledge of the vibration characteristics of the structure or that of speckle noise from an experienced vibrometer user, they may attempt to reconcile the inherent uncertainty.

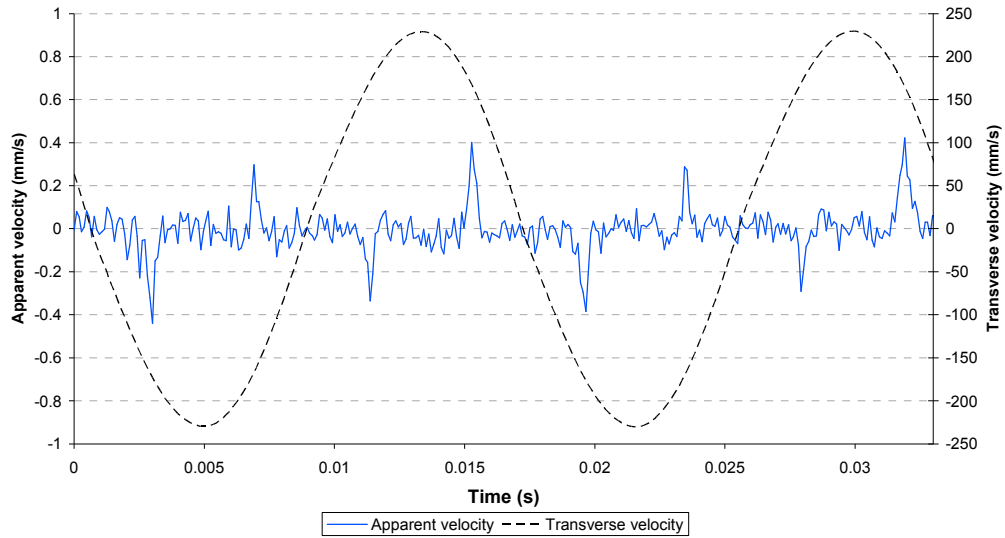


Figure 2.4 - Typical data of the apparent and transverse velocity using a beam spot diameter of $D=600\mu\text{m}$ on a surface with $R_a 1.0\mu\text{m}$.

The vibration engineer can attempt to assess the uncertainty in the frequency domain and this is discussed in the next sub-section. Transverse sensitivity, quantified in Chapter 5, can be used to ascertain the uncertainty in a measurement, such as the one presented in Figure 2.4.

2.2.2 A tilting surface

Figure 2.5 shows a typical spectrum of a ‘measurement’ from a surface which is tilting and has nominally zero vibration in the direction of the beam. This spectrum shows distinct peaks across a very broad frequency range, characteristic of a signal which is dominated by pseudo-vibration. Pseudo-vibration is broadband and can occupy hundreds of harmonics with the same fundamental frequency as the genuine surface motion.

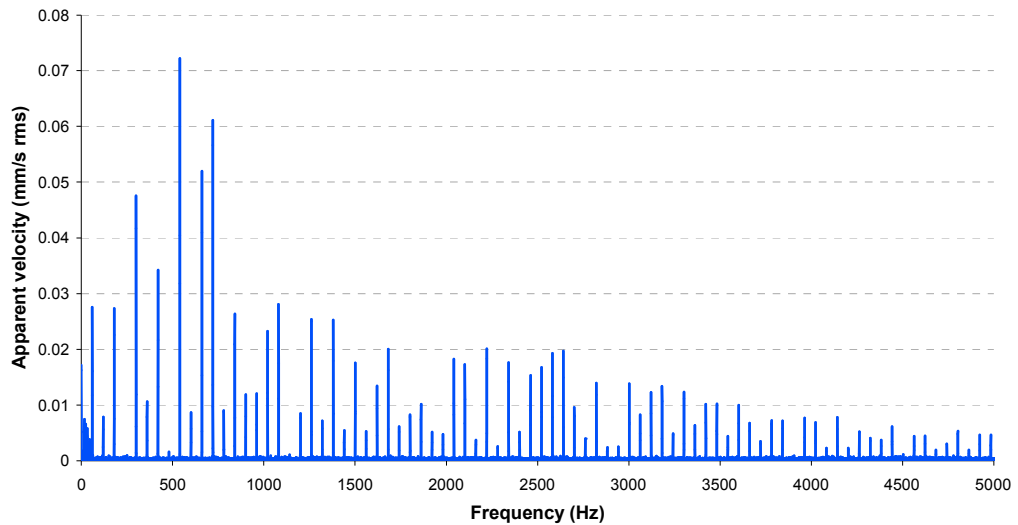
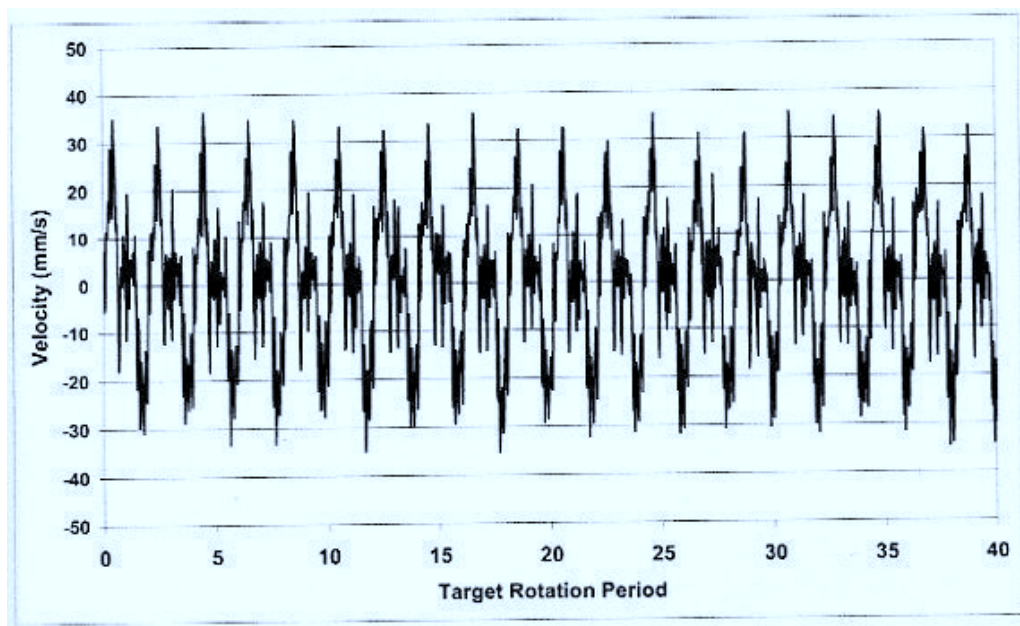


Figure 2.5 – A typical spectrum of apparent velocity dominated by speckle noise from a tilting target.

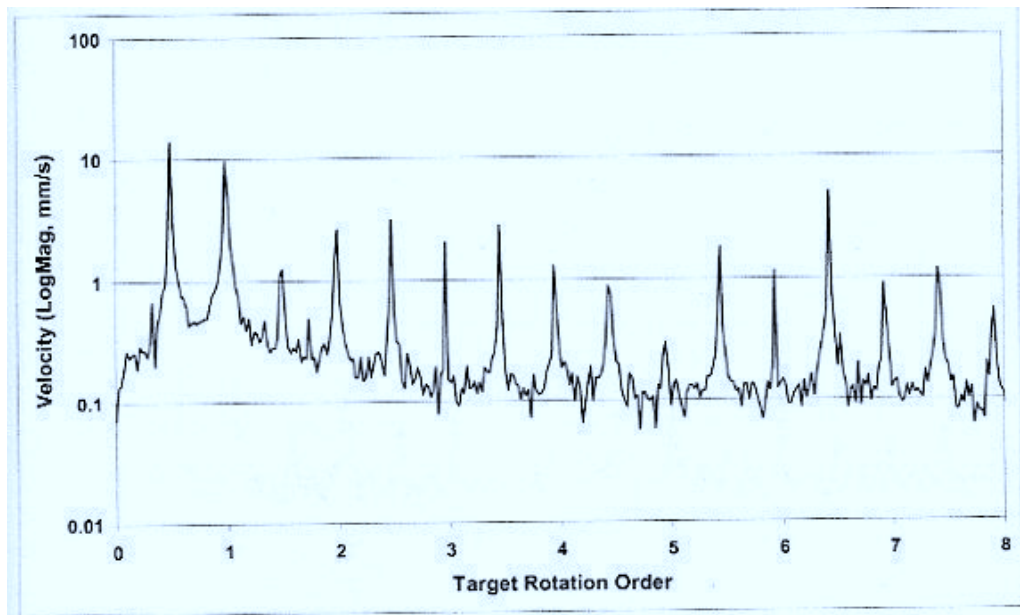
Depending on the laser vibrometer configuration and the surface motion, the amplitude of these harmonics do not diminish over many harmonics and they can be seen to sporadically increase or decrease as the harmonic order increases. It is not unusual for genuine vibrations to be sinusoidal with harmonic distortion but these genuine motions typically cover a smaller number of harmonics at a much lower band of frequencies, with the amplitude generally dropping as the harmonic order increases. With this knowledge of the vibration characteristics of the structure the vibration engineer can make a judgement by observing the amplitude of the peaks in the frequency domain as the harmonic order increases. However, this is not always the case and genuine vibrations of the structure can occupy broad frequency bands. Without knowledge of speckle noise, the vibration engineer, could misinterpret the data in Figure 2.5 as a genuine vibration, particularly if only observing a frequency range covering the first few orders. Chapter 5 quantifies tilt sensitivity and this information can be used, by the vibration engineer, to determine the expected amplitude, at each order, in data such as that presented in Figure 2.5.

2.2.3 A rotating surface

Target rotation is another surface motion causing pseudo-vibration. Figure 2.6 shows data from a radial vibration measurement [2.7] from a 4-stroke, 4-cylinder, 2-litre diesel engine. The vibrometer's laser beam is aligned on the circumferential surface of the flywheel, measuring the radial vibration of the engine's crankshaft.



(a)



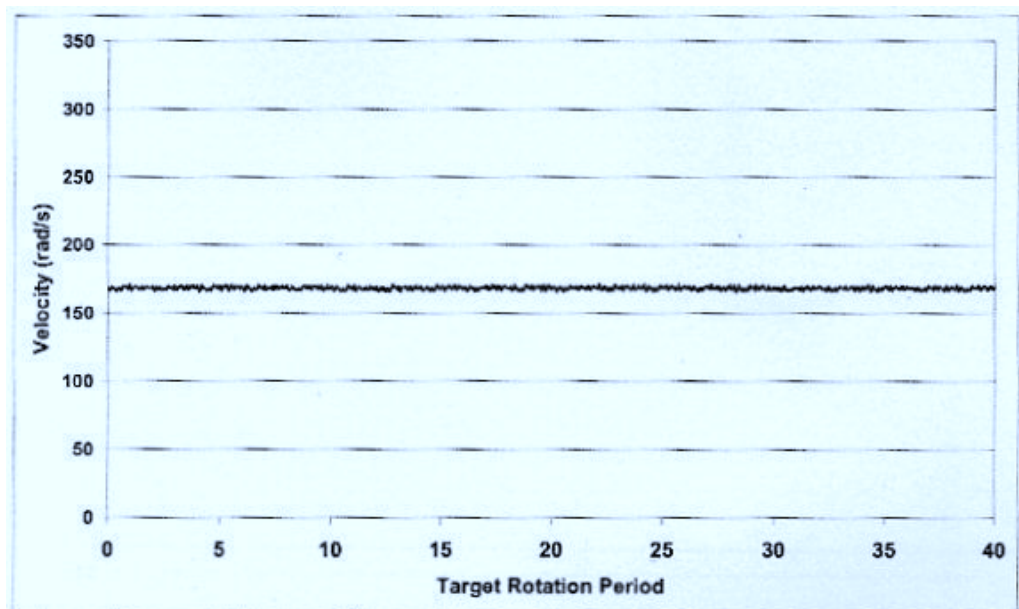
(b)

Figure 2.6 – Radial vibration of 4-stroke, 4-cylinder, 2-litre diesel engine (a) time and (b) frequency domain [2.7]

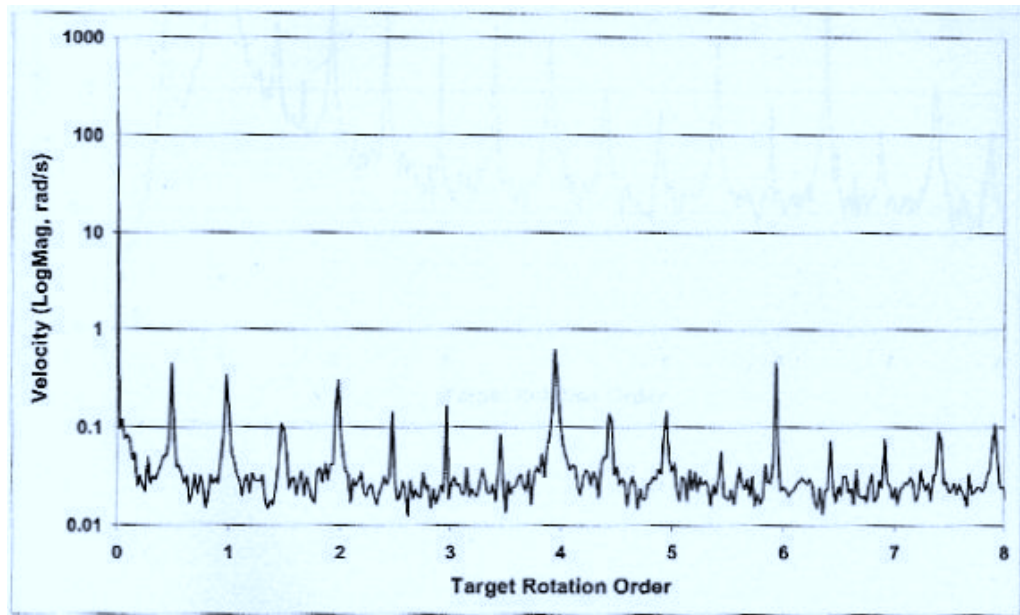
Figure 2.6 (a) is the radial vibration measurement in the time domain showing higher frequency components superimposed on the lower frequency components. The higher frequency components may be genuine velocity, but the vibration engineer should be questioning this. The speckle pattern will repeat at the same frequency as the rotation and so one should expect pseudo-vibration at the rotation frequency plus many harmonics. Figure 2.6 (b) shows the radial vibration measurement in the frequency domain presented in terms of rotation order. Many harmonic peaks can be seen with a fundamental $\frac{1}{2}$ order rotation typical of 4-stroke engine vibration. Therefore, pseudo-vibration will coincide with the genuine vibration at integer harmonics and it is difficult to distinguish the pseudo-vibration from genuine vibration. Chapter 4 addresses this by quantifying rotation sensitivity. From this the vibration engineer can determine the level of noise expected at each harmonic order of the rotation frequency.

2.2.4 Parallel beam laser vibrometer configuration

This particular measurement involves using a vibrometer which emits a pair of parallel laser beams, quantifying the rotation velocity through a difference in the velocity. This sort of measurement and, indeed, any differential measurement exacerbates the effects of speckle noise in the output of the vibrometer. Figure 2.7 shows a measurement of the rotation speed of the aforementioned 4-cylinder diesel engine using a parallel beam vibrometer [2.7].



(a)



(b)

Figure 2.7 – Rotation velocity of 4-stroke, 4-cylinder, 2-litre diesel engine (a) time and (b) frequency domain using parallel beam vibrometer [2.7]

Figure 2.7 (a) is the temporal data of the rotation velocity and, on the scale shown, subtle fluctuations in the velocity can be seen. In the frequency domain, shown in Figure 2.7 (b), this can be seen as harmonic peaks with a $\frac{1}{2}$ order fundamental. Some of this will likely be genuine torsional vibrations but pseudo-vibration is also affecting this data. The question can reasonably be raised, how much speckle noise can be expected on this measurement? This question can be answered using the rotation sensitivity for parallel beams quantified in Chapter 5.

2.2.5 Differential measurements

Any differential measurement exaggerates the effects of speckle noise. This is even more the case when performing a differential measurement using two parallel beam laser vibrometers. Figure 2.8 shows a differential velocity

measurement [2.8] between the crankshaft pulley and alternator pulley of a diesel engine. Two laser rotational vibrometers are used to measure the angular velocity of the two pulleys. A difference is calculated from the tangential velocities and the resulting spectrum is shown in Figure 2.8.

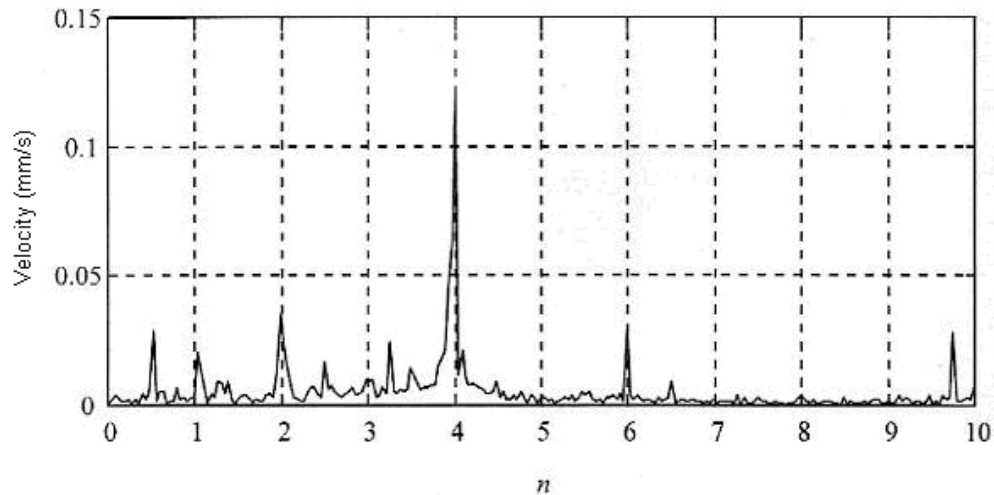


Figure 2.8 – Differential velocity measurement across an alternator belt of a diesel engine [2.8]
(n is rotation order)

In this measurement Bell [2.8] highlights that the magnitude of the resulting velocity is typically large in comparison to the speckle noise levels. This was an assumption, a reasonable one by an experienced vibrometer user, but an assumption none the less. Bell raises the point that, without further progress, speckle noise is a limiting factor for other such measurements where differences in the measured velocities can be small such as in a measurement of shaft twist, requiring closely spaced measurements axially separated along the shaft. This deficiency is addressed from the experimental study shown in Chapter 5.

One situation where distinguishing the genuine differences in velocity fluctuations could be limited by speckle noise levels is in measurement of dynamic backlash in a gear train. The next section investigates the possibility of this novel measurement with particular consideration given to speckle noise.

2.3 Pseudo-vibration in differential measurements: dynamic backlash

Using two laser rotational vibrometers, it was proposed that a novel differential measurement can be performed to measure the dynamic backlash within a meshing pair of rotating gears. The individual measurements will contain speckle noise and the uncorrelated nature of the speckle patterns amplifies the effect of speckle noise in the differential measurement. For the purposes of verification, images of the mesh point were produced using a high speed digital camera.

2.3.1 Experimental Configuration

Figure 2.9 (a) shows the experimental setup. Two rotational vibrometers measure oscillations in rotational velocity on a meshing pair of rotating spur gears. The two pairs of beams were incident on the bosses of the respective gears and aligned parallel with each other and perpendicular to each rotational axis as shown in Figure 2.9 (b). The gears had pitch circle diameters (PCD) of 72mm and 40mm with 90 teeth and 50 teeth respectively, with a circular pitch of 2.513mm. Drive was via direct coupling of a 12V DC motor to the 40PCD gear with the 72PCD gear unloaded. Each gear boss was treated with retro-reflective tape. The meshing point of the gears was white light illuminated with a halogen lamp and imaged with a high speed digital camera which had a frame rate of 4.5kHz and a spatial resolution of approximately 28 μ m/pixel. The

motor was driven with a DC voltage on top of which a nominally sinusoidal oscillation can be induced. The variation in motor drive voltage promotes a fluctuation in rotational speed of the drive gear and sets up a dynamic backlash.

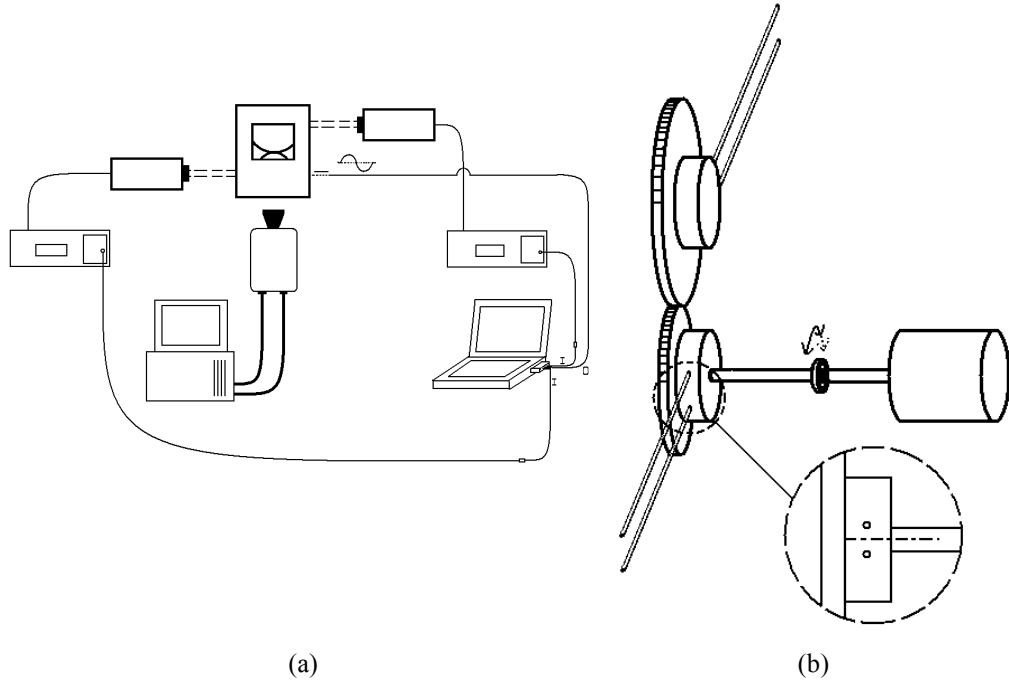


Figure 2.9- Experimental set-up of dynamic backlash measurement

Dynamic backlash is calculated using the relative tangential separation between a pair of meshing rotating spur gears over a time period. The relative tangential separation, $s(t)$ is given by

$$\begin{aligned}
 s(t) = & \left(r_A \theta_A(0) - r_B \theta_B(0) \right) + \left(r_A \bar{\Omega}_A - r_B \bar{\Omega}_B \right) t \\
 & + \left(r_A \int_0^t \Delta \Omega_A(\tau) d\tau - r_B \int_0^t \Delta \Omega_B(\tau) d\tau \right)
 \end{aligned} \tag{2.3}$$

where subscripts A and B denote relation to gears A and B respectively, r_A and r_B are the contact radii, $\theta_A(0)$ and $\theta_B(0)$ are the initial angular positions,

$\Omega_A = \bar{\Omega}_A + \Delta\Omega_A$ and $\Omega_B = \bar{\Omega}_B + \Delta\Omega_B$, Ω_A and Ω_B are the total angular velocities, $\bar{\Omega}_A$ and $\bar{\Omega}_B$ are the mean angular velocities and $\Delta\Omega_A(\tau)$ and $\Delta\Omega_B(\tau)$ are the alternating components of the angular velocities. The first bracketed term is the initial relative position. This cannot be extracted from the vibrometer data and, unless acquisition is taken from a known relative position which in general is impractical, this quantity will remain unknown. The second bracketed term is the mean component of the relative tangential displacement and is zero for meshing gears. The third term is the alternating component of the relative tangential displacement and is defined here as the dynamic backlash.

The backlash in the gears is governed by the contact radius for each gear. It is entirely possible that the separation distance between centres of rotation may not be the sum of the pitch circle radii, in which case contact will not occur at the pitch circle radii. The contact radii are dictated by the number of gear teeth, the distance between the centres of rotation and the pitch circle radii but the tangential velocities of each gear are always equal at the contact position when there is contact and the ratio of mean angular velocities is always uniquely set by the ratio of the number teeth. Therefore, the following relationships apply

$$\frac{N_A}{N_B} = \frac{\bar{\Omega}_B}{\bar{\Omega}_A} = \frac{r_A}{r_B} = \frac{r_{APCR}}{r_{BPCR}} = \frac{\Delta r_A}{\Delta r_B} \quad (2.4)$$

where N_A and N_B are the number of teeth on each gear, r_{APCR} and r_{BPCR} are the pitch circle radii, and Δr_A and Δr_B are the distances from pitch circle radii to the point of tooth contact along a line between the axes of rotation of the gears. The pitch circle radii are known quantities and are convenient as a means for comparison between gear sets. However any relative tangential position can be measured as long as the radial positions conform to the ratio as seen in Equation (2.4). Therefore, dynamic backlash is further defined as the time

dependent tangential separation at the pitch circle radii using the third term in Equation (2.3).

2.3.2 Verification using high speed digital camera

Verification of the dynamic backlash is made by correlating data calculated from the vibrometers with measurements taken from video images. Verification is made at the pitch circle radii, but with knowledge of the separation it is possible to calculate the relative tangential displacement at the radial contact position. The video footage from the high speed camera is dissected into its individual frames. Pixel measurements of the circular pitch are made and a spatial resolution calculated. Pixel measurements are taken from between teeth at the pitch circle radii and converted into a backlash measurement. A backlash range can be found by measurements taken from subsequent tooth face impacts.

Figure 2.10 shows an example of the method by which the measurements are taken to calculate the backlash range. A vertical broken line shows the position of the pitch circle radius of the bottom drive gear and a vertical solid line shows the position of the pitch circle radius of the top driven gear. In frame 00180 at the pitch circle radii there is a tangential distance of 11 pixels which equates to a backlash measurement of -0.307mm, in frame 00218 the backlash measurement is 0.195mm, therefore the dynamic backlash range equates to 0.5026mm.



Figure 2.10 - Backlash measurement on consecutive tooth face impacts.

2.3.3 Dynamic backlash using two laser rotational vibrometers

Experiments have been conducted with sinusoidal rotational excitation of the drive gear, with and without whole body rotation. With whole body rotation and sinusoidal oscillation, the gear undergoes a speed fluctuation about the mean rotational speed. With sinusoidal excitation, only, the gear oscillates angularly about a mean position.

Figure 2.11 is an extract from video footage of a 60Hz sinusoidal oscillation of the drive gear in the absence of whole body rotation. The individual frames show the meshing process with 13 frame intervals. Imaged is the mesh point of a drive gear (bottom) and driven gear (top). For oscillating targets with or without whole body rotation, the motion of the gears can be described as follows:

Frame 1: Teeth in contact, clockwise rotation of the drive gear and anti-clockwise rotation of the driven gear.

Frames 2&3: After reaching the extreme of its oscillation cycle, the drive gear begins to rotate anti-clockwise, contact is lost and the driven gear continues to rotate anti-clockwise.

Frame 4: Drive gear continues to rotate anti-clockwise until impact occurs between teeth. This rapidly decelerates the driven gear and causes it to rotate clockwise.

Frames 5&6: After reaching the extreme of its oscillation cycle, the drive gear begins to rotate clockwise again, contact is lost and the driven gear continues to rotate clockwise.

With whole body rotation, the behaviour of the gears is identical, the oscillations are simply superimposed on top of the mean rotations.

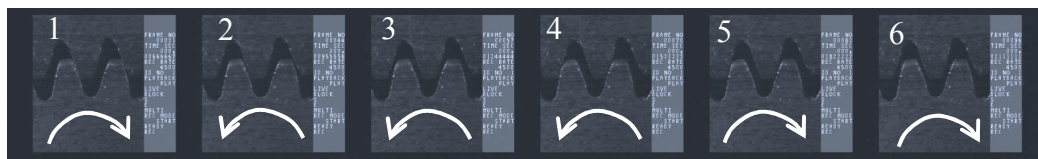


Figure 2.11–Video footage showing gear motion with 60Hz sinusoidal excitation (no whole body rotation). Bottom gear is the drive gear and top gear is the driven gear.

For the drive gear rotating at 217rpm (rotation speed is limited to approximately 280rpm when using the high speed video) with a 60Hz sinusoidal excitation, Figure 2.12 shows the dynamic backlash as calculated from Equation (2.3). Figure 2.13 displays the dynamic backlash at the pitch circle radii for a gear set with 60Hz sinusoidal oscillation but without whole body rotation. The dynamic backlash ranges and duration of events are consistent between Figure 2.12 and Figure 2.13. This confirms that this method can reliably evaluate backlash under rotating conditions. A periodic waveform of fundamental frequency 60Hz is observed and this is attributed to the sinusoidal modulation of the drive. Interpretation of the waveform is consistent

with the process described in Figure 2.11. The sections of virtually zero slope at (approximate) maxima and minima are the periods of tooth contact, on average of 2.3ms duration. This duration is consistent with the 2.4 ± 0.2 ms estimated from the relevant frames of the video footage. Within these regions of tooth contact are small oscillations. The magnitude of these oscillations is below $8\mu\text{m}$ which is below the resolution limit of the camera. These oscillations are likely to be a bounce [2.9]. The sections with a large change in dynamic backlash equate to periods where the driven gear is not in contact with the drive gear and this is the transition stage from one tooth face to another. The average duration of this transition is estimated to be 5.9ms which is a little larger than the 5.5 ± 0.2 ms estimated from the video footage. The dynamic backlash range on average is 0.51mm which, as described in Section 2.3.2, is consistent with that found from the video footage.

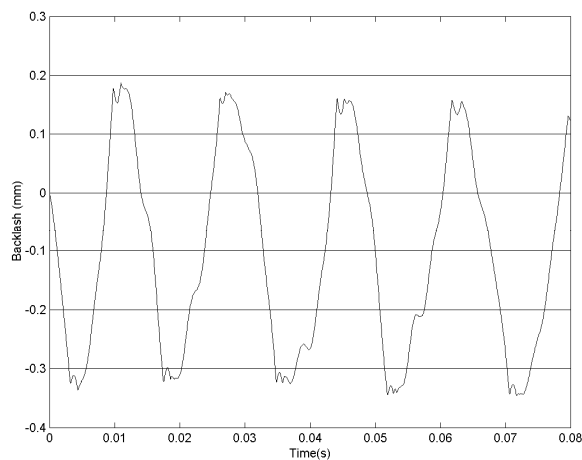


Figure 2.12 - Backlash with sinusoidal excitation at 60Hz, with whole body rotation of the drive gear at 217rpm

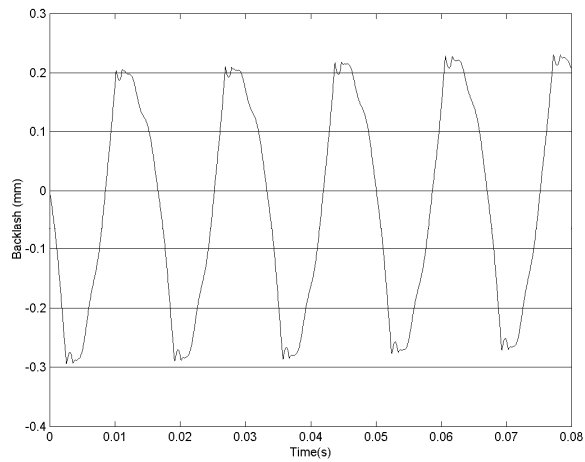


Figure 2.13 - Backlash with sinusoidal excitation at 60Hz, without whole body rotation

This limited rotational speed is not representative of typical industrial applications so experiments were conducted to observe any issues associated with a measurement at increased rotational speed. Figure 2.14 shows calculated backlash when the drive gear is rotating at 1800rpm with a periodic but harmonically distorted oscillation with a 50Hz fundamental frequency superimposed on the drive. This oscillation is a prominent feature of the waveform containing regions of tooth contact and also periods of tooth separation. In this experiment, a reduced gear separation of the centres has resulted in a slightly decreased peak dynamic backlash.

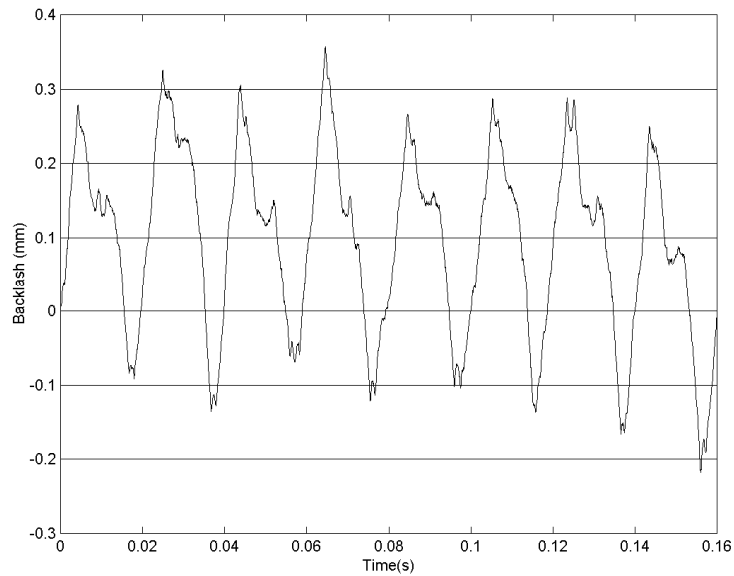


Figure 2.14 – Backlash, drive gear rotating at 1800rpm and oscillating with 50Hz fundamental frequency.

Speckle noise is present in the data presented in Figures 2.12 to 2.14. However it is difficult to observe the specific influence speckle noise has on the dynamic backlash measurement and therefore this is to be investigated using simulation which is discussed in the next sub-section.

2.3.4 Simulation of dynamic backlash

The effect speckle noise has on the dynamic backlash measurement technique has been examined through simulation. The simulator begins with the user specified information regarding the acquisition, experimental information such as the number of gear teeth and also information about the signal waves. Two sine waves are created and then adjusted to replicate the motion of the gears. The gear set motion has been simplified and scaled appropriately to create two waveforms to represent the voltage outputs from the vibrometers as shown in Figure 2.14. In the simulation, the drive gear oscillates sinusoidally and the

driven gear remains at a constant velocity until tooth contact occurs. The drive gear sinusoidal motion has been clipped to make the angular velocity constant during periods of contact. The duration of contact is made equivalent (15% of period) to that observed in real vibrometer data and video footage. To simulate speckle noise, pseudo-random signals are created by a normally distributed random number generator. The signals repeat at the same frequency as rotation frequency and are scaled in accordance with an estimate from the noise seen on the real vibrometer data.

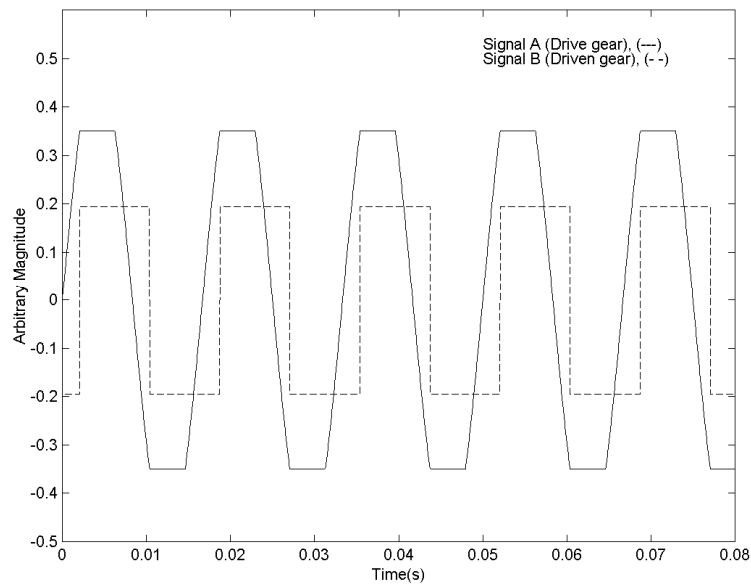


Figure 2.15 - Simulated signals of vibrometer output without the addition of speckle noise

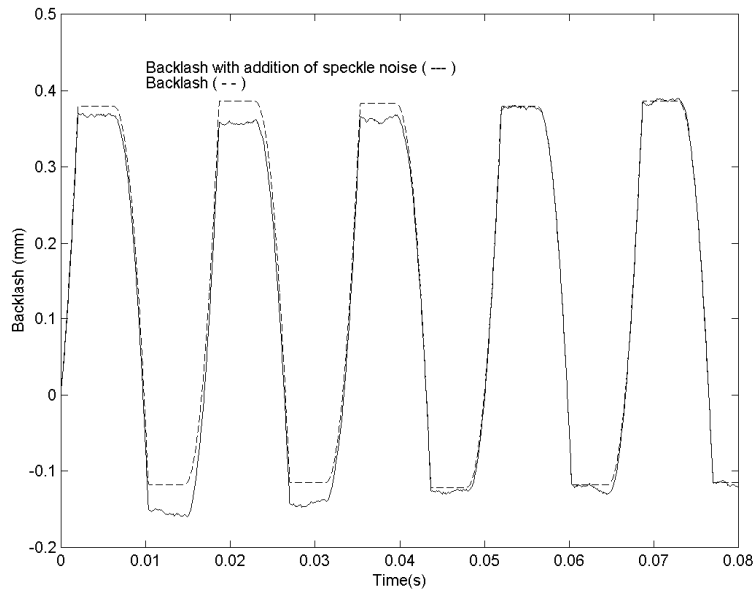


Figure 2.16 – Calculated dynamic backlash from simulated vibrometer outputs before and after the addition of noise.

The influence speckle noise has on the time series is shown in Figure 2.16. The calculated dynamic backlash, with the addition of speckle noise, shows a drift across the data length in comparison to the dynamic backlash data without additional noise. This is due to the integration of low frequency information added by the influence of speckle noise. Small variations in the backlash can also be seen and this is also due to the influence of speckle noise. The pseudo-random signals, created to simulate speckle noise, produce peaks at the fundamental frequency of simulated rotation and subsequent harmonics which maintain their amplitude up to a high order. The fundamental frequency of the drive sinusoidal oscillation is a dominant component within the spectrum.

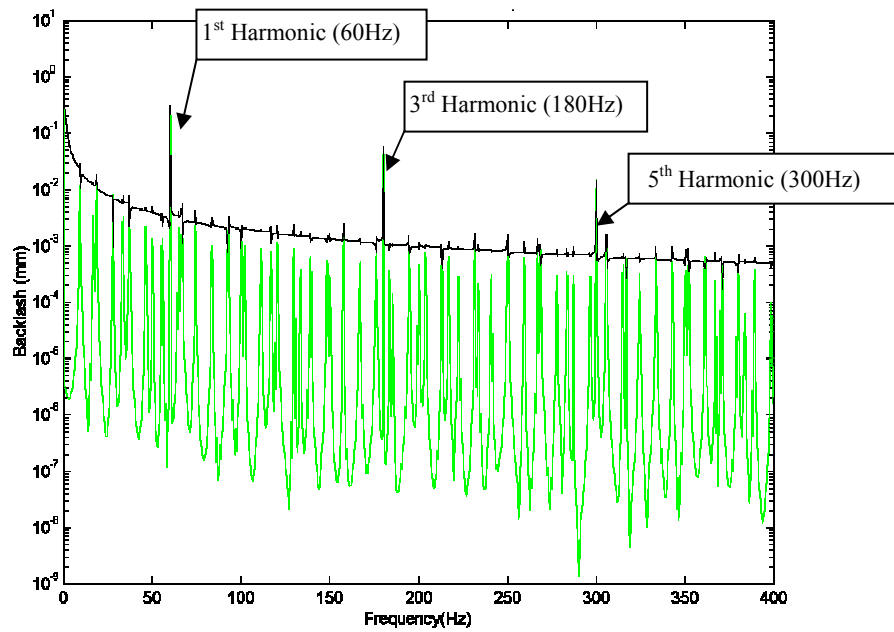


Figure 2.17 - Backlash calculated with integration in time domain (black) and frequency domain (green, hanning windowed to reduce leakage). Drive gear rotating 1000rpm, oscillation at 60Hz

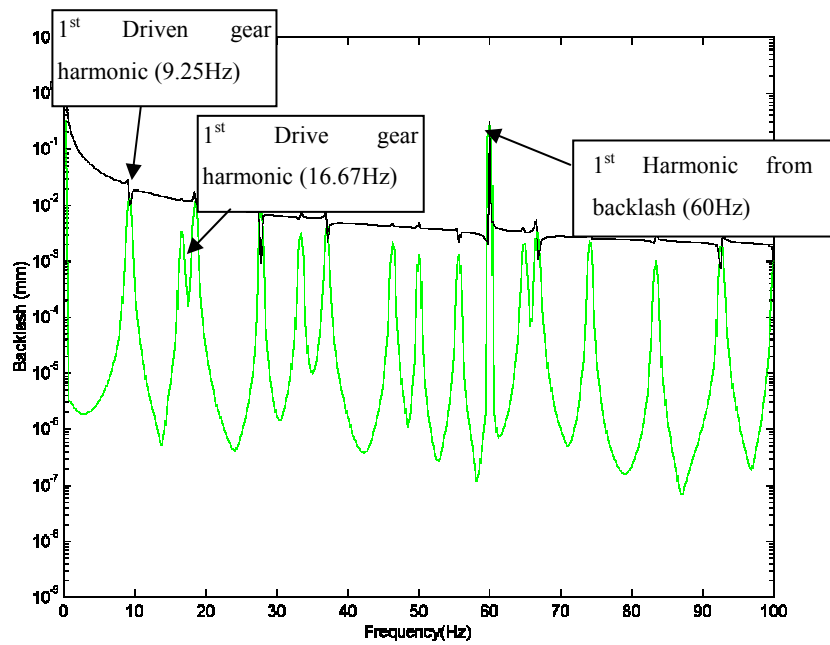


Figure 2.18 – Pseudo-random signal harmonics (speckle harmonics) on backlash spectrum

Figure 2.17 shows the 1st, 3rd and 5th harmonic of the oscillation frequency. The calculated backlash exhibits odd diminishing harmonics and is typical of the spectrum produced by a square wave. Evident are also the harmonics of the pseudo random signal simulating the speckle repetition, Figure 2.17. The simulation mimics the experimental data seen in Figure 2.12. Leakage is a significant factor for consideration in spectral analysis as it spreads the energy to adjacent frequencies and therefore diminishes the content at specific frequencies. Leakage adds low frequency content to the spectrum which is exaggerated by the integration. Visualisation in the time domain requires the inverse Fourier Transform function to be applied to the backlash data. On performing the inverse Fourier transform of the backlash, the lower frequency content caused by leakage is apparent. Windowing reduces the effect of leakage but on performing the inverse Fourier transform, the data becomes distorted at the extremities of the data length. It can be seen from Figure 2.17 and Figure 2.18 that windowing and using the frequency domain integration retains lower level information.

Figure 2.19 shows a comparison of the simulated backlash and the measured experimental backlash using frequency domain integration. The simulated backlash is scaled to the same level as that seen in the experimental data. Evident in both experimental and simulated backlash data are peaks associated with speckle periodicity. The speckle periodicity is apparent at both drive gear and driven gear rotation frequencies and is evident in the experimental and simulated backlash.

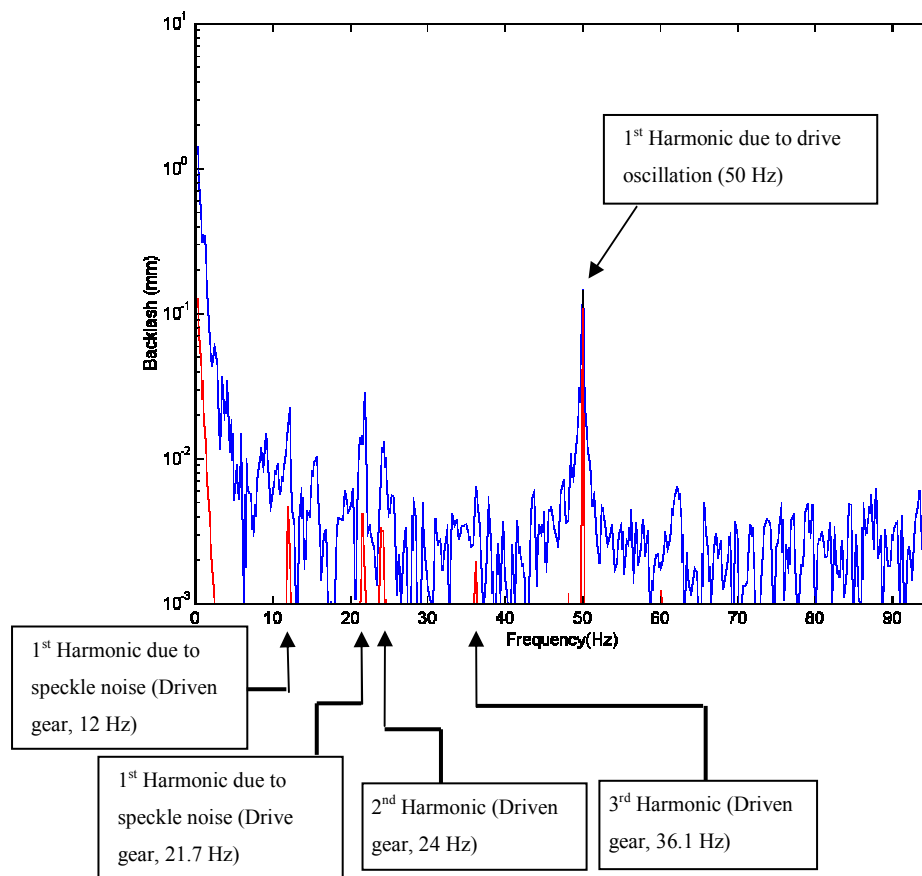


Figure 2.19 – Experimental (blue) and Simulated (red) backlash using frequency domain integration, drive gear rotating at 1300rpm with 50Hz oscillation.

If the gears were the same size then the influence of speckle noise from each gear would occur at the same frequency. This would amplify the affect of speckle noise, statistically, by a factor of about $\sqrt{2}$. Additionally if the oscillation frequency of the drive gear operates at the same frequency as either of the rotation frequencies then speckle noise would be coincident with the genuine angular vibration and more difficulty would be found in interpreting the data. However, this research has shown that although speckle noise does influence the differential measurement, dynamic backlash can be measured successfully.

A novel measurement of dynamic backlash has been presented showing the influence speckle noise can have in a differential measurement. In the simulation of dynamic backlash an estimate was made of the level of speckle noise (from the experimental data). Although this estimate indicated the influence pseudo-vibration can have in a differential measurement it was not sufficient to predict the sensitivity. The rotation sensitivity for parallel beam vibrometers described in Chapter 5 is sufficient to predict the rotation sensitivity for each rotational vibrometer. Therefore if the frequency of the whole body rotation of one or both gears is coincident with the oscillation frequency the rotation sensitivity for parallel beam vibrometers can be used to better interpret the apparent dynamic backlash observed.

3 Properties of a stationary speckle

In a laser vibrometer, the light incident on the photodetector surface consists of the contributions from a target beam and a reference beam. At least one of these and in some instances both will be in the form of a speckle pattern. As previously described, the speckle pattern is formed from the scattering of coherent light from an optically rough surface. The microscopic surface detail is unknown. So the speckle pattern formation is considered a stochastic process and statistics are used to describe the properties. First order statistics are used to describe the statistics at a single point in space and this chapter uses them to form characteristic properties of a speckle.

3.1 Formation of a speckle

As discussed in Section 1.2.1, the illumination of an optically rough surface causes diffuse scatter. Observation of the scatter, a distance away from the target surface, is the resultant of the field intensity of many elementary scattered field contributions. Each of the elementary contributions from the surface scatterers can be considered as a phasor. The resultant field is a summation of many phasors and is analogous with the classical problem of a random walk in a complex plane.

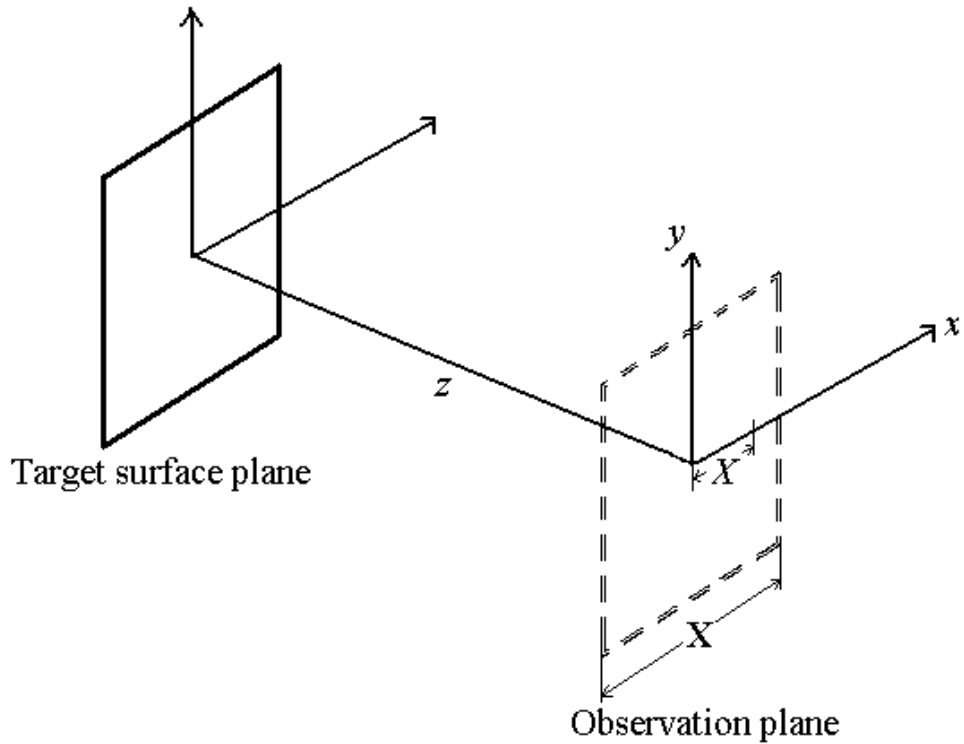


Figure 3.1 - Schematic of the coordinate system used in the statistical properties

At any point on the observation plane (x,y,z) , visualised in Figure 3.1, the complex field with amplitude, E_0 , and phase, Φ , can be written in terms of P elementary phasor contributions [3.1, 3.2, 3.3].

$$E_0 \exp[j\Phi] = \sum_{p=1}^P e_p \exp[j\varphi_p] \quad (3.1)$$

Where e_p and φ_p are the amplitude and phase of the p^{th} elementary phasor respectively. The sum shown in equation (3.1) can be represented as a two dimensional random walk as in Figure 3.2.

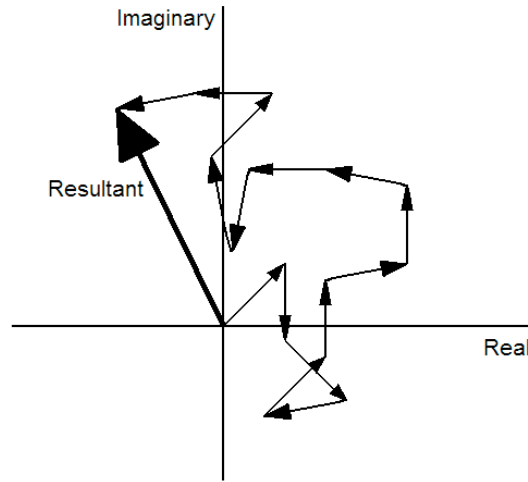


Figure 3.2 - Random walk in a complex plane

The target surface roughness is considered such that the phases are uniformly distributed between π and $-\pi$ [3.1] and therefore the phasors shown in Figure 3.2 have an equal probability of pointing in any given direction. If all phasor amplitudes are considered equal such that $e_p = e$ for all p , the summation of the real and imaginary parts allows the square of the amplitude of equation (3.1) to be written.

$$E_0^2 = e^2 \left[\sum_{p=1}^P \cos \varphi_p \right]^2 + e^2 \left[\sum_{p=1}^P \sin \varphi_p \right]^2 \quad (3.2)$$

which can be expanded to give

$$E_0^2 = e^2 \left[\sum_{p=1}^P \sum_{m=1}^P \cos \varphi_p \cos \varphi_m + \sum_{p=1}^P \sum_{m=1}^P \sin \varphi_p \sin \varphi_m \right] \quad (3.3)$$

and it follows that

$$E_0 = e \left[\sum_{p=1}^P \sum_{m=1}^P \cos(\varphi_p - \varphi_m) \right]^{1/2} \quad (3.4)$$

and the tangent of the phase can simply be written

$$\tan \Phi = \frac{\sum_{p=1}^P \sin \varphi_p}{\sum_{p=1}^P \cos \varphi_p} \quad (3.5)$$

Equations (3.4) and (3.5) are used in Chapter 7 in the formation of speckles in simulations for estimating speckle noise. Averaging the real and imaginary components for an ensemble of similar optically rough surfaces using equation (3.1), with uniformly distributed phases in the range $-\pi$ to π yields [3.1]

$$\langle \Re [E_0 \exp[j\Phi]] \rangle = e \sum_{p=1}^P \langle \cos \varphi_p \rangle = 0 \quad (3.6)$$

$$\langle \Im [E_0 \exp[j\Phi]] \rangle = e \sum_{p=1}^P \langle \sin \varphi_p \rangle = 0 \quad (3.7)$$

where the angle brackets denote a mean value. Calculating the variance of the real and imaginary components, respectively, can be shown by [3.1]

$$\left\langle \left(\Re[E_0 \exp[j\Phi]] - \langle \Re[E_0 \exp[j\Phi]] \rangle \right)^2 \right\rangle = \left\langle \left(\Re[E_0 \exp[j\Phi]] \right)^2 \right\rangle \quad (3.8)$$

$$\begin{aligned} \left\langle \left(\Re[E_0 \exp[j\Phi]] \right)^2 \right\rangle &= e^2 \sum_{p=1}^P \sum_{m=1}^P \langle \cos \varphi_p \cos \varphi_m \rangle \\ &= P \frac{e^2}{2} \end{aligned} \quad (3.9)$$

$$\left\langle \left(\Im[E_0 \exp[j\Phi]] - \langle \Im[E_0 \exp[j\Phi]] \rangle \right)^2 \right\rangle = \left\langle \left(\Im[E_0 \exp[j\Phi]] \right)^2 \right\rangle \quad (3.10)$$

$$\begin{aligned} \left\langle \left(\Im[E_0 \exp[j\Phi]] \right)^2 \right\rangle &= e^2 \sum_{p=1}^P \sum_{m=1}^P \langle \sin \varphi_p \sin \varphi_m \rangle \\ &= P \frac{e^2}{2} \end{aligned} \quad (3.11)$$

This shows that the real and imaginary components of the phasor summation have zero mean and equal variances; the significance of this result is discussed in Section 3.2.

3.2 Speckle intensity and phase

The process of creating a speckle is stochastic and therefore probability theory is used to ascertain the probable intensity and phase of a speckle. A simple way to represent a speckle is the resultant of the complex field shown in equation (3.1). As discussed in Section 3.1, the amplitude and phase of a speckle are the summation of many random phasor contributions. The Central Limit Theorem states that the sum of a large number of independent random variables with finite mean and variance will tend to a Gaussian distributed probability density function [3.4, 3.5]. As shown by Equations (3.6) to (3.11) the real and imaginary parts both have zero mean and identical variances and therefore the Central Limit Theorem applies. In a complex plane, this produces a circularly symmetric Gaussian density function whose mean and variance does not alter with time. From this, the joint probability density of the amplitude and phase takes the form [3.1, 3.2]

$$P(E_0, \Phi) = \frac{E_0}{\pi \langle E_0^2 \rangle} \exp \left[-\frac{E_0^2}{\langle E_0^2 \rangle} \right] \quad (3.12)$$

Intensity rather than amplitude is of more practical concern and therefore using the transformation of variables [3.2] it is possible to show the joint probability density function of the intensity and phase as

$$P(I, \Phi) = \frac{1}{2\pi \langle I \rangle} \exp\left[-\frac{I}{\langle I \rangle}\right] \quad (3.13)$$

where $\langle I \rangle$ is the mean intensity. Integrating the joint probability density between appropriate limits, the corresponding marginal densities of intensity

$$P(I) = \int_{-\pi}^{\pi} P(I, \Phi) d\Phi \quad (3.14)$$

$$P(I) = \begin{cases} \frac{1}{\langle I \rangle} \exp\left[-\frac{I}{\langle I \rangle}\right] & I \geq 0 \\ 0 & \text{otherwise} \end{cases} \quad (3.15)$$

and phase

$$P(\Phi) = \int_0^{\infty} P(I, \Phi) dI \quad (3.16)$$

$$P(\Phi) = \begin{cases} \frac{1}{2\pi} & -\pi \leq \Phi \leq \pi \\ 0 & \text{otherwise} \end{cases} \quad (3.17)$$

can be found. It can be seen that $P(I, \Phi) = P(I)P(\Phi)$ and therefore the probability density function of intensity is statistically independent from the phase [3.1]. Equation (3.17) shows the phase is uniformly distributed between $-\pi$ and π . Equation (3.15) visualised in Figure 3.3 with a unit mean intensity shows the intensity distribution for a complex Gaussian process is a negative

exponential [3.2, 3.6, 3.7, 3.8, 3.9, 3.10] with the most likely outcome of zero intensity.

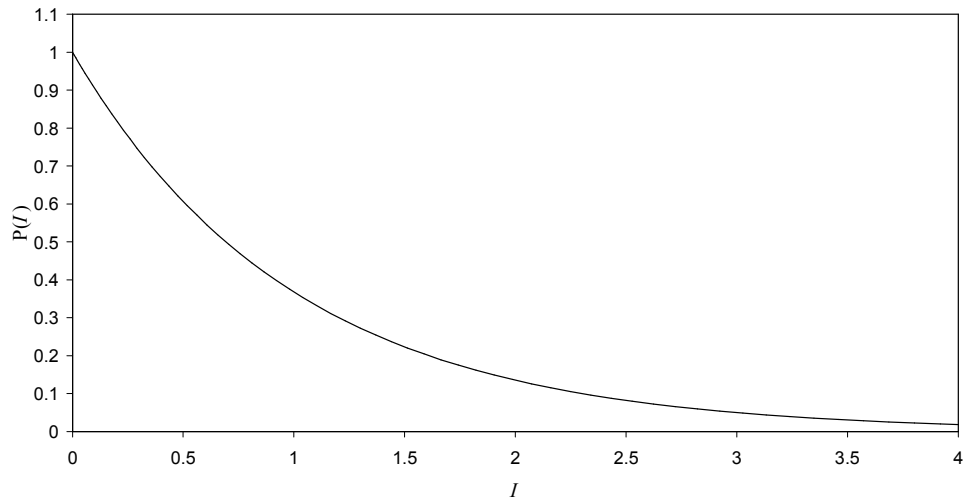


Figure 3.3 - Probability density function of intensity for a speckle pattern with unit mean

Experimentally this relationship has been well documented and perhaps the most comprehensive is that of McKechnie [3.10] who made 23,000 measurements of intensity as shown in Figure 3.4.

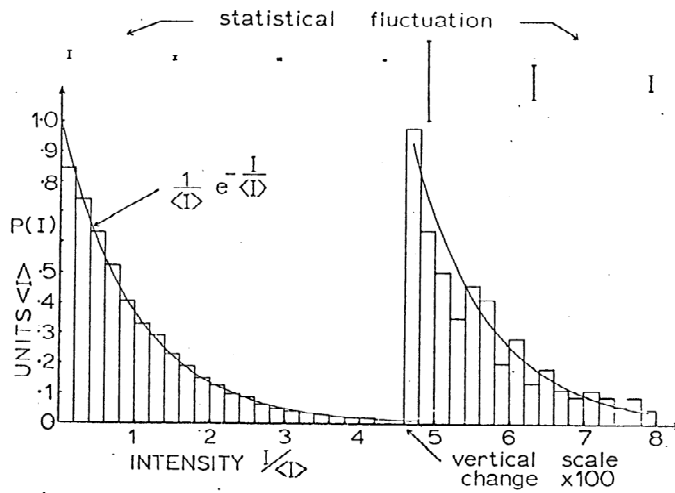


Figure 3.4 - McKechnie's histogram based on 23,000 intensity measurements taken from a speckle pattern [3.10].

The statistics of intensity and phase are used in Chapter 7 in numerical simulations for the development of speckle behaviour encountered in laser vibrometry.

3.3 Contrast

Another notable quantity is a measure of the spread of the intensity relative to the average and is known as the contrast, C . This can be quantified using the ratio of the standard deviation to the mean intensity [3.3, 3.7, 3.8, 3.9].

$$C = \frac{\sqrt{\langle I^2 \rangle - \langle I \rangle^2}}{\langle I \rangle} \quad (3.18)$$

The variance, for a fully developed speckle pattern, can be shown to equal the square of the mean intensity [3.8, 3.9]. Therefore, with this definition, it can be

seen that the contrast of a fully developed speckle pattern is always unity. However this result is not true if the surface roughness or the number of scatterers is reduced and the phase variations are not uniformly distributed in the full $-\pi$ to π range [3.7, 3.8, 3.11, 3.12]. The contrast is used to quantify the degree of development in various speckle patterns observed in Chapter 6.

3.4 Speckle Size

The size of a speckle is formed from statistical parameters of the spatial distribution of the intensity. Evident from the speckle pattern images seen in Figures 1.7, 1.8 and 2.2 together with the probability density function seen in Section 3.1 the spatial structure of a speckle pattern is a chaotic distribution of intensity peaks and nulls. The size of a speckle not only aids in a description of the spatial structure, it also identifies the spatial extent resulting in a notable change in the field. The average speckle size is defined by the spatial autocorrelation function of intensity. This function quantifies the statistical relationship of two points in space based on their intensity and hence provides a method of quantifying the size of the speckle. The coordinate system used in the autocorrelation function can be visualised in Figure 3.1. The mean speckle size is defined by the spatial delay or width of the autocorrelation function. The width is characterised by the first minimum or by $\exp[-2]$ if the autocorrelation function has Gaussian form. Expressions for the size of a speckle differ depending on the geometry of the illuminating beam. For a uniform square illuminating beam of dimension L_B the mean speckle size can be found from the autocorrelation function, $\Gamma_{\Delta I}$, [3.9]

$$\Gamma_{\Delta I}(X) = \langle I \rangle^2 \left[1 + \text{sinc}^2 \left(\frac{L_B X}{\lambda z_S} \right) \right] \quad (3.19)$$

Where X is the separation distance in the x direction on the observation plane, z_S is the axial distance from target to observation plane and λ is the wavelength of the illuminating beam. The mean speckle size is taken as the average width and is defined by the value of X when the sinc^2 term first falls to zero. At this point, $L_B X / \lambda z_S$ is equal to unity and therefore the average size of a speckle, $\langle \sigma_0 \rangle$, can be expressed as

$$\langle \sigma_0 \rangle = \frac{\lambda z_S}{L_B} \quad (3.20)$$

For a uniform circular illuminating beam with diameter D_c the expression for the autocorrelation function is as follows [3.10]:

$$\Gamma_{\Delta I}(X) = \langle I \rangle^2 \left[\frac{2J_1 \left[\frac{\pi D_c X}{\lambda z_S} \right]}{\frac{\pi D_c X}{\lambda z_S}} \right]^2 \quad (3.21)$$

Where J_1 is a first order Bessel function and the minimum of this autocorrelation function first occurs when the argument $(\pi D_c X / \lambda z_S)$ of the Bessel function is equal to 1.22π . The speckle size can be expressed as

$$\langle \sigma_0 \rangle = \frac{1.22 \lambda z_S}{D_c} \quad (3.22)$$

Most appropriate for the many configurations in laser vibrometry, the expression for the normalised autocorrelation, $\gamma_{\Delta I}$, with a Gaussian illumination and beam diameter, D , of $\exp[-2]$ [3.13].

$$\gamma_{\Delta l}(X) = \exp\left[-\left(\frac{\pi D}{2\lambda z_s}\right)^2 |X|^2\right] \quad (3.23)$$

The width of the speckle can be characterised by the $\exp[-2]$ point of the autocorrelation function which can be expressed as

$$\langle \sigma_0 \rangle = \frac{2\sqrt{2}\lambda z_s}{\pi D} \quad (3.24)$$

It can be seen from these three relationships that the speckle size is proportional to the wavelength of light and the distance from the target to the observation plane and inversely proportional to the width of the profile of the scattering spot.

3.4.1 Autocorrelation from the power spectral density (Wiener-Khinchin Theorem)

Statistically, a speckle pattern is a stationary stochastic process where, by definition, the statistical parameters of the distribution, such as the mean and variance, do not change with time or space. With this in mind, the Wiener-Khinchin theorem can be applied [3.2, 3.8, 3.14]. The Wiener-Khinchin theorem relates the power spectral density, $S(\mathbf{X})$ of a stationary random process to its autocorrelation function, $\Gamma_{\Delta l}(X)$, in that they are a Fourier transform pair. For a single dimension, this expression can be written as follows

$$\begin{aligned}
S(\mathbf{X}) &= \left\langle \frac{1}{\mathbf{X}} \left| \int_{-\mathbf{X}/2}^{\mathbf{X}/2} I(x) \exp \left[j2\pi \frac{x}{\mathbf{X}} \right] dx \right|^2 \right\rangle \\
&= \int_{-\infty}^{\infty} \Gamma_{\Delta}(X) \exp \left[j2\pi \frac{X}{\mathbf{X}} \right] dX
\end{aligned} \tag{3.25}$$

where \mathbf{X} is the spatial width in x , seen in Figure 3.1. From this the inverse Fourier transform of the power spectral density is the autocorrelation function [3.5].

$$\text{FT}^{-1} [S(\mathbf{X})] = \Gamma_{\Delta}(X) \tag{3.26}$$

The delay bound by $\exp[-2]$ of the normalised amplitude is used to determine the average width of a speckle. This method is applied in Chapter 7 to estimate the average speckle size resulting from surfaces with various finishes.

4 Properties of a dynamic speckle

The principle of laser vibrometry, as discussed in Chapter 1, relies on the detection of the Doppler shift of scattered light. The Doppler shift can also be considered as a time dependent change to the phase of the photodetector output resulting from summation of the many scattered elements as the surface moves in parallel with the optical axis. For a Gaussian beam, where the diameter alters with propagation distance, this means the speckle size, discussed in Section 3.4 alters with time [4.1, 4.2]. This motion however is not a significant source of speckle noise in laser vibrometry due to the very small changes in the resulting speckle pattern.

It is not uncommon, however, for measurements to be made in the presence of components of target velocity that are not parallel with the optical axis. Such surface motions change the phase of the elementary scattered phasors as a function of time and consequently the speckles exhibit motion. As described in Chapter 2, these motions can generate significant levels of speckle noise in laser vibrometry. A speckle's behaviour is characterised by a description of how the time dependent intensity of the speckle changes in a 2D observation plane. Speckles are described, without exclusivity, to translate and evolve. The form of speckle motion is governed by the optical configuration and the particular movement of the surface. There are three fundamental surface motion types which cause speckle motions: transverse to the optical axis, tilt and rotation [4.3].

This chapter uses literature to examine the behaviour of speckles to test the concept that an understanding of speckle noise generation (which is driven by changes in phase) can be found using correlations of intensity. This is also investigated experimentally in Chapter 6. The properties of a speckle in motion, known as dynamic speckle, can be described using the space-time correlation function of intensity. This function quantifies the statistical relationship between the intensities at two points in space separated by a temporal delay and this function together with its application for the primary surface motions types is described in Section 4.1.

4.1 Space-Time Correlation Function

The normalised space-time correlation function of the intensity fluctuations is a useful tool to quantify the properties of the motions of a dynamic speckle. A speckle pattern produced from a target surface moving perpendicular to the optical axis with a velocity of v in a plane ζ, η is observed on a plane x, y a distance z_s away

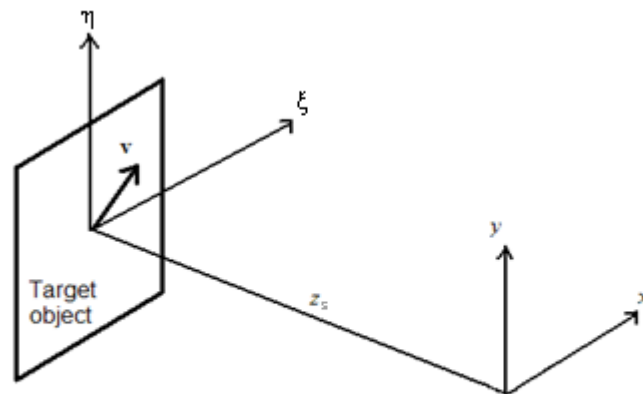


Figure 4.1 – Schematic of coordinate system for time varying speckles

The space-time correlation function describes the relation, on an observation plane, between the intensity at one point in space and time to the intensity at another point in space and time. The space-time correlation function is often expressed as a normalised quantity using the autocorrelation at the initial position and time of interrogation. The correlation function is restricted to observations which are made in the same direction as the surface motion. The component of velocity of the surface, v , and the spatial delay, X , are therefore parallel. The normalised space-time correlation function of the intensity fluctuation with a temporal delay, τ , can be written [4.4, 4.5]

$$\gamma_{\Delta t}(X, \tau) = \exp\left[-4\frac{|v|^2 \tau^2}{D^2}\right] \exp\left[-\left(\frac{\pi D}{2\lambda z_s}\right)^2 |X - \sigma v \tau|^2\right] \quad (4.1)$$

where

$$\sigma = 1 + \frac{z_s}{r} \quad (4.2)$$

Setting $\tau = 0$ the normalised space correlation function is obtained which represents the space correlation function of the speckle intensity fluctuation for a stationary speckle pattern and hence the average size of the speckle

$$\gamma_{\Delta t}(X, 0) = \exp\left[-\left(\frac{\pi D}{2\lambda z_s}\right)^2 |X|^2\right] \quad (4.3)$$

Characterising the average width by the spatial delay when the correlation function reduces to a value of $\exp[-2]$

$$|X| = \frac{2\sqrt{2}\lambda z_s}{\pi D} = \langle \sigma_0 \rangle \quad (4.4)$$

which is identical to equation (3.26). Therefore the space-time correlation function of speckle intensity fluctuation can be re-written in terms of the average size of the speckle

$$\gamma_{\Delta t}(X, \tau) = \exp\left[-4\frac{|v|^2 \tau^2}{D^2}\right] \exp\left[-\frac{2}{\langle \sigma_0 \rangle^2} |X - \sigma v \tau|^2\right] \quad (4.5)$$

Equation (4.5) is the basis of much of the analysis of dynamic speckles. However, in addition to the normalised correlation function for point space statistics is the normalised space time correlation function for spatially integrated speckle intensity fluctuations. This function describes the relationship of an area at one instant in time to the same area located at another position in another instant in time. This theory is applicable in laser vibrometry as the surface detecting the intensity has finite size. The normalised space time correlation function of the spatially integrated speckle intensity fluctuations is written [4.5, 4.6, 4.7]

$$\gamma_{\Delta t}(X, \tau) = \exp\left[-4\frac{|v|^2 \tau^2}{D^2}\right] \exp\left[-\frac{4}{2\langle \sigma_0 \rangle^2 + L_d} |X - \sigma v \tau|^2\right] \quad (4.6)$$

where L_d is an approximation to the diameter of the integrating aperture by the $\exp[-2]$ width of a Gaussian function, otherwise known as a Gaussian ‘soft aperture’. Reducing the aperture dimension to a negligible value, setting $L_d = 0$, reduces the spatially integrated space-time correlation function to a point space statistical analysis and equation (4.6) tends to equation (4.5).

Although this study is of interest and applicable in laser vibrometry, the results obtained are not used in estimations of speckle noise shown in Chapter 7. Equation (4.6) does show a dependence on the size of the detecting aperture and observation of this is made in Sections 4.1.1 to 4.1.3.

4.1.1 Properties of dynamic speckles when a surface moves transverse to the optical axis

The space time correlation function shown in equation (4.5) describes the correlation function for a surface which moves transverse to the optical axis of the beam. The time duration over which a point in space remains statistically similar or the time duration of the fluctuation of the intensity can be described by the normalised time correlation function and is useful to characterise statistically how long a speckle exists. The time correlation function can be found by setting $X = 0$ in equation (4.5).

$$\gamma_{\Delta l}(0, \tau) = \exp\left[-\frac{\tau^2}{\tau_c^2}\right] \quad (4.7)$$

where τ_c is the correlation time of the time varying speckle characterised by the time delay when the correlation function drops to $\exp[-2]$. This describes the duration of correlation at a single point in space and can be written:

$$\tau_c = \frac{1}{|v|} \left(\frac{D^2 \langle \sigma_0 \rangle^2}{2 \langle \sigma_0 \rangle^2 + \sigma^2 D^2} \right)^{1/2} \quad (4.8)$$

It can be seen from equation (4.8) that τ_c depends on the velocity of the target, the diameter of the Gaussian illuminating beam incident on the target, the

radius of the wave-front curvature and also the separation distance, z_S . Equation (4.8) can be re-written in terms of the surface displacement required for decorrelation, a_C , by simply applying $|a_C| = |v| \tau_C$.

$$|a_C| = \left(\frac{D^2 \langle \sigma_0 \rangle^2}{2 \langle \sigma_0 \rangle^2 + \sigma^2 D^2} \right)^{1/2} \quad (4.9)$$

Equation (4.9) shows statistically how far the surface must displace for the intensity of a single point in space observed at a distance z_S away to become different.

Intuitively to minimise speckle noise, the correlation time τ_C and hence $|a_C|$ must be maximised. Observation of equation (4.8) and (4.9) suggests an optimum beam diameter, D_{OPT} , at a separation distance, z_S , or standoff distance which maximises $|a_C|$. D_{OPT} can be evaluated by differentiation of equation (4.9) with respect to the beam diameter

$$\frac{d|a_C|}{dD} = \langle \sigma_0 \rangle (2 \langle \sigma_0 \rangle^2 - \sigma^2 D^2) (2 \langle \sigma_0 \rangle^2 + \sigma^2 D^2)^{-3/2} = 0 \quad (4.10a)$$

$$D_{OPT} = \left(\frac{4 \lambda z_S}{\pi \sigma} \right)^{1/2} \quad (4.10b)$$

$$|a_C| = \frac{1}{2} D \quad (4.10c)$$

which is half the beam diameter on the surface. This situation would be applicable in practical situations where the work space limits the positioning of the vibrometer. However if this restriction does not exist it is possible to further

increase the correlation time and this can be evaluated by differentiating equation (4.9) with respect to the standoff distance.

$$\frac{d|a_c|}{dz_s} = \sigma D^3 \langle \sigma_0 \rangle \left(\frac{\sigma}{z_s} - \frac{1}{r} \right) \left(2 \langle \sigma_0 \rangle^2 + \sigma^2 D^2 \right)^{-3/2} = 0 \quad (4.11)$$

occurs when $z_s = -r$ and when $z_s \rightarrow \infty$. The surface displacement for speckle correlation takes its maximum possible value of

$$|a_c| = \frac{1}{\sqrt{2}} D \quad (4.12)$$

and this occurs when $z_s = -r$ and $\sigma = 0$. This shows that the maximum surface displacement for speckle correlation is only dependent on the beam diameter and therefore this suggests using the largest beam diameter as practically possible to reduce the influence of speckle noise.

Equation (4.6) describes the spatially integrated speckle intensity fluctuations over time. When the surface moves in-plane to the optical axis consideration of the surface displacement for speckle correlation yields

$$|a_c| = \frac{1}{\sqrt{2}} \left[\frac{D^2 \left(2 \langle \sigma_0 \rangle^2 + L_d^2 \right)}{2 \langle \sigma_0 \rangle^2 + L_d^2 + \sigma^2 D^2} \right]^{1/2} \quad (4.13)$$

and similarly to equation (4.9), equation (4.13) has a maximum of $\frac{1}{\sqrt{2}} D$ when $z_s = -r$.

4.1.2 Properties of dynamic speckles when a surface tilts on the optical axis

The properties of dynamic speckles when a surface tilts as shown in Figure 4.2 can also be analysed using the space time correlation function ,.

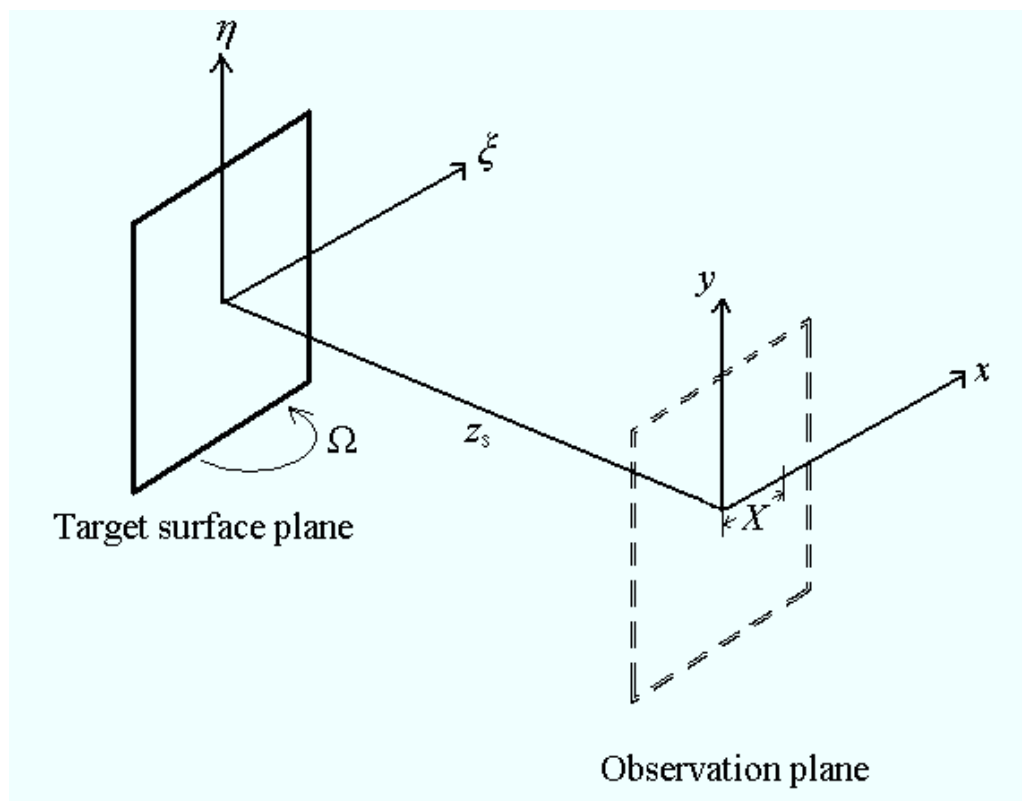


Figure 4.2 - Schematic of configuration for the autocorrelation for a surface which tilts

The surface deviations are considered as small mirror-like facets and a rotation around the η axis with a velocity Ω results in a translation of the speckles in the observation plane by an amount $X = 2\Omega z_s \tau$ [4.3, 4.8]. In this study $v = 0$ and the space time correlation function can be shown to be

$$\gamma_{\Delta I}(\Omega, \tau) = \exp\left[-\frac{2}{\langle\sigma_0\rangle^2}(2|\Omega|z_S\tau)^2\right] \quad (4.14)$$

The time required to reduce the space time correlation function to a value of $\exp[-2]$ is

$$\tau_c = \frac{1}{|\Omega|} \frac{\langle\sigma_0\rangle}{2z_S} = \frac{1}{|\Omega|} \frac{\sqrt{2}\lambda}{\pi D} \quad (4.15)$$

and the angular displacement of the surface which decorrelates the intensity at a point in space, θ_c , to a value of $\exp[-2]$ is

$$|\theta_c| = \frac{\langle\sigma_0\rangle}{2z_S} = \frac{\sqrt{2}\lambda}{\pi D} \quad (4.16)$$

Equation (4.16) shows that the angular displacement of the surface which decorrelates the intensity is independent of the standoff distance, z_S . From equation (4.16) the correlation displacement in the observation plane, $2|\theta_c|z_S$, is equal to the average size of the speckle.

A finite aperture, integrating the intensity spatially, for a tilting surface modifies equation (4.14) in the following way

$$\gamma_{\Delta t}(\Omega, \tau) = \exp \left[-\frac{4}{2\langle \sigma_0 \rangle^2 + L_d^2} (2|\Omega|z_S\tau)^2 \right] \quad (4.17)$$

and the angular surface displacement for correlation is found from the $\exp[-2]$ value of this correlation function and shown to be

$$|\theta_C| = \frac{1}{2\sqrt{2}z_S} (L_d^2 + 2\langle \sigma_0 \rangle^2)^{1/2} \quad (4.18)$$

from which it can be seen that as $L_d \gg \langle \sigma_0 \rangle$ the translation distance in the observation plane, $2|\theta_C|z_S$, approaches $\frac{1}{\sqrt{2}}L_d$. If $L_d \ll \langle \sigma_0 \rangle$ the translation distance approaches that found for point space statistics where $2|\theta_C|z_S \rightarrow \langle \sigma_0 \rangle$. Additionally, it can be seen that, unlike equation (4.16), equation (4.18) does not show independence from z_S .

4.1.3 Properties of dynamic speckles when a cylindrical surface rotates

A rotor of radius, R , which rotates at an angular velocity, Ω , and is illuminated by a Gaussian beam, as shown in Figure 4.3, produces similar speckle motions to those produced by a surface moving transverse to the beam but the cylindrical shape modifies the wavefront as shown by Figure 4.4. The rotor of radius R modifies the incident radius of curvature, r , producing an effective wavefront of curvature radius, r' .

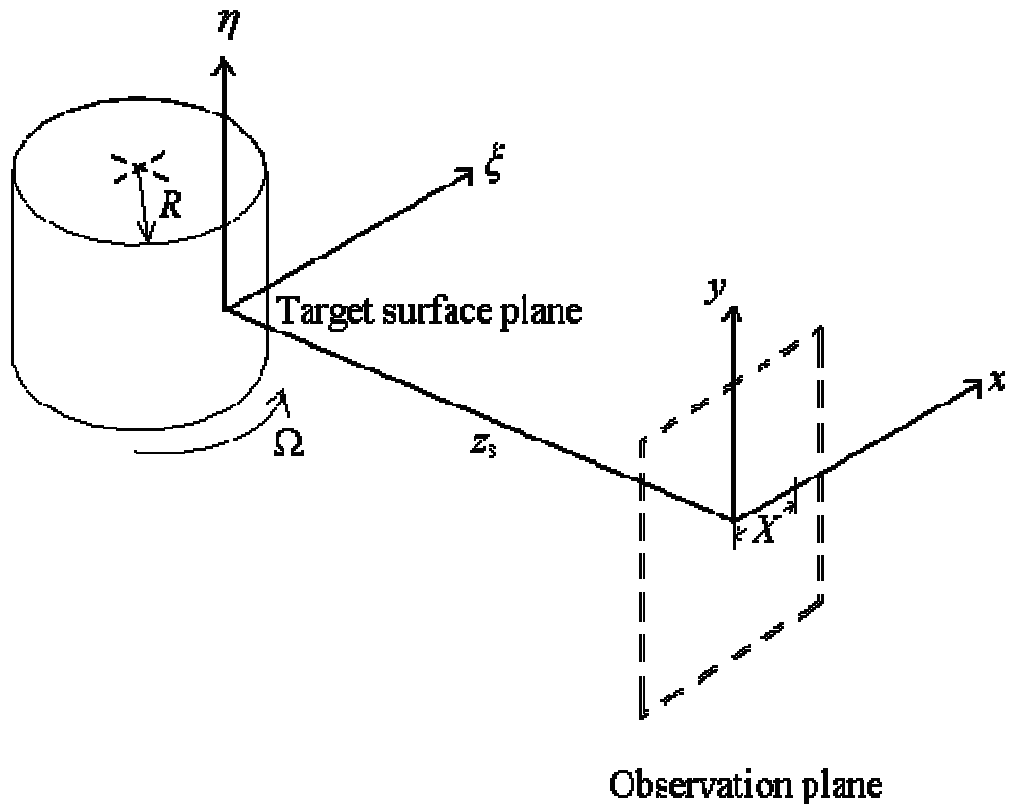


Figure 4.3 – Schematic of configuration for autocorrelation function from a rotating cylindrical surface

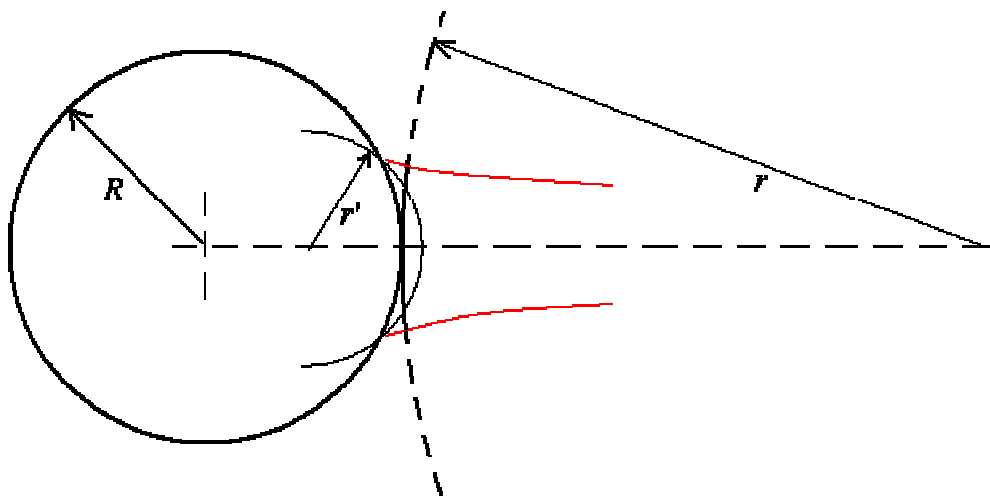


Figure 4.4 – Effective wavefront curvature from a cylindrical object surface

The space time correlation function for a rotating surface can be written [4.9, 4.10, 4.11]

$$\gamma_{\Delta t}(X, \tau) = \exp\left[-4 \frac{(|\Omega|R)^2 \tau^2}{D^2}\right] \exp\left[-\frac{2}{\langle\sigma_0\rangle^2} |X - \sigma_\varepsilon \Omega R \tau|^2\right] \quad (4.19)$$

where

$$\sigma_\varepsilon = \sigma - \frac{2z_s}{R} \quad (4.20)$$

The time required to reduce the correlation to a value of $\exp[-2]$, where the spatial delay is again made zero, is

$$\tau_c = \frac{1}{|\Omega|R} \left(\frac{D^2 \langle\sigma_0\rangle^2}{2\langle\sigma_0\rangle^2 + \sigma_\varepsilon^2 D^2} \right)^{1/2} \quad (4.21)$$

This equates to an angular displacement of the surface of

$$|\theta_c| = \frac{1}{R} \left(\frac{D^2 \langle\sigma_0\rangle^2}{2\langle\sigma_0\rangle^2 + \sigma_\varepsilon^2 D^2} \right)^{1/2} \quad (4.22)$$

which takes a maximum value of $\frac{1}{\sqrt{2}} \frac{D}{R}$ when $\sigma_\varepsilon = 0$. This suggests that

speckle noise is minimised when $\frac{2z_s}{R} - \frac{z_s}{r} = 1$. From this it can be seen that

with consideration to standoff distance and radius of curvature speckle noise can be reduced.

A spatial integration of the speckle intensity fluctuations when a surface rotates modifies the normalised space time correlation function in equation (4.19) as follows [4.5, 4.8, 4.11]

$$\begin{aligned} \gamma_{\Delta t}(X, \tau) = & \exp \left[-4 \frac{(|\Omega| R)^2 \tau^2}{D^2} \right] \\ & \times \exp \left[-\frac{4}{2\langle\sigma_0\rangle^2 + L_d} |X - \sigma_\varepsilon \Omega R \tau|^2 \right] \end{aligned} \quad (4.23)$$

and the angular displacement for correlation characterised by the temporal delay when time correlation function drops to $\exp[-2]$.

$$|\theta_C| = \frac{1}{\sqrt{2}} \frac{1}{R} \left[\frac{D^2 (2\langle\sigma_0\rangle^2 + L_d^2)}{2\langle\sigma_0\rangle^2 + L_d^2 + \sigma_\varepsilon^2 D^2} \right]^{1/2} \quad (4.24)$$

Equation (4.24) takes a maximum value of $\frac{1}{\sqrt{2}} \frac{D}{R}$ when $\sigma_\varepsilon = 0$. The tangential displacement of the surface is therefore $\frac{1}{\sqrt{2}} D$ showing similarity to the maximum transverse displacement shown by equation (4.9).

4.2 Speckle motions

A dynamic speckle has two behaviour regimes which are used to describe its motion. One of these regimes is speckle translation; the speckle entity translates in space and does not change in size or shape. The second regime is often termed ‘boiling’; the speckle evolves over time, changing its size and shape. The speckle entities evolve independently of one another but the statistical parameters are temporally stationary. These regimes often occur together but one will generally dominate the decorrelation. For a surface moving transverse to the optical axis of the beam the speckles will exhibit both behaviours. Therefore Sub-sections 4.2.1 and 4.2.2 use this space-time correlation function to quantify speckle translation and speckle evolution respectively. Sub-section 4.2.3 determines which regime dominates the decorrelation.

4.2.1 Speckle translation

If a speckle translates, the peak of the normalised correlation function of speckle intensity fluctuation has a spatial delay as well as a temporal delay. Using a temporal delay of τ , speckle translation, determined by the spatial delay, X , can be found by the displacement of the peak value of the correlation function. It can be seen from equation (4.5) that the correlation function for an in-plane surface motion is at a maximum when $X = \sigma v \tau$ [4.14, 4.15]. Speckle translation, X_T , can therefore be expressed in terms of the surface displacement as $X_T = \sigma a(t)$ where the σ term, aptly referred to as the gearing term [4.16], defines the magnitude of the speckle translation as a factor of the surface displacement.

4.2.2 Speckle evolution

Speckle evolution is a temporal variation in the size and shape of the speckle. The normalised space-time correlation function can be used as a tool to quantify the life-span of the speckle. Speckle evolution causes a reduction in the amplitude of the correlation function. A speckle will often translate and evolve and so, to isolate the speckle evolution, the spatial delay is matched with the amplitude of the speckle translation. Therefore inserting $X = X_\tau$ into equation (4.5) gives the peak value of

$$\gamma_{\Delta t}(X, \tau) = \exp\left[-4 \frac{|v|^2 \tau^2}{D^2}\right] \quad (4.25)$$

The speckle is decorrelated when this function reduces to a value of $\exp[-2]$ which occurs when the surface has displaced by $\frac{1}{\sqrt{2}}D$. This result in conjunction with the result obtained in equation (4.12) shows that the correlation time is maximised when pure boiling is present which occurs when $z_s = -r$ [4.12].

4.2.3 Dominant speckle motion

All surface motions are likely to cause a speckle to translate and evolve. For a tilting surface, speckle translation is by far the dominant motion due to the limited alteration to the scattering surface elements over the angular motion. This section, therefore, focuses on the dominant speckle motions from a transverse surface motion and a rotating surface. Equation (4.9), the surface displacement for speckle correlation for a single point in space from a surface

which is moving transversely to the optical axis of the laser beam, can be re-written

$$|a_c| = \frac{1}{\sqrt{2}} D \left(\frac{1}{1+T^2} \right)^{1/2} \quad (4.26)$$

characterising the translation of the speckle, in the time it takes a speckle to evolve, as a function of the speckle size, where

$$T = \frac{\frac{1}{\sqrt{2}} \sigma D}{\langle \sigma_0 \rangle} \quad (4.27)$$

similarly from equation (4.22), the surface tangential displacement for correlation, for a single point in space, from a rotating cylindrical surface can be re-written as

$$|\theta_c| R = \frac{1}{\sqrt{2}} D \left(\frac{1}{1+T_\varepsilon^2} \right)^{1/2} \quad (4.28)$$

and

$$T_\varepsilon = \frac{\frac{1}{\sqrt{2}} \sigma_\varepsilon D}{\langle \sigma_0 \rangle} \quad (4.29)$$

In equation (4.26) and equation (4.28) $\frac{1}{\sqrt{2}}D$ is the maximum possible displacement of the surface before the speckle has decorrelated and this occurs when $|T|, |T_\varepsilon| = 0$ i.e. when there is no speckle translation. The translation of the speckle can only ever reduce the surface displacement for speckle correlation and consequently increase speckle noise. When the absolute value of T is greater than unity the speckle has translated further than a speckles width and translation can be expected to dominate the decorrelation. When T is zero, boiling is the only regime present in the speckle motion. Speckles can translate in the same direction or the opposite direction to the surface motion and this depends on the sign of the gearing term, σ . T can, therefore, take positive or negative values. An estimation of which regime dominates is evaluated from the absolute value of T [4.12] and is illustrated in Table 4.1 and Figure 4.5

$ T $ or $ T_\varepsilon $	Dominant motion	$ a_c $ or $ \theta_c R$
0	Pure Boiling	$\frac{1}{\sqrt{2}}D$
> 0 < 1	Boiling	$> \frac{1}{2}D$ $< \frac{1}{\sqrt{2}}D$
1	Equal influence	$\frac{1}{2}D$
> 1	Translation	≥ 0 $< \frac{1}{2}D$

Table 4.1 - Indication of dominant speckle motion regime

For example, if you take the scenario where speckle boiling and speckle translation have equal influence on the decorrelation, it can be seen that the surface must displace half of the beam spot diameter for a speckle to fully evolve, during which time the speckle will have translated the same distance as its expected width.

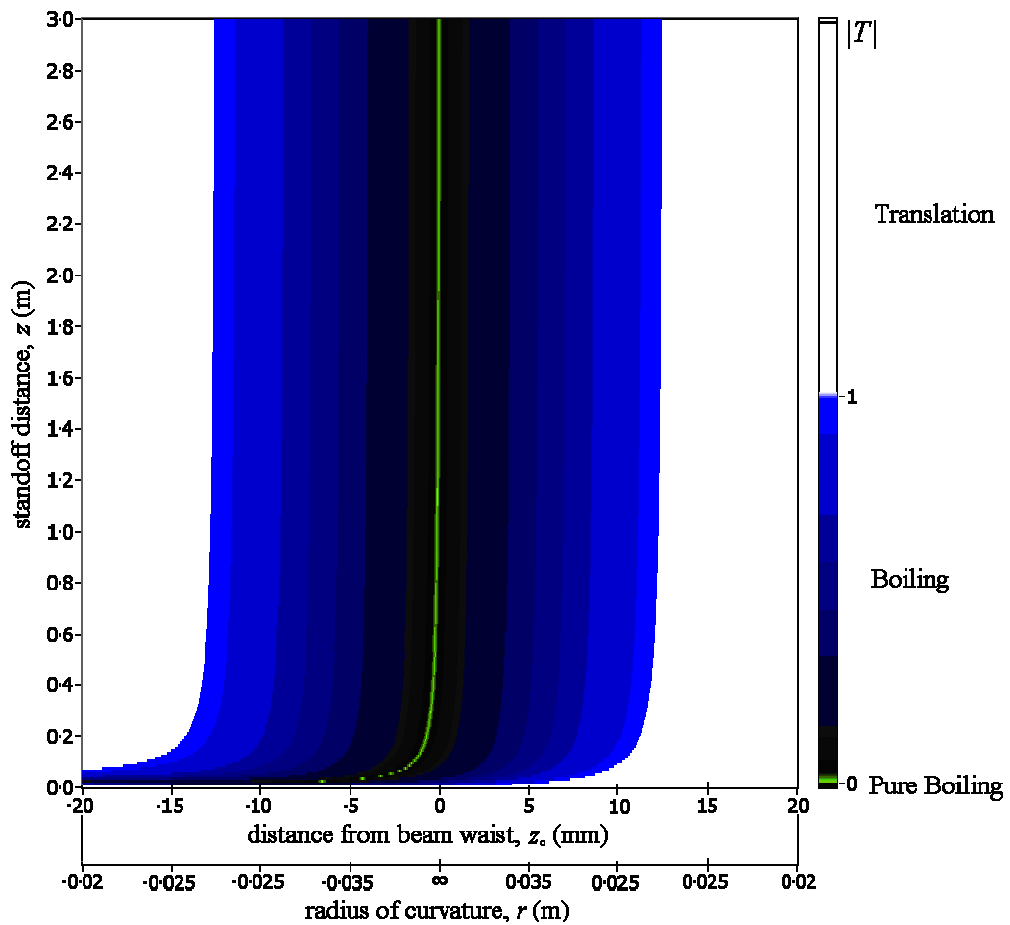


Figure 4.5 – Example of an indication of dominant speckle motion regime for a surface translating transverse to the optical axis. Beam waist diameter, $D_0=100\mu\text{m}$

Figure 4.5 gives an indication of whether translation or boiling dominates the decorrelation when the surface translates transverse to the optical axis of a laser beam with a waist diameter of $100\mu\text{m}$. It shows the standoff distance, z_s ,

against surface location relative to the beam waist, z_0 . The radius of curvature of the beam at the range of surface locations is also shown. The threshold transition from blue to white indicates where $|T|=1$, where boiling and translation have an equal influence on the decorrelation. Pure boiling is shown by the green line, which indicates when $z_s = -r$ and $|T|=0$. Often the laser beam is focussed on or near the surface and it can therefore be seen that boiling is more likely to be the dominant regime for the general application of the laser vibrometer for a surface moving transverse to the optical axis of the beam.

When the laser beam is focussed on the surface of a rotating cylindrical shaft, however, this is not necessarily the case. This is a more complex scenario as the shaft radius becomes a significant parameter. Often speckle translation is expected to be the dominant regime [4.17] but for larger shaft diameters and, particularly, small beam diameters where speckles are large, $|T_\varepsilon| \rightarrow 0$ and evolution can dominate. It can also be seen by equation (4.21) that as the radius of the shaft increases, the correlation time reduces. The effect on speckle noise due to the shaft radius, beam diameter and also the point of focus (altering the radius of curvature) is investigated experimentally in chapter 5.

Equation (4.26) and (4.28) are applicable at a point in space and when speckle translation dominates these correlations it does not mean it necessarily dominates the finite sized aperture correlations applicable to a laser vibrometer. For spatially integrated speckle correlations on a rotating shaft equation (4.24) can be re-written

$$|\theta_c|_R = \frac{1}{\sqrt{2}} D \left[\frac{1 + \frac{1}{2} M^2}{1 + \frac{1}{2} M^2 + T_\varepsilon^2} \right]^{\frac{1}{2}} \quad (4.30)$$

where

$$M = \frac{L_d}{\langle \sigma_0 \rangle} \quad (4.31)$$

It can be seen that evolution can dominate even if $|T_\varepsilon| > 1$ when $|T_\varepsilon| \ll M$. What this means is that if the size of the detector, in the direction of the speckle motion, is large in comparison to the speckle translation distance then the evolution of the region of the speckle pattern can dominate the decorrelation. This predicts that increasing the size of the detecting aperture can reduce the effects of speckle noise, but only when speckle translation is dominant. It can be seen from Equation (4.30) that, as $|T_\varepsilon| \rightarrow 0$ and evolution becomes dominant, the size of the detecting aperture becomes irrelevant as $|\theta_c| R \rightarrow \frac{1}{\sqrt{2}} D$. Therefore, if speckle evolution dominates the point space correlations, including a finite sized aperture into the analysis makes no difference. Increasing the aperture size seems to have potential to reduce speckle noise, when speckles translate. This is out the scope of the experimental study in this thesis but the simulations, detailed in Chapter 7, investigate this with the simulations of transverse sensitivity.

The next chapter is an experimental study of speckle noise in laser vibrometry. It quantifies the transverse, tilt and rotation sensitivities due to pseudo-vibration for commercial laser vibrometers, looking at the effects of beam diameter and target surface finish. Chapter 6 is an experimental study of the correlation of intensity of dynamic speckles using images of actual speckle patterns. It investigates the concept of a relationship between speckle noise

generation using the sensitivities evaluated in Chapter 5 and intensity correlations from experimentation. Chapter 7 uses dynamic speckle to model speckle behaviour and simulate transverse and tilt sensitivity.

5 Quantifying pseudo-vibration sensitivity by experimentation

This chapter quantifies experimentally, for the first time, pseudo-vibration sensitivities (transverse sensitivity, tilt sensitivity and rotation sensitivity) typically encountered in laser vibrometry applications. It maps expected sensitivities for two beam spot sizes, produced from commercial laser vibrometers, from surfaces with a range of roughnesses and finishes. It is commonplace to provide transverse sensitivity information with traditional contacting transducers, such as accelerometers [5.1], but as of yet an equivalent practice has not yet been transferred to laser vibrometry. The sensitivities presented in this chapter will be a valuable tool for the vibration engineer, increasing confidence in measured data, which might otherwise require careful interpretation. The research provides a greater understanding of the mechanisms which generate speckle noise and an insight into methods of reducing its effects. This is important in terms of data quality and limits of uncertainty for any measurement undertaken using a laser vibrometer.

Section 5.1 describes the typical signals apparent in these particular measurements, identifying speckle noise which ultimately is quantified. Section 5.2 presents the processing technique so the sensitivities can be presented in a useful, quantitative format to the vibration engineer. The different surface motions require particular approaches to quantify the sensitivities and Section 5.2 describes how speckle noise is isolated for each

surface motion. The chapter continues with Section 5.3 which maps out and presents the sensitivities, together with descriptions and explanations of the typical characteristics found in the measurements.

5.1 Vibrometer signal features

Transverse, tilt and rotation sensitivities have been observed from all surfaces, even those that are smooth and produce specular reflections. For the majority of the descriptions in this section and the sections following, the effect of the sensitivity in the measured data shall be termed ‘speckle noise’. This is done for the purposes of consistency but for smoother surfaces it is recognised that the term becomes less appropriate. This section describes typical signal features in the measurements. A particularly important feature is the way a single frequency vibration leads to broadband speckle noise and in a typical spectrum, such as was shown in Figure 2.3, energy appears at many orders.

Speckle noise is proportional to the time dependent phase changes, due to speckle motions, and manifests itself in the output signal of the vibrometer. Speckle motions cause amplitude and phase modulations of the Doppler signal. There are two particular features which are manifest in the output signal from the vibrometer - signal dropouts and speckle noise. These features can be generated by the same mechanism and, not surprisingly, can often be confused as one and the same effect. Dropouts can occur when the Doppler signal amplitude drops so low that the vibrometer cannot accurately demodulate it and the apparent velocity cannot adequately be resolved. This occurs when the average intensity of the collected light is too low or when speckle additions over the photodetector result in a low Doppler signal amplitude. Often low Doppler signal amplitudes occur simultaneously with large Doppler signal phase changes. Therefore the mechanisms which produce speckle noise can

also generate dropouts. However, the interpretation that dropouts are speckle noise over-emphasises the effect of the amplitude modulation. Speckle noise is produced from the phase modulation of the Doppler signal and remains present in the output from the vibrometer even when the Doppler signal amplitude is adequate. This section attempts to distinguish the two effects which are both present in the output signals from laser vibrometers.

5.1.1 Signal Dropouts

Signal dropouts appear most frequent in measurements from a rough surface. This is believed to be principally due to low light intensity collected by the vibrometer. However, dropouts were witnessed in measurements from all surfaces, including a surface treated with retro-reflective tape. Figure 5.1(a) shows a signal from a tilting surface, with the laser beam aligned off the rotational axis of the surface, exhibiting broadband speckle noise and also significant periodic dropouts. With slight manipulation of the beam position relative to the surface, so the sampled region of the speckle pattern changes slightly, the signal dropouts seen in Figure 5.1(a) can progress into an unusable signal with high apparent velocities, shown in Figure 5.1(b). With modest manipulation of the beam location, the signal dropouts can also be made to disappear to enable high quality measurements.

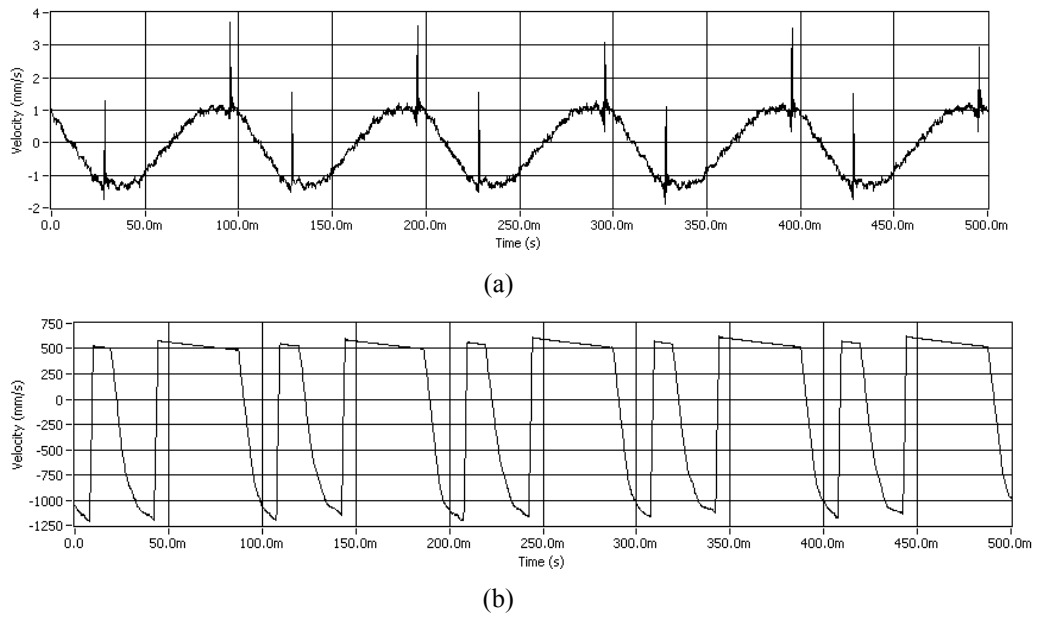


Figure 5.1 - Vibrometer outputs showing (a) periodic dropouts (b) unusable signal. Tilting surface with roughness $Ra2.39 \mu\text{m}$ oscillating at 10Hz

Figure 5.2 displays a closer analysis of the dropouts seen in Figure 5.1(a), clearly showing a significant reduction of the amplitude in the Doppler signal prior to the dropout.

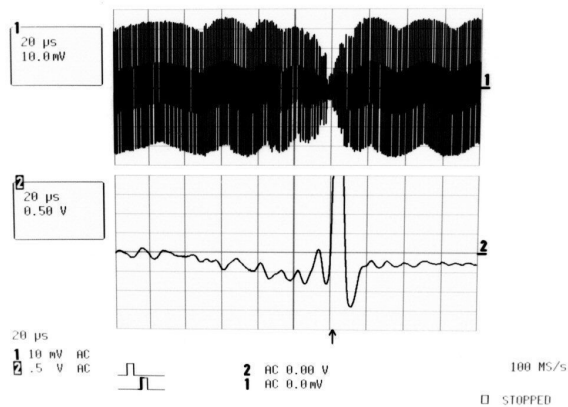
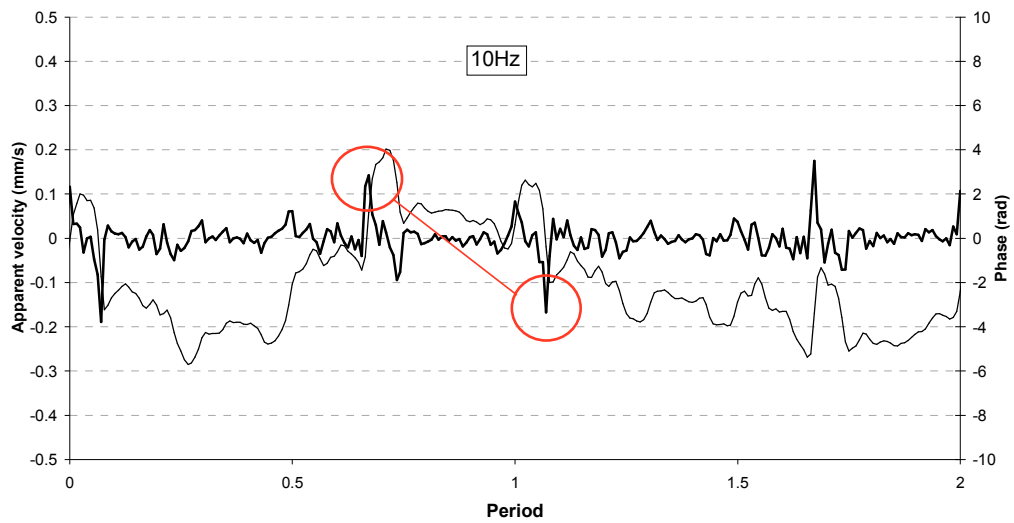


Figure 5.2 - Doppler signal (top) synchronised with the vibrometer output signal (bottom) showing a typical signal dropout from a tilting surface treated with retro-reflective tape oscillating at 30Hz on 200 μs timescale

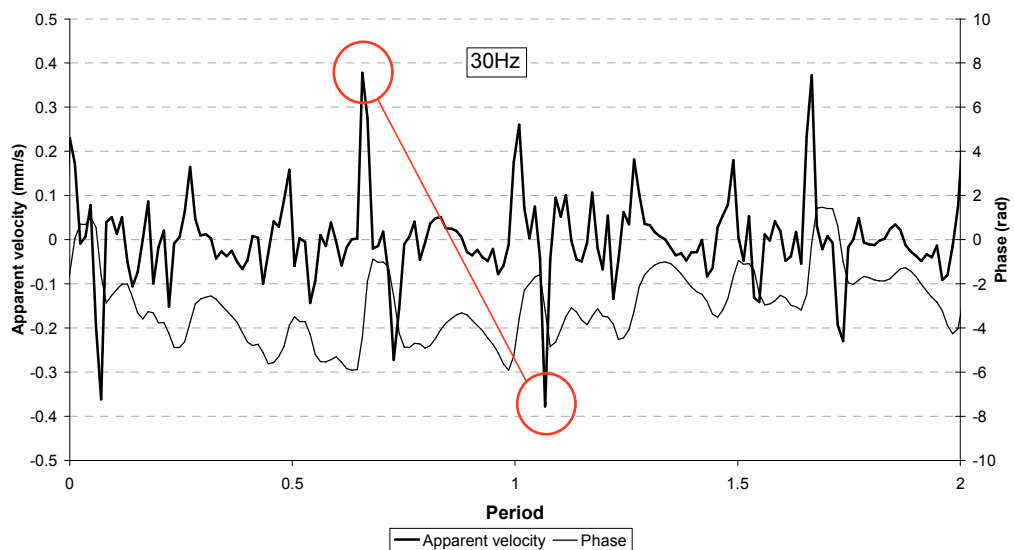
The generation of such impulses has also been seen in simulations, described in Chapter 7, which show large phase changes occurring alongside large changes in Doppler signal amplitudes. These impulses contain significant energy and can raise the broadband noise to levels where a useful measurement becomes compromised. The data presented in Figure 5.2 is from a target treated with retro-reflective tape. Therefore, the use of retro-reflective tape, which does increase the intensity of the light in backscatter, does not guarantee a signal clear of dropouts. However, the signal can usually be cleared of such dropouts by slight adjustment of the measurement location on the test surface. This improves the signal by sampling a region of the speckle pattern from which higher Doppler signal amplitude is maintained without any sudden changes in that amplitude.

5.1.2 Speckle noise

Figure 5.3 shows vibrometer outputs from a measurement on a tilting target with the incident beam positioned such that the measured velocity is minimised i.e. the beam is positioned on the rotational axis. The apparent velocities, which are dominated by speckle noise, were acquired with vibration frequencies of 10Hz and 30Hz. In particular, the measurements at each frequency were sampling similar (nominally identical) dynamic speckle patterns for two periods of sinusoidal motion with equal displacement amplitudes. The secondary plot shows the resulting phase in radians, calculated from the integral of the output signal.



(a)



(b)

Figure 5.3 – Apparent velocity (nominally speckle noise) in mm/s and phase in radians from two measurements sampling similar speckle patterns from a tilting target surface treated with retro-reflective tape oscillating at (a) 10Hz and (b)30Hz

The distinguishing peaks, encircled in Figure 5.3, are prominent features in speckle noise. They negate and reflect about an instant in time corresponding to the extreme of the displacement cycle, i.e. mid-way between the peaks. This

is due to the phase change that can be seen in the speckle noise integral. As the target moves from one extreme of its displacement cycle to the other extreme, the phase of the resultant Doppler signal changes in a continuous sequence as the sampled speckle pattern changes. In the second half of the displacement cycle, the phase of the resultant Doppler signal passes through the same sequence of phases as the first half of the cycle but in reverse. Consequently, the changes in phase have the same magnitude in the second half of the cycle but have an opposite sign. Increasing the vibration frequency, while maintaining the amplitude of the angular displacement, shows an increased level of speckle noise. The speckle noise integral plots show that the phase change remains consistent regardless of the vibration frequency. Increasing the vibration frequency means the phase change occurs more quickly and consequently speckle noise levels increase in direct proportion to vibration frequency. This is typical temporal data from which speckle noise is quantified in this chapter.

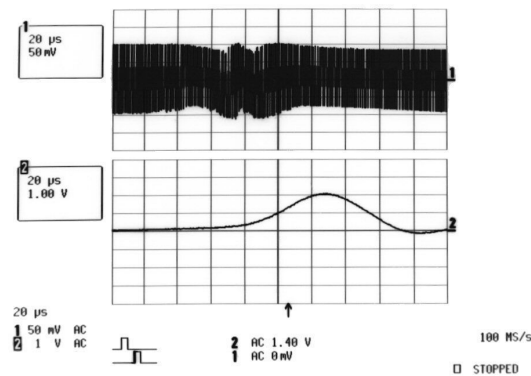


Figure 5.4 - Doppler Signal (top) synchronised with the vibrometer output (bottom) showing typical speckle noise peak. Tilting surface treated with retro-reflective tape oscillating at 30Hz on a 200 μ s timescale.

Closer assessment of these peaks, synchronised with the Doppler signal, is shown in Figure 5.4. The Doppler signal amplitude shows a significant variation prior to the peak shown in the vibrometer output. This is the result of a significant change in the summation of speckles on the photodetector, leading to both the amplitude modulation shown in the Doppler signal and the phase modulation appearing in the demodulated output. This shows how, even when the Doppler signal amplitude remains adequate and accurate demodulation is attainable, speckle changes still cause phase modulations and speckle noise appears in the output from the vibrometer. Three factors differentiate the signals seen in Figure 5.4 from those in Figure 5.2; the degree of Doppler signal amplitude modulation; the resulting speckle noise amplitude are much lower and the peaks occur continuously in Figure 5.4. Minor adjustment of the location of the beam modifies the peaks associated with speckle noise but it does not eliminate them from the signal and therefore does not reduce the noise levels.

5.2 Processing and capturing speckle noise

This section shows how a measurement exhibiting speckle noise is processed so that it can be presented in an appropriate and practical way. The section begins with a description of how speckle noise is processed to remove the effect of the vibration frequency and reduce the effect of the vibration amplitude. The section concludes by presenting the methods to quantify speckle noise for the particular periodic motions under scrutiny.

Speckle noise is quantified by reducing the component of surface velocity in the direction of the beam to (nominally) zero, which results in a measurement dominated by speckle noise. This is done through the design of the rig and through appropriate alignment of the beam relative to the surface motion.

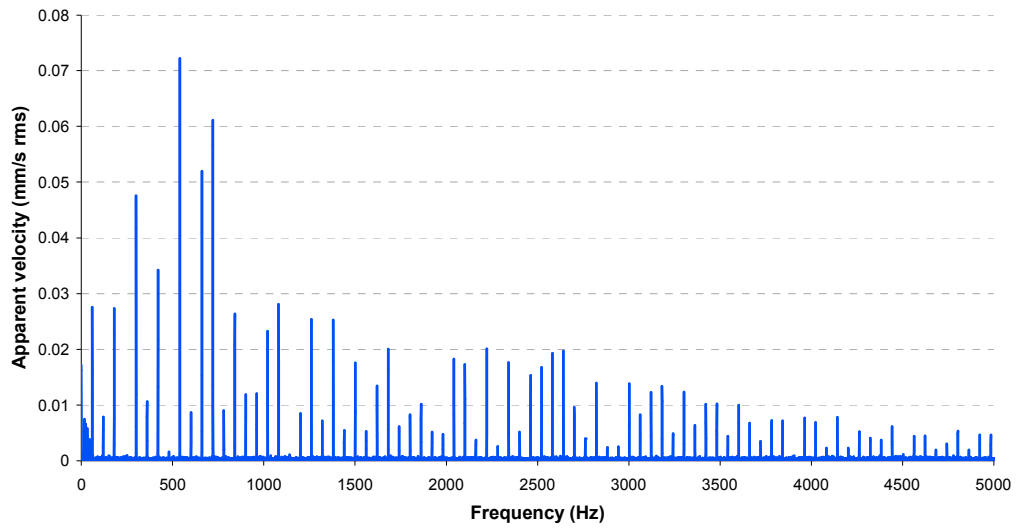
Speckle noise is quantified through the measurement of at least two parameters in unison. A measurement which attempts to capture speckle noise in some capacity is the measured velocity. This will often contain components of genuine surface velocities in the direction of the beam, despite every effort to remove them. Therefore a second measurement is taken which attempts to isolate the component of genuine velocity in the direction of the beam. Subtracting the genuine velocity from the measured velocity provides the best estimate of speckle noise and results in the best assessment of the sensitivities; the result of this calculation is termed the apparent velocity. The periodic motions are set up using specially designed mechanical rigs. In their design, these rigs minimise the components of genuine surface velocity in the direction of the beam and thereby cause speckle noise to dominate the measured velocity. Surface finish influences the degree of development of the speckle patterns created and therefore the effect of the surface finish is considered in the experimentation.

The transverse and tilt motion investigations use 4 different surfaces. The surface roughnesses are Ra 11nm, 75nm and 1.0 μ m. This range provides a very smooth surface producing predominantly specular reflections (Ra 11nm), a rough surface producing speckle patterns which are considered fully developed (Ra 1.0 μ m) and surface which is in between (Ra 75nm). A fourth surface is used which is treated with retro reflective tape, a common surface treatment to increase signal amplitude.

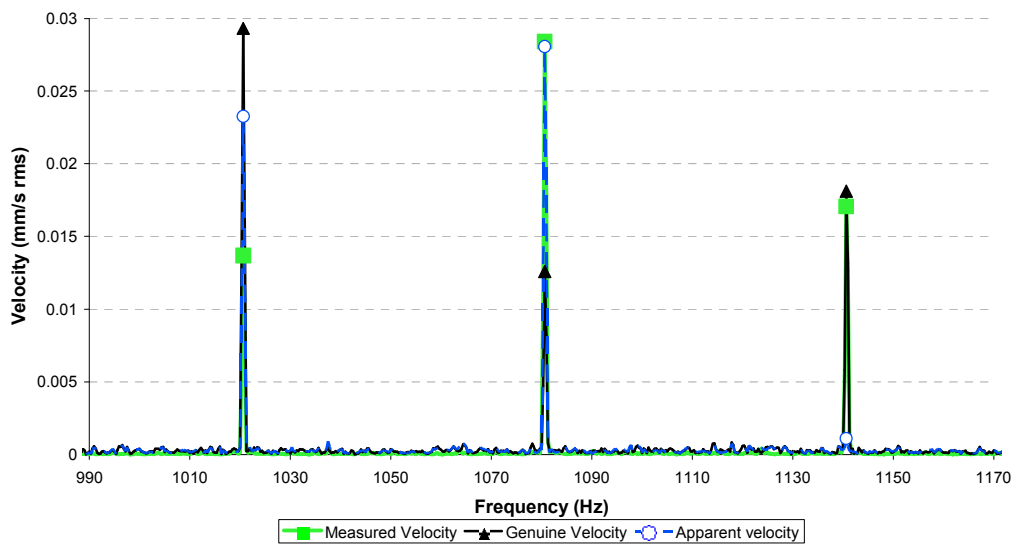
The rotation rig uses 5 different surfaces. Again they range in surface roughness from Ra 11nm to Ra 1.0 μ m as well as a surface treated with retro-reflective tape, to provide a range of combinations of specular reflections and speckle patterns. Typically, with rotating targets, retro-reflective tape is used.

5.2.1 Processing speckle noise

Isolation of speckle noise is dependent on the particular surface motion under scrutiny and this is discussed in the relevant subsections of Section 5.2. The apparent velocity which is dominated by speckle noise is isolated from the measured velocity and is Fourier transformed. A typical example of the spectrum of the apparent velocity is shown in Figure 5.5 (a). Figure 5.5 (a) shows the broadband characteristics of speckle noise, which maintains its amplitude over the 80 harmonics shown of the fundamental frequency of the surface vibration. Speckle noise influences many harmonics, sufficient to mask the genuine vibration velocity. Inspection of a few spectral peaks from a typical set of spectra for the measured velocity, genuine velocity and the resulting apparent velocity is shown in Figure 5.5 (b). This figure highlights the influence speckle noise can have on the measured velocity. It can be seen, by the peaks in Figure 5.5 (b), that depending on the amplitude and phase relative to the genuine velocity, speckle noise can increase, reduce or have very little influence on the amplitude of the measured velocity, as shown by the peaks identified in the figure by the markers. At 1020Hz, speckle noise has reduced the amplitude of the measured velocity well below the genuine velocity. At 1080Hz, the amplitude of the measured velocity is much greater than the genuine velocity because of speckle noise. At 1140Hz, speckle noise has little influence on the measured velocity.



(a)



(b)

Figure 5.5 – (a) typical spectrum of apparent velocity dominated by speckle noise. (b) influence of speckle noise on the measured velocity

To estimate the sensitivity to the surface motion, the peak value of each harmonic of the apparent velocity is quantified. The spectrum is discrete and therefore the harmonic frequencies do not necessarily coincide with a spectral

line. This so-called “picket fence” effect is therefore compensated for to improve estimates of the amplitudes of the speckle noise harmonics [5.2]. As described in Section 5.1 and evident from Figure 5.3, the vibration frequency linearly affects speckle noise. To remove the effect of the vibration frequency, the apparent velocity is normalised by the vibration velocity amplitude at the fundamental frequency. Figure 5.6 presents an example of the sensitivity to a tilting surface motion in terms of order which provides a functional presentation of the sensitivity, allowing extrapolation to any vibration frequency. The 50 order range shown in Figure 5.6 is beyond that typically of interest to the vibration engineer but provides a good indication of the spectral shape of speckle noise.

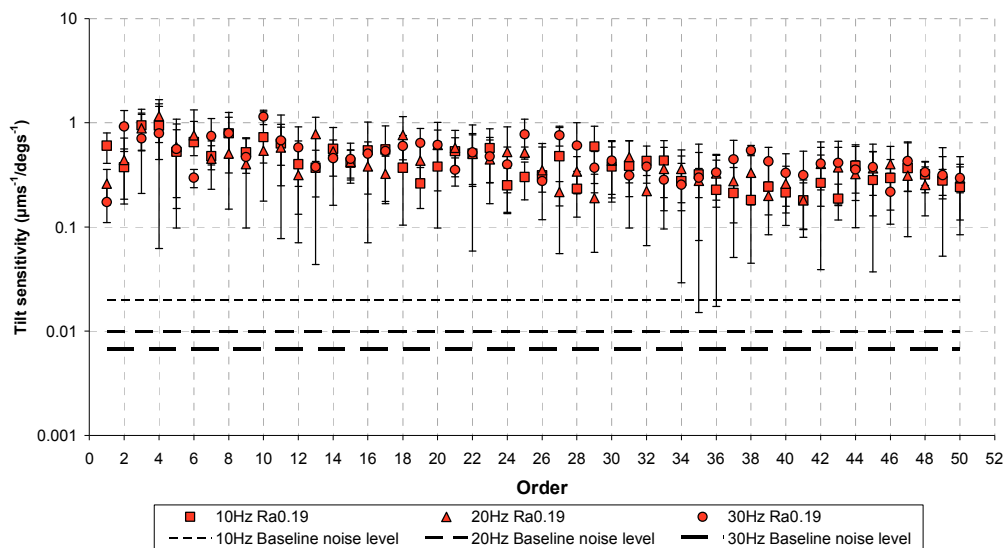


Figure 5.6 – Example of tilt sensitivity in units of $\mu\text{ms}^{-1} / \text{deg}^{-1}$ for a tilting surface with roughness Ra 190nm over a range of vibration frequencies from 10Hz to 30Hz.

Each data point is the average of each order calculated from measurements at 10 independent locations. The figure shows the mean sensitivity, +/- one standard deviation. In this case, measurements are from a tilting surface with roughness Ra 0.19 μm vibrating at fundamental frequencies of 10Hz, 20Hz and

30Hz indicating the independence of the sensitivity to the fundamental vibration frequency.

The sensitivities are quantified in two formats. The first is a mean level per order with a standard deviation and is calculated from the first 10 orders. 10 orders is chosen as a typical bandwidth over which the vibration engineer is likely to be interested. The second format is the total rms of the sensitivity across 50 orders.

5.2.2 Periodic transverse surface motion

For a periodic transverse surface motion, the surface oscillates perpendicular to the optical axis of the laser beam. A transverse motion requires a pure translational motion, i.e. along the axis z shown in Figure 5.7. The measurement surface is attached to a high precision linear rail via a supporting carriage. A linear shaker excites the carriage through a stinger. The stinger is axially aligned with the centre of gravity of the carriage assembly to minimise eccentric forces. A nominally sinusoidal signal is applied to the shaker providing an axial motion of the carriage and measurement surface. An accelerometer is used to measure the velocity, \dot{z} , of the measurement surface.

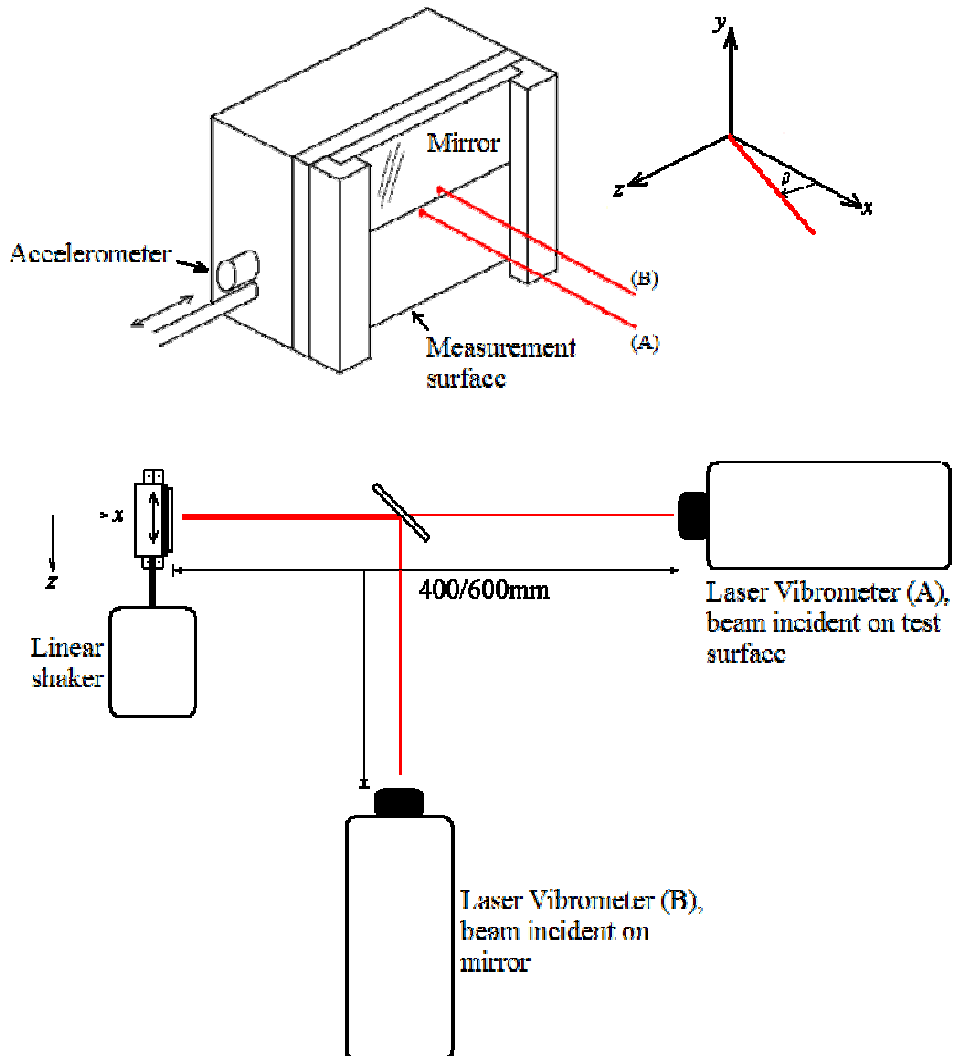


Figure 5.7 - Schematic of transverse sensitivity measurement

The origin of the measurement axes is coincident with the beam spot on the stationary surface; the z axis is defined parallel with the surface translation and the x - z plane is defined by the beam incidence vector. The sensed genuine velocity, U_m , is given by [5.3]

$$U_m = \cos \beta \left[\dot{x} - \dot{\theta}_y a_z \right] - \sin \beta \left[\dot{z} \right] \quad (5.1)$$

The aim of the experiment is to reduce U_m to zero, causing the effect of speckle noise to dominate the output of the vibrometer. The rig design minimises the components of angular velocity around the x , y and z axes. It also minimises the displacements in the x and y directions. Products of these small angular velocities and displacements are considered negligible and so have not been included in equation (5.1). The design of the rig minimises \dot{x} and $\dot{\theta}_y$, but due to manufacturing tolerances these velocities cannot be totally eliminated. However, \dot{z} is many times greater than the velocities in the first bracketed term and Equation (5.1) shows that by reducing the angle, β , the genuine velocity sensed by the vibrometer can be minimised.

The following procedure describes the alignment and adjustment to minimise β for a speckle noise measurement on a target with a transverse motion. As illustrated in Figure 5.7, two vibrometers are used; vibrometer A is used to capture the measured velocity from the test surface, which is dominated by speckle noise, and vibrometer B is used to estimate the genuine velocity component in the measured velocity, shown by Equation (5.1). To quantify the genuine velocity, the light detected by vibrometer B needs to have minimal, ideally zero, speckle noise. This was achieved using a mirror, which was clamped to the required measurement surface. This mirror was also used to align both beams normal to the surface. For practicality reasons, the vibrometer used to measure the genuine velocity was aligned via a second mirror, mounted independently of the vibrating structure, preventing contamination in the genuine velocity measurement. The two beams are aligned parallel with each other and normal to the mirror clamped to the front of the measurement surface. With the beams incident on the mirror, speckle noise is considered to be at a minimum, and the vibration velocity in the direction of the beam was assessed. Angle β was adjusted, for the measurement surface and the attached mirror, the beams were realigned and the component of transverse velocity

contributing to the genuine velocity (the second term in equation (5.1)) was reassessed. This process was repeated until a minimal genuine velocity was achieved. The clamped mirror is then repositioned to expose the required measurement surface to vibrometer beam A while remaining the target surface for vibrometer beam B. Vibrometer beams A and B are parallel so the genuine velocity for beam A is measured from the mirror surface with beam B. The angle β and consequently the genuine velocity in the direction of the beam are considered minimised. Subtracting the genuine velocity measured by vibrometer beam B from the sensed velocity measured by vibrometer beam A results in an apparent velocity which is dominated by speckle noise.

5.2.3 Periodic tilt surface motion

Speckle noise is present in a measurement from a tilting surface. A mechanical rig has been specially designed to tilt a test surface, and cause speckle noise to dominate a vibrometer measurement. In this way, tilt sensitivity can be quantified for the first time. A test surface is subjected to a periodic angular vibration and the laser beam, which is used to measure the measured velocity, is positioned so the measured genuine velocity is minimised. This pure target motion requires all motions except a single angular velocity, $\dot{\theta}_z$, to be zero, as shown in Figure 5.8.

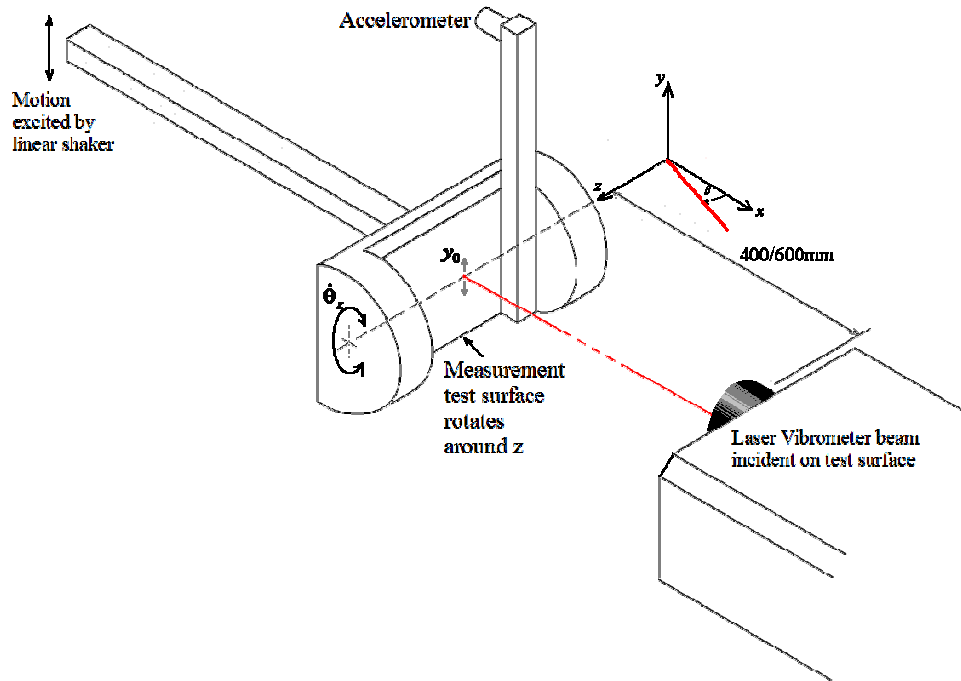


Figure 5.8 - Schematic of tilt experimental configuration

The surface angular oscillation was created using a lever mechanism attached to a linear shaker driven by a sinusoidal signal. The true angular surface motion is measured using an accelerometer at a known radial distance from the axis of rotation. The plane of the surface is coincident with the rotational axis of the tilt motion. The design of the rig minimises undesired surface motions, but again these cannot necessarily be eliminated. The measurement axes are defined as being positioned on the surface with the rotational axis coincident with the z axis as shown by Figure 5.8. The laser beam is aligned normal to the test surface while it is stationary, using a mirror which minimises the angle β to nominally zero. With the least significant components disregarded, the sensed genuine velocity can be expressed as [5.3]

$$U_m = \dot{x} - y_0 \dot{\theta}_z \quad (5.2)$$

This reduces the genuine velocity to a function which is dependent on the position of the beam relative to the rotational axis, denoted by the offset y_0 . The laser beam spot is positioned on the rotation axis and this occurs when y_0 is zero. Experimentally, a micro-positioning device, attached to the vibrometer, controls y_0 . The offset y_0 is minimised by assessing the measured velocity, in the time and frequency domains, and the measured velocity is then assumed to be dominated by speckle noise. A measurement of the genuine velocity is taken from the bearing housing using a second vibrometer which is aligned parallel with the measured velocity beam and in the same plane as the rotation axis. This is generally how measurements of radial vibrations are made on rotating devices using traditional contacting transducers. Subtracting the genuine velocity from the measured velocity allows tilt sensitivity to be quantified.

5.2.4 Rotating surface

A nominally circular shaft is rotated at a rotation speed, Ω , and speckle noise is quantified in a measurement of radial vibration.

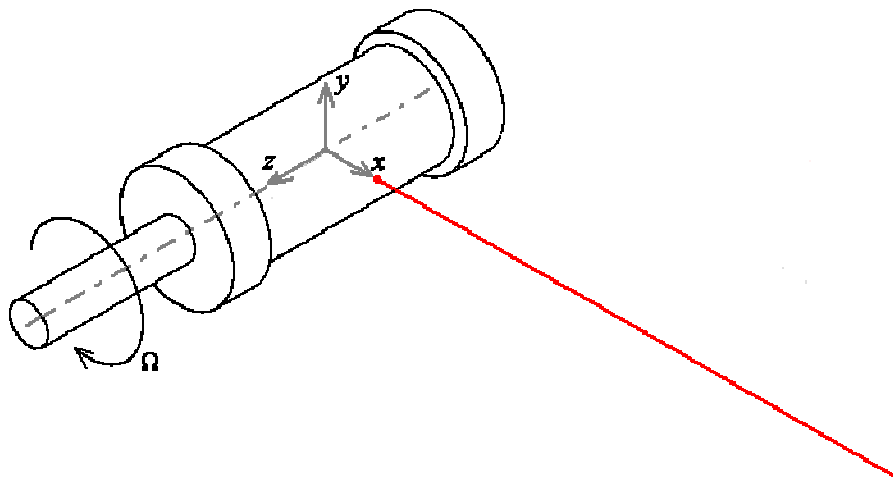


Figure 5.9 – Radial vibration measurement from a rotating shaft

The measurement axes are defined such that the z axis is coincident with the rotation axis of the shaft. A radial vibration measurement requires that the beam is aligned so its trajectory intersects the rotational axis of the rotor normally. Therefore the x axis is defined on a line which coincides with the trajectory of the beam as shown in Figure 5.9. The genuine velocity sensed by the vibrometer measuring the radial vibration can be written in the following form

$$U_m = \dot{x} + \Omega a_y \quad (5.3)$$

where the components sensitive to angular motions, other than the shaft rotation itself, are considered insignificant [5.3]. The design of the rig minimises the vibration displacements in the x and y directions which should reduce U_m to a quantity which is dominated by speckle noise. However, the velocity sensed by the vibrometer depends on the location from which the collected light originates. When surfaces are smooth and specular reflections are present, the shape of the surface, the roundness in particular, changes the origin of the collected light. This causes the effective centre of the beam to dither about the rotation axis, varying the sensed velocity. For the purposes of the U_m calculation, a pseudo y displacement amplitude, \tilde{a}_y , is introduced, representing the distance of the effective centre of the beam from the rotation axis of the shaft. \tilde{a}_y differs from any genuine y displacement in a manner that is difficult to quantify.

$$U_m = \dot{x} + \Omega \tilde{a}_y \quad (5.4)$$

It has been found that on smoother surfaces, the effect of shaft out-of-roundness can be significant, particularly at low orders, affecting rotation

sensitivity and the assessment of genuine vibration velocity. When specular reflections are not present and fully developed speckle patterns are produced from the surface, such as from the Ra 1.0 μm surface or the surface treated with retro-reflective tape, shaft out-of-roundness does not affect the measurement. This is because each speckle is a combination of wavelets scattered from all regions illuminated by the beam spot. Therefore, despite changes to the local orientation of the surface, the effective centre of the beam does not change. Figure 5.10 shows the effect of the shaft out-of-roundness on the sensitivity of a radial vibration measurement.

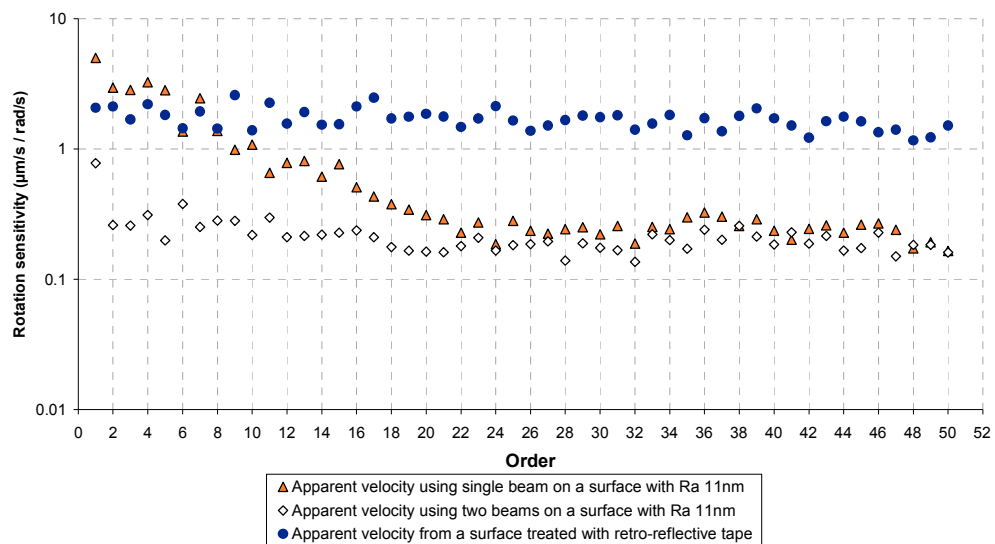


Figure 5.10 – Effect of shaft out-of-roundness on a measurement using beam diameters of 520 μm

The triangular markers show the sensitivity using a single beam on a smooth surface with Ra 11nm. The circles show the sensitivity from an adjacent location on the same shaft but treated with retro-reflective tape (The diamond markers present an approach which uses two beams to quantify the sensitivity and is discussed later in this section). It can be seen that the first 10-20 orders of the rotation frequency are affected significantly on the smooth surface and

this is believed to be due to the out-of-roundness as shown in Figure 5.11. Figure 5.11 presents a roundness measurement on the shaft with Ra 11nm at a position close to the location of the measurements shown in Figure 5.10.

P = 2.98 microns
V = 3.49 microns
P+V = 6.46 microns

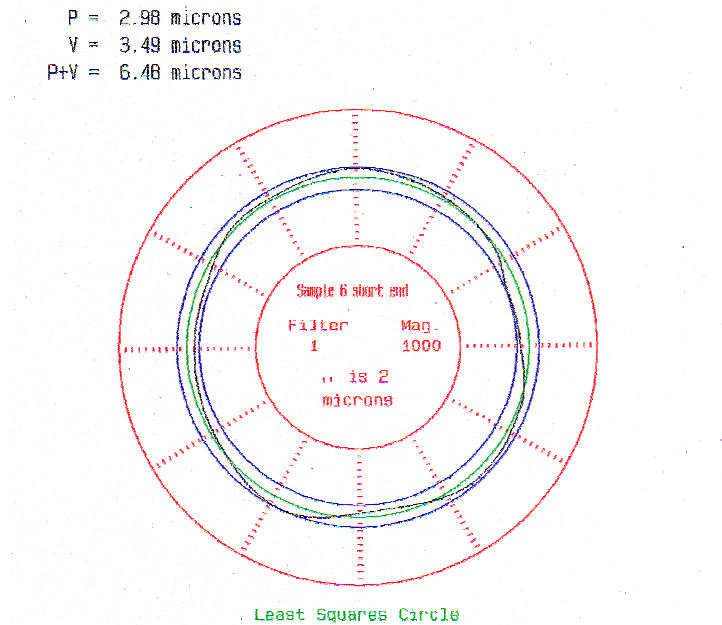


Figure 5.11 – Roundness measurement from the surface with Ra11nm

Rotation sensitivity is quantified from the difference in measured velocities using two vibrometers. The vibrometer beams are aligned as illustrated in Figure 5.12. The beams are parallel with each other and aligned to measure the radial vibration of the shaft.

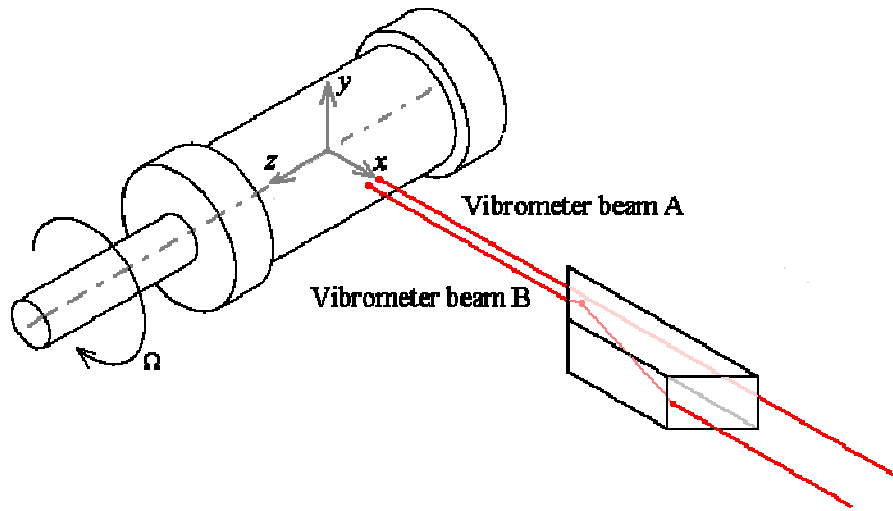


Figure 5.12 - Schematic of rotation sensitivity measurement

The beam spots are positioned close to each other (along the z-axis) so that the measured velocities are affected by similar (nominally the same) out-of-roundness and genuine velocity components, but distinct from each other to produce independent speckle patterns. This allows the out-of-roundness components and genuine velocity components to be cancelled leaving speckle noise to dominate the differential measurement.

$$\Delta U_m \approx \frac{1}{2k} \left(\frac{d\Delta\Phi_A}{dt} - \frac{d\Delta\Phi_B}{dt} \right) \quad (5.5)$$

Statistically, the rms of the difference or sum of uncorrelated noises, each with identical statistical parameters, is $\sqrt{2}$ of either of the individual rms levels. Sensitivity is calculated from the difference in measured velocities. This is divided by $\sqrt{2}$ to estimate the rotation sensitivity. This method is supported by Figure 5.13 for a surface treated with retro-reflective tape which shows rotation sensitivity calculation based on a single beam and on two beams. This figure shows similar sensitivities from the two methods validating the calculation of

rotation sensitivity based on two beams with a $\sqrt{2}$ correction applied. Total rms using a single beam is $3.86 \mu\text{ms}^{-1} / \text{rads}^{-1}$ and total rms using two beams is $3.81 \mu\text{ms}^{-1} / \text{rads}^{-1}$. Each individual measured velocity is susceptible to radial vibrations but the low orders, in Figure 5.13, are of a similar magnitude for both methods which suggests that the genuine velocity, $\dot{x} + \Omega a_y$, is low and has little influence in U_m for the test rig used here.

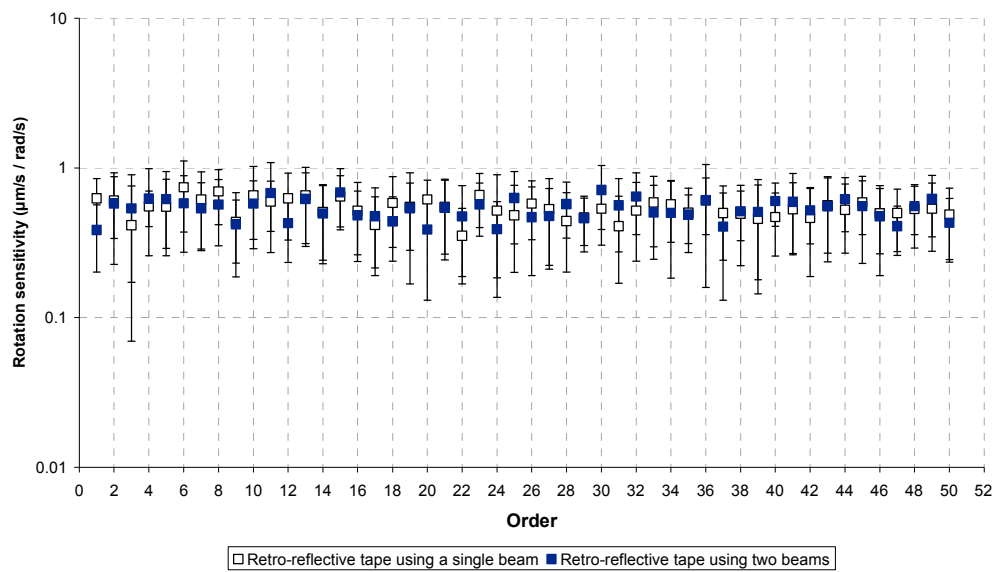


Figure 5.13 – Rotation sensitivity from a surface treated with retro-reflective tape using a single beam and two beams (with $\sqrt{2}$ correction) indicating the statistical relationship between the two approaches. Beam diameters are $90\mu\text{m}$.

The data set (marked with diamonds) shown earlier in Figure 5.10 was the adjusted rotation sensitivity for the surface with Ra 11nm, illustrating the effectiveness of this dual beam measurement approach. Therefore, the speckle noise from a single beam measurement is estimated from this dual beam measurement in order to minimise the influence of the genuine velocity (for all measurements) and shaft out-of-roundness (for smoother surfaces).

5.3 Pseudo-vibration sensitivities to surface motions

This section presents estimations of the sensitivities for each surface motion using experimental configurations. The data are processed and analysed as described in Section 5.2. Two commercial vibrometers are used, one producing a beam spot diameter on the surface which is nominally 100 μm and the other producing a beam spot diameter which is nominally 600 μm . The vibrometers are positioned at their recommended stand off distances which are 600mm and 400mm respectively. The beams are focussed at these distances and therefore both beams are considered to have planar wavefronts on the surface.

5.3.1 Transverse sensitivity

The test surfaces are oscillated sinusoidally at a frequency of 60Hz with a translational displacement of 420 μm rms providing at least one whole beam spot diameter translation for the configurations being tested. Figure 5.14 shows typical captured data from a surface moving perpendicular to the optical axis. Figure 5.15 shows the speckle noise which is calculated from the difference between the measured velocity and the genuine velocity.

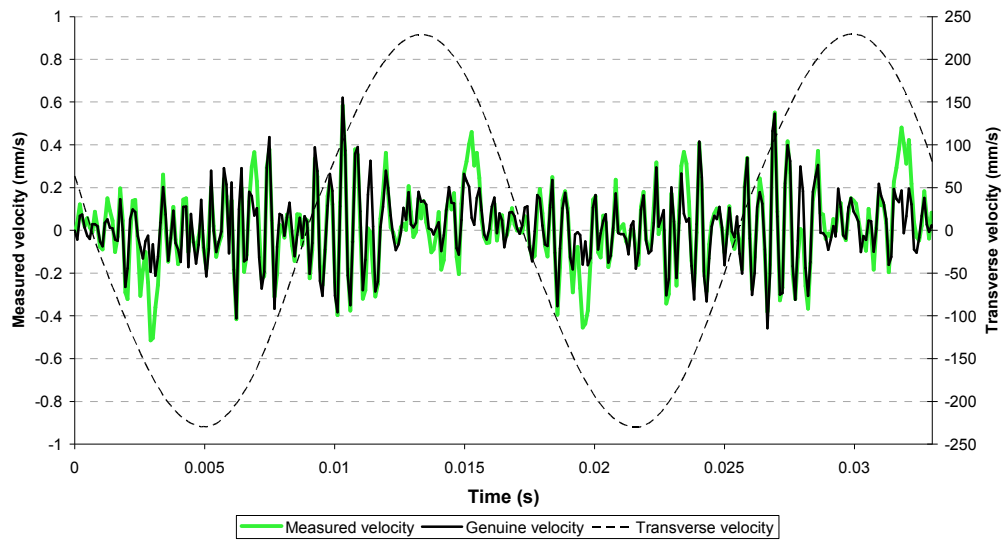


Figure 5.14 - Typical data of measured velocity, genuine velocity and transverse velocity.
 Beam diameter, $D=600\mu\text{m}$. Surface roughness, $R_a 1.0\mu\text{m}$.

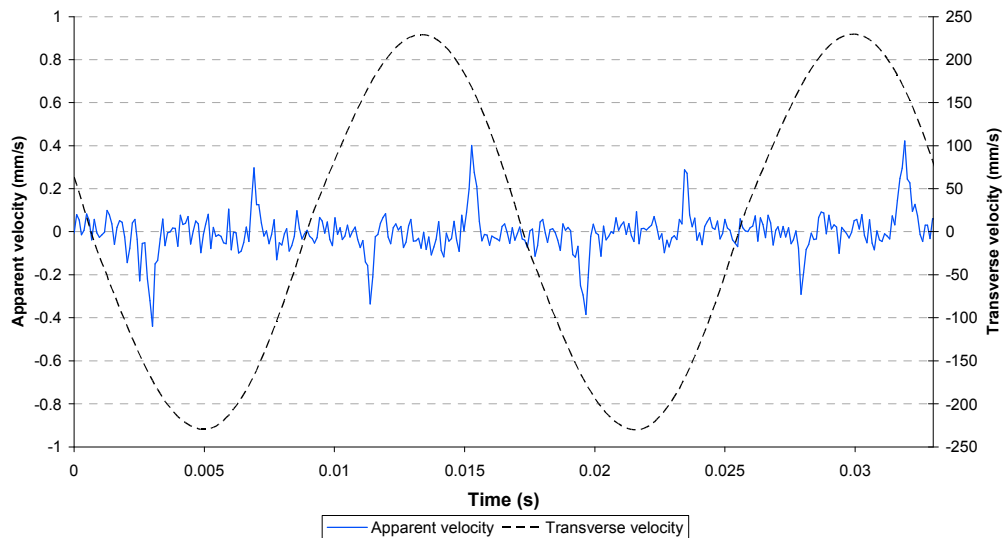
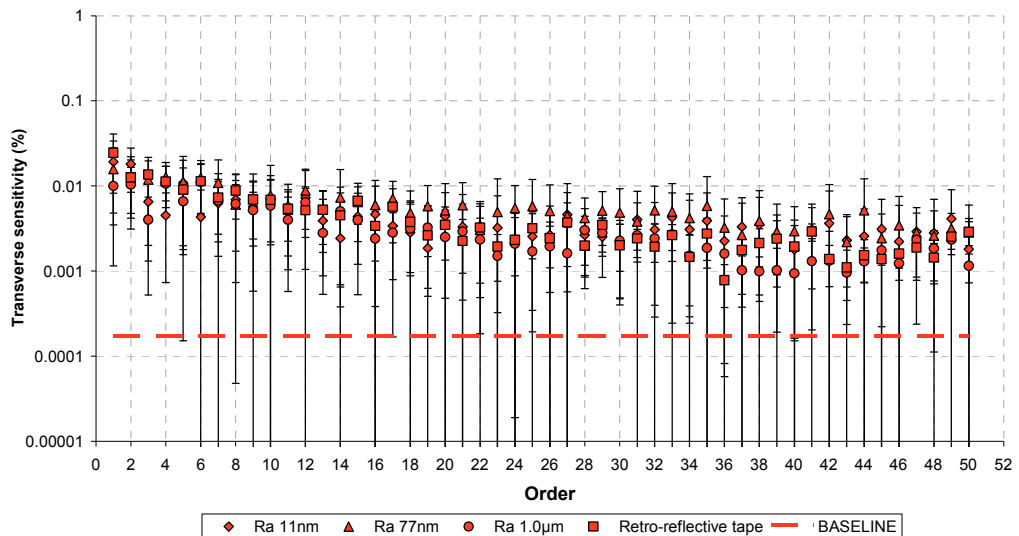


Figure 5.15 - Typical data of the apparent and transverse velocity using a beam spot diameter of $D=600\mu\text{m}$ on a surface with $R_a 1.0\mu\text{m}$.

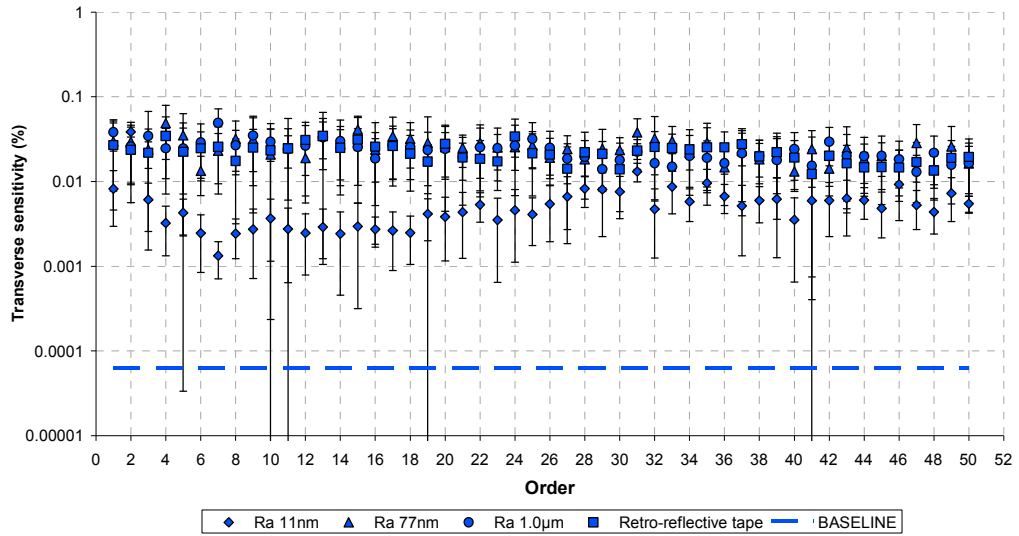
The sinusoidal motion of the surface causes speckle noise to appear to reflect and negate around the instances in time when the surface is stationary. The more prominent peaks of speckle noise occur in the temporal vicinity of

maximum surface velocity and this is not uncommon in measurements of speckle noise. The increased velocity of the surface causes the speckles, which evolve and translate, to change at a greater rate on the photodetector surface resulting in more rapid changes in the phase of the Doppler signal. This feature is also present in simulations of speckle noise described later in Section 7.1.4.

Data such as that shown in Figure 5.15 is processed as described in Section 5.2.1 where it is Fourier transformed, normalised by the transverse velocity at the fundamental frequency and presented in terms of order. A statistical average is produced for each test surface and beam diameter configuration and the mean \pm one standard deviation of speckle noise presented as a percentage of the transverse velocity, as shown for 50 orders in Figure 5.16.



(a)



(b)

Figure 5.16 – Transverse sensitivity map for a surface with a displacement of $420\mu\text{m}$ rms. (a) transverse sensitivity using $600\mu\text{m}$ beam spot diameter. (b) transverse sensitivity using $100\mu\text{m}$ beam spot diameter.

The configurations with the $600\mu\text{m}$ and $100\mu\text{m}$ beam spot diameter are shown in Figure 5.16 (a) and (b) respectively. The various surface finishes can be identified by the styles shown within the keys. The baseline noise levels differ because the configurations use two different vibrometer models. Table 5.1 and Table 5.2 show the transverse sensitivities for the beam diameters of $600\mu\text{m}$ and $100\mu\text{m}$ respectively. These tables present the first quantification of transverse sensitivity for laser vibrometers. Figure 5.16 and Table 5.1 together with Table 5.2 show clear evidence that increasing the beam spot diameter on the surface can reduce the transverse sensitivity. Increasing the beam spot diameter reduces the rate of change of the resultant phase because the speckles remain correlated for a longer period of time as discussed in Section 4.1.1.

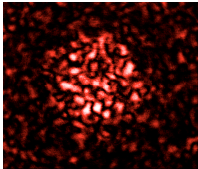
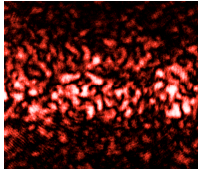
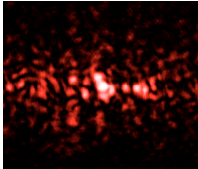

$D = 600\mu\text{m}$				
<i>Transverse sensitivity: apparent velocity per unit transverse velocity (%)</i>				
<i>Surface finish</i>	Retro-reflective tape	Ra 1.0μm (1.6λ)	Ra 75nm (0.12λ)	Ra 11nm (0.02λ)
<i>Typical scattered light patterns</i>				
<i>Mean level by order (orders 1-10)</i>	0.011	0.0077	0.011	0.0090
<i>Standard deviation (orders 1-10)</i>	0.0070	0.0055	0.0080	0.0081
<i>Total RMS level across 50 orders</i>	0.044	0.030	0.047	0.039

Table 5.1 - Transverse sensitivity for a target with a displacement of 420 μm rms using beam diameter of 600 μm

Transverse sensitivity is quantified at a mean level of approximately 0.01% to 0.03% over the first 10 orders for the beam spot diameters of 600 μm and 100 μm respectively. The total level over 50 orders is about 0.05% for a 600 μm beam spot diameter and less than 0.2% for a 100 μm beam spot diameter. In general, the surface roughness appears to make little difference to sensitivities except for the smoothest surface (Ra 11nm) with the 100 μm beam spot diameter which appears to reduce transverse sensitivity. Transverse sensitivities for the Ra 75nm surface, which produces a partially developed speckle pattern, appear to be comparable with sensitivities from the rougher surfaces which produce fully developed speckle patterns. This suggests the underlying, partially developed speckle pattern is a significant component in the collected light from which the measurement is taken.

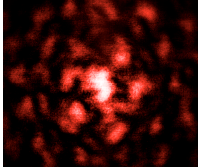
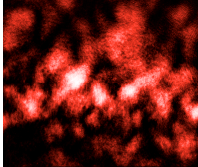
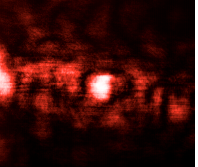
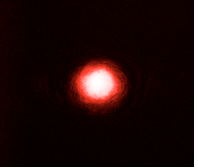
$D = 100\mu\text{m}$				
<i>Transverse sensitivity: apparent velocity per unit transverse velocity (%)</i>				
<i>Surface finish</i>	Retro-reflective tape	Ra 1.0μm (1.6λ)	Ra 75nm (0.12λ)	Ra 11nm (0.02λ)
<i>Typical scattered light patterns</i>				
<i>Mean level by order (orders 1-10)</i>	0.025	0.032	0.029	0.0073
<i>Standard deviation (orders 1-10)</i>	0.018	0.020	0.021	0.0026
<i>Total RMS level across 50 orders</i>	0.16	0.17	0.19	0.055

Table 5.2 - Transverse sensitivity for a target with a displacement of 420 μm rms using beam diameter of 100 μm

As an additional note, it was observed that sensitivities can be affected by curvatures to surfaces, particularly for focussed beams on smooth surfaces producing predominantly specular reflections. The curvature causes the scattering angle, γ_s , shown in equation (1.6) to change as a function of time. Although these angles are small, components of the surface velocity become present in the sensed velocity and observations have suggested that they can be significant enough to dominate the measurements. This is evident as an increased 1st order component in the data and is observed as an alteration to the angle of the reflected light from the surface as it moves. In this study, it was necessary to keep the effect of this to a minimum for the Ra 11nm surface. This was achieved by localising the measurements to regions where the tangent to

the surface remained relatively constant and perpendicular to the incident beam. In these locations 1st order components in the data are reduced and the light reflected from the surface appears on the vibrometer aperture and remains relatively unperturbed by surface translations.

The results presented in Table 5.1 and Table 5.2 show transverse sensitivities for four surface finishes. Data suggest that Ra 11nm with 100µm beam spot results in lower sensitivity than all other surfaces for that beam spot diameter, but further analysis can be made to see whether these differences are significant. This analysis is performed using ANOVA which is a statistical test to check whether the means of several groups are all equal. The one-way ANOVA test is made using a 95% level of confidence and hypothesising that there are no differences between the means. This means that when the hypothesis is determined to be true it is expected to be a correct decision 95% of the time.

Source of Variation	Sum of squares	Degrees of freedom	Variance	F Ratio	Probability value	Critical F ratio
D=600µm						
<i>Between Groups</i>	7.5x10 ⁻⁰⁹	3	2.5x10 ⁻⁰⁹	2.59	0.068	2.87
<i>Within Groups</i>	3.5x10 ⁻⁰⁸	36	9.7x10 ⁻¹⁰			
<i>Total</i>	4.2x10 ⁻⁰⁸	39				
D=100µm						
<i>Between Groups</i>	3.6x10 ⁻⁰⁷	3	1.2x10 ⁻⁰⁷	27.6	1.9x10 ⁻⁰⁹	2.87
<i>Within Groups</i>	1.6x10 ⁻⁰⁷	36	4.3x10 ⁻⁰⁹			
<i>Total</i>	5.1x10 ⁻⁰⁷	39				

Table 5.3 – ANOVA test results for the significance in the mean sensitivities from the various surface finishes when using beam spot diameters of 600µm and 100µm.

Vibration displacement 420µm.

The results are shown in Table 5.3. The hypothesis is deemed true if the ‘F ratio’ is less than the critical F ratio. The F ratio is found from the ratio of the variance between groups to that from within the groups and the critical F ratio is determined from the number of degrees of freedom in the samples

For the 600µm beam spot diameter configurations it was found that this hypothesis is true. An F ratio of 2.59 against a critical F ratio of 2.87 indicates there is no significant difference between the mean levels of transverse sensitivity with a 95% level of confidence. For the beam spot diameter of 100µm, the ANOVA test produces an F ratio of 27.6 against a critical F ratio of 2.87 so the differences in the mean transverse sensitivities are significantly different with a probability of 1.9×10^{-9} % that this difference is purely by chance. The ANOVA test only highlights when there is a significant difference between sample means in the group. It does not highlight which particular sample means are significantly different. To determine which surfaces have significantly different mean transverse sensitivities, Tukey’s test is used. This is a multiple comparison statistical test, comparing all possible pairs of means. Tukey’s test, as shown in Table 5.4, highlights that the mean transverse sensitivity for the surface with Ra 11nm is significantly different from the rest. It also shows that the other surfaces are not significantly different from each other falling within the critical parameter of 3.81 set out by Tukey’s test.

<i>Surface finish</i>	Retro-reflective tape	Ra 1.0µm	Ra 75nm	Ra 11nm
Retro-reflective tape	-	3.44	2.06	8.28
Ra 1.0µm	3.44	-	1.39	11.73
Ra 75nm	2.06	1.39	-	10.34
Ra 11nm	8.28	11.73	10.34	-

Table 5.4 – Results of Tukey’s test for beam diameter of 100µm configurations identifying which surfaces are significantly different. Vibration displacement 420µm rms.

It has already been shown, in Section 5.2.1, that vibration frequency appears to affect sensitivities linearly, and transverse sensitivity has been quantified and presented so it can be extrapolated to any vibration frequency. The 420 μm vibration amplitude was chosen so as to decorrelate the speckles at least once during an entire cycle. Further understanding of speckle noise comes when observing transverse sensitivity while reducing the vibration amplitude. Figure 5.17 shows the transverse sensitivity from a surface with Ra 1.0 μm which vibrates at a frequency of 60Hz but the vibration displacement amplitude is reduced by a factor of two, three times over. The standard deviation bars are not presented for clarity on presentation. It can be seen that the spectral shape changes as the vibration displacement amplitude is altered. As the vibration displacement is reduced it can be seen that the low order harmonics of transverse sensitivity increase while the higher orders reduce albeit with a small variation. This means speckle noise appears to have a slightly non-linear relation to the displacement amplitude.

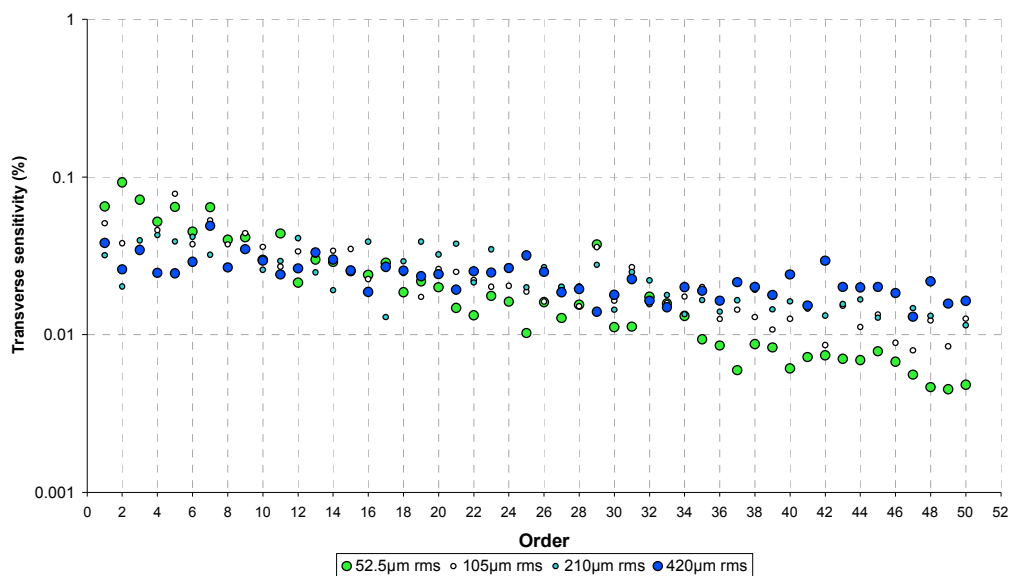


Figure 5.17 – Transverse sensitivity while varying the vibration displacement amplitude using a beam diameter of 100 μm and a surface Ra 1.0 μm .

Table 5.5 shows the transverse sensitivities and presents evidence that, as the vibration displacement reduces, apparent transverse sensitivity increases slightly. This is because speckle noise does not reduce proportionally with the vibration displacement amplitude. This alters the appearance of the spectral shape. The transverse sensitivity at lower orders is increased and the higher orders reduce because there are fewer speckle decorrelations in the time period.

$D = 100\mu\text{m}$				
<i>Transverse sensitivity: apparent velocity per unit transverse velocity (%)</i>				
Surface displacement amplitude	420μm rms	210μm rms	105μm rms	52.5μm rms
<i>Mean level by order (orders 1-10)</i>	0.032	0.034	0.046	0.057
<i>Standard deviation (orders 1-10)</i>	0.020	0.023	0.028	0.038
<i>Total RMS level across 50 orders</i>	0.17	0.18	0.20	0.22

Table 5.5 - Transverse sensitivity while varying the vibration displacement amplitude using a beam diameter of 100 μm and a surface Ra 1.0 μm .

The ANOVA test shows that there is a significant difference in the mean transverse sensitivities for the different displacement amplitudes and the results of Tukey's test are shown in Table 5.6. With a critical parameter of 3.81, Table 5.6 shows evidence that the significant differences lie between 52.5 μm rms and 420 μm rms, and 52.5 μm rms and 210 μm rms. Therefore, the transverse sensitivities presented in Table 5.2 are adequate for vibration displacements, which are greater than the beam diameter. The difference has been identified with a statistical significance and can be seen that it is separated by a factor of approximately two. However, it is important to note that the difference is small

in a practical sense showing only about 0.025% difference in transverse sensitivity for the first 10 orders.

<i>Surface displacement amplitude</i>	420µm rms (4.2D)	210µm rms (2.1D)	105µm rms (1.05D)	52.5µm rms (0.525D)
420µm rms (4.2D)	-	0.47	3.7	6.6
210µm rms (2.1D)	0.47	-	3.2	6.1
105µm rms (1.05D)	3.7	3.2	-	2.9
52.5µm rms (0.525D)	6.6	6.1	2.9	-

Table 5.6 –Tukey’s test for beam diameter of 100µm configurations.

Figure 5.18 presents the transverse sensitivities for the 100µm beam spot diameter for the surface vibration displacements of 420µm rms and 52.5µm rms and also the transverse sensitivity for the 600µm beam for a surface displacement of 420µm. It shows the similarity of the spectral shapes between the transverse sensitivities produced when using 100µm beam diameter for a surface displacement of 52.5µm rms and the 600µm beam diameter for a surface displacement of 420µm rms. In both these cases the surface displaces by approximately the same proportion of the beam diameter. Figure 5.18 therefore verifies the spectral shape for transverse sensitivity when surface displacements are smaller than the beam diameter. The transverse sensitivities presented in Table 5.1 therefore slightly over-estimate the sensitivities for surface displacement amplitudes which are greater than the beam diameter, particularly for the mean sensitivities over orders 1 to 10. However, it must be emphasised that the expected levels of transverse sensitivity will not, generally, be appreciably different in a practical sense.

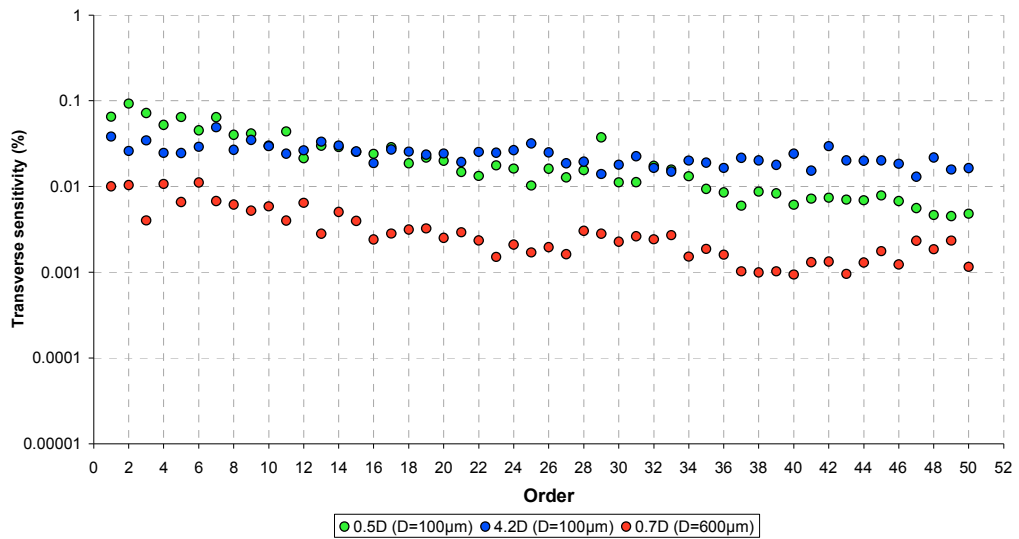


Figure 5.18 – Comparison of transverse sensitivity for 100µm beam spot diameter and 600µm beam spot diameter

The data presented in this section have provided a greater understanding of speckle noise generation. Increasing the beam diameter has the greatest significance in lowering the transverse sensitivity. Therefore methods to alter the beam diameter are of value for the vibration engineer. One of the simplest methods is to defocus the beam. If defocus is not practical, a simple alternative method can be to introduce an aperture into the path of the laser beam as it is emitted from the laser vibrometer. The aperture has two effects on the optical configuration; it diffracts the beam and it also causes a reduced receiving aperture to the vibrometer. The latter effect has little consequence on the transverse sensitivity and this is shown in simulations presented in Section 7.1.4.2.

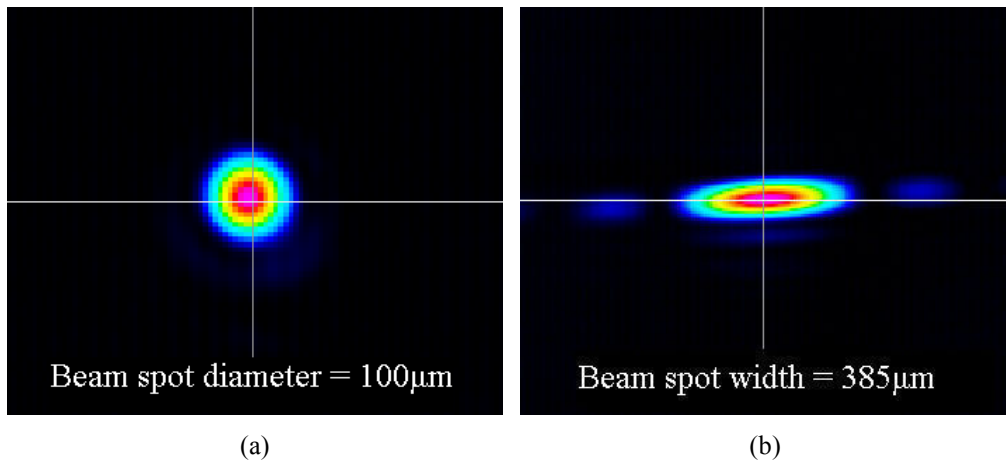


Figure 5.19 – (a) beam spot on surface with no additional aperture in the laser beam path, (b) beam spot with an additional vertical 1mm wide aperture in the laser beam path.

((a) and (b) not to the same scale)

The first effect does have a significant effect on the transverse sensitivities. The diffraction increases the beam spot diameter on the surface but it is only necessary to increase the beam spot dimension in the direction in which the surface is moving to reduce speckle noise levels. Figure 5.19 shows images of the beam spots created when (a) there is no additional aperture introduced into the beam path and (b) when a 1mm wide vertical slit aperture is introduced into the beam path. Figure 5.20 and Table 5.7 present transverse sensitivity from a surface treated with retro-reflective tape, showing the effect of introducing a vertical aperture 1mm wide. The increased beam spot dimension in the direction of the surface translation causes the speckles to decorrelate over a greater time and with fewer decorrelations in the cycle period. This ultimately reduces speckle noise and it can be seen that the simple addition of an aperture can reduce transverse sensitivity levels by approximately half.

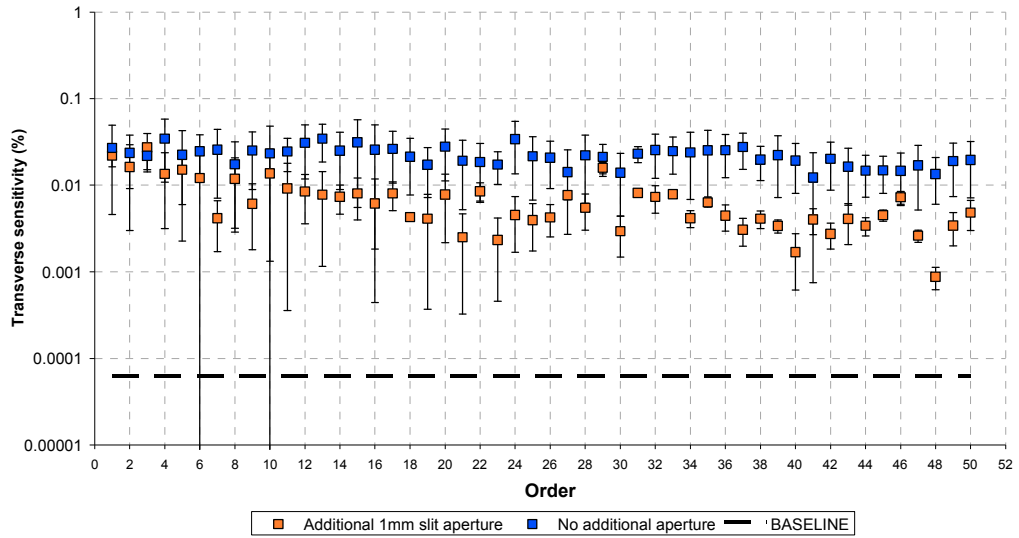


Figure 5.20 – The effect of introducing an additional vertical 1mm wide aperture into the vibrometer beam path, using an undisturbed beam spot diameter of 100 μm on a surface treated with retro-reflective tape, vibration displacement 420 μm .

Transverse sensitivity: apparent velocity per unit transverse velocity (%)

<i>Configuration</i>	No additional aperture ($D=100\mu\text{m}$)	Additional 1mm wide vertical aperture ($D=385\mu\text{m}$)
Retro-reflective tape		
<i>Mean level by order (orders 1-10)</i>	0.025	0.014
<i>Standard deviation (orders 1-10)</i>	0.018	0.0093
<i>Total level across 50 orders</i>	0.16	0.063

Table 5.7 – Transverse sensitivities showing the effect of introducing an aperture into the laser beam path. Vibration displacement 420 μm .

5.3.2 Tilt sensitivity

The test surfaces are oscillated sinusoidally at a frequency of 60Hz with an angular displacement of 0.78° rms. As discussed in Section 4.1.2, the speckles are expected to translate predominantly. This angular displacement results in speckle translation distances of 45mm at 600mm and 30mm at 400mm which exceed the vibrometer receiving aperture dimensions. Figure 5.21 shows a typical plot of speckle noise together with the angular velocity of the surface. This particular plot is taken from tests with a beam diameter of $100\mu\text{m}$ and the surface has a roughness of $R_a 1.0\mu\text{m}$. As described in Section 5.1.2, speckle noise again appears to reflect and negate around the instances in time when the surface is stationary.

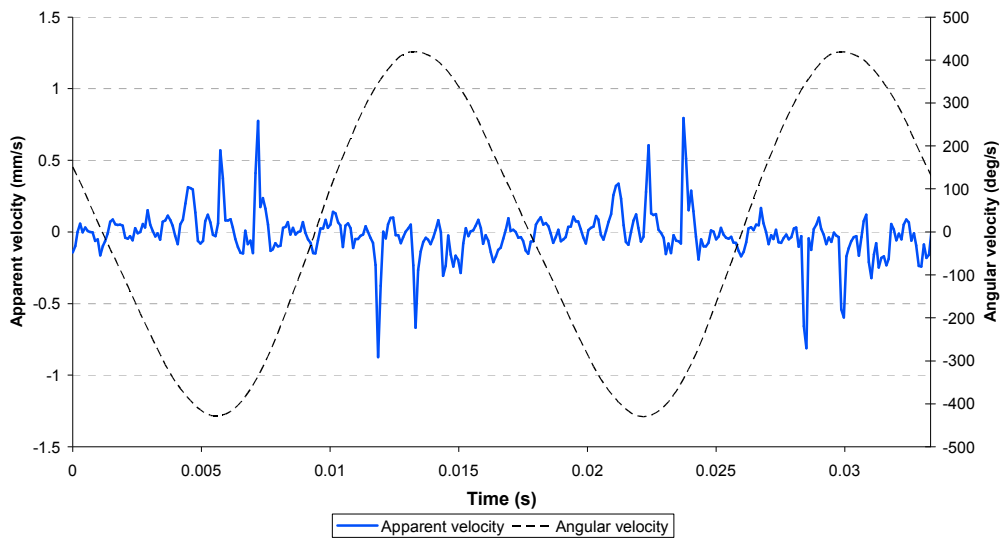
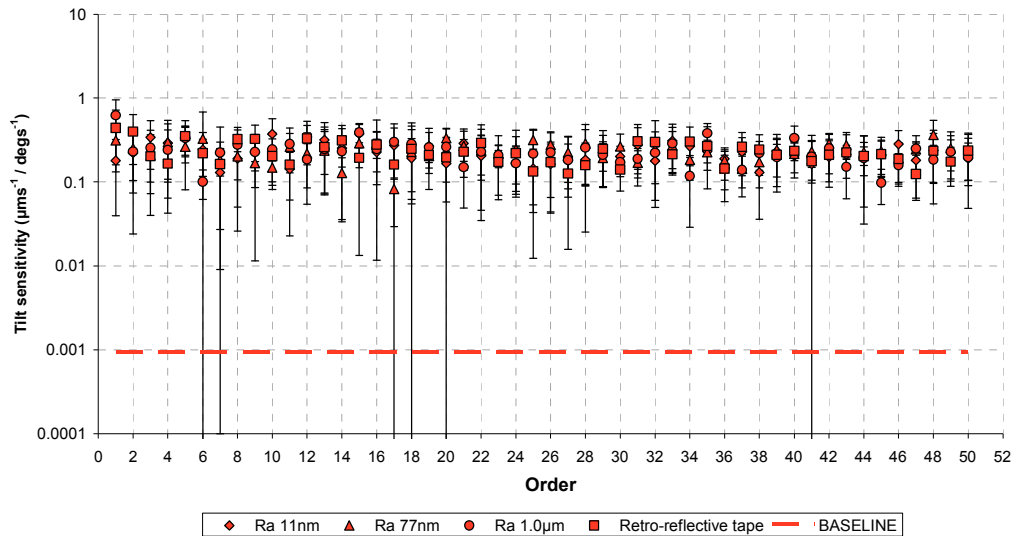


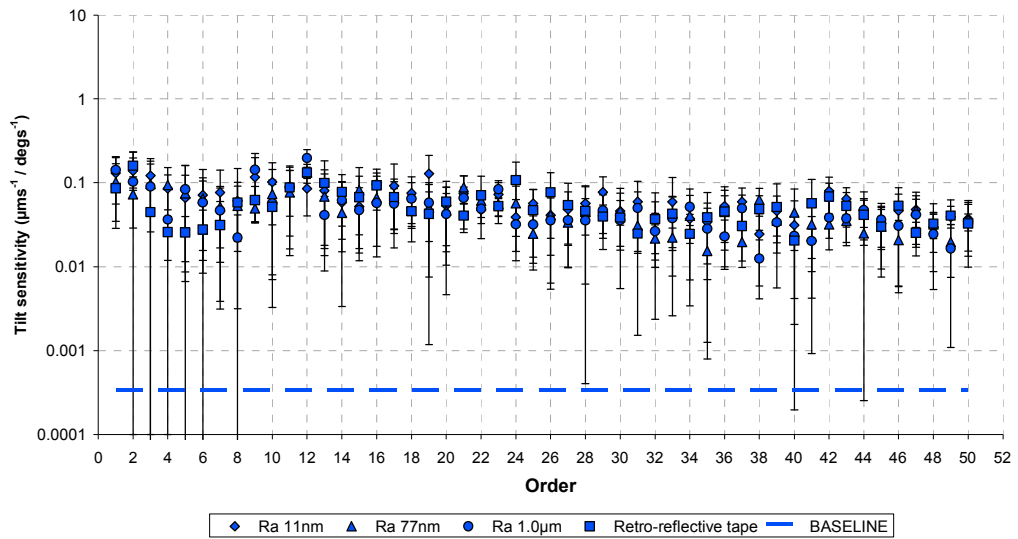
Figure 5.21 - Typical data of speckle noise and angular velocity from tilting target surface.
Beam diameter, $D=100\mu\text{m}$. Surface roughness, $R_a 1.0\mu\text{m}$.

The more prominent peaks of speckle noise occur in the temporal vicinity of maximum surface velocity and this is not uncommon in measurements of speckle noise. The increased velocity of the surface causes the speckles to

move with a greater velocity resulting in more rapid changes in the resultant phase of the Doppler signal which manifest in the apparent velocity. This feature of speckle noise is also evident in simulations shown later in Section 7.2.4. Data such as that presented in Figure 5.21 is captured for each test surface and beam diameter configuration and is processed as described in Section 5.2.1. Figures 5.22 (a) and (b) map the tilt sensitivity for beam diameters of 600 μm and 100 μm respectively. They present the statistical mean \pm one standard deviation normalised by the angular velocity at the fundamental frequency with units of $\mu\text{ms}^{-1} / \text{degs}^{-1}$ in terms of order.



(a)



(b)

Figure 5.22 –Tilt sensitivity map for a surface with angular displacement 0.78° rms. (a) tilt sensitivity using $600\mu\text{m}$ beam spot diameter. (b) tilt sensitivity using $100\mu\text{m}$ beam spot diameter.

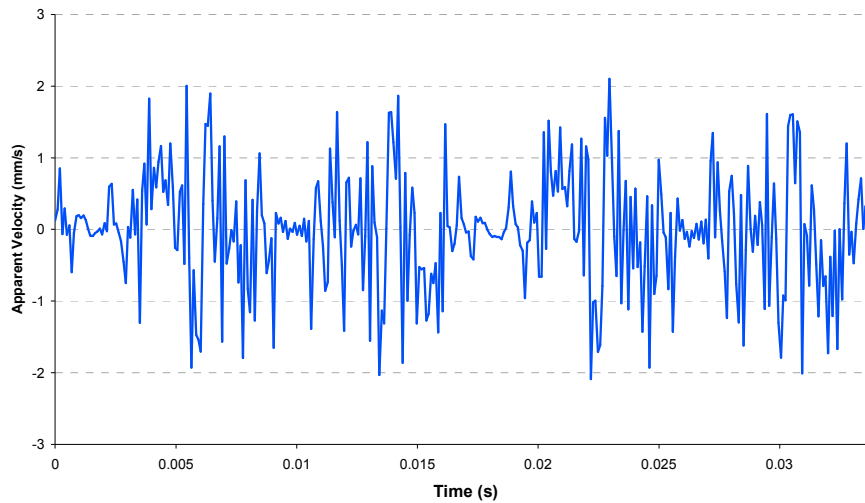
Figures 5.22 (a) and (b), show that reducing the beam diameter can significantly reduce tilt sensitivity, particularly at higher order harmonics. The sensitivity rolls-off as the harmonic order increases and this roll-off is slightly greater for the beam diameter of $100\mu\text{m}$. A smaller laser spot diameter on the surface increases the size of the speckle. Larger speckles cause phase variations to occur over a greater time and therefore reduce the tilt sensitivity. Figures 5.22 (a) and (b) suggest that surface finish does not make a significant difference to the tilt sensitivities. Table 5.8 shows tilt sensitivity is quantified at a mean level of approximately $0.1 \mu\text{ms}^{-1}/\text{degs}^{-1}$ to $0.3 \mu\text{ms}^{-1}/\text{degs}^{-1}$ over the first 10 orders for the beam spot diameters of $100\mu\text{m}$ and $600\mu\text{m}$ respectively. The total level over 50 orders is about $0.4 \mu\text{ms}^{-1}/\text{degs}^{-1}$ for a $100\mu\text{m}$ beam spot diameter and $1.3 \mu\text{ms}^{-1}/\text{degs}^{-1}$ for a $600\mu\text{m}$ beam spot diameter.

<i>Tilt sensitivity: apparent velocity per unit angular velocity $\mu\text{ms}^{-1} / \text{degs}^{-1}$</i>				
<i>Surface finish</i>	Retro-reflective tape	Ra 1.0μm (1.6λ)	Ra 75nm (0.1λ)	Ra 11nm (0.02λ)
<i>D = 600μm</i>				
<i>Mean level by order (orders 1-10)</i>	0.28	0.28	0.24	0.25
<i>Standard deviation (orders 1-10)</i>	0.15	0.16	0.17	0.17
<i>Total level across 50 orders</i>	1.7	1.7	1.7	1.7
<i>D = 100μm</i>				
<i>Mean level by order (orders 1-10)</i>	0.057	0.078	0.073	0.097
<i>Standard deviation (orders 1-10)</i>	0.042	0.064	0.053	0.063
<i>Total level across 50 orders</i>	0.43	0.44	0.40	0.50

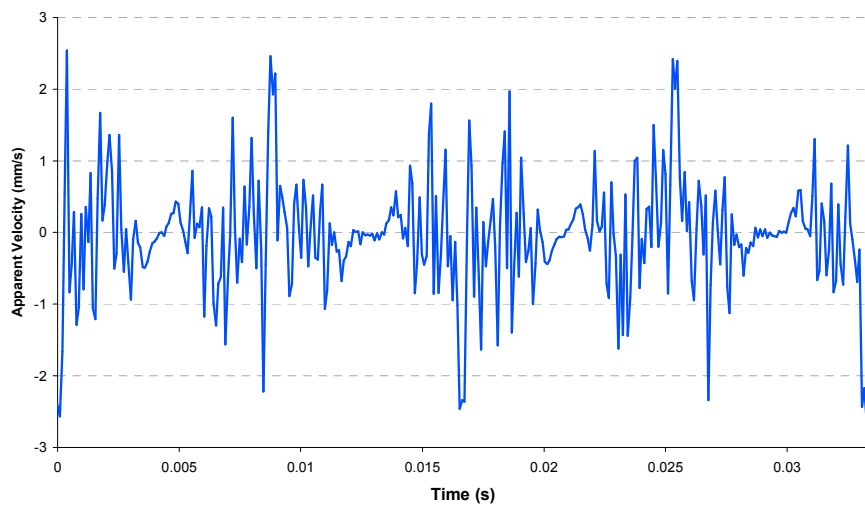
Table 5.8 - Tilt sensitivity ($\mu\text{ms}^{-1} / \text{degs}^{-1}$) for a target with an angular displacement of 0.78° rms.

The ANOVA tests show the configurations using the 600 μm beam spot diameter produce an F ratio of 0.625 and the configurations using the 100 μm beam spot diameter produce an F ratio of 3.17. With a critical F ratio of 3.23, the ANOVA tests show quantifiable evidence that the surface finish makes no significant difference to the tilt sensitivities. Despite being the smoothest, the Ra 11nm surface shows noise levels which are as large as speckle noise. Figure

5.23 (a) and (b) show typical time histories of the apparent velocity from a surface with Ra 1.0 μ m and Ra 11nm respectively, over two oscillations of the surface. These figures show a similarity in the apparent velocity produced from an optically rough surface and a smooth surface.



(a)



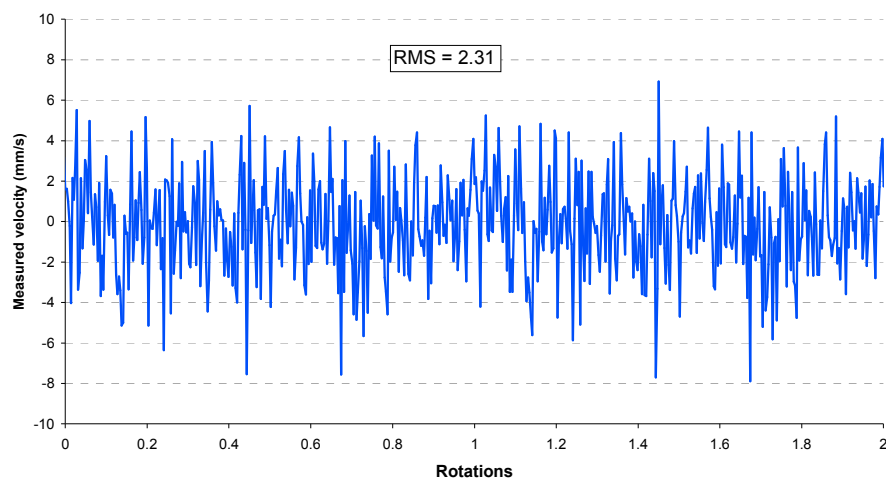
(b)

Figure 5.23 - Typical data of the apparent velocity from tilting target surface with roughness of (a) Ra 1.0 μ m and (b) Ra 11nm. Beam diameter, $D=600\mu$ m.

The results, from a tilting target, suggest focussing the beam whenever possible to reduce tilt sensitivity. This is in fundamental accord with Drain [5.4], who remarked ‘increasing the spot size...increases sensitivity to tilt of the surface’. This is consistent with conventional wisdom on minimising frequency broadenings by minimising the range of Doppler shifts across the finite extent of the incident laser beam.

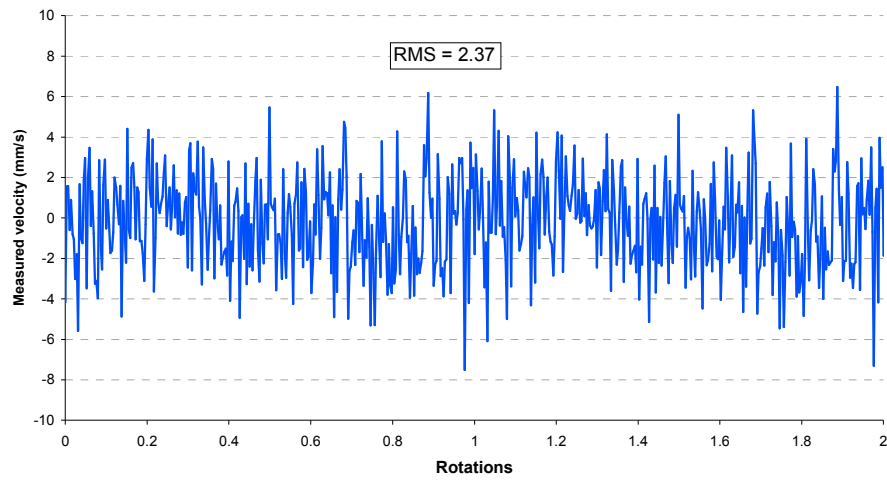
5.3.3 Rotation sensitivity

The test surfaces have diameters of 15mm and are rotated nominally at 35Hz for the rotation sensitivity maps. The configurations used are 90 μ m beam spot diameter at 600mm standoff distance and 520 μ m at 400mm standoff distance*.

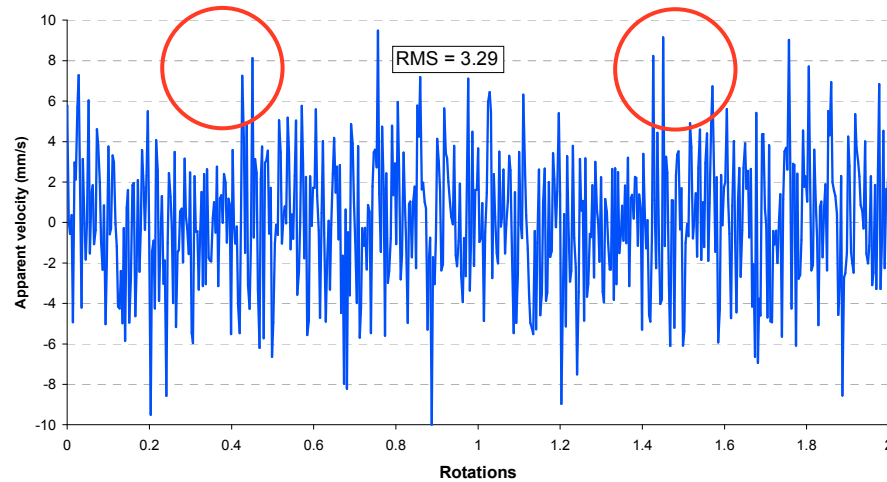


(a)

* These configurations show different beam spot diameters compared to those used in the transverse and tilt sensitivity measurements. The differences are due to an improved instrument to measure the spot diameters prior to these sensitivity experiments. Therefore, although values shown are different, the configurations are considered the same.



(b)

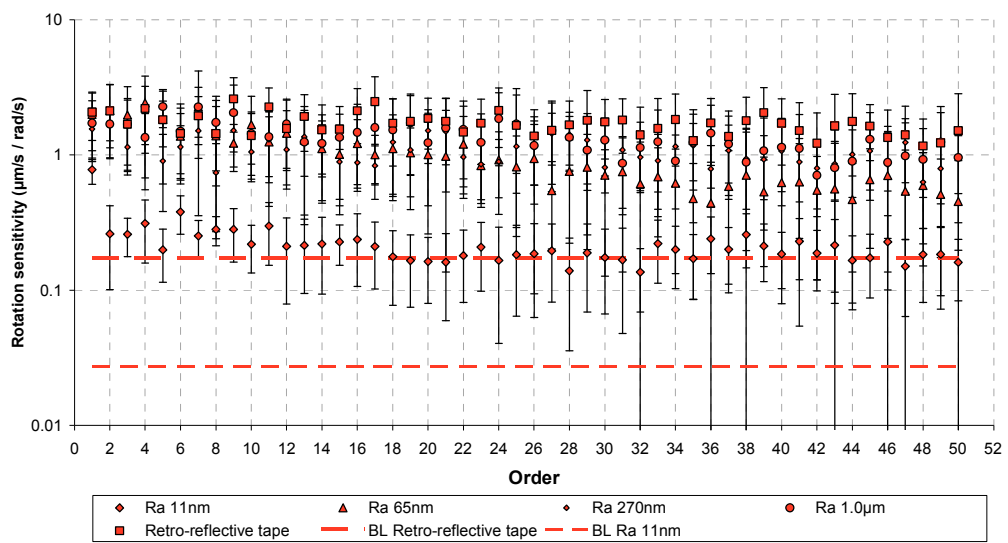


(c)

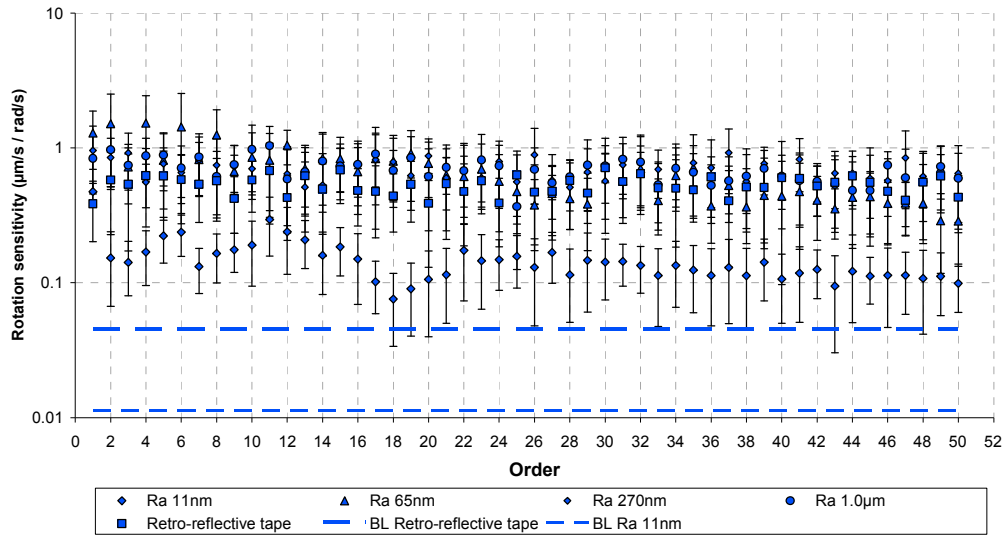
Figure 5.24 – Typical measured velocities from (a) vibrometer A (b) vibrometer B and (c) the calculated differential velocity from a rotor with surface roughness R_a $1.0\mu\text{m}$ using beam spot diameters of $90\mu\text{m}$

Figures 5.24 (a) and (b) show typical data, from the two vibrometers, over two rotations of a shaft with a roughness of R_a $1.0\mu\text{m}$. Figure 5.24 (c) is a trace of the difference between these measured velocities. The distinctive peaks highlighted by the circles in Figure 5.24 (c) illustrate the repetition of speckle noise caused by the speckle motions repeating as the surface rotates. It can be

seen by the rms levels displayed in Figures 5.24 (a)-(c) that the measured velocities, which are dominated by speckle noise, are uncorrelated as the rms of the difference is approximately $\sqrt{2}$ of either of the individual rms levels. It is important that the noise on each measurement is uncorrelated so that when the difference is calculated, to give the apparent velocity, the rotation sensitivity can be estimated using the $\sqrt{2}$ factor.



(a)



(b)

Figure 5.25 – Rotation sensitivity map for a shaft 15mm in diameter (a) rotation sensitivity using a 520µm beam spot diameter (b) rotation sensitivity using a 90µm beam spot diameter.

BL= Baseline

Figures 5.25 (a) and (b) show the rotation sensitivities, based on the difference calculation and the $\sqrt{2}$ correction, of a target 15mm in diameter for different surface finishes using beam spot diameters of 520µm and 90µm respectively. Table 5.9 and Table 5.10 present the corresponding rotation sensitivities. Figures 5.25 (a) and (b) and Table 5.9 together with Table 5.10 suggest reducing the beam spot diameter where possible to minimise sensitivity. This evidence together with visual observations shows speckle translation is the dominant speckle motion for the target rotation. Smaller beam diameter means a larger speckle size, which increases the correlation time and in turn reduces the rotation sensitivity.

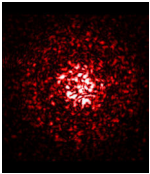
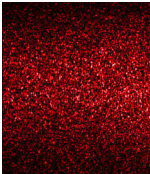
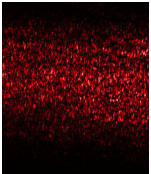
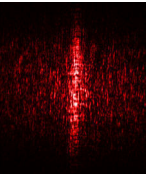
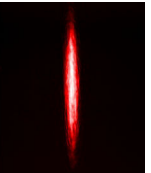
$D = 520\mu\text{m}$					
<i>Rotation sensitivity: apparent velocity per unit rotational velocity ($\mu\text{ms}^{-1} / \text{rads}^{-1}$)</i>					
<i>Surface finish</i>	Retro-reflective tape	Ra 1.0μm (1.6λ)	Ra 270nm (0.4λ)	Ra 65nm (0.1λ)	Ra 11nm (0.02λ)
<i>Typical scattered light patterns</i>					
<i>Mean level by order (orders 1-10)</i>	1.87	1.77	1.26	1.82	0.321
<i>Standard deviation (orders 1-10)</i>	1.89	1.73	1.23	1.75	0.274
<i>Mean level by order (orders 41-50)</i>	1.44	0.981	0.907	0.566	0.188
<i>Standard deviation (orders 41-50)</i>	0.942	0.727	0.498	0.516	0.0993
<i>Total level across 50 orders</i>	12.25	9.84	7.90	7.91	1.68

Table 5.9 - Rotation sensitivity ($\mu\text{ms}^{-1} / \text{rads}^{-1}$) using a beam diameter of 520 μm . Shaft diameter = 15mm

Rotation sensitivity is expected to reduce as surfaces become smoother. The more mirror-like the surface, the less diffuse the scatter and the correlation time increases. However, the 2nd smoothest surface with Ra 65nm, which is approximately one tenth of the wavelength of the light (0.1 λ), has produced sensitivities which are greater than that produced from rougher surfaces. The manufacture of the test shafts, which had the capability to vary the surface roughness, had less control of the roundness. The out-of-roundness for the

surface with Ra 65nm is particularly large, quantified at 27 μ m (other shafts in the range of 1-7 μ m).

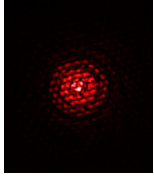
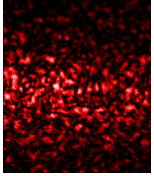
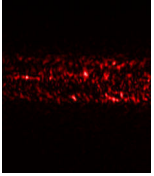
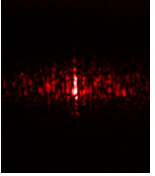

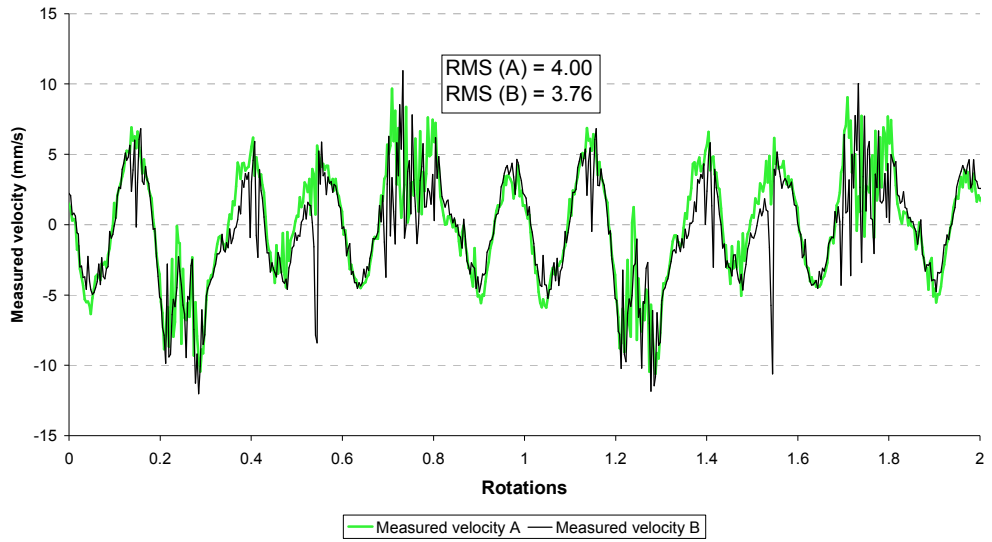
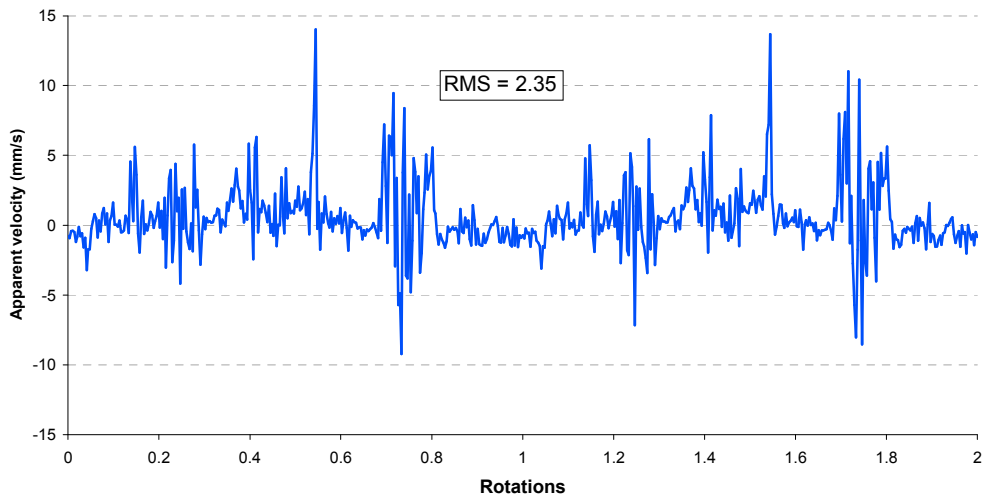
D = 90μm					
<i>Rotation sensitivity: apparent velocity per unit rotational velocity (μms⁻¹ / rads⁻¹)</i>					
<i>Surface finish</i>	Retro-reflective tape	Ra 1.0μm (1.6λ)	Ra 270nm (0.4λ)	Ra 65nm (0.1λ)	Ra 11nm (0.02λ)
<i>Typical scattered light patterns</i>					
<i>Mean level by order (orders 1-10)</i>	0.542	0.821	0.664	1.09	0.206
<i>Standard deviation (orders 1-10)</i>	0.572	0.841	0.658	1.04	0.188
<i>Mean level by order (orders 41-50)</i>	0.533	0.586	0.588	0.384	0.112
<i>Standard deviation (orders 41-50)</i>	0.252	0.279	0.290	0.193	0.0575
<i>Total level across 50 orders</i>	3.81	5.02	4.58	5.19	1.15

Table 5.10 - Rotation sensitivity (μ ms⁻¹ / rads⁻¹) using a beam diameter of 90 μ m. Shaft diameter = 15mm



(a)



(b)

Figure 5.26– Typical measured velocities from (a) vibrometer A & vibrometer B and (b) the calculated difference velocity from a rotor with surface roughness Ra 65nm using beam spot diameters of 90 μ m

Figure 5.26 (a) shows typical data for the measured velocities produced from the surface with Ra 65nm over two rotations. The measured velocities show a high degree of similarity and this is the result of the out-of roundness. Figure

5.26 (b) shows the calculated difference of the apparent velocities shown in Figure 5.26 (a). The effect of the out-of-roundness is reduced in the difference calculation and ‘speckle noise’ is more evident. It can be seen by the rms levels displayed in Figures 5.26 (a) and (b) that the measured velocity signals are correlated as the rms of the difference is considerably less than $\sqrt{2}$ of either of the individual signals. This can also be seen in the spectrum. Figure 5.27 shows typical spectra of the two measured velocities from vibrometers A and B together with the calculated difference. Although the beams are parallel and the spots are as close to one another as possible to cancel the genuine velocity and any shaft out-of-roundness, lower orders still dominate the measurement, and these are believed to result from out-of-roundness.

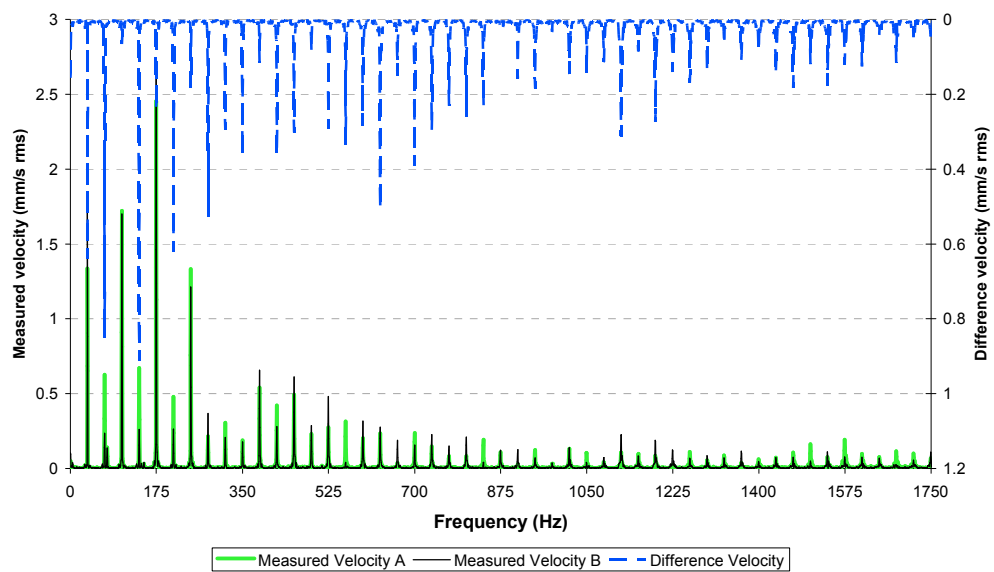


Figure 5.27 – Spectra of measured velocities A and B and calculated difference velocity from surface with Ra 65nm, $D=90\mu\text{m}$.

The out-of-roundness affecting the low orders was also seen in Figure 5.10 in the single beam measurement on the surface with Ra 11nm. Pseudo-vibration retains its amplitude over an extremely large bandwidth, affecting the

amplitude of high orders nearly as much as low orders. Shaft out-of-roundness affects low orders of the sensitivity and therefore to provide a more appropriate comparison of the surfaces the mean rotation sensitivities and the standard deviation for higher orders (41-50) are shown in Table 5.9 and Table 5.10 where out-of-roundness has little effect. The sensitivities at higher orders shown in Table 5.9 and Table 5.10 are more consistent with expected sensitivities i.e. rotation sensitivity reduces as roughness reduces.

Table 5.9 shows a mean rotation sensitivity of up to approximately $1.4 \mu\text{ms}^{-1} / \text{rads}^{-1}$ over orders 41 to 50 and a total rms over 50 orders of approximately $12 \mu\text{m s}^{-1} / \text{rad s}^{-1}$ for a beam spot diameter of $520\mu\text{m}$. A smaller beam diameter of $90\mu\text{m}$, shown in Table 5.10, produces mean rotation sensitivity over orders 41 to 50 of approximately $0.6 \mu\text{ms}^{-1} / \text{rads}^{-1}$ and a total rms of $5 \mu\text{ms}^{-1} / \text{rads}^{-1}$ over 50 orders.

The ANOVA tests show that there is a significant difference in the mean sensitivities over orders 41 to 50 in the group of surface finishes for both the larger beam diameter and the smaller beam diameter. Therefore, to see where the significant differences lie, Tukey tests are performed for the groups of surface finishes. The results of the Tukey tests are shown in Tables 5.11 and 5.12 for the $520\mu\text{m}$ and $90\mu\text{m}$ beam spot diameters respectively.

For a 95% confidence level, a critical value of 4.01 exists and the significant differences have been highlighted in the respective tables. The results from Tukey's test produced from the beam spot diameter of $520\mu\text{m}$ show the mean rotation sensitivities from all surfaces are significantly different, except those between the surface with Ra $1.0\mu\text{m}$ and Ra 270nm . Table 5.12 shows that the smoothest surfaces, with Ra 65nm and Ra 11nm , produce distinct mean rotation sensitivities from all other surfaces.

<i>Surface finish</i>	Retro-reflective tape	Ra 1.0μm	Ra 270nm	Ra 65nm	Ra 11nm
Retro-reflective tape	-	5.64	8.28	12.94	20.03
Ra 1.0μm	5.64	-	2.64	7.30	14.39
Ra 270nm	8.28	2.64	-	4.66	11.75
Ra 65nm	12.94	7.30	4.66	-	7.08
Ra 11nm	20.03	14.39	11.75	7.08	-

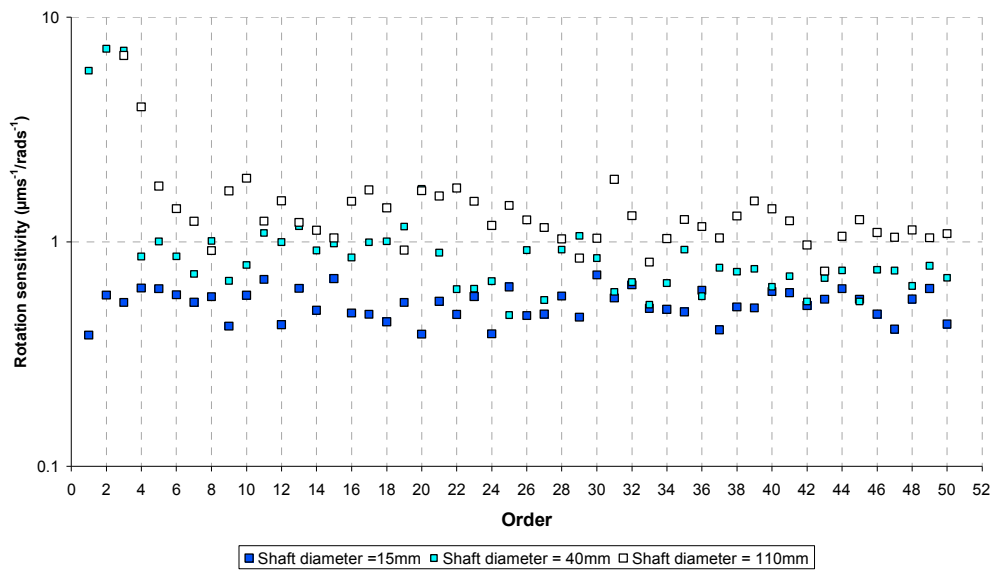
Table 5.11 – Results of Tukey’s test for the surfaces when using a beam diameter of 520 μ m using orders 41-50. Shaft diameter = 15mm

<i>Surface finish</i>	Retro-reflective tape	Ra 1.0μm	Ra 270nm	Ra 65nm	Ra 11nm
Retro-reflective tape	-	2.46	2.54	6.83	19.30
Ra 1.0μm	2.46	-	0.09	9.29	21.76
Ra 270nm	2.54	0.09	-	9.38	21.85
Ra 65nm	6.83	9.29	9.38	-	12.47
Ra 11nm	19.30	21.76	21.85	12.47	-

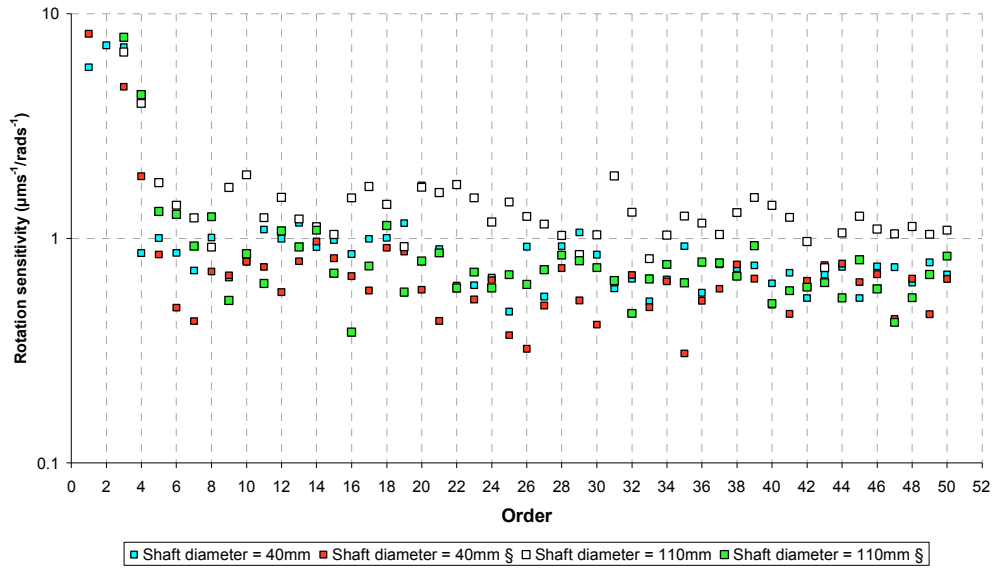
Table 5.12 – Results of Tukey’s test for the surfaces when using a beam diameter of 90 μ m using orders 41-50. Shaft diameter = 15mm

The rotation sensitivities shown in Figures 5.25 (a) and (b) are produced from a target shaft with a diameter of 15mm. The cross-correlations shown in Section 4.1.3 predict that the radius of the target shaft can affect the sensitivity, particularly when using smaller beam spot diameters. Figure 5.28 (a) shows the effect on the rotation sensitivity from an increased shaft diameter. Using three targets of diameter 15mm, 40mm and 110mm it shows the rotation sensitivity

when using a beam spot diameter of $90\mu\text{m}$. The target shafts are treated with retro-reflective tape to remove any effect of the out-of-roundness. Vibration at lower orders was evident for the larger shaft diameters and this was because a different experimental rig was used. Of particular note, it was found that altering the focal point can affect the rotation sensitivity and Figure 5.28 (b) presents results obtained by focussing the beam at the rotational axis as well as on the shaft surface.



(a)



(b)

Figure 5.28 – Rotation sensitivity showing (a) the effect of an increased shaft diameter and (b) changing the focal point. (§ - focussed on the rotation axis)

$D = 90\mu\text{m}$					
<i>Rotation sensitivity: apparent velocity per unit rotational velocity ($\mu\text{m s}^{-1} / \text{rad s}^{-1}$)</i>					
<i>Shaft diameter</i>	15mm	40mm	40mm §	110mm	110mm §
<i>Mean level by order (orders 41-50)</i>	0.533	0.682	0.618	1.07	0.625
<i>Standard deviation (orders 41-50)</i>	0.252	0.344	0.221	0.466	0.314

Table 5.13 – Rotation sensitivity of orders 41-50 with various shaft diameters treated with retro-reflective tape and also showing the effect of focussing on the rotation axis of the shaft. (§ - focussed on the rotation axis)

Table 5.13 presents the rotation sensitivities based on orders 41-50 from the three shafts examined, including the results when focussing the beam near the

rotation axis rather than the shaft surface. The largest difference in rotation sensitivity can be seen for the largest shaft diameter of 110mm. Focussing the beam near the rotation axis shows a noticeable difference to focussing on the surface, particularly for the larger shaft diameter. The rotation sensitivity using a shaft diameter of the 15mm and 40mm while focussing on the shaft surface and also 40mm and 110mm while focussing on the rotation axis all show a noticeable similarity. When shaft diameters are small, there is little physical difference whether the beam is focussed on the surface or near the centre of rotation. As the diameter of the shaft is increased the correlation time is expected to reduce and this can be seen in Figure 5.29, which shows the expected correlation times, using equation (4.24), for the speckle pattern when the shaft rotates at 35Hz.

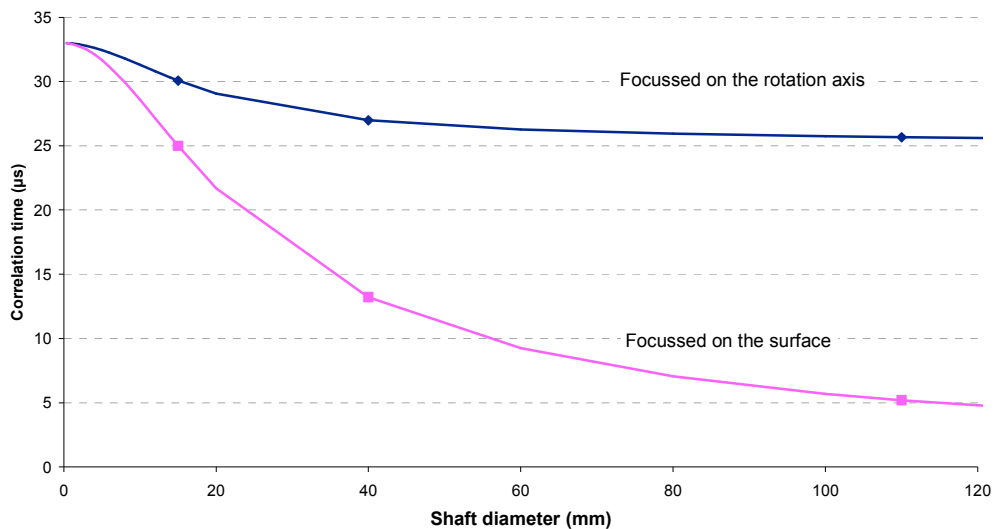


Figure 5.29 – Expected correlation times for a shaft rotating at 35Hz when using a 90µm beam, either focussing on the shaft surface or focussing on the rotation axis. The three shafts used in this study are identified by the data points presented in the plot.

This is reflected in Figure 5.28 and Table 5.13 by the increase in rotation sensitivity when the diameter is increased to 110mm. However when

measurements are required on larger diameter shafts, the sensitivities can be reduced by changing the focal point. Focussing the beam near the rotation axis brings the greatest reduction in the rotation sensitivity. It must be noted however that the cross-correlations of intensity predict that the correlation times continue to increase the further the focal point is beyond the surface, suggesting a reduction in rotation sensitivity. It was found that this is not the case and focussing on the rotational axis has the greatest effect in reducing sensitivities. Speckle noise is driven by the derivative of the phase change with respect to time. Focussing near to the rotation axis reduces the broadening of the Doppler frequency. This shows a greatest reduction in rotation sensitivity. Observation of the speckle motions has revealed a predominant translation when measurements are taken from the two shafts with smaller diameters (15mm and 40mm) and also when the beam is focussed on the rotation axis on the larger diameter shaft (110mm). However when focussing the beam onto the surface of the larger shaft, speckle evolution appears to dominate. These observations are supported by the cross correlations of intensity shown in Section 4.2.3.

<i>Shaft diameter</i>	15mm	40mm	40mm §	110mm	110mm §
15mm	-	1.73	2.94	5.62	2.81
40mm	1.73	-	1.22	7.34	1.09
40mm §	2.94	1.22	-	8.56	0.13
110mm	5.62	7.34	8.56	-	8.43
110mm §	2.81	1.09	0.13	8.43	-

Table 5.14 – Tukey’s test for various shaft diameters. (§ - focussed on the rotation axis)

Tukey’s test, presented in Table 5.14, shows that the rotation sensitivity from the 110mm diameter shaft, when focussed on the surface, is significantly

different from all other rotation sensitivities. This gives evidence that the increased rotation sensitivity caused by a large shaft diameter can be remedied, by simply re-focussing the beam on the rotational axis of the shaft. Therefore in addition to a small beam waist it is recommended that the beam is focussed to the rotational axis when radial measurements are required on rotating targets.

Evident in Tables 5.9 and 5.10, using the shaft with a 15mm diameter and focussing the beam on the surface of the shaft, the smaller beam diameter (90 μm) has a reduced rotation sensitivity, three times less than the larger beam (520 μm). Using this factor and Table 5.13, the rotation sensitivity for a beam diameter of 520 μm on a 110mm diameter shaft might be around 3 μms^{-1} / rads^{-1} . This estimation suggests that a smaller beam diameter (focussed on the rotation axis) may provide a great advantage over using a larger beam diameter (focussed on the surface), potentially reducing the rotation sensitivity by a factor of five.

5.3.4 Parallel beam rotation sensitivity

Pseudo-vibration sensitivities are also important for parallel beam vibrometers and equivalent investigations to those presented in this chapter can be performed. Rotation sensitivity is perhaps the most important of these and is the subject of this section. As described in Section 1.1.2, parallel beam vibrometers measure the angular velocity of a surface. Typically, rotational vibrometers are used to measure torsional vibrations in rotating shafts. This section studies the rotation sensitivity for a parallel beam vibrometer on a rotating shaft. Often the shafts are treated with retro-reflective tape to maximise backscattered light. If the surface is left untreated the localised

surface orientation reflects the beam away from the receiving aperture of the vibrometer and this was observed the experimentation presented here.

A shaft is treated with retro-reflective tape and is rotated at 30Hz. Figure 5.30 shows the configuration to quantify the rotation sensitivity for a parallel beam vibrometer.

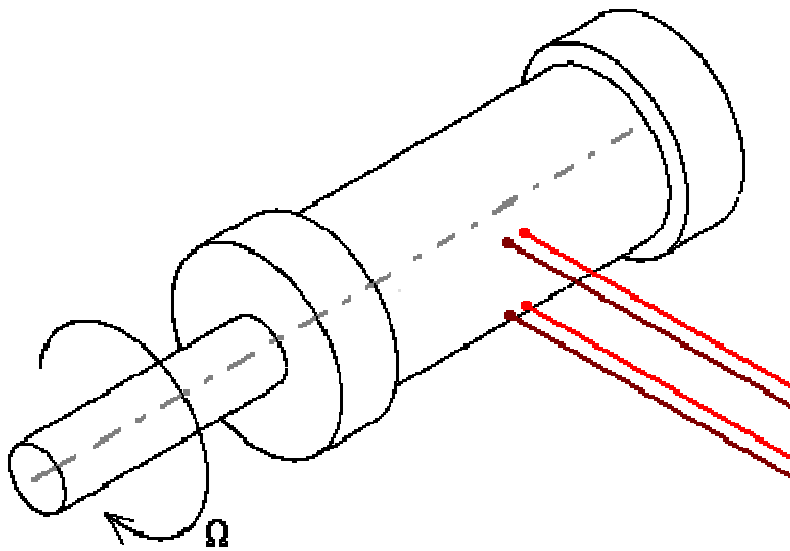


Figure 5.30 - Parallel beam rotation sensitivity arrangement

A rotational vibrometer is located 400mm from the shaft and is orientated to measure the angular vibration of the rotating shaft. The pair of beams are aligned perpendicular to the rotation axis. The beam spots, 520 μ m in diameter, are positioned equidistant from the rotation axis. The pair of beams from a second rotational vibrometer are aligned parallel with the first and the beam spots are positioned as close as practically possible (one to a few millimetres apart) with no overlap. The measured velocities output from each of the two

vibrometers contain components of nominally the same angular velocity but also components of unrelated noise. As using the approach established in Section 5.3.3, the rotation sensitivity is calculated from the difference in measured velocities divided by $\sqrt{2}$.

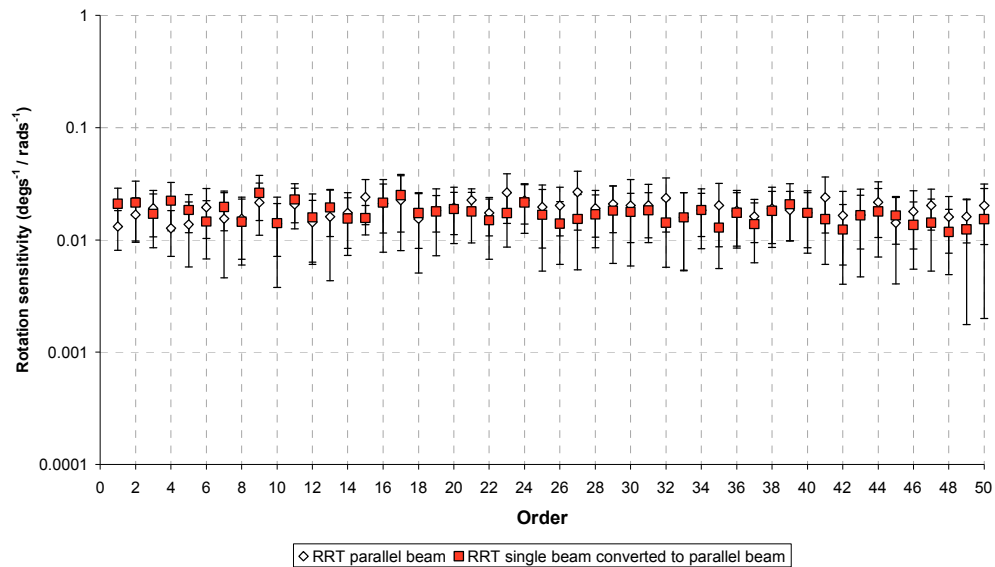


Figure 5.31 - Parallel beam rotation sensitivity for a shaft 15mm in diameter, $D=520\mu\text{m}$.

RRT – Retro-reflective tape

Figure 5.31 shows the calculated rotation sensitivity for the parallel beam arrangement together with the single beam rotation sensitivity, from Section 5.3.3, which has been converted to an equivalent rotation sensitivity for two beams.

It can be seen that the spectral shape of the parallel beam configuration maintains its amplitude across the broad frequency range presented (50 orders). The amplitude and spectral shape of the rotation sensitivity for parallel beam rotation sensitivity is markedly similar to the equivalent rotation sensitivity calculated from the single beam measurements. Table 5.15 presents the rotation

sensitivity for parallel beam vibrometers and also the equivalent rotation sensitivity calculated from a single beam, shown previously in Table 5.9. The rotation sensitivity for single beam laser vibrometers which has the same configuration (i.e. the same beam diameter and standoff-distance) can, conveniently, be used to estimate the rotation sensitivity for parallel beam laser vibrometers. Using equation (1.7) and (1.10) the factor $\sqrt{2} \frac{180}{\pi d} 10^{-6}$ (where d is the beam separation distance) can be found to convert from the rotation sensitivity in $\mu\text{ms}^{-1}/\text{rads}^{-1}$ to an equivalent for parallel beams with the differential rotation sensitivity in $\text{degs}^{-1}/\text{rads}^{-1}$.

<i>Rotation sensitivity: apparent velocity per unit angular velocity degs⁻¹ / rads⁻¹</i>		
<i>configuration</i>	Parallel beam	Single beam (converted)
<i>Mean level by order (orders 1-10)</i>	0.016	0.019
<i>Standard deviation (orders 1-10)</i>	0.008	0.009
<i>Total level across 50 orders</i>	0.134	0.124

Table 5.15 - Rotation sensitivity ($\text{degs}^{-1} / \text{rads}^{-1}$) using beam diameters of $520\mu\text{m}$. Shaft diameter = 15mm , $D=520\mu\text{m}$. Surface is treated with retro-reflective tape.

The apparent velocity per unit angular velocity is expressed as $\text{degs}^{-1} / \text{rads}^{-1}$ as this is appropriate for the output velocity used by rotational vibrometers. In Section 5.3.3 orders 41-50 were used to estimate the mean rotation sensitivity per order for single beam laser vibrometers and this was because the out-of-roundness from smooth surfaces affects lower orders of rotation sensitivity.

However, these experiments were performed using retro-reflective tape and therefore the mean level can appropriately be calculated using the first 10 orders. The parallel beam rotation sensitivity is quantified as $0.016 \text{ degs}^{-1} / \text{rads}^{-1}$ per order over the first 10 orders and a total rms of $0.134 \text{ degs}^{-1} / \text{rads}^{-1}$ over the first 50 orders. This shows that single beam rotation sensitivity can adequately be used to quantify parallel beam rotation sensitivity, despite the beam spot positions being in slightly different locations on the shaft.

This chapter has presented two methods of quantifying pseudo-vibration sensitivity. The first method presented, used in Sections 5.3.1 and 5.3.2, requires correction of the vibrometer measurement with an independent measurement of genuine velocity to produce an apparent velocity dominated by the required noise components. The second method, used in Section 5.3.3 and 5.3.4, requires a differential measurement using two identical vibrometers to cancel common components such as genuine velocity, leaving only uncorrelated noise from each measurement in the resulting apparent velocity. Method one is convenient if one vibrometer is available and a reliable measurement of the genuine velocity can be made. Method two requires two identical vibrometers and is a robust method to quantify pseudo-vibration sensitivity.

6 Observation of dynamic speckle

This chapter presents observations of speckle patterns and speckle motions for a variety of surface finishes, including roughness levels ranging from Ra 11nm ($\approx\lambda/60$) to $1\mu\text{m}$ ($\approx 1.6\lambda$) and a surface treated with retro-reflective tape, with two vibrometers producing beam spot diameters of $90\mu\text{m}$ and $520\mu\text{m}$. Speckle patterns are described as translating or evolving, or some combination of these two behaviours. Using high resolution sequential images, this chapter observes the changes to the intensity distributions of speckle patterns. It uses Cross-correlation, of these sequential images, as a tool to observe the speckle pattern changes qualitatively for transverse, tilt and rotation surface motions ultimately attempting to relate these to laser vibrometer pseudo-vibration sensitivities.

6.1 Speckle patterns

Figures 6.1 (a) to (h) show typical intensity distributions from surfaces treated with retro-reflective tape and a range of surface roughness producing fully and partially developed speckle patterns which are to be examined in this chapter. A surface treated with retro-reflective tape produces an intensity pattern which can be interpreted as the superposition of two intensity distributions caused by two effects. The retro-reflective optics produce an overall Airy disc intensity distribution while the microscale deviations in the depth of the surface produce the speckle pattern.

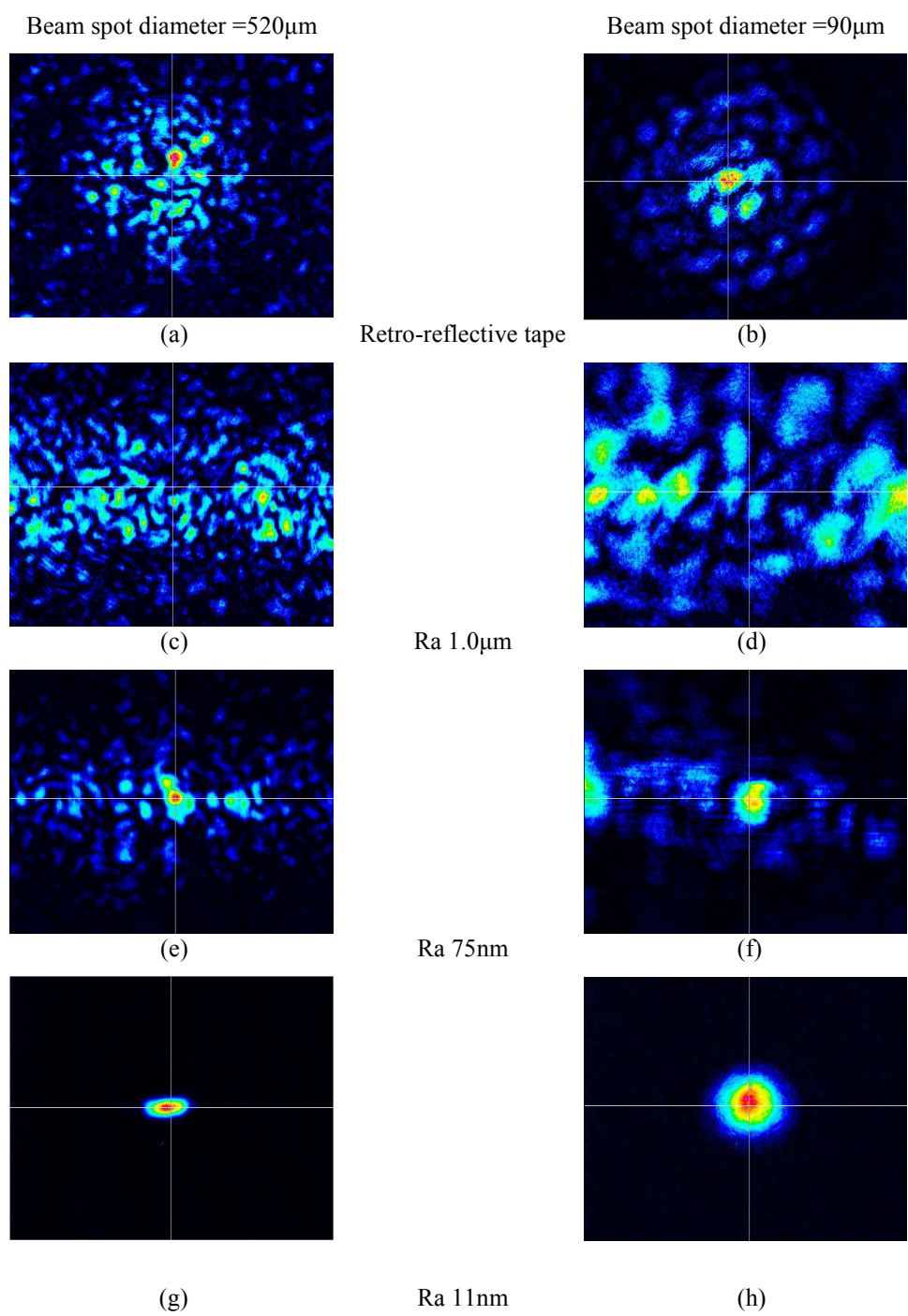


Figure 6.1 - Speckle patterns from a variety of surfaces using beam spot diameters of 520 μ m and 90 μ m

The speckle pattern formed when using the smaller beam diameter of $90\mu\text{m}$ on the retro-reflective tape, Figure 6.1 (b), appears to have a regularity in its speckles. The retro-reflective tape is composed of approximately $50\mu\text{m}$ diameter glass beads embedded into the surface of the tape as shown previously in Figure 2.1. From this it is easy to see how a beam spot diameter of $90\mu\text{m}$ scatters from only a few glass beads which in turn produces a finite number of phase varied Airy disc intensity distributions and hence a degree of regularity to the observed intensity pattern.

A progression from the fully developed speckle pattern produced from the roughest surface (Ra $1.0\mu\text{m}$) through the combination of partially developed speckle pattern and specular reflection (Ra 75nm) to the specular reflection produced from the smooth surface (Ra 11nm) can also be observed in the figures. Further observation of these images shows a distinct effect of orientation to the scatter, from the surfaces without tape. This is as a consequence of the features on the surface produced by the machining direction. The surface finish is dominated by corrugations parallel with the machine finish direction. Consequently, the beam scatters more prominently perpendicular to this direction producing a band of speckles. The band of speckles is seen in a horizontal direction for the range of surface roughness finishes Ra $1.0\mu\text{m}$ to 75nm shown in Figures 6.1 (c) to (f). The Ra 11nm surface produces an intensity distribution comparable with a mirror-like reflection. This roughness is approximately $1/60^{\text{th}}$ of the wavelength of the light, (He-Ne $\lambda = 632.8\text{nm}$).

6.1.1 Speckle size

Using the images of the speckle patterns, the average speckle size in the image can be measured. Statistically, the average speckle size in a fully developed speckle pattern was shown by equation (3.24). The auto-correlation function is therefore required. A two-dimensional auto-correlation can be used, either directly or by applying the two-dimensional Wiener-Khinchin theorem shown in Section 3.4.1. The Wiener-Khinchin method has proven to be a computationally less intensive operation, providing the auto-correlation function through the inverse Fourier transform of the power spectral density. The $\exp[-2]$ width of a two-dimensional Gaussian fit to the auto-correlation function is measured producing the average width of the speckle in the image. The contrast of a speckle pattern, calculated by the ratio of the standard deviation to the average of the intensity, shown by equation (3.18) can be used as an indication of how well developed the speckle pattern is. For a fully developed speckle pattern, the contrast is unity.

Speckle pattern surface	Figure 6.1. reference	Expected speckle size ($\langle \sigma_0 \rangle, \mu\text{m}$)	Measured speckle size ($\sigma_x, \mu\text{m}$)	Measured speckle size ($\sigma_y, \mu\text{m}$)	Contrast
Retro-reflective tape	(a)	235 (D = 520 μm)	418	498	1.36
Ra 1.0 μm	(c)		301	350	0.94
Ra 75nm	(e)		559	696	1.59
Ra 11nm	(g)		NA	NA	3.97
Retro-reflective tape	(b)	898 (D = 90 μm)	859	1055	1.36
Ra 1.0 μm	(d)		870	1010	0.84
Ra 75nm	(f)		843	1083	1.34
Ra 11nm	(h)		NA	NA	2.87

Table 6.1- Expected speckle sizes, measured speckle sizes and contrasts of speckle patterns

Table 6.1 shows predicted speckle sizes, measured speckle sizes (σ_x, σ_y) and the contrast for the speckle patterns shown in Figure 6.1. The best match to the predictions, from the statistics, is expected from the Ra 1.0 μm surface because this surface should generate a fully developed speckle pattern. As expected,

speckles are larger for the smaller beam spot diameter. The measured speckle sizes are larger than that predicted by classical statistics for fully developed speckle patterns. The mirror-like reflection produced by the Ra 11nm surface produces a contrast far removed from that of a fully developed speckle pattern. As expected, the combination of specular reflection and a speckle pattern observed in Figures 6.1 (e) & (f) and produced by the Ra 75nm surface produces contrast results suggesting a partially developed speckle pattern. Interestingly, the contrasts calculated for the speckle patterns produced when using retro-reflective tape, for both beam spot diameters, are comparable with the contrasts produced by a smooth surface with Ra 75nm. Classical speckle statistics do not include superposition of the overall Airy disc intensity distributions produced by retro-reflective tape, and therefore it is not surprising to see non-conformance.

Measurement and observation of the speckle size can be related to measured pseudo-vibration sensitivities. Measurements of tilt sensitivity, presented in Section 5.3.2, have shown that using a smaller beam diameter can reduce levels of noise. Increasing the speckle size reduces the rate of change of phase caused by the speckle motion, reducing speckle noise measured by the vibrometer.

6.2 Qualitative observation of speckle behaviour

As described previously in Chapter 4, speckles can translate or evolve (sometimes called ‘boiling’) and can exhibit both behaviours. In this section, the behaviour of speckles produced from transverse and tilt target surface motions is to be examined. Incremental transverse and tilt target surface displacements are produced using displacement stages with resolutions of 10 μ m and 0.1 $^\circ$ respectively, and sequential images (1200x1024 pixels, resolution of 6.45 μ m square) are generated.

6.2.1 Speckle translation during surface tilt

Illumination of a surface which is tilting produces a speckle motion in the intensity patterns which is dominated by translation. For this study, the test surfaces were set in a plane containing the axis of rotation and the beam was aligned to illuminate the surface on the rotational axis. For a tilting surface, the speckles are predicted to translate on the observation plane by amount $2\theta z_S$ where θ is the angular displacement (rads) as explained in section 4.1.2.

A region of the pattern on the CCD is used later in the quantitative analysis, described in Section 5.2. The angular increment of the surface (0.1°) would produce speckle translation distance on the CCD of 0.75mm and 0.5mm for the beam spot diameters of 520 μm and 90 μm respectively.

Figure 6.2 shows example speckle patterns and corresponding sectional profiles as the surface is angularly displaced over 0.4° in 0.1° increments, causing the speckle pattern to translate from the right to the left in the images. An example of the translation can be seen in the sectional profiles produced from the Ra 1.0 μm surface, Figure 6.2 (a)(ii)-(vi). The same bright speckle in each sequential profile is tracked, emphasising the direction of the speckle translational motion. The speckles do not significantly alter in amplitude or shape and the speckles are considered to be dominated by the translational motion. At this point it is worth noting that as the surface tilts, relative to the beam, the beam spot elongates and becomes elliptical. This illuminates new surface features and will modify the speckle pattern, but the effects of this appear insignificant for the angular scales observed.

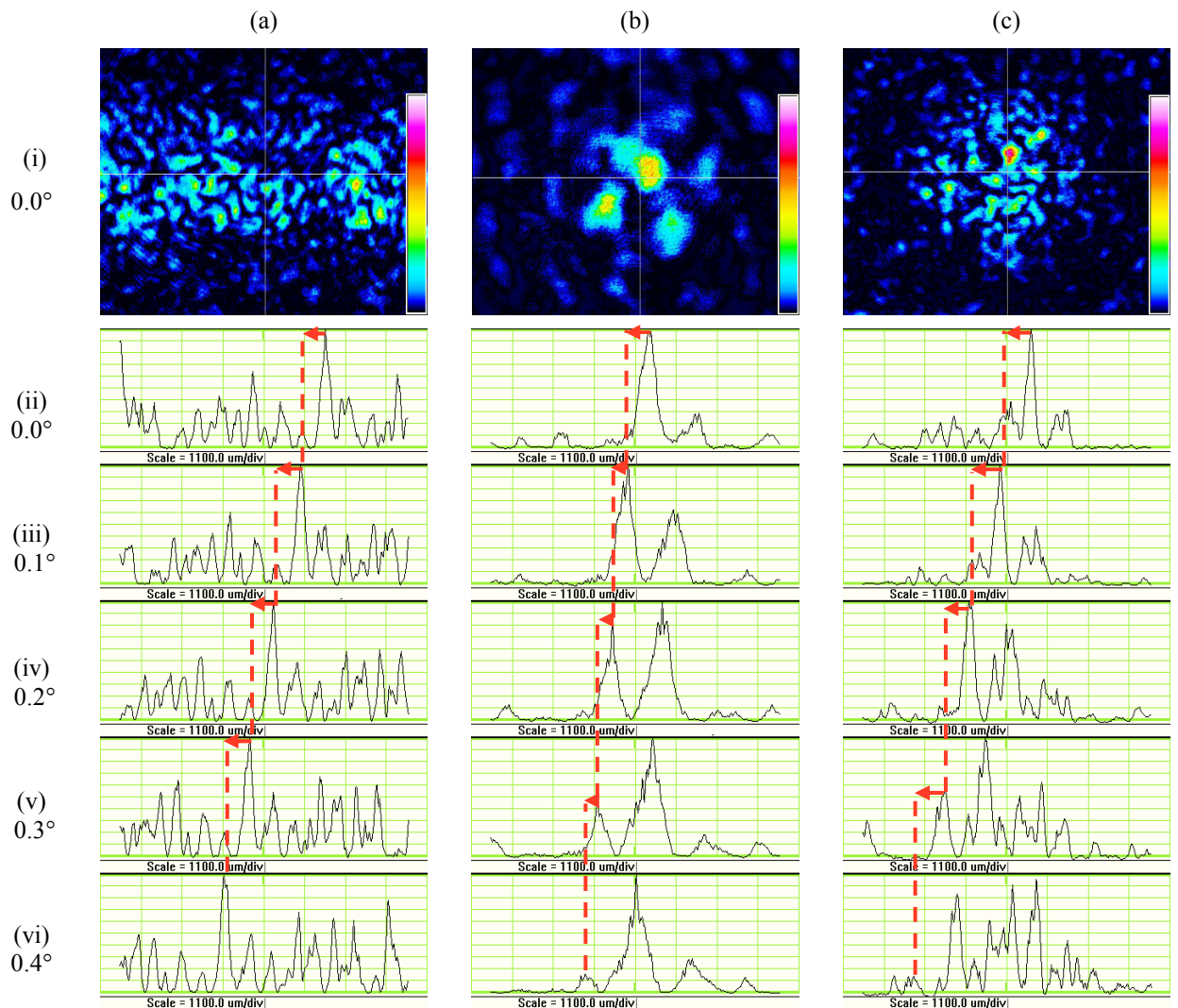


Figure 6.2 – Speckle pattern sectional profiles as the surface tilts at incremental displacements of 0.1°
Ra $1.0\mu\text{m}$ ($D=520\mu\text{m}$) Retro-reflective tape ($D=90\mu\text{m}$) Retro-reflective tape ($D=520\mu\text{m}$)

Speckle translation also exists in the speckle motions when using retro-reflective tape. However, the Airy disc intensity distribution causes the intensity of the speckles to alter as they translate. This is clearer in the sectional profiles of the transitions when using the smaller beam diameter of $90\mu\text{m}$, where the speckles are relatively large, Figures 6.2 (b). A speckle identifiable in Figure 6.2 (b)(ii) as having the greatest intensity can be seen to translate, in

Figures 6.2 (b)(ii)-(vi), as the angular displacement of the surface increases. However, its intensity diminishes as it translates and approaches the first minima of the Airy profile. Concurrently, a second speckle in the speckle pattern, with a significantly lower intensity in Figure 6.2 (b)(ii) also translates across the Airy profile but its intensity increases. This transition can also be seen in the sectional profiles in Figures 6.2 (c) from speckle patterns produced from the increased beam spot diameter of $520\mu\text{m}$ and retro-reflective tape

6.2.2 Speckle evolution during surface translation

Speckle evolution occurs when there is a significant change to the population of illuminated surface features. This can be the dominant speckle behaviour when the surface translates in a direction transverse to the beam. For this study, the beam is aligned to be nominally parallel with the surface normal. Figures 6.3 (a)-(f) show speckle patterns and their corresponding sectional profiles when a surface with $R_a 1.0\mu\text{m}$ is translated, with increments of $1/5$ of the beam diameter, over a total range of one beam spot diameter ($90\mu\text{m}$).

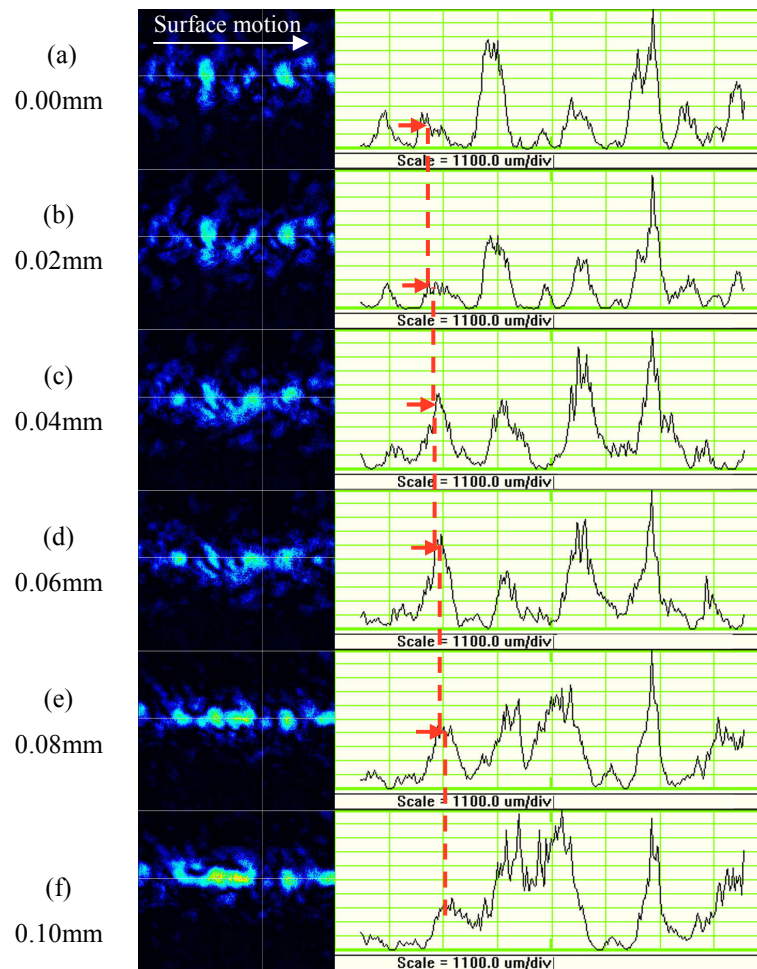


Figure 6.3 – Speckle patterns and sectional profiles from a Ra 1.0µm surface using $D=90\mu\text{m}$ showing speckle evolution

Figures 6.3 (a)-(f) show fluctuations in the intensity of the speckles, as well as a slight translation as the surface moves. This change in intensity and shape is the result of the change to the population of illuminated surface scatterers.

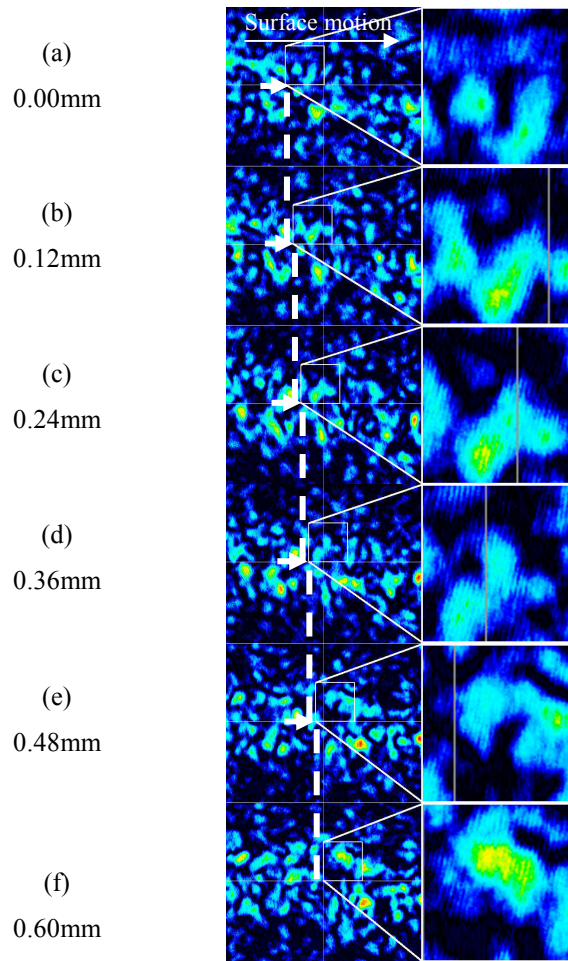


Figure 6.4 – Speckle patterns and a region of a speckle pattern from a Ra $1.0\mu\text{m}$ surface using $D=520\mu\text{m}$ showing speckle evolution

Figures 6.4 (a)-(f) present evolution of a region of the speckle pattern from a surface with Ra $1.0\mu\text{m}$ as the surface is displaced in increments of $1/5$ of the beam spot diameter ($D=520\mu\text{m}$). A region of the speckle pattern is tracked at the same increment as the surface displacement and enlarged. This largely eliminates the effect of translation in the images and concentrates attention solely on the evolution of the speckle pattern. The speckles can be seen to alter in shape and intensity as the surface moves. From the images, the speckles

appear to have decorrelated after the surface has translated by 0.36mm. For specific configurations, it is predicted that a surface can translate up to a maximum of $\frac{1}{\sqrt{2}}D$, by which point the speckles will always be uncorrelated.

The decorrelation of the speckle pattern is dependent on the surface motion as a proportion of the beam diameter. For a larger beam diameter, the surface is likely to translate further before the correlation is lost and this has been shown to reduce the influence of speckle noise. Quantitative analysis of this speckle behaviour would provide a useful description of this motion and this is the subject of the next section.

6.3 Quantitative analysis of speckle behaviour

Quantification of speckle behaviours would facilitate a valuable analysis of the mechanisms behind speckle noise. It is proposed to use cross-correlations of the images, in the nominal direction of the speckle translational motion, to quantify the amount of translation and evolution of the speckles. This is a novel approach which attempts to determine a relationship between speckle pattern intensity changes and speckle noise in laser vibrometry. The changes in intensity, ultimately, are to be related to speckle noise levels but speckle noise is generated principally by phase change, which is not so easily observed. This analysis therefore relies on the relationship between the measured intensity and its phase, in that the mechanism that causes a change to the intensity will also drive a change in phase. The analysis will examine how far observations based on intensity can be related to a noise generation driven by phase change.

6.3.1 Cross-correlation analysis

Sequential images of speckle patterns produced from incrementally displacing the surfaces are used to quantify the translation and the evolution of the speckles. An example of the process used is shown in Figures 6.4 to 6.6 using a sequence of speckle patterns produced from a tilting surface which is treated with retro-reflective tape and illuminated with a beam spot diameter of $520\mu\text{m}$.

A region of the speckle pattern, comparable (in the direction of the speckle motion) to that collected on the vibrometer aperture and located centrally in the initial image, see Figure 6.4(a), is selected as the interrogation region. This region is correlated with the entire image as shown in Figures 6.4(b) and (c) and a normalised auto-correlation, shown in Figure 6.4(d), is produced. In the next stage, this interrogation region from the initial image, is cross-correlated with sequential speckle pattern images produced from the incremental angular displacements, as shown in Figures 6.5. These cross-correlations are normalised against the peak of the auto-correlation and presented in Figure 6.6 as a function of delay expressed in terms of aperture width.

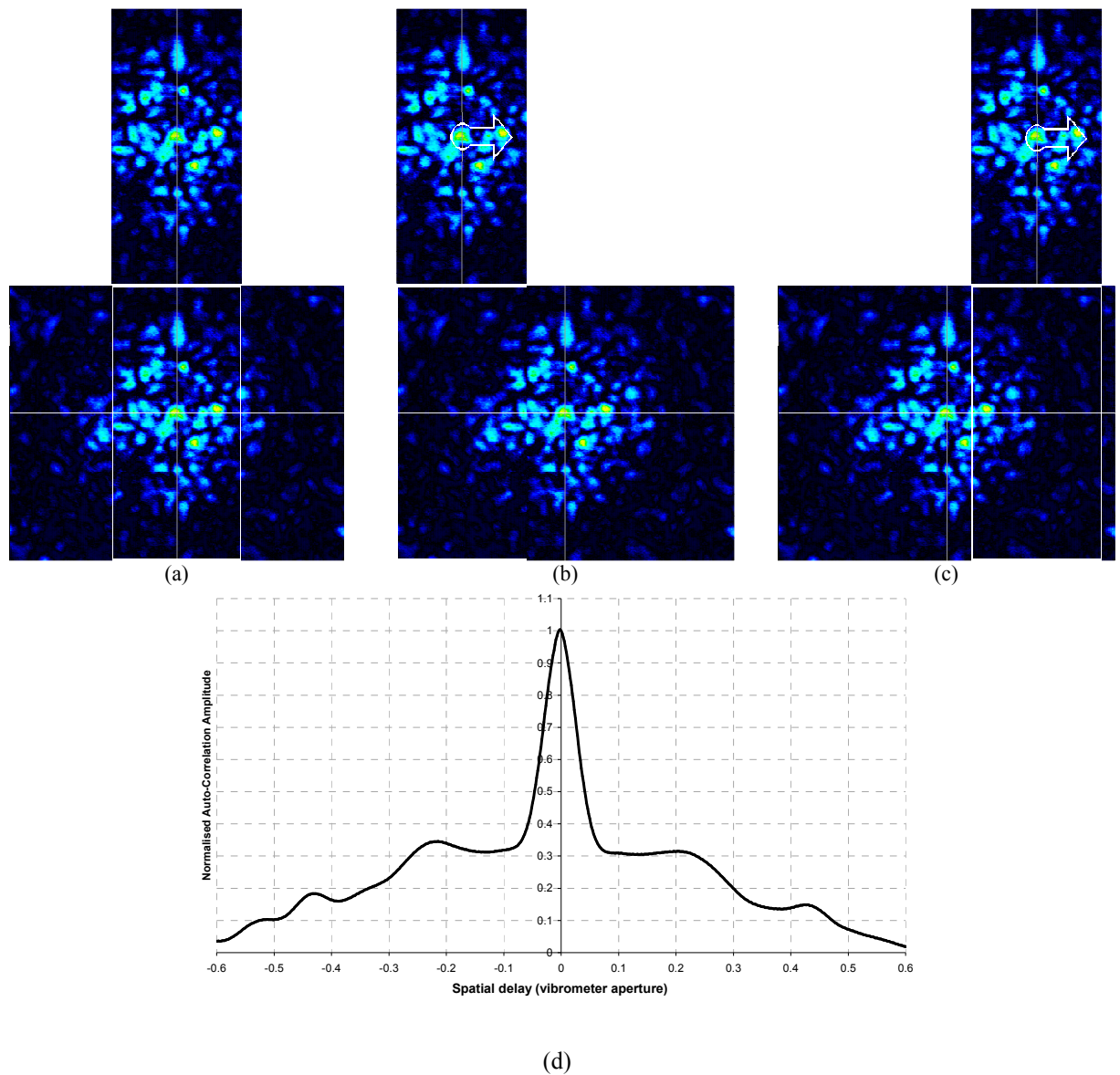


Figure 6.5 - Normalised auto-correlation of surface treated with retro-reflective tape (0.0°)

The average peak spatial delays and corresponding cross-correlation amplitudes can be used to quantify speckle translations and the degree of evolution respectively. A pure speckle translation produces a spatial delay of the peak of the normalised cross-correlations without change in the amplitude. Pure evolution produces no spatial delay to the peak of the normalised cross-correlations and only a change to the amplitude. A combination of the two

speckle motions will produce not only a spatial delay but also a change to the amplitude of the peak of the normalised cross-correlation. However the change in normalised correlation amplitude is also affected by Airy disc intensity distribution when using retro-reflective tape on a surface which is tilting.

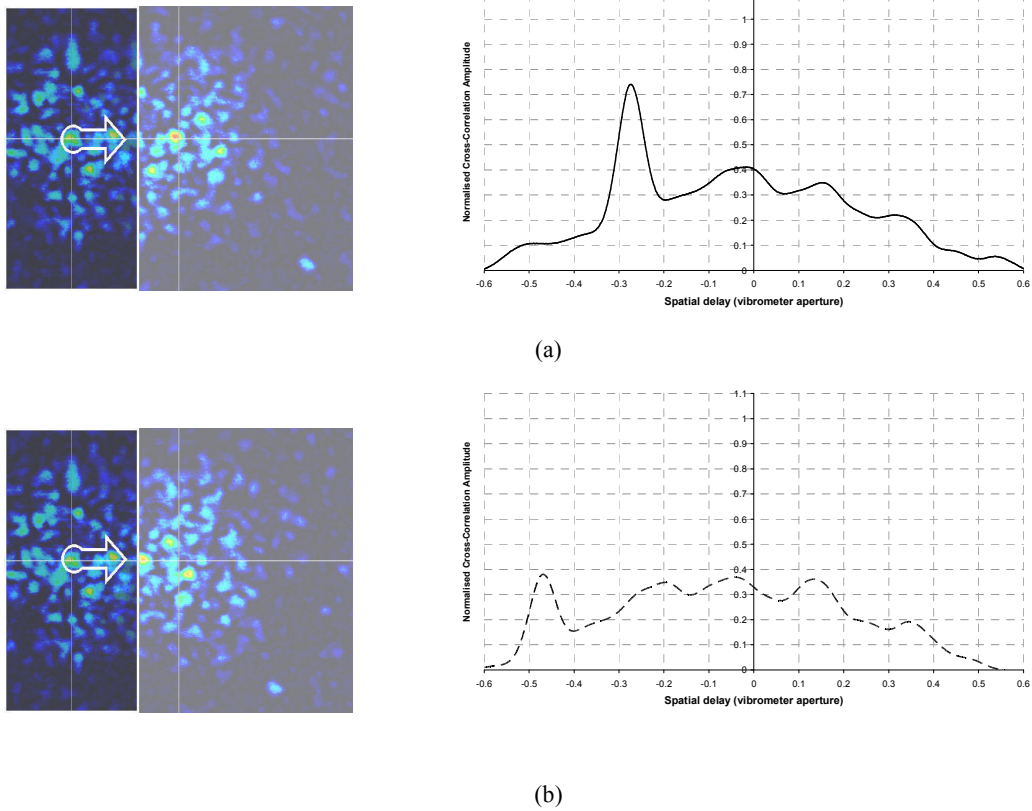


Figure 6.6 - Normalised cross-correlations for (a) 0.1° and (b) 0.2°

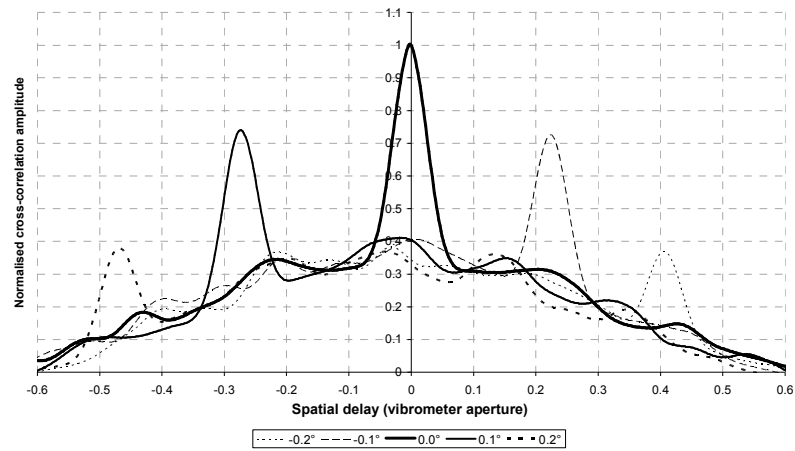


Figure 6.7 - Normalised cross-correlation for tilting surface treated with Retro-Reflective Tape using a beam spot diameter of $520\mu\text{m}$

The normalised cross-correlations of intensity are observed for the typical speckle patterns encountered in Chapter 5 from which pseudo-vibration sensitivity is quantified. The following sections describe the quantification of speckle motions for the three surface motions: transverse to the optical axis, a tilt and a rotation.

6.3.2 Transverse surface motion

The surfaces used in Section 5.3.1 of Chapter 5 are translated with an incremental displacement of $1/10^{\text{th}}$ of the beam diameter. The laser beam spot diameters are $520\mu\text{m}$ and $90\mu\text{m}$, the same as those used in the experimental study of pseudo-vibration sensitivities, presented in Chapter 5. The beam is aligned perpendicular to the translation direction. Sequential images of the resulting scatter are captured at each displacement increment and the average normalised cross-correlation is calculated. Figure 6.8 shows the average normalised cross-correlation when using a beam diameter of $520\mu\text{m}$, including one standard deviation of the spatial delay and the normalised cross-correlation

amplitude. Figure 6.8 shows reasonable agreement with the theory, previously shown in Section 4.1.1, although spatial delays appear slightly smaller than expected. This is more likely a combination of the tolerances in the translation stage and the difficulty in the peak location of the cross-correlation.

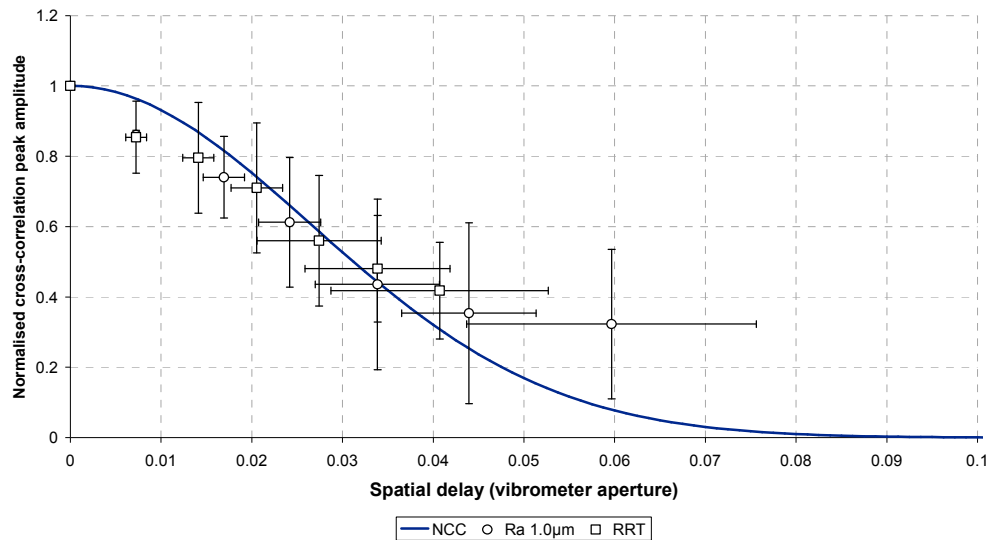


Figure 6.8 – Normalised cross-correlation peaks of speckle motions from a surface moving transverse to the optical axis, using a beam diameter of $520\mu\text{m}$.

As the surface roughness reduces, cross-correlation becomes less able to characterise the motion of partially developed speckle patterns as the specular reflection is too dominant. Figure 6.9 shows an example of the normalised cross-correlation from a Ra 75nm surface where, although speckles are present, the intensity of the specular reflection is the prominent feature of the scatter. The specular reflection dominates the cross-correlation and the speckle motions are indistinguishable.

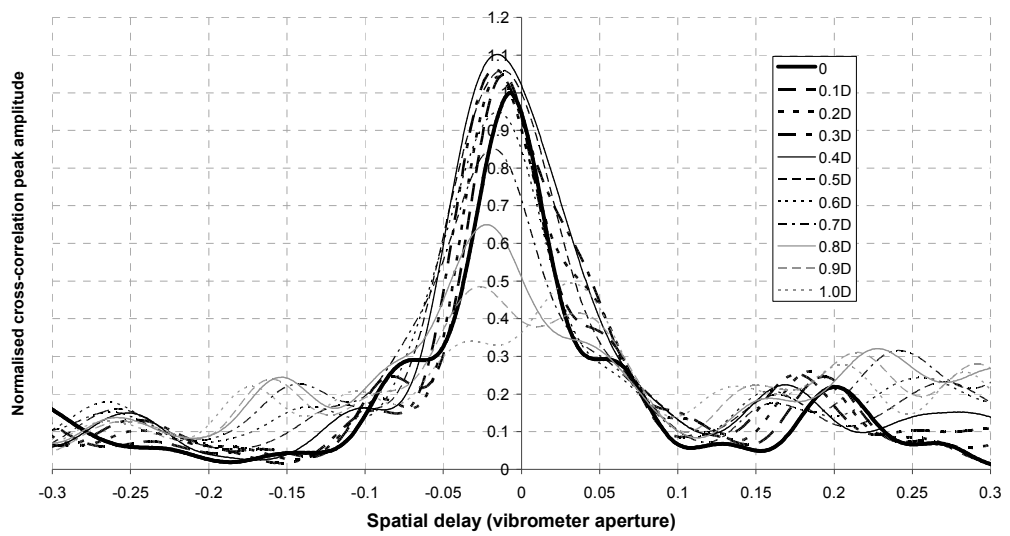


Figure 6.9 – Example normalised cross-correlation from a surface with Ra 75nm moving transverse to the optical axis ($D=520\mu\text{m}$)

Figure 6.10 shows the normalised cross-correlation amplitude and corresponding spatial delays when using a beam diameter of $90\mu\text{m}$ for Ra $1.0\mu\text{m}$ and a surface treated with retro-reflective tape. The spatial results show significant difference from that expected by theory, shown by the solid line on the right half of the plot. This data illustrates an interesting and initially counter-intuitive behaviour of the speckles.

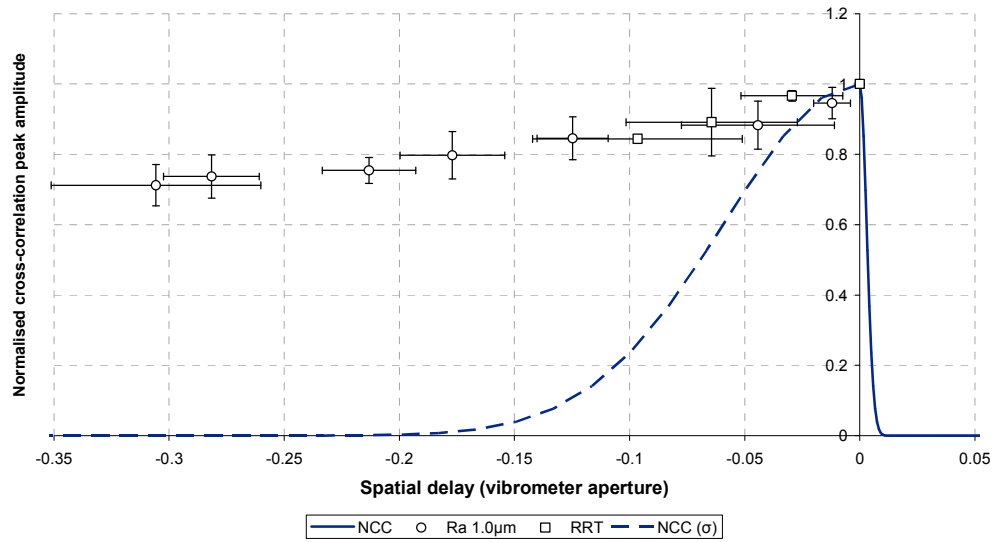


Figure 6.10 – Normalised cross-correlation amplitude from a surface moving transverse to the optical axis using a beam spot diameter of $90\mu\text{m}$.

The measured spatial delays are negative and slightly greater than expected. This means that, in this test, the speckles are actually moving in the opposite direction to the surface motion. Figure 6.10 also shows a dashed line (in the left half of the plot, $\text{NCC}(\sigma)$) which is a recalculated normalised cross-correlation, using a refined estimate of the gearing term, shown by equation (4.2), from the best fit presented in Figure 6.11. Figure 6.11 is a plot of the actual speckle translation against the expected speckle translation. From this an estimation of the gearing term is calculated using the best linear fit crossing through zero. A negative gearing term suggests the beam has been focussed beyond the surface developing a negative radius of curvature. Using the estimated gearing term and equation (4.2) an estimate of r is found to be approximately -31mm . Using equation (1.12) and this estimation of the radius of curvature the location beyond the surface which the beam appears to be focussed to is approximately 3.7mm . This estimation shows that the beam was likely focussed a few millimetres beyond the surface. It is worth noting that this will not happen for the larger beam spot diameter ($520\mu\text{m}$). This is because the minimum radius of

curvature does not become comparable with the standoff distances, in this test, and the gearing term will never be negative. Larger beam spot diameters are unlikely to develop negative gearing terms in most applications of the laser vibrometer.

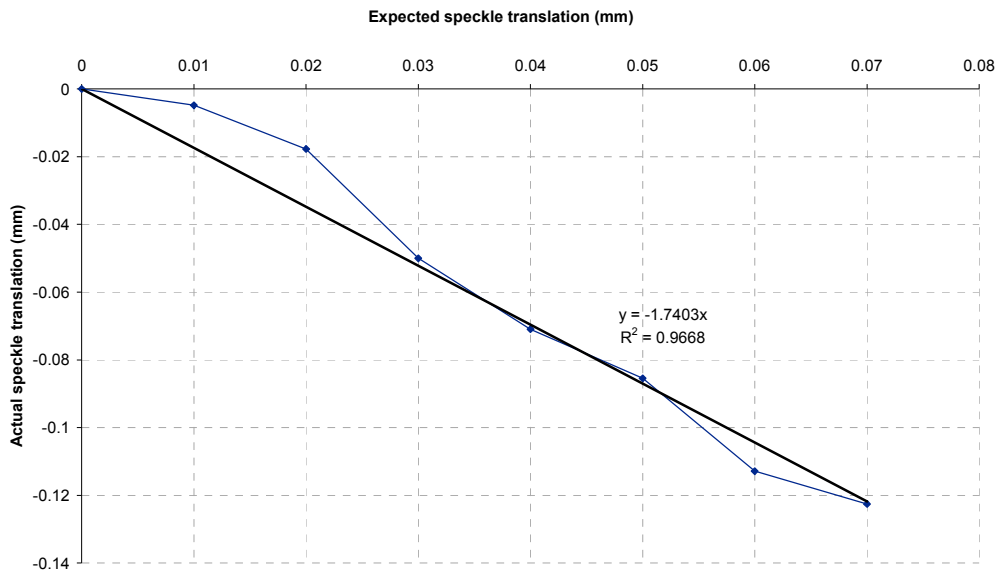


Figure 6.11 – Estimated gearing term using the measured spatial delays and the expected spatial delays using data from Ra 1.0 μ m surface located at the camera

With the refined gearing term the fit to theory is improved but, in Figure 6.10, it can still be seen that the measured cross-correlation amplitudes remain higher than expected. Figure 6.12 shows the full normalised cross-correlations of the speckles from a Ra 1.0 μ m surface. It can be seen that the cross-correlations based on measured data do not fall to zero as theory suggests and as observed in Figure 6.9 for the larger beam. They remain at a high level, irrespective of the spatial delay, and this prevents the peak amplitudes reducing to levels suggested theoretically in Figure 6.10.

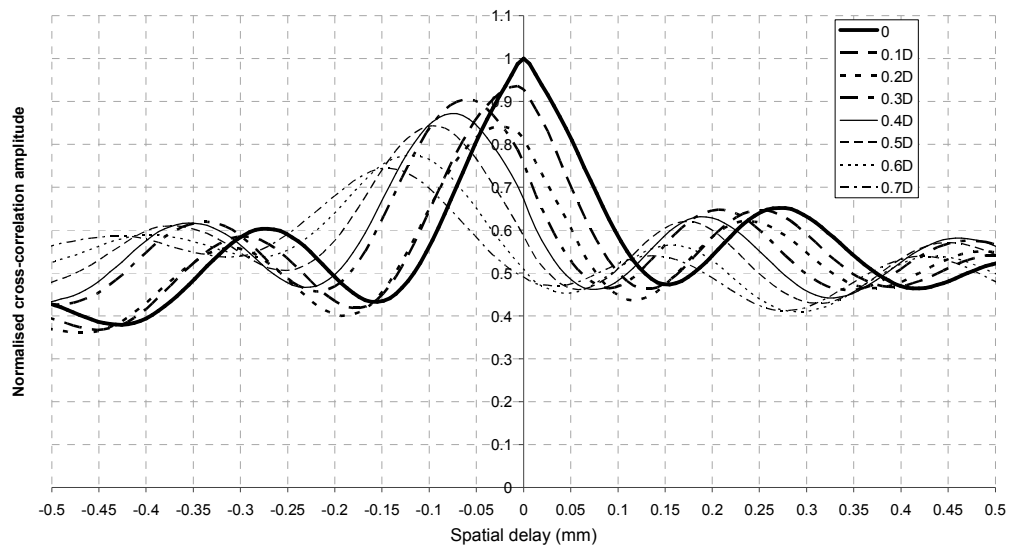


Figure 6.12 - Example normalised cross-correlation from a surface with $R_a 1.0\mu\text{m}$ moving transverse to the optical axis. $D=90\mu\text{m}$

The normalised cross-correlation of the speckle motions from retro reflective tape has a limited capacity. The Airy disc intensity profile created in the scatter from retro-reflective tape dominates the spatial delay of the cross-correlation of the speckles.

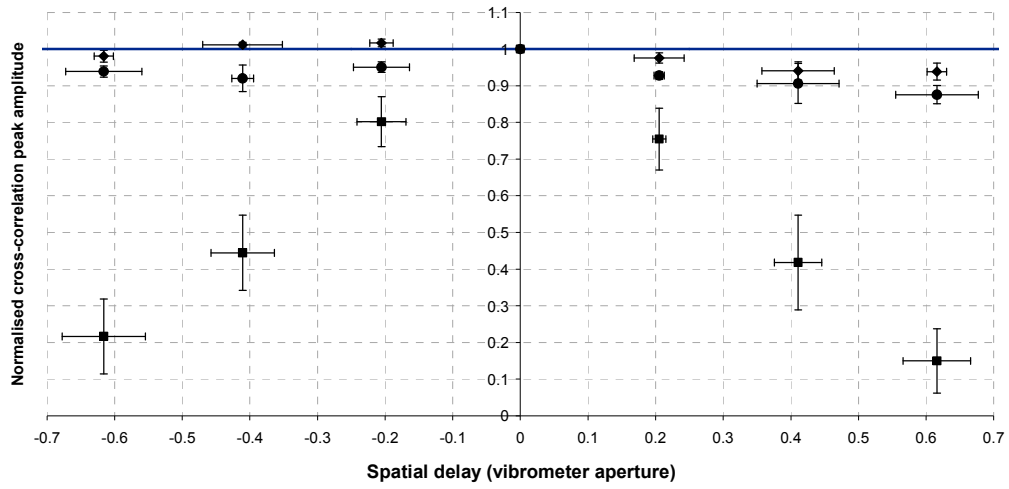
It can be seen by Figure 6.8 that for transverse surface motion evolution dominates the cross-correlation amplitude in the region of the vibrometer aperture because the cross-correlation amplitude falls to a low level for a spatial delay which is much smaller than the vibrometer aperture. This is also the expected case for that seen in Figure 6.10. Figure 6.10 indicates how manipulation of the focal point relative to the surface position (ultimately the radius of curvature on the surface), can affect not just the magnitude of speckle translation but also its direction. The effect of modifying the radius of curvature is investigated further in Chapter 7 through simulation. Section 5.3.1 suggests that there is no significant difference in transverse sensitivity for the surfaces examined in this section, with $R_a 1.0\mu\text{m}$ and a surface treated with

retro-reflective tape. For both beam diameters, the cross-correlations, shown in Figures 6.8 and 6.10, support this notion for the transverse sensitivity.

6.3.3 Tilt surface motion

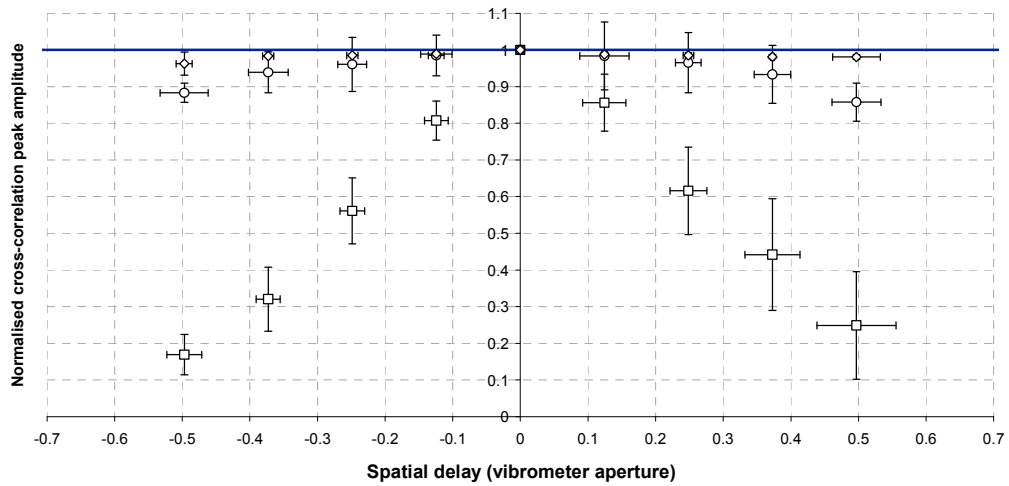
Figure 6.13 shows average peaks of the normalised cross-correlations for the roughest surface, Ra 1.0 μ m, the smoothest surface, Ra11nm, and a surface treated with retro-reflective tape. Figure 6.13 (a) and (b) present data from 520 μ m and 90 μ m beam spot diameters respectively. The data points represent the normalised cross-correlation peaks when the surface tilts at 0.1 $^\circ$ increments. The spatial delay and normalised cross-correlation amplitude error bars represent one standard deviation of each respectively.

The data presented in Figure 6.13 shows that, for the individual beam diameters, all surfaces show similar spatial delays and, other than retro-reflective tape, similar cross-correlation amplitudes. This observation is reflected in Section 5.3.2 which showed that surface finish and treatment made little difference to the tilt sensitivity. Increasing the beam diameter has been shown to increase the tilt sensitivity and this is reflected in the speckle motions, observed in Figure 6.13. The cross-correlations from the Ra 1.0 μ m surface fit well to theory. Translation is the dominant motion, so much so that the data looks the same as the Ra 11nm surface, which is dominated by specular reflection. The Ra 75nm surface is not included in Figures 6.13 (a) and (b) for clarity as this also produces the same cross-correlations.



■ RRT ($D=520\mu\text{m}$) ● Ra $1.0\mu\text{m}$ ($D=520\mu\text{m}$) ◆ Ra 11nm ($D=520\mu\text{m}$) — NCC

(a)



□ RRT ($D=90\mu\text{m}$) ○ Ra $1.0\mu\text{m}$ ($D=90\mu\text{m}$) ◇ Ra 11nm ($D=90\mu\text{m}$) — NCC

(b)

Figure 6.13 – Normalised cross-correlation of the speckle motions from a tilting target using (a) $D=520\mu\text{m}$ and (b) $D=90\mu\text{m}$.

The cross-correlations from retro-reflective tape show a difference in cross-correlation amplitude as the speckles translate across the vibrometer aperture. Figure 6.13 shows clear evidence of the effect, on the normalised cross-correlation amplitude, of the Airy disc profile. The intensity drops to around

20-30% of the peak intensity as the speckles translate to the boundaries of the vibrometer aperture but the phase of the speckle should not be affected by the transition. The photodetector output is the result of a phasor summation over all the collected speckles, with changes in resultant phase appearing as speckle noise. When the speckle pattern behaviour generating speckle noise is dominated by translation, the changing phase of the photodetector output is governed by new speckles entering the collected region while existing speckles leave. This appears to be the dominant feature for the surfaces without retro-reflective tape but, when tape is used, the summation is affected by the relatively low amplitudes of the new speckles entering and the existing speckles leaving the region sampled. Additionally, the speckles that continue to contribute to the phasor summation change in amplitude as they translate across the Airy disc profile. The normalised cross-correlation amplitudes imply that, although the fundamental mechanism generating speckle noise the same for every surface, additional factors appear for a surface treated with retro-reflective tape.

The spatial delays, per increment of surface displacement, are greater for the larger beam diameter (520 μm). This causes a quicker decorrelation because the speckle pattern is changing more rapidly on the photodetector which in turn suggests the tilt sensitivity will increase. However, the differences in spatial delay do not appear to reflect the difference, proportionally, in the tilt sensitivity. This suggests that the cross-correlation of intensity provides a good indication of fundamental speckle behaviour, suitable for implementation in simulation, but the differences in pseudo-vibration sensitivity between, for example, beam diameter cannot be picked out from intensity correlations.

6.3.4 Rotating surface

The shafts used in Chapter 5 are rotated with an incremental displacement of 0.1° . The vibrometers are located 400mm and 600mm from the rotor surface with beam spot diameters of $520\mu\text{m}$ and $90\mu\text{m}$ respectively. The beam is aligned so its trajectory intersects the axis of rotation normally. Sequential images of the resulting scatter are captured at each displacement increment and the average cross-correlation is calculated.

Figure 6.14 shows the average normalised cross-correlation when using a beam diameter of $520\mu\text{m}$, including the standard deviation of the spatial delay and the normalised cross-correlation amplitude. The trace labelled as ‘NCC’ in Figure 6.14 represents the expected normalised cross-correlation for fully developed speckle patterns, calculated using equation 3.32.

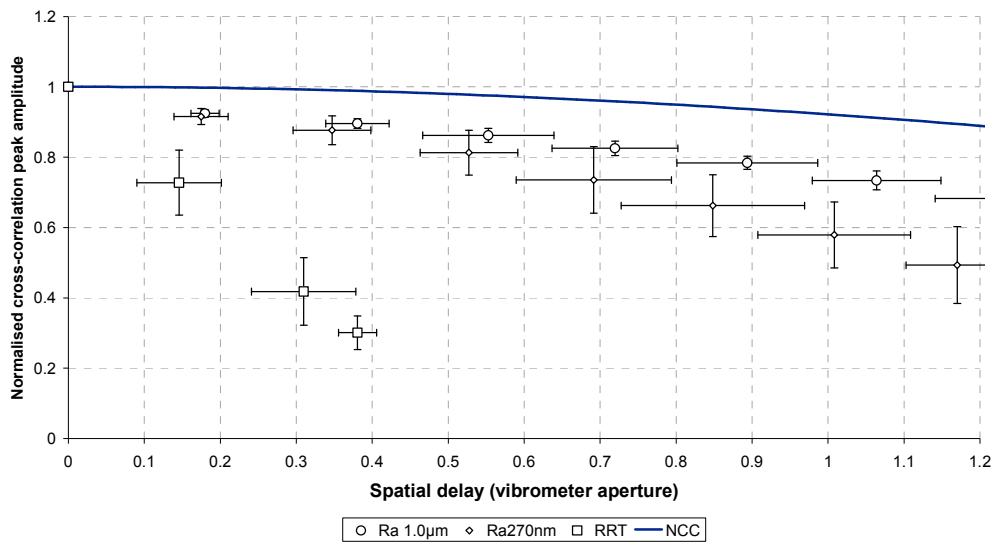


Figure 6.14 – Normalised cross-correlation of speckle motions from a rotating cylindrical surface using a beam spot diameter of $520\mu\text{m}$.

The normalised cross-correlations of the Ra 1.0 μ m surface show an increased spatial delay and a increase in amplitude across the vibrometer aperture, in comparison to the Ra 270nm surface. The reduced spatial delay and cross-correlation amplitude are attributed to the nominal scatter producing an intensity profile generated by the Ra 270nm surface. The surface produces a band of speckles which reduce in intensity towards the edge. The reduction in intensity causes the cross-correlation amplitude to decrease and also a slight reduction in the spatial delay. This is evident in the image shown in Table 5.9. Table 5.11 showed that, for a 520 μ m beam spot diameter, retro-reflective tape produced statistically different rotation sensitivity to the Ra 1.0 μ m and Ra 270nm surfaces, with the latter two surfaces having sensitivities that are statistically similar. Therefore this suggests there is little significance in the difference in the cross-correlation amplitudes for the Ra 1.0 μ m and Ra 270nm surfaces observed in Figure 6.14. Table 5.9 showed that the rotation sensitivity for retro-reflective tape was greater than that produced from both the Ra 1.0 μ m and the Ra 270nm surface. This is supported by the cross-correlations observed in Figure 6.14 as retro-reflective tape has a reduced speckle correlation distance. With the exception of retro-reflective tape, Figure 6.14 shows the dominance of speckle translation across the vibrometer aperture. The speckle motions when using retro-reflective tape show a reduced spatial delay and, from the reduction in amplitude, an apparent increased rate of evolution. However, as discussed in Section 6.3.2, special consideration needs to be given when observing speckle motions from retro-reflective tape. This apparent increased rate of speckle evolution is more likely a result of the Airy disc intensity distribution. When considering speckles which translate outwardly from the centre of the Airy disc, they translate into less intense regions which reduces the cross-correlation amplitude. This means the speckles in the outer region of the aperture have less influence in the intensity cross-correlations

than the speckles in the centre of the aperture, but this may not hold for the mechanism producing speckle noise.

The cross-correlations for retro-reflective tape are affected by the Airy disc intensity profile, which not only reduces the intensity, giving the impression of an increased rate of evolution but it also limits the number of data points that can be plotted. An example of the normalised cross-correlation from a surface treated with retro-reflective tape is shown in Figure 6.15. A great deal of interpretation is required to distinguish the genuine speckle motion correlation peaks from the fluctuations in correlation amplitude. The Airy disc not only appears to influence the correlation amplitude it also appears to skew the apparent translation distance of the speckles resulting in a reduced spatial delay.

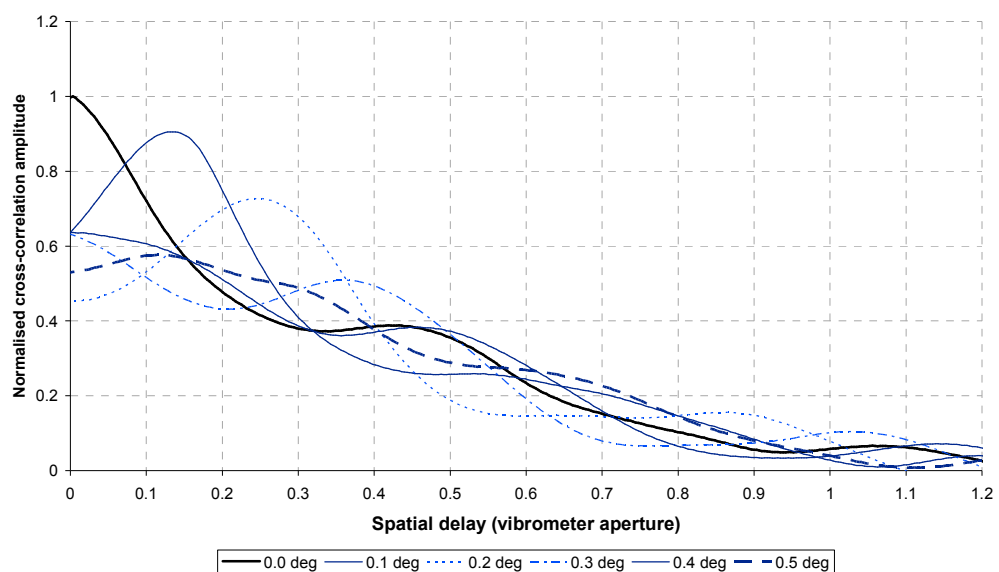


Figure 6.15– Example normalised cross-correlation from a surface treated with retro-reflective tape

When the normalised cross-correlation is calculated using the scatter which has a predominant specular reflection the speckle motions are unidentifiable. Figure 6.16 shows an example of the normalised cross-correlation from a surface with a roughness Ra11nm. The specular reflection caused by the smooth surfaces dominates the cross-correlation. The spatial delay of the specular reflection is very small and does not represent the motion of the speckles, even in partially developed speckle patterns where both specular reflection and speckles are present. Therefore the speckle motions from the smoother surfaces, with roughness Ra65nm and Ra11nm are not included in the quantification of the speckle motions shown in Figures 6.14 or 6.17.

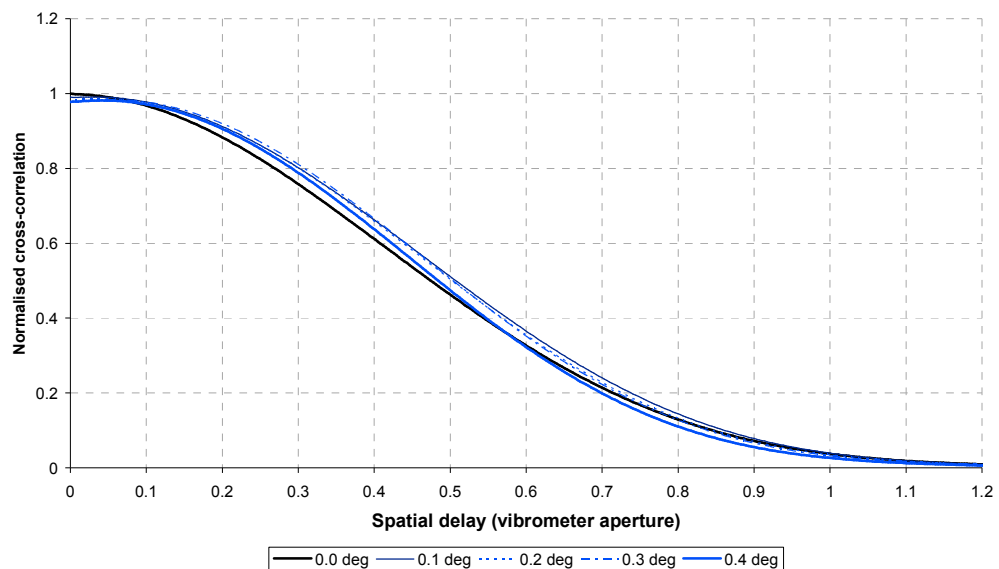


Figure 6.16 – Example normalised cross-correlation from a surface with Ra11nm

Figure 6.17 shows the normalised cross-correlation of intensity of the speckles from a rotating surface when using a beam spot diameter of 90 μ m. The spatial delays show a speckle translation that crosses the entire aperture width and the reduction of the normalised cross-correlation amplitude shows that there is also evolution during the transition.

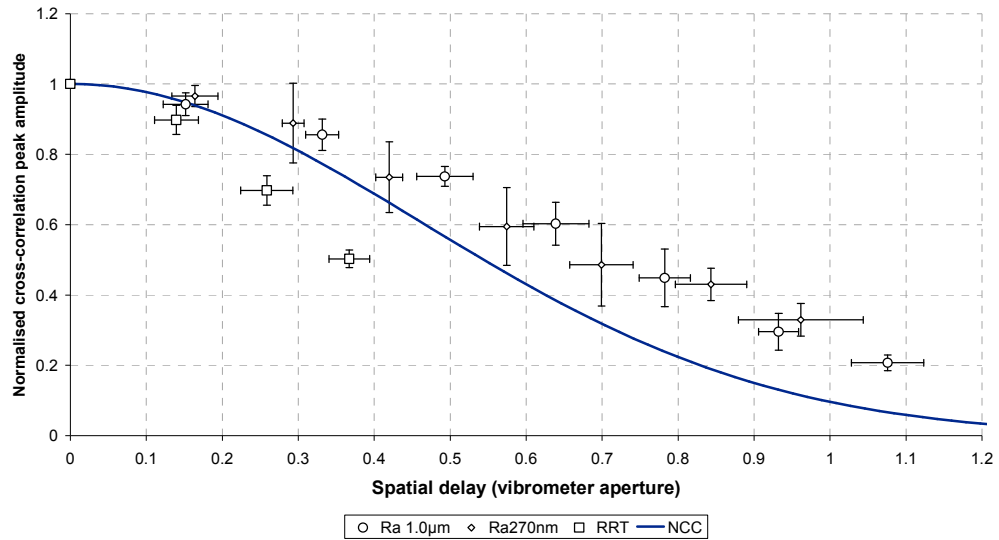


Figure 6.17 - Normalised cross-correlation of speckle motions from a rotating cylindrical surface using a beam spot diameter of $90\mu\text{m}$

Similarly to the $520\mu\text{m}$ beam spot diameter, the cross-correlations for surfaces treated with retro-reflective tape show a reduced spatial delay and a greater reduction in correlation amplitude, compared to the other surfaces. The spatial delays of the speckles from Ra 270nm are also slightly reduced compared to those from the Ra $1.0\mu\text{m}$ surface. This is attributed to the narrower band of speckles created by the Ra 270nm surface. This was evident in the image of the speckle pattern generated by the Ra 270nm surface and shown in Table 5.10. Figure 6.17 shows very little difference in the cross-correlation amplitude between the Ra $1.0\mu\text{m}$ surface and the Ra 270nm surface. Table 5.12 shows there is no significant difference in the rotation sensitivities produced from any of these three surfaces. This therefore suggests there is no significance to the variations in the spatial delays or the cross-correlation amplitudes seen by using retro-reflective tape as far as speckle noise is concerned.

As the speckles translate across the vibrometer aperture, for the smaller beam diameter ($90\mu\text{m}$), the normalised cross-correlation amplitude reduces to

approximately 0.3 at the vibrometer apertures extent. With this magnitude of decorrelation, it is difficult to confirm whether speckle translation or speckle evolution dominates the changes on the vibrometer aperture. However the increased evolution, in comparison to the observations with the larger beam spot diameter (520 μ m), suggests a different speckle behaviour in the mechanism generating speckle noise.

Both Figures 6.14 and 6.17 suggests that the mechanism producing speckle noise generated from retro-reflective tape are different to the other surfaces presented. All other surfaces presented show little variation. The most significant variation in rotation sensitivity, shown in Section 5.3.3, appears to come from a change to the beam spot diameter. The speckle translation distance, shown by the spatial delays in Figures 6.16 and 6.17, are very similar for each beam diameter. Speckle translation and speckle evolution are the only components in the mechanism generating speckle noise. If the speckle translations are similar for each beam spot diameter, as is the case, then the most significant variation in the rotation sensitivity is attributed to the difference in speckle evolution. The speckles evolve more when using the smaller beam spot diameter. If this is significant in the mechanism producing speckle noise it would suggest an increased rotation sensitivity. This is because the region of the speckle pattern in the vibrometer aperture decorrelates in a shorter time period. Section 5.3.3 showed, however, that the smaller beam diameter reduces the rotation sensitivity which suggests that evolution is not a significant component of the mechanism.

6.4 Summary of dynamic speckle

The observations of dynamic speckle have helped to see speckle motions in practice for transverse, tilt and rotating surface motions. It has shown that the speckle motions compare well with statistical theory based on intensity. Speckle noise is generated by a complex mechanism which includes speckles that often translate and evolve simultaneously. The normalised cross-correlation by intensity has proven to be a useful tool in analysing speckle motions but speckle noise is primarily governed by changes in phase. While the mechanism that drives a change in intensity also drives a change in phase, the analysis using cross-correlation of intensity has provided limited understanding of the relationship between intensity changes and pseudo-vibration sensitivities. The observations of dynamic speckle, therefore, haven't confirmed the differences in sensitivity, such as those related to different beam diameters, but it does provide confidence in the speckle behaviours used to simulate speckle noise and predict pseudo-vibration sensitivities. The next chapter models the speckle motions from that observed in this chapter and what has been understood from Chapters 3 and 4, using numerical simulations to quantify transverse sensitivity and tilt sensitivity.

7 Estimating pseudo-vibration sensitivity by simulation

Numerical simulators can be used to estimate levels of pseudo-vibration sensitivity. The intention of the simulations presented in this chapter is to model speckle behaviours in a simple way, concentrating on the key aspects of the mechanisms generating speckle noise. This assists in identifying significant features of the speckle behaviour, provides a greater understanding of the processes involved in producing speckle noise and can offer methods to help minimise speckle noise.

Previous numerical models have concentrated on estimations of speckle noise from rotating targets [7.1]. This chapter extends those investigations by presenting estimations of pseudo-vibration sensitivity from a target surface which moves transverse to the optical axis or tilts. The novel numerical simulations model speckle motions estimating transverse sensitivity and tilt sensitivity. The data produced by these simulations are analysed in the same way as those from the experimental examinations presented in Chapter 5, allowing a direct comparison and a verification of the simulations.

The two numerical simulations to be discussed in this chapter both use the same fundamental statistics examined in Chapter 3 and Chapter 4 to model the simulated speckles and their dynamics. However, the difference in the speckle behaviours for the two surface motions encourages a different approach in the

implementation of these statistics and each approach is discussed in the relevant sections.

7.1 Transverse sensitivity simulator

The simulation is written to model speckle noise that results when a target beam is incident on a surface which is optically rough and moves perpendicular to the optical axis with a sinusoidal motion. The in-plane surface motion causes speckles to translate, evolve or, more commonly, they will exhibit a behaviour which is some combination of the two regimes. The time for a speckle to evolve and the distance a speckle will translate depends on the particular optical configuration and the surface motion. As the surface moves the beam illuminates a changing population of surface elements and the amplitude and phase of the scattered E-field components alter. This change to the E-field components causes a change to the composition of the speckle, evolving and translating it over time. A speckle is modelled by the resultant of a summation of phasor contributions. Speckle boiling is modelled by modifying the summation over time. A change to the summation causes the speckles to vary independently from one another and provides a basis for the model of the evolution regime. To the author's knowledge, this is the first time the mechanism of speckle evolution using numerical simulation in the context of laser vibrometry has been modelled.

7.1.1 Formation of a simulated speckle

A simulated speckle must be a reliable representation of a ‘real’ speckle. Their suitability is evaluated by examination of their conformity to the statistics of ‘real’ speckles, in a fully developed state, discussed in Chapter 3. The extent of the simplification for the structure of the simulated speckle is also dictated by their dynamic behaviour. The evolutionary behaviour of the speckles for a transverse surface motion requires the simulated speckles to be constructed by a summation of phasor contributions with appropriate amplitudes and phases, shown by equation (3.1). The reasons for this are discussed further in Section 7.1.3.1, where modelling the speckle evolution regime is examined in more detail. Modelling the simulated speckles using a summation of phasors represents the addition of E-fields scattered from a surface, which interfere and form a speckle, as shown by equation (3.1). This raises the question, how many phasors must be summed for the simulated speckles to be a reasonable representation of a speckle? A program created to produce 25,000 speckles each built from a finite number of summed phasors is used to assess the consistency with the statistical distributions discussed in Chapter 3. 25,000 speckles is considered more than sufficient as a population of speckles to provide an adequate distribution for statistical representation. Each phasor has the same amplitude and its phase is produced from a uniformly distributed random number operating between the limits of $-\pi$ to π . As shown in Chapter 3, the statistics of the intensity of the speckles should have negative exponential distribution and the phase should be uniformly distributed over a 2π range.

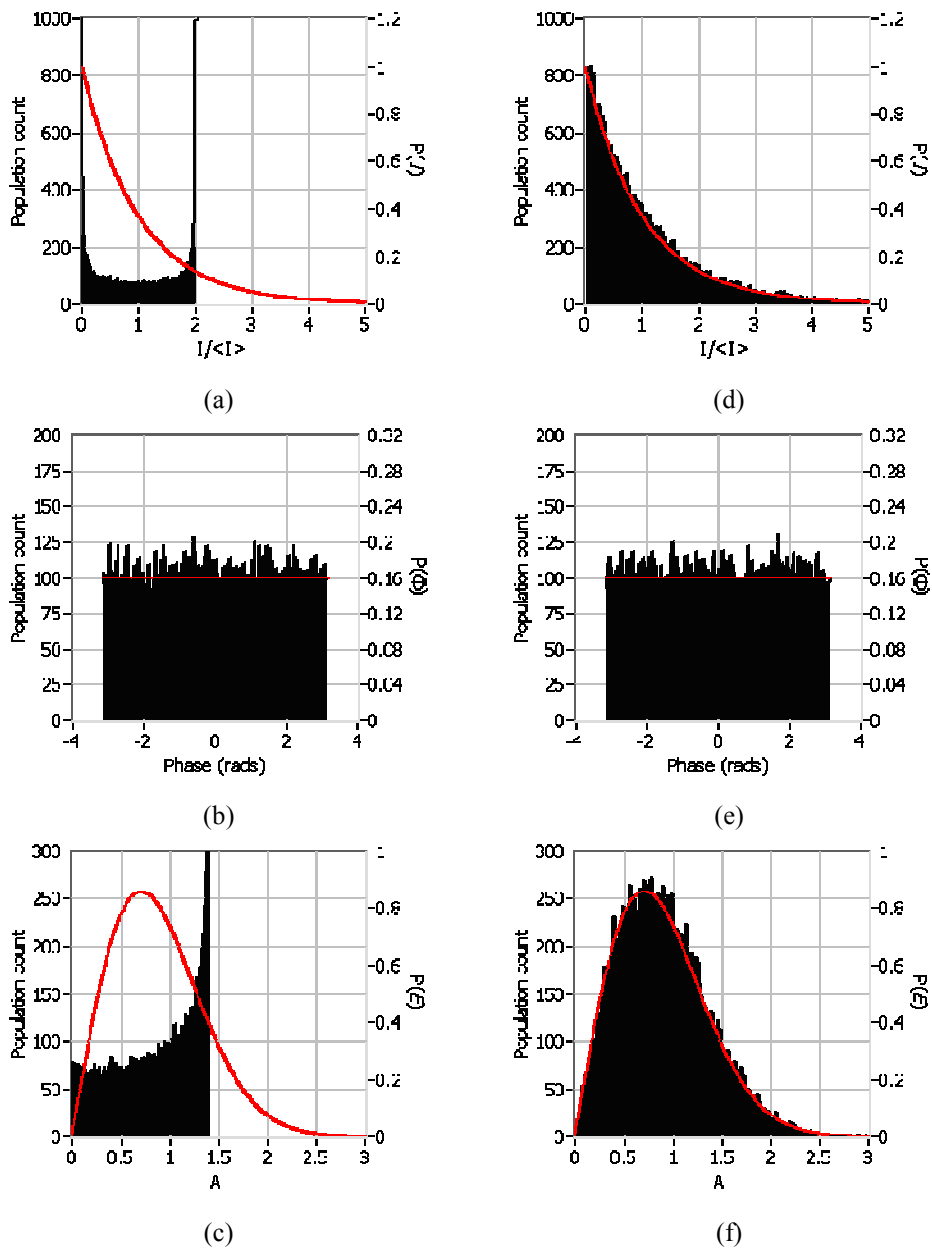


Figure 7.1 – Statistical distribution of 25,000 simulated speckles (black) together with the expected probability density functions (red). Summing 2 phasors per speckle (a) Intensity distribution; (b) Phase distribution; (c) Amplitude distribution. When summing 15 phasors per speckle (d) Intensity distribution; (e) Phase distribution; (f) Amplitude distribution.

Figures 7.1(a)-(f) present the histograms of simulated speckles when two phasors and fifteen phasors are summed, together with red traces showing the

probability density functions expected by speckle statistics shown in Section 3.2. Figures 7.1(a) and (d) show the resulting intensity distributions of the simulated speckles, Figures 7.1(b) and (e) show the resulting phase distributions and Figures 7.1(c) and (f) present the distribution of the amplitude of the resulting speckle. Figures 7.1(a)-(c) illustrate the non-conformity to speckle statistics, particularly for the intensity and the amplitude, when fewer phasors are summed than required. Figures 7.1(d)-(f) present evidence that fifteen phasors are sufficient for satisfactory distribution of intensity and phase. The simulated speckles for the transverse sensitivity simulator must, therefore, adhere to this criterion.

7.1.2 Modelling a speckle pattern

Figure 7.2 illustrates the simulation process and shows how it is related to physical scattering. A surface moves in-plane to the laser beam which has a Gaussian intensity profile. The scattered beam in reality produces a speckle pattern like that identified by a real speckle pattern which is a cross-section of the speckle pattern image shown in Figure 7.3 (a). The model assumes a simplification of the continuous profile of the real speckle pattern, modelling discrete speckles shown by Figure 7.3 (b). The speckle pattern is collected by a receiving aperture, in the form of a lens or a photodetector, and the intensity is measured. Figure 7.3(a) is an image of a real speckle pattern, showing the irregular distribution of speckles which vary in size, shape, intensity and phase. The intention of the simulator is to concentrate on the core mechanisms which ultimately produce speckle noise. Figure 7.3(b) is an example of a speckle matrix used in the simulator. The complexity of a speckle pattern is reduced to an ordered pattern of simulated speckles. The simulated speckles have statistically appropriate intensities and phases as shown by Section 7.1.1 and

every simulated speckle in the matrix is an equal size, governed by the expected size shown in equation (3.24), and is a square shape.

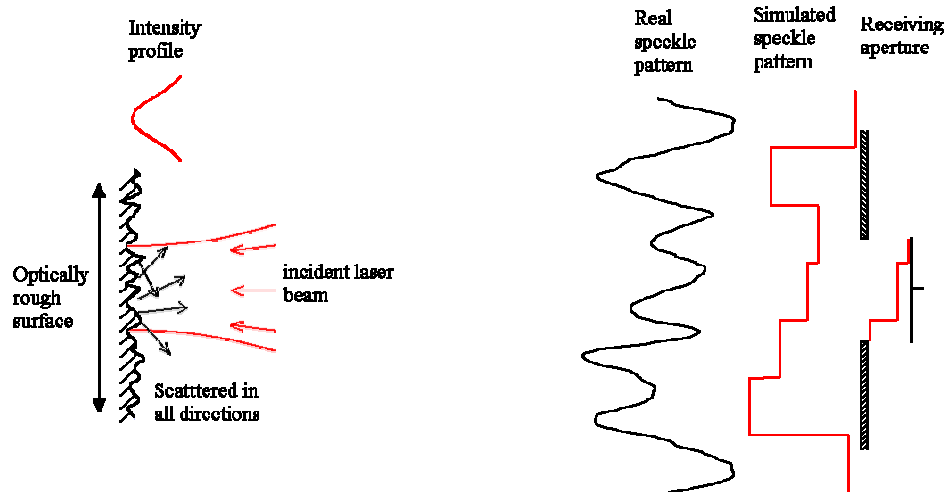
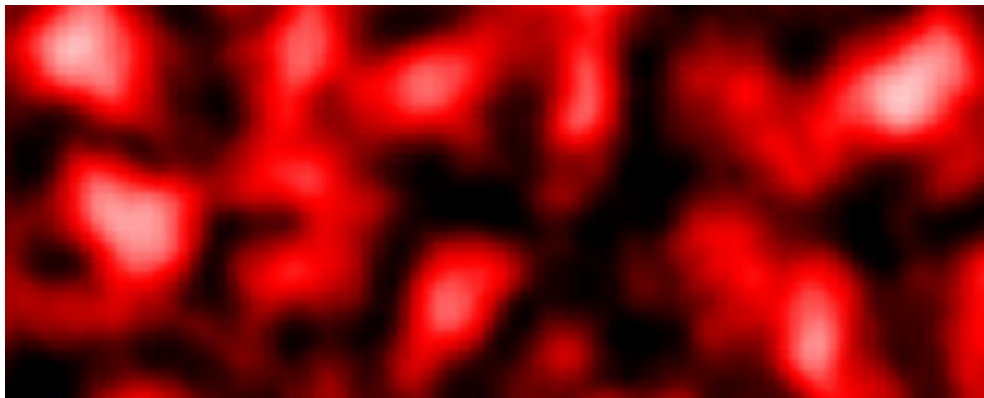
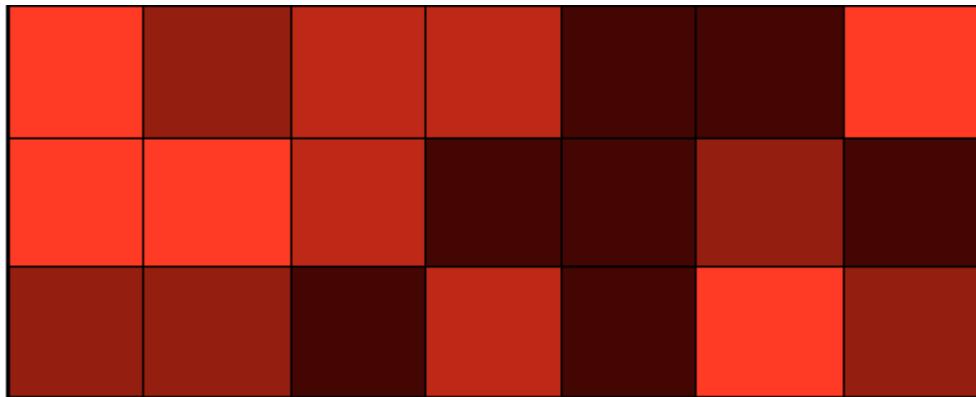


Figure 7.2 – Profile of a speckle pattern and a model of a simulated speckle pattern



(a)



(b)

Figure 7.3 – (a) portion of an image of a ‘real’ speckle pattern (b) example of a simulated speckle pattern

The simulation begins by taking optical parameters, (beam diameter; receiving aperture width; radius of curvature at the surface; standoff distance), measurement parameters (number of points per oscillation; number of oscillations) and target parameters (vibration frequency; displacement amplitude). Using these parameters, the simulation determines the dimensions of the simulated speckle pattern to be created, sufficient in size for the whole cycle of the surface motion being investigated.

7.1.2.1 Speckle size

Section 7.1.1 showed how the amplitude and phase of each speckle can be appropriately represented. The simulated speckles must also be the correct size to adequately represent the spatial characteristics of real speckles. The primary simplification of the simulation is that the simulated speckles in each study are assumed to be equal in size, be of a regular shape and have a uniform intensity and phase across their extent. The laser beam is assumed to have a wavelength of 633nm and the illumination spot has a Gaussian intensity profile, both typical of He-Ne lasers used in vibrometry. The simulation takes user inputted optical parameters such as the beam diameter and the standoff distance,

particular to the study being investigated, and a speckle width is calculated using $\langle \sigma_0 \rangle = \frac{2\sqrt{2}\lambda z_S}{\pi D}$ (equation (3.24)). The average speckle size is defined by the $\exp[-2]$ width of the spatial autocorrelation function with Gaussian beam illumination, and is the expected width of a speckle using a beam diameter of D at a distance z_S away from the surface. This provides an appropriate size to each speckle given the physical parameters being represented. The number of speckles to create is determined by the number of speckles collected at any one time, and that is found using the size of the detector which is discussed in the next section.

7.1.2.2 Detector size

As described in Section 1.1.1, a vibrometer uses a photodetector to measure the light intensity of the backscattered light from a target surface. The detector dimension is considered as square, but for consideration of the practicalities of the simulation, its dimension is dependent on the optical apparatus in the vibrometer being considered. A simplified schematic of a vibrometer is illustrated in Figure 7.4, showing the returning beam for a vibrometer without a focussing lens. The speckle pattern entering the vibrometer is mixed with the reference beam at the beamsplitter and the resulting intensity of the interference is measured by the photodetector. The detector dimension, for this optical apparatus, is considered as the detector dimension itself. This is easily measured together with the additional propagation distance required by the internal geometry of the vibrometer. Often a lens is incorporated into a vibrometer to focus the beam and a schematic of the returning component beams considered by the simulation for a vibrometer with a lens is shown in Figure 7.5. The lens modifies the geometry of the returning light, which is in the form of a speckle pattern. The speckle pattern then mixes with the reference beam at the beam splitter and the intensity is measured by the photodetector.

The profile of the propagation geometry, including reference beam is quite complex, and speckle width is not easily known between the lens system and the photodetector. As long as the interference dimension, ie the reference beam width, remains constant relative to the speckle width, however it does not matter where in the path the intensity is measured. For practical reasons it is simplest to consider the interference at the front surface of the lens system. In this way, if the vibrometer has a lens, the detector aperture dimension is considered to be the beam size as it emerges from the lens.

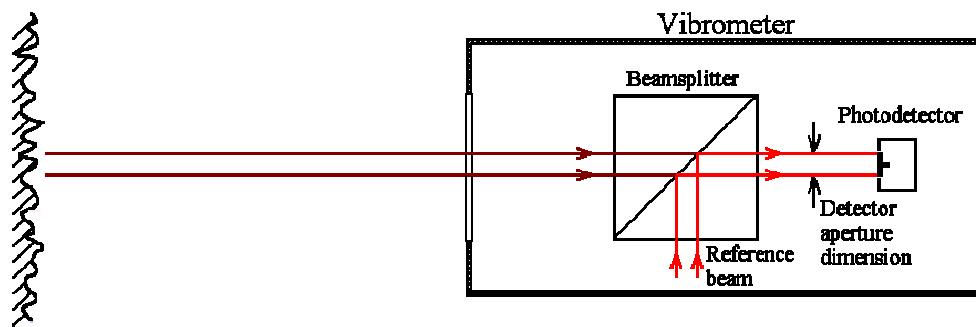


Figure 7.4 – Schematic of returning beam components for a vibrometer without a lens

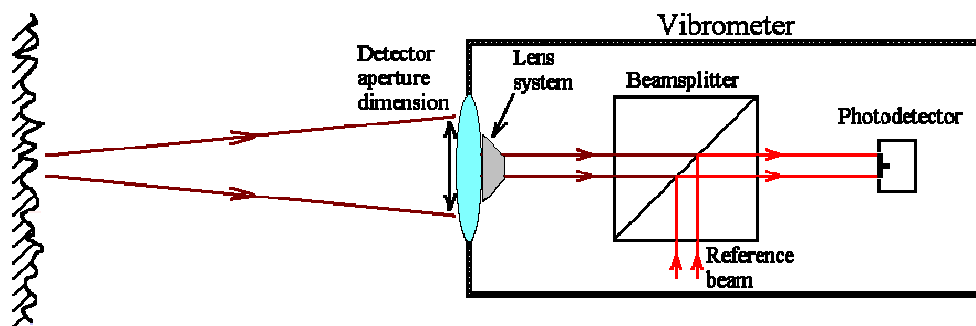


Figure 7.5 - Schematic of returning beam components for a vibrometer with a lens

Both a lens and a photodetector isolate a portion of the backscattered light and act as receiving apertures in the beam path. The number of speckles in the

detector dimension, M , is determined by the ratio of the receiving aperture width to the speckle size. In a vibrometer, the intensity is measured and the Doppler signal is created from the fluctuating component. The next section describes how the simulator creates the Doppler signal.

7.1.2.3 Simulating the Doppler signal

As described above, the vibrometer receives a portion of the resulting speckle pattern through an aperture. Illustrated in Figure 7.6, by the region bordered in blue, the receiving aperture is a constant size and maps out the portion of the speckle matrix which forms the target speckle pattern component of the instantaneous Doppler signal. The variation of the row positions shown in Figure 7.6 disrupts the regular pattern presented to the detecting aperture and this is discussed further in Section 7.1.3.2.

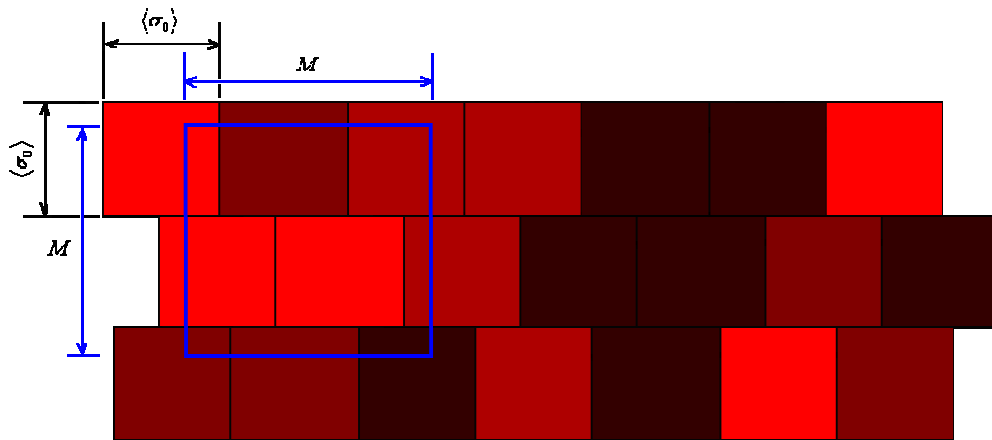


Figure 7.6 – Speckle pattern matrix and an example of the detecting aperture positioning

The target beam, composed of a speckle pattern, is mixed with a reference beam on a surface measuring the total light intensity and the fluctuating component is the Doppler signal. As discussed in Section 1.1.1, the total light intensity is the time average of the square of the total light amplitude which is a

summation of complex amplitudes of the incident E-fields. The complex summation can be represented as a phasor addition, an example of which is illustrated in Figure 7.7. The target speckle pattern is represented by a random walk of black phasors, which when combined with the reference beam, shown by the red phasor, produces the resultant shown in blue which represents the total light amplitude on the detector.

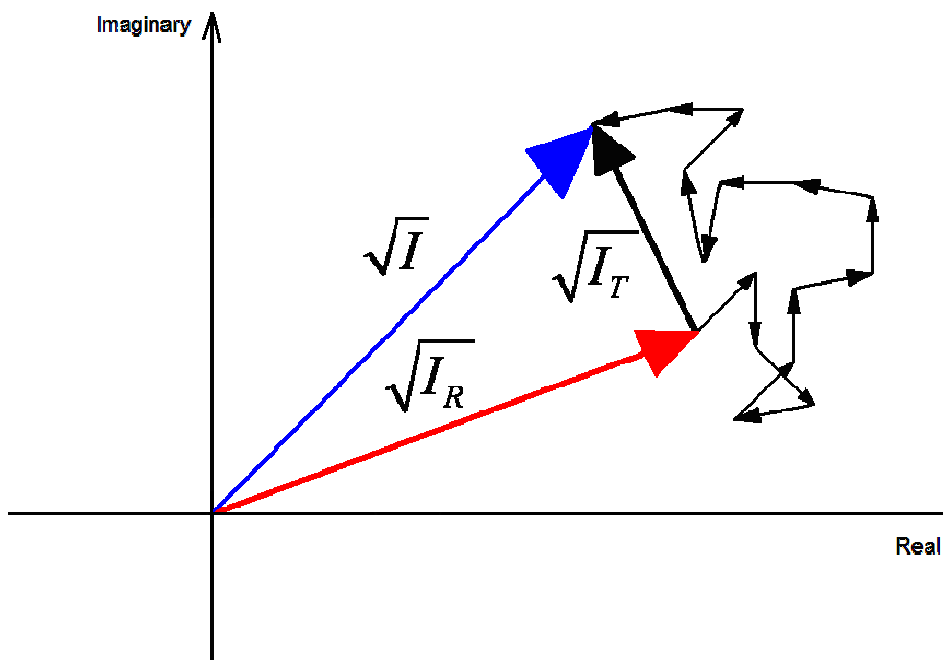


Figure 7.7 - Example Argand diagram of total light amplitude on a simulated detector

Concentrating on the effects of speckle motions, with no surface motion in the direction of the beam, parallel with the optical axis, and recalling equation (2.1), the total light intensity is expressed as

$$I = I_R + I_T(t) + I_{res}(t) \cos[\omega_R t + \Phi_{res}(t)] \quad (7.1)$$

where the simulated Doppler signal amplitude $I_{res} = 2\sqrt{I_R I_T}$ and phase $\Phi_{res} = \Phi_R - \Phi_T$. If S speckles are mixed with a uniform reference beam, which are incident on the detecting aperture, the instantaneous amplitude of the Doppler signal can be calculated by summing the incident speckles as follows

$$I_{res} = \frac{2\sqrt{I_R}}{M^2} \left[\sum_{s=1}^S \sum_{u=1}^S A_s A_u E_s E_u \cos(\Phi_s - \Phi_u) \right]^{1/2} \quad (7.2)$$

where

$$\sqrt{I_T} = \frac{1}{M^2} \left[\sum_{s=1}^S \sum_{u=1}^S A_s A_u E_s E_u \cos(\Phi_s - \Phi_u) \right]^{1/2} \quad (7.3)$$

where E_s and E_u are the amplitudes and Φ_s and Φ_u are the phases of speckle s and speckle u respectively. A_s and A_u are factors for the area of speckle s and speckle u on the detector, to be discussed further in Section 7.1.3.2. The instantaneous phase, Φ_{res} , of the Doppler signal can be expressed as

$$\Phi_{res} = \tan^{-1} \left(\frac{\sum_{s=1}^S A_s E_s \sin(\Phi_R - \Phi_s)}{\sum_{s=1}^S A_s E_s \cos(\Phi_R - \Phi_s)} \right) \quad (7.4)$$

and

$$\Phi_T = \tan^{-1} \left(\frac{\sum_{s=1}^S A_s E_s [\sin(\Phi_s)]}{\sum_{s=1}^S A_s E_s [\cos(\Phi_s)]} \right) \quad (7.5)$$

When Φ_{res} is made a function of time, speckle noise is calculated using $\frac{1}{2k} \frac{d\Phi_{res}(t)}{dt}$ shown by equation (2.2). Φ_{res} is made a function of time by changing the weighting of the individual phasors in the summation for speckle s . This models an evolving speckle and is described in the next subsection. Simultaneously translating the speckles across receiving aperture causes A_s to be a function of time. The next section describes how the simulated speckles evolve.

7.1.3 Simulating speckle dynamics

When a surface moves perpendicular to the optical axis (of the laser beams considered), speckles exhibit both an evolution as well as a translation. Both these motions are modelled in the simulation. Section 7.1.3.1 deals with modelling of the evolution and provides the necessary parameters to evolve a simulated speckle over time. The parameters required to translate a simulated speckle are discussed in Section 7.1.3.2.

7.1.3.1 Modelling speckle evolution

Each speckle is formed by the summation of the complex amplitude of a sufficient number of phasors as discussed in Section 7.1.1. A full set of phasors for each dynamic speckle is created, sufficient in number for the whole cycle of the transverse surface motion under consideration. Each phasor takes the form of $e \exp[j\phi]$ and at any instant in time a speckle is formed by summing a set of the phasors as shown by equation (3.1).

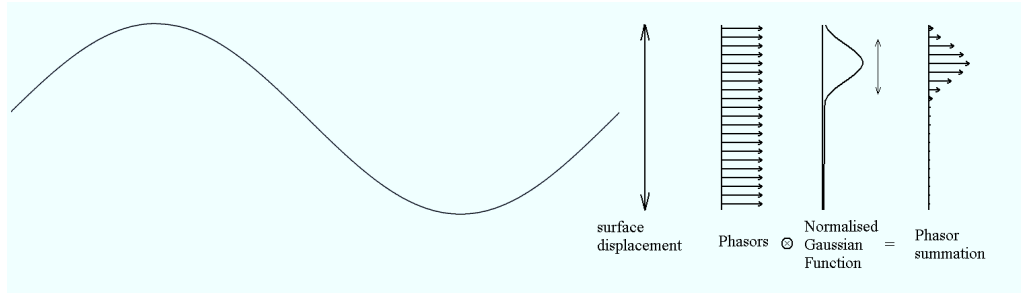


Figure 7.8 – Surface displacement and convolution routine

In a vibrometer, the beam typically has a Gaussian intensity profile and this has to be accounted for during the evolution. A normalised Gaussian function is convolved with the set of phasors, as a function of the surface displacement, modelling the evolution of the speckle.

$$E_s(a) = \sum_p e_{s,p} \exp[j\varphi_{s,p}] \exp\left[-2 \frac{(p\Delta D - a(t))^2}{D^2}\right] \quad (7.6)$$

where the surface displacement, a , takes a sinusoidal form

$$a(t) = a_0 \sin(2\pi f_a t) \quad (7.7)$$

and p is the phasor index to the set of phasors created for the whole cycle. The second exponential function in the summation of equation (7.6) is the normalised Gaussian function which dictates the weight of each phasor in the sum of phasors for speckle s . The Normalised Gaussian function, weighting the phasors, is representative of the Gaussian laser beam illuminating discrete scattering elements on the surface. The phasors are uniformly distributed within the range of the displacement cycle. The phasor separation distance, ΔD , is the target displacement corresponding to one phasor exchange in the simulation. This value together with the total number of phasors in the cycle

range is governed by the desired number of samples per cycle or the time increment in equation (7.7). ΔD is chosen to be equivalent to the smallest target displacement occurring during the fixed increment of time, which limits the minimum phasor step to 1. Normal operation of the Gaussian function should extend the tails to infinity but this is impossible within the limitations of a numerical simulation. Practically, the Gaussian function must have a boundary limit. This boundary is set by the $\exp[-2]$ width and therefore only the phasors bound by this value in the Gaussian function are summed. As stipulated by Section 7.1.1, the number of phasors within this boundary must be at least fifteen. Figure 7.8 illustrates the displacement cycle of the surface and shows the convolution. As the surface moves and time progresses, the Gaussian function transits through the set of phasors, modifying the summation and evolving the speckle.

The evolution of the simulated speckle needs to be consistent with that observed with real speckles. Evaluation of the evolution is made using the cross correlation of the simulated speckles as they evolve during the surface motion. Figure 7.9 shows the normalised cross correlation amplitude of the intensity against the surface displacement in units of beam diameter. The surface moves with a uniform velocity and is therefore comparable to the statistics shown in Chapter 4. The peak value of the average of 10 normalised cross correlations of a matrix of 40x40 speckles is used to evaluate the evolution. The black trace shows the normalised cross correlation amplitude of the simulated speckles, the red trace indicates the limit of the correlation which is set at $\exp[-2]$ and the blue trace is the correlation expected by theoretical real speckles. When the red trace intersects the black and blue traces, the simulated and real speckles have evolved respectively.

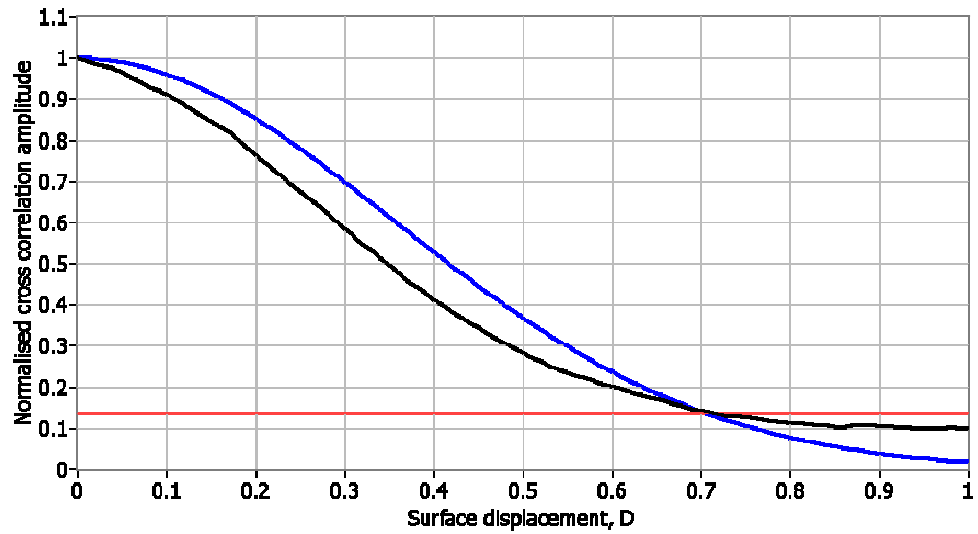


Figure 7.9 – Cross correlation of patterns of 40x40 speckles, purely evolving with speckles at surface displacement = 0. Simulated speckles - black, real speckles – blue and limit of correlation at $\exp[-2]$ - red.

The cross correlation of the simulated speckles can be seen to take a Gaussian like decay and is similar to that which is to be expected. There is a slight distortion of the Gaussian decay because of the practical limitations of the Gaussian function required by the simulation. The distance required to evolve the simulated speckles, can be seen to be approximately $0.7D$, intersecting the red trace at the same point as the blue trace. Observation of the cross correlation for the fluctuating intensity seen in Chapter 4, shown by equation (4.12) and equation (4.13) when the speckles are in pure evolution, shows the surface displacement for speckle correlation is $|a_c| = \frac{1}{\sqrt{2}}D$, which is consistent with the approximate value of $0.7D$ observed in the cross correlations. This means the simulated speckles are expected to take the same time to evolve as real speckles. The speckles not only evolve they also translate and the next section discusses the simulated speckle translation.

7.1.3.2 Modelling speckle translation

The motion of the surface also causes the speckles to translate. The speckle translation distance is found from the spatial delay of the peak of the normalised cross correlation $X_T = \sigma a(t)$, as described in Section 4.2.1. The distance a speckle can translate is restricted by the evolution of the speckle and quantified by the reduction of the correlation peak. The peak of the normalised cross correlation reduces to $\exp[-2]$ when the surface has translated $\frac{1}{\sqrt{2}} D$. In other words, in the time it takes for the speckle to evolve completely the speckle will have translated $\frac{1}{\sqrt{2}} \sigma D$, where σ is the speckle translation gearing term. The speckles translate in the width of the speckle pattern matrix. The cumulative speckle translation distance is used to determine the width of the speckle pattern matrix.

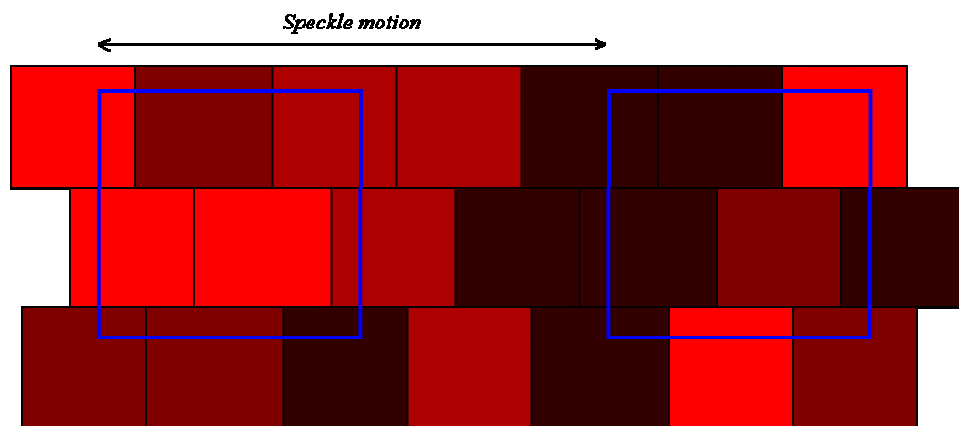


Figure 7.10 – Speckle translation

The unregimented pattern of speckles presented to the receiving aperture, shown in Figure 7.10, allows the speckles to leave the detector at different

moments and represents more appropriate Doppler signal transitions when the number of speckles in the detector dimension, $M > 1$. The offset rows and height of the matrix means a speckle can overlap the border of the receiving aperture and not contribute in its entirety to the resultant Doppler signal.

Previous work has found that the rate of change of phase can be significantly underestimated if considered as constant throughout a single speckle transition [7.1]. This was overcome by subdividing the speckle into an appropriate number of partial speckles. However in previous work it was not necessary to model the boiling motion of the speckle which, under the proposed model, can require significantly more computational resources. The simulator uses an alternative to sub-dividing the speckle. Using a factor which is proportional to the speckles area on the receiving aperture an appropriate contribution to the Doppler signal can be calculated. The factor for the area of speckle s , A_s , whether the speckle is partially or fully on the receiving aperture can be calculated using the following

$$A_s(a) = [1 - (h_{s,0} + h_{s,1})] [1 - (w_{s,0}(a) + w_{s,1}(a))] \quad (7.8)$$

The factors $w_{s,0}$ and $h_{s,0}$, shown in equation (7.8) and illustrated in Figure 7.11, are used for the quantity of speckle s off of the receiving aperture. The factor $w_{s,0}$ is defined in the horizontal direction from the left most edge and $h_{s,0}$ is defined in vertical directions from the top most edge of the speckle. The factors $w_{s,0}$ and $h_{s,0}$ are initially generated by sets of independent uniformly distributed random numbers operating between 0 and 1 and they control the random positioning of the receiving aperture. The factors $w_{s,1}$ and $h_{s,1}$ depend on the quantity of the speckle off of the receiving aperture from the right most edge and the bottom most edge of each speckle, and are only ever non-zero for the

right most speckles and bottom most speckles on the receiving aperture respectively.

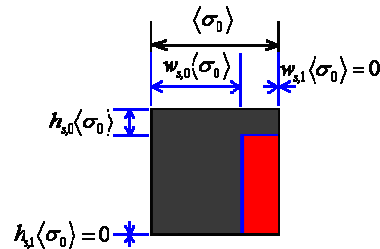


Figure 7.11 - An example of the area of a speckle incident on the receiving aperture showing the appropriate dimension parameters

The area factor of each speckle is used in equation (7.2) and equation (7.5) to calculate the Doppler signal amplitude and phase, respectively, allowing an estimate of speckle noise to be produced. The next section describes the estimation of speckle noise using the simulator. Section 7.1.4.1 verifies the simulator using experimental estimates while Section 7.1.4.2 studies ways in which speckle noise is affected by the optical parameters and investigates ways to reduce the levels.

7.1.4 Transverse sensitivity using the simulator

An example of a typical simulated speckle pattern on the receiving aperture is shown in Figure 7.12 with the dimensions in number of speckles. In this instance the aperture is approximately 1.5 by 1.5 speckles square, which is applicable for the vibrometer configuration with a beam diameter of 600 μ m on the surface. The appropriate weighting factor for the area, calculated from equation (7.8), is applied to each speckle and the Doppler signal amplitude and phase are calculated from equation (7.2) and equation (7.5) respectively. The Doppler signal components are calculated for one whole period of target

oscillation. Figures 7.13 (a) to (d) show typical results from the simulation for one period of sinusoidal in-plane surface displacement of $420\mu\text{m}$ rms with a beam of diameter $600\mu\text{m}$ and an infinite radius of curvature at the surface. The receiving aperture is positioned 700mm from the surface and the speckles translate as well as evolve.

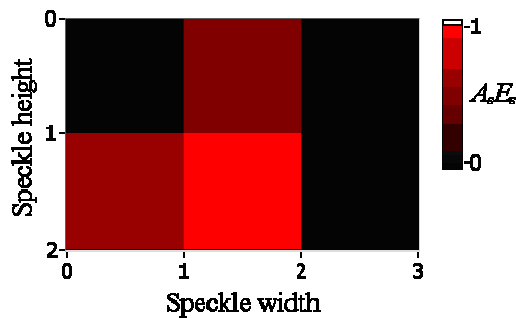
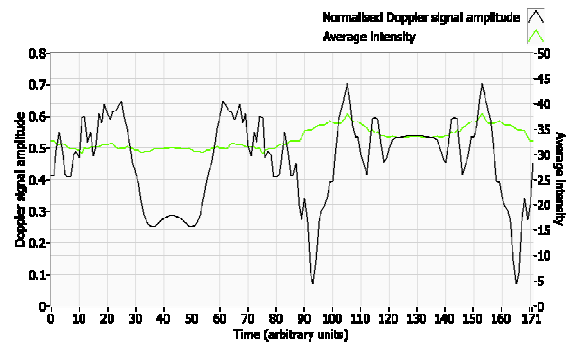


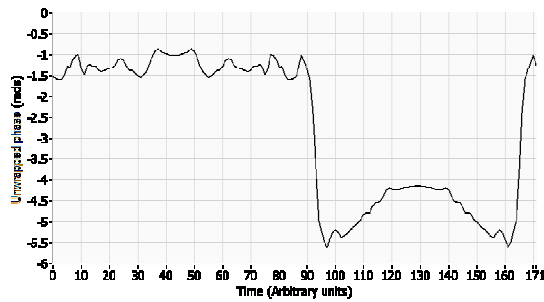
Figure 7.12 - Speckles incident on the receiving aperture

Figures 7.13 (a) and (b) show a sequence of changes in Doppler signal amplitude and phase as the speckle pattern motion influences the data respectively. As the target moves from one extreme to another in the displacement cycle, the Doppler signal changes in a continuous sequence. In the second half of the displacement cycle, the phase of the resultant Doppler signal passes through the same sequence of phases as the first but in reverse. Consequently the speckle noise appears to reflect and negate about any instant in time corresponding to zero velocity in the surface motion cycle. The most significant changes in phase, evident in Figure 7.13 (c), occur simultaneously with low Doppler signal amplitude and occur most often near instants in time where the surface speed is highest, shown in Figure 7.13 (d). Also evident is that these phase changes are not as a consequence of low light amplitude shown by the average intensity in Figure 7.13 (a). The average intensity is calculated from the intensity of the speckles incident on the receiving aperture and is used as an indicator to the quality of the signal as a result of the light

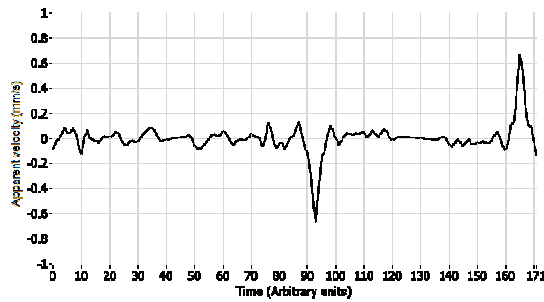
levels. This means the more rapid changes in phase and low Doppler signal amplitude are more likely as a consequence of an unfavourable collection of speckles rather than the level of light. This indicates that irrespective of the light levels which can be increased with higher laser power or surface treatments, like retro-reflective tape, low Doppler signal amplitudes and rapid changes in phase still occur. Changes to the speckle pattern result in a change to the resultant amplitude and the resultant phase. When the resultant amplitude is relatively low, a small change in speckle collection can result in a rapid alteration to the phase of the resultant phasor. The faster these phase changes occur the greater the level of speckle noise. This means speckle noise peaks are likely to be close to the time when the surface velocity is greatest. Figure 7.14 shows the sampled resultant phasor path over time with the red phasor representing the resultant at one point of maximum surface displacement and the green phasor representing the resultant at the other point of maximum surface displacement. From this plot it can be seen how the phase and amplitude change as the simulation transits through the dynamic speckle pattern.



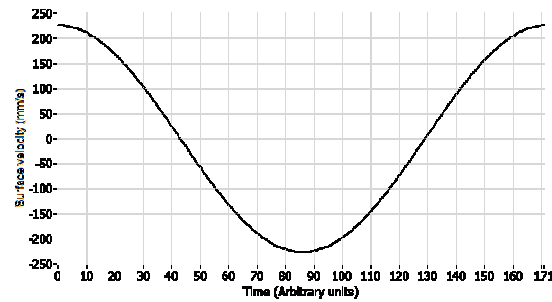
(a)



(b)



(c)



(d)

Figure 7.13 – (a) Doppler signal amplitude and the average intensity for one whole cycle, (b) Unwrapped phase of the Doppler signal for one whole cycle, (c) Apparent velocity for one whole cycle, (d) In-plane surface velocity for one whole cycle

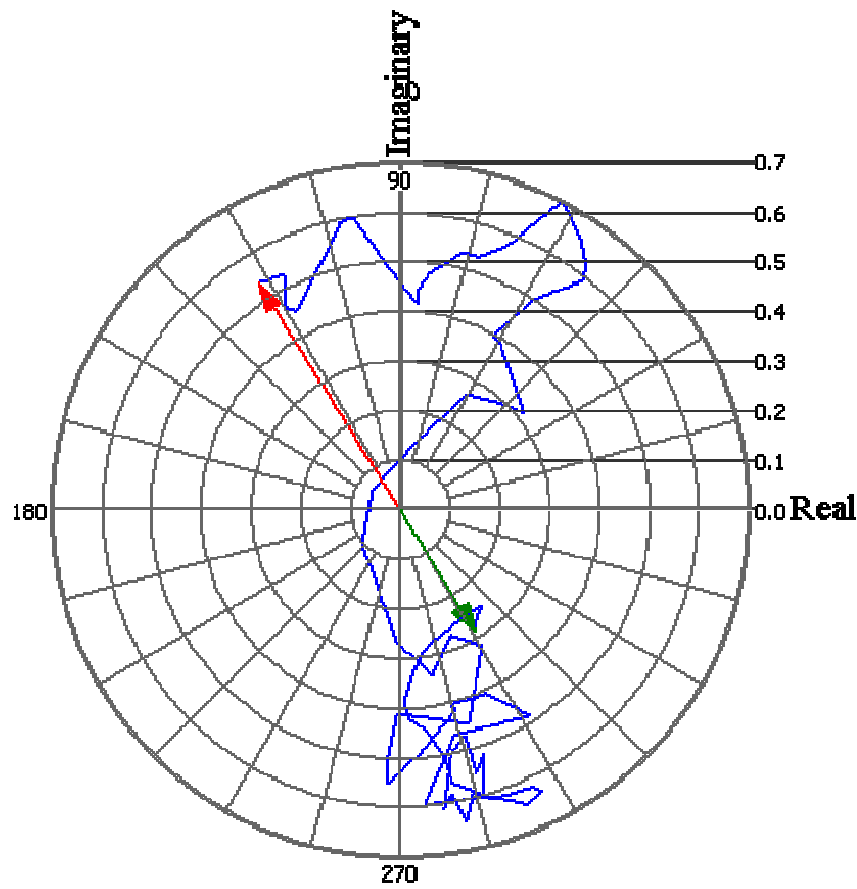


Figure 7.14 - Polar plot of the path (locus) of the resultant from the target speckle pattern. Green phasor (time step 43) to red phasor (time step 129) is the same duration as the peak to peak range of the surface displacement

7.1.4.1 Verification of the simulator

The simulator is verified by producing equivalent quantitative data to those seen in Chapter 5 where pseudo-vibration sensitivities were quantified from experimentation. The optical parameters, measurement parameters and target parameters for the simulation are matched to the experimental arrangement. The commercial vibrometer which produces a beam diameter of 600 μ m has a detecting surface about 1mm wide which is approximately 700mm from the

surface (vibrometer standoff distance plus the path length inside the vibrometer head). The other commercial vibrometer in this study uses a lens to focus the beam to a diameter of $100\mu\text{m}$. The lens acts as a collecting aperture and as such the speckle motions for this vibrometer are considered at the front of the lens which is 600mm away from the surface and the beam size as it emerges from the lens is approximately 12mm wide. The speckle pattern is still mixed with a reference beam, except it is considered as occurring on the front of the lens.

The resulting data is produced and analysed in the same manner as the experimental data. The estimations of transverse sensitivity are made from averages of 50 simulations with the same controlling parameters allowing a statistical comparison. Matching the experimental configuration requires 96 whole periods of oscillation of data such as that seen in Figure 7.13 (c) to be Fourier transformed. Whilst eliminating the ‘picket fence’ effect, the peak values of the first 50 orders of the vibration frequency are found and an average is calculated for each order. Figure 7.15 shows the average peak values of the first 50 orders of speckles noise which are shown as a percentage of the transverse surface velocity at the fundamental frequency. Figure 7.15 also shows the equivalent experimental data presented in the same way for comparison. Figure 7.15 shows that the simulation produces comparable results to the experimental estimates. The simulations suggest that the $100\mu\text{m}$ beam diameter produces higher levels of speckle noise compared to the $600\mu\text{m}$ beam diameter and this is confirmed by experimentation. The spectral shape produced by the simulations over the 50 orders is also comparable with the experimentation. Table 7.1 shows a comparison of the quantitative data produced from the values in Figure 7.15. The experimental values presented in Table 7.1 are produced from a surface with $R_a 1.0\mu\text{m}$ which should produce a fully developed speckle pattern, matching that modelled by the simulator. The values are presented in two ways, one showing speckle noise estimates over the

first 10 orders, likely to be of interest to the vibration engineer, the second showing the total rms for the first 50 orders. Table 7.1 shows the remarkable similarity of the estimations of transverse sensitivity produced by the simulations with those produced experimentally, especially for the larger 600 μm beam diameter.

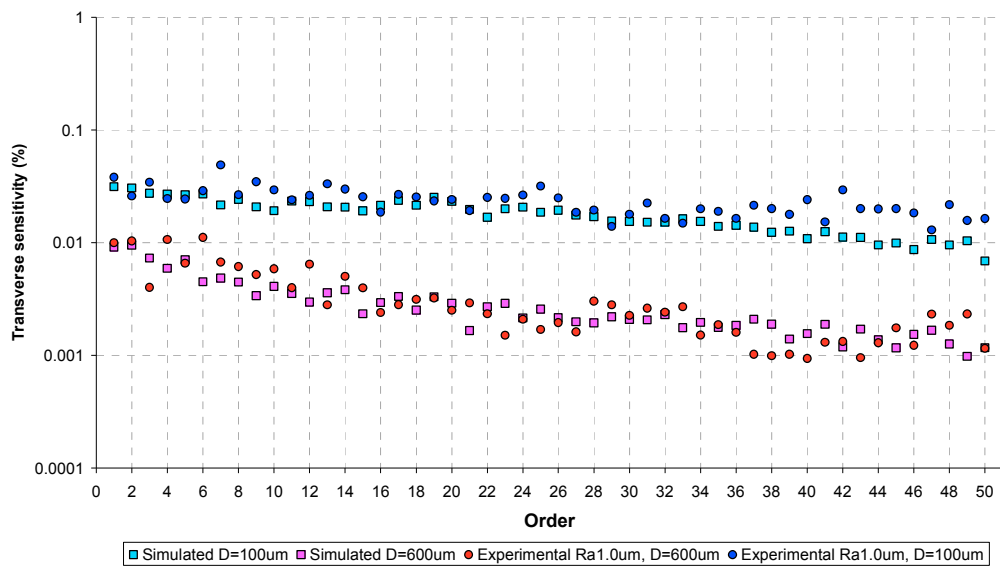


Figure 7.15 –Comparison of simulated and experimental transverse sensitivity

<i>Transverse sensitivity: apparent velocity per unit transverse velocity (%)</i>		
<i>Surface finish</i>	Simulation	Experimentation
<i>D = 600μm</i>		
<i>Mean level by order (orders 1-10)</i>	0.0060	0.0077
<i>Standard deviation (orders 1-10)</i>	0.0052	0.0055
<i>Total level across 50 orders</i>	0.025	0.030
<i>D = 100μm</i>		
<i>Mean level by order (orders 1-10)</i>	0.026	0.032
<i>Standard deviation (orders 1-10)</i>	0.020	0.020
<i>Total level across 50 orders</i>	0.13	0.17

Table 7.1 – Comparison of simulated estimates to experimental estimates of speckle noise. Experimental transverse sensitivity is taken from Ra 1.0 μm surface, as shown in Tables 5.1 and 5.2.

The simulators estimate transverse sensitivity at around 0.006%, per order, for the first 10 orders or 0.025% for the total rms over 50 orders for a beam diameter of 600μm. For a beam diameter of 100μm, transverse sensitivity is estimated as 0.026%, per order, for the first 10 orders and approximately 0.13% for the total rms over 50 orders. Despite the marginally larger speckle noise estimates from the experimental levels for a beam diameter of 100μm,

the simulated estimates are suitably confirmed. Further verification of the simulations comes from estimations of speckle noise produced when altering the vibration amplitude of the surface. Figure 7.16 and 7.17 show the simulated and the experimental estimates of transverse sensitivity using a beam diameter of $100\mu\text{m}$ for surface vibration displacement amplitudes of $52.5\mu\text{m}$ rms and $210\mu\text{m}$ rms respectively. Figure 7.16 and 7.17 show the similarity of the spectral shapes of the simulated data to the experimental. However the roll-off for the simulated estimates in Figure 7.16 is not as pronounced as the experimental data. Table 7.2 shows the simulated and experimental transverse sensitivity for the reduced vibration displacement amplitudes including $105\mu\text{m}$ rms surface vibration. Both simulated and experimental transverse sensitivity appears to increase as the vibration amplitude reduces. This is because transverse sensitivity does not reduce proportionally with the vibration displacement amplitude. Generally the transverse sensitivity estimates for the simulation are marginally lower. Figure 7.16 shows that for lower orders (orders 1 to 20) the estimations of transverse sensitivity, for a surface vibration amplitude which is less than the beam diameter, appear much less than the experimental.

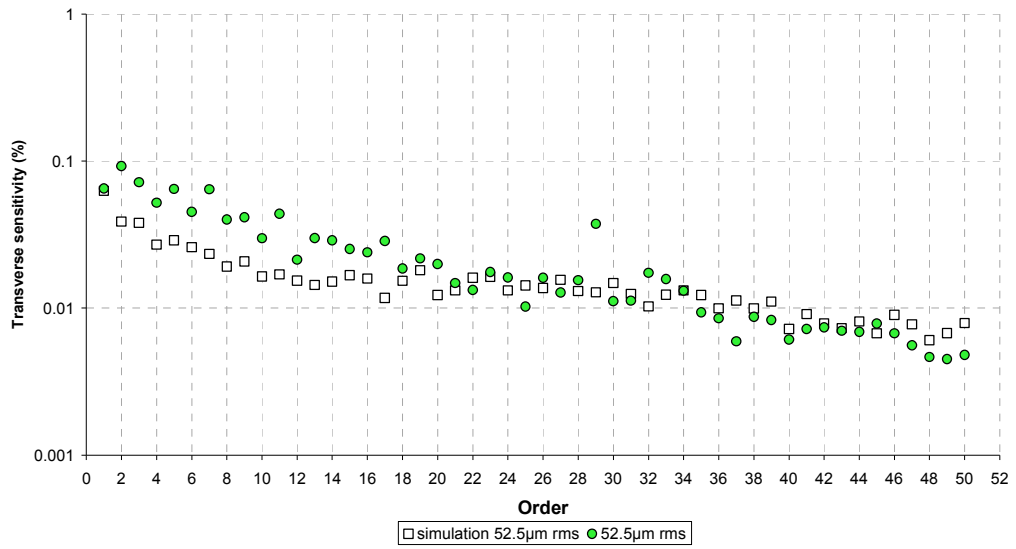


Figure 7.16 – Simulated and experimental estimates of transverse sensitivity. Surface vibration displacement amplitude is 52.5µm and $D=100\mu\text{m}$

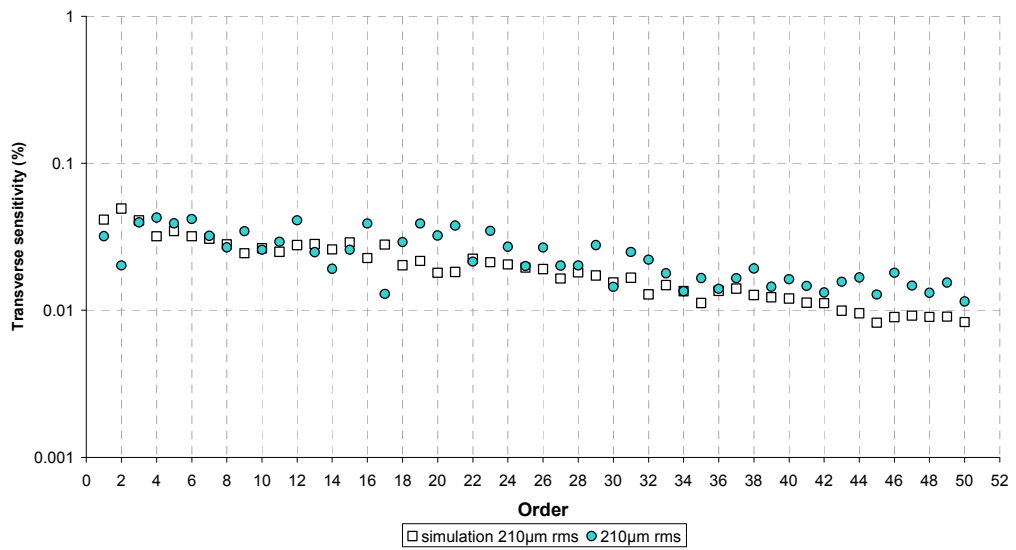


Figure 7.17 – Simulated and experimental estimates of transverse sensitivity. Surface vibration displacement amplitude is 210µm and $D=100\mu\text{m}$

<i>Transverse sensitivity: apparent velocity per unit transverse velocity (%)</i>			
$D = 100\mu\text{m}$			
Simulated (Experimental)			
Surface displacement amplitude	210μm rms	105μm rms	52.5μm rms
<i>Mean level by order (orders 1-10)</i>	0.034 (0.034)	0.039 (0.046)	0.030 (0.057)
<i>Standard deviation (orders 1-10)</i>	0.025 (0.023)	0.032 (0.028)	0.029 (0.038)
<i>Total RMS level across 50 orders</i>	0.16 (0.18)	0.16 (0.20)	0.13 (0.22)

Table 7.2 - Simulated and experimental (Ra 1.0 μm) transverse sensitivities for various vibration amplitudes

The simulator for transverse surface motion has shown that it can adequately estimate transverse sensitivity for different optical configurations and also for different target vibration amplitudes, although this is limited.

7.1.4.2 Speckle noise reduction

Section 7.1.4.1 has verified the simulator using experimental data. This section looks at using the transverse sensitivity simulator to investigate ways to reduce speckle noise.

Figure 7.18 and Table 7.3 shows the transverse sensitivity for a beam diameter of 100 μm and constant speckle translation distance, but where the aperture is varied in size from approximately 0.2 speckles up to near to 10 speckles. Altering M , the ratio of aperture dimension to the speckle size, is comparable

with altering the aperture dimension itself. The rationale behind this is that as more speckles are collected the change in phase occurs more slowly and reduces speckle noise. When the beam is focussed on the surface it can be seen that altering M does not affect the levels of transverse sensitivity throughout the entire 50 orders, maintaining the spectral shape and level. This is because boiling is the dominant speckle motion and the correlation time is independent of the number of speckles collected. This is also evident in equation (4.13) when the speckle translation term, σD , is much less than the aperture dimension in the direction of the speckle translation L_d . Often the beam will be focussed, or near to being focussed, on the surface under scrutiny. The radius of curvature will therefore, in general, be large and speckle boiling will more often than not dominate the decorrelation.

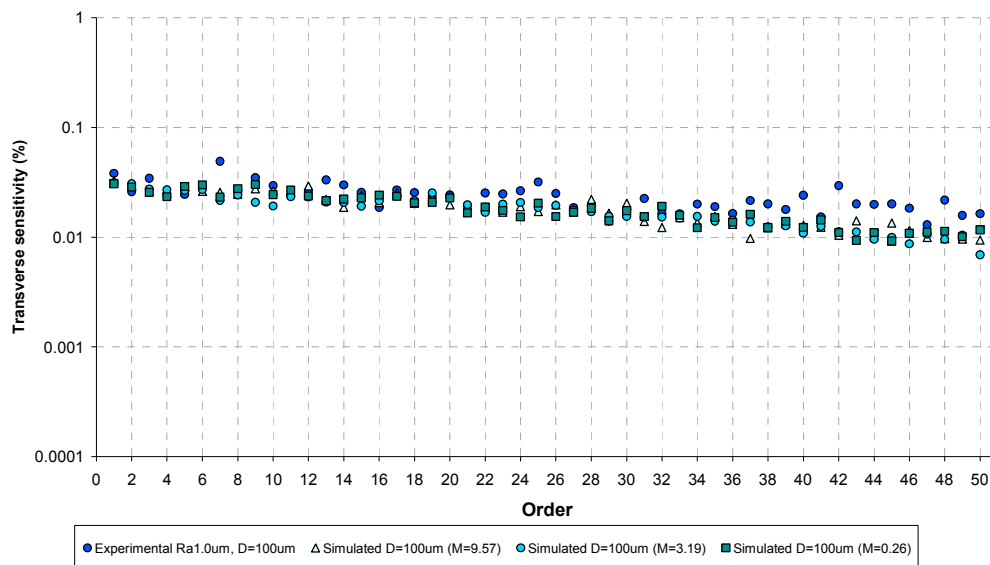


Figure 7.18 – Transverse sensitivity when altering the aperture to speckle size ratio, M

$D = 100\mu\text{m}$, Simulated ($T=0.02$)			
<i>Transverse sensitivity: apparent velocity per unit transverse velocity (%)</i>			
<i>Aperture to speckle size ratio, M</i>	$M=0.26$	$M=3.19$	$M=9.57$
<i>Mean level by order (orders 1-10)</i>	0.027	0.026	0.027
<i>Standard deviation (orders 1-10)</i>	0.020	0.020	0.021
<i>Total RMS level across 50 orders</i>	0.13	0.14	0.13

Table 7.3 – Transverse sensitivity estimations for various aperture dimensions for the laser vibrometer with a $100\mu\text{m}$ beam diameter. The speckle translation distance is maintained at $T=0.02$

The simulation also offers the ability to observe what happens to the expected levels of transverse sensitivity when speckle translation dominates the decorrelation. This can occur if the radius of curvature is small comparably with the standoff distance. Figure 7.19 and Table 7.4 present evidence for estimations of speckle noise when translation becomes dominant. The beam diameter on the surface is maintained at $100\mu\text{m}$. The aperture dimension is kept constant, at $M = 0.26$ (1mm), and the radius of curvature is altered. Altering the radius of curvature changes the distance of the speckle translation by altering the speckle gearing term, σ . Realistically, the beam diameter would likely alter as the radius of curvature is changed but, for the purposes of this analysis, the beam diameter is kept constant. The radius of curvature takes values of -600mm, 660mm, 5mm and 1mm causing the speckle translation term T to take values of 0, 0.02, 2.5 and 12.4 respectively. When speckle translation dominates, speckles enter and leave the aperture without

decorrelating. This causes speckle translation to dominate the decorrelation on the photodetector. It can be seen that as the speckle translation term increases, the expected level of speckle noise also increases. When T is small ($T = 0$ and $T = 0.02$), boiling remains the dominant speckle motions for the decorrelation. When $T = 2.5$ or $T = 12.4$ speckle translation dominates and speckle noise increases. This is consistent with the theory presented in Chapter 4. Observation of equation (4.13) shows that when speckle translation increases, the correlation time will reduce and, therefore, speckle noise is expected to increase. The radius of curvature required to achieve a value of 12.5 for T is 1mm. This radius of curvature, being so small, is generally beyond realistic possibility but it is used here to illustrate the maximum transverse sensitivity that might be expected for an optically rough surface.

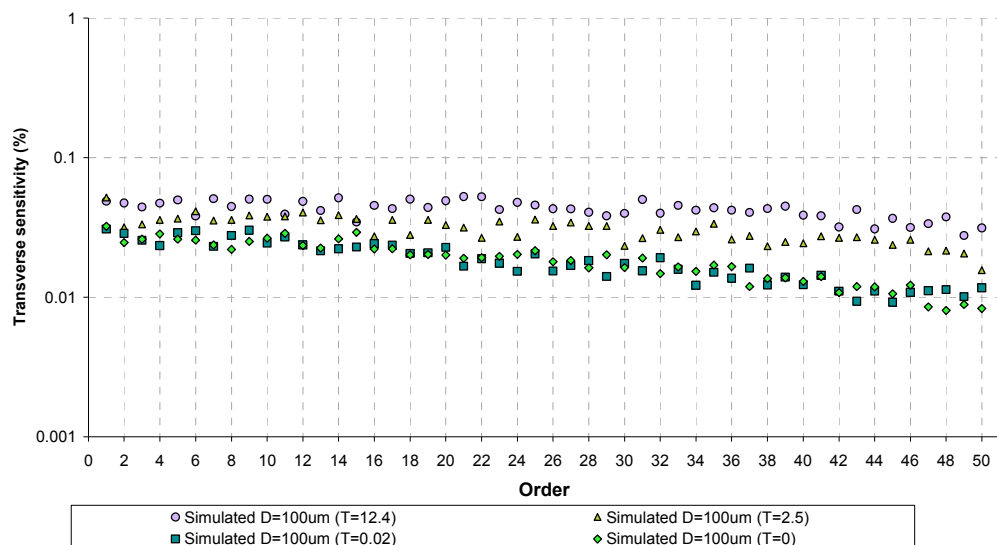


Figure 7.19 – Transverse sensitivity estimations for various speckle translation distances, varying T while M remains constant at 0.26

$D = 100\mu\text{m}$, Simulated ($M=0.26$)				
<i>Transverse sensitivity: apparent velocity per unit transverse velocity (%)</i>				
<i>Speckle translation to speckle size ratio, T</i>	$T=0$	$T=0.02$	$T=2.5$	$T=12.4$
<i>Mean level by order (orders 1-10)</i>	0.026	0.026	0.038	0.047
<i>Standard deviation (orders 1-10)</i>	0.020	0.020	0.030	0.036
<i>Total RMS level across 50 orders</i>	0.14	0.13	0.22	0.30

Table 7.4 –Speckle noise estimations for various speckle translation distances while maintaining the aperture size at $M=0.26$

The speckle translation distance, governed by the beam diameter and the radius of curvature, will always be limited by the beam geometry. Equation (4.13) suggests that, as the speckle translation distance continues to increase, the correlation time and consequently, speckle noise can be limited by the aperture dimension. Figure 7.20 and Table 7.5 present evidence that, if the aperture dimension were increased so translation no longer dominates, speckle noise can be reduced. The aperture dimension is set at $M = 3.19$ and the speckle translation is controlled to take the same values as those presented in Figure 7.19. For this scenario $T = 2.5$ means speckle boiling dominates and the resulting speckle noise is reduced. Comparing Figure 7.20 to Figure 7.19 shows that increasing the aperture dimension beyond the speckle translation distance can reduce speckle noise levels.

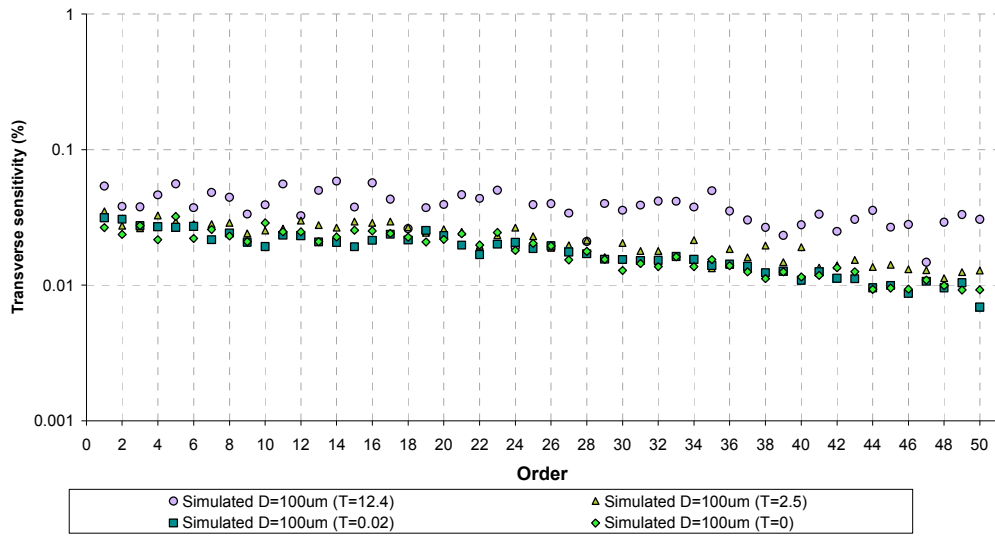


Figure 7.20 – Transverse sensitivity estimations for various speckle translation distances, varying T while M remains constant at 3.19

$D = 100\mu\text{m}$, Simulated ($M=3.19$)

Transverse sensitivity: apparent velocity per unit transverse velocity (%)

Speckle translation to speckle size ratio, T	$T=0$	$T=0.02$	$T=2.5$	$T=12.4$
<i>Mean level by order (orders 1-10)</i>	0.025	0.026	0.029	0.043
<i>Standard deviation (orders 1-10)</i>	0.018	0.020	0.021	0.038
<i>Total RMS level across 50 orders</i>	0.14	0.13	0.16	0.28

Table 7.5 - Speckle noise estimations for various speckle translation distances while maintaining the aperture size at $M=3.19$

The speckle translation, presented in Tables 7.4 and 7.5, of 12.4 speckles, is beyond that likely to be encountered in a practical situation. Therefore, from this, it is reasonable that the transverse sensitivity can be expected to fall below 0.04% for a beam diameter of 100 μ m. If speckle translation dominates the decorrelation, increasing the aperture size can cause speckle boiling to dominate the decorrelation which reduces transverse sensitivity. Section 7.1.4.1 showed that speckle noise can be significantly reduced if a larger beam diameter is used. However increasing the beam diameter reduces the total light intensity collected and could make a measurement impractical. The beam diameter can be increased by defocusing the beam on the surface. Defocusing the beam will change the speckle translational characteristics and if the translation becomes significant speckle noise levels could potentially increase. If defocus is necessary then it would be recommended to focus the beam beyond the surface so the beam is convergent. This illuminates the surface with a beam that has a negative radius of curvature which gives a little more tolerance for keeping transverse sensitivity at a lower level.

7.2 Tilt sensitivity simulator

The simulator is written to model speckle noise from a laser vibrometer when a ‘measurement’ is taken from an optically rough surface which tilts around an axis perpendicular and intersecting the optical axis. The tilting motion causes the speckles to predominantly translate across the receiving aperture. The changing population of speckles in the aperture alters the amplitude and phase of the Doppler signal which ultimately manifests in the output of the laser vibrometer as speckle noise. The behaviour of the speckles concentrate on the key aspects of the mechanism producing speckle noise in a laser vibrometer. The translation is modelled by translating the receiving aperture across a matrix of simulated speckles.

7.2.1 Formation of a simulated speckle

Unlike section 7.1.1 where speckle evolution was required, translation is the only speckle motion considered and the structure and composition of the simulated speckle remain fixed during the surface motion. The intensity and phase of each speckle are therefore developed from the appropriate properties of a stationary speckle discussed in Section 2.2 rather than by combination of individual random phasors. The normalised intensity of a speckle, $I/\langle I \rangle$ is produced using a random number, $rnd\#$, distributed uniformly between 10^{-10} and 1 in the form

$$\frac{I}{\langle I \rangle} = -\ln[rnd\#] \quad (7.9)$$

where $\langle I \rangle$ is the mean intensity. The lower limit of the random number generator, 10^{-10} , prevents the evaluation of $\ln[0]$ and limits the distortion of the probability distribution. The phase of each simulated speckle is generated using a separate random number generator operating uniformly between $-\pi$ and π . A program is used to create 25,000 simulated speckles to confirm the statistical distribution of the intensity, phase and for completeness the amplitude. Figure 7.21 (a) shows the histogram of the intensity together with the expected probability distribution shown in red. Figure 7.21 (b) shows the phase distribution and Figure 7.21 (c) shows the amplitude. Figure 7.21 (a) to (c) present evidence that the simulated speckles conform to the appropriate statistics discussed in Section 3.2.

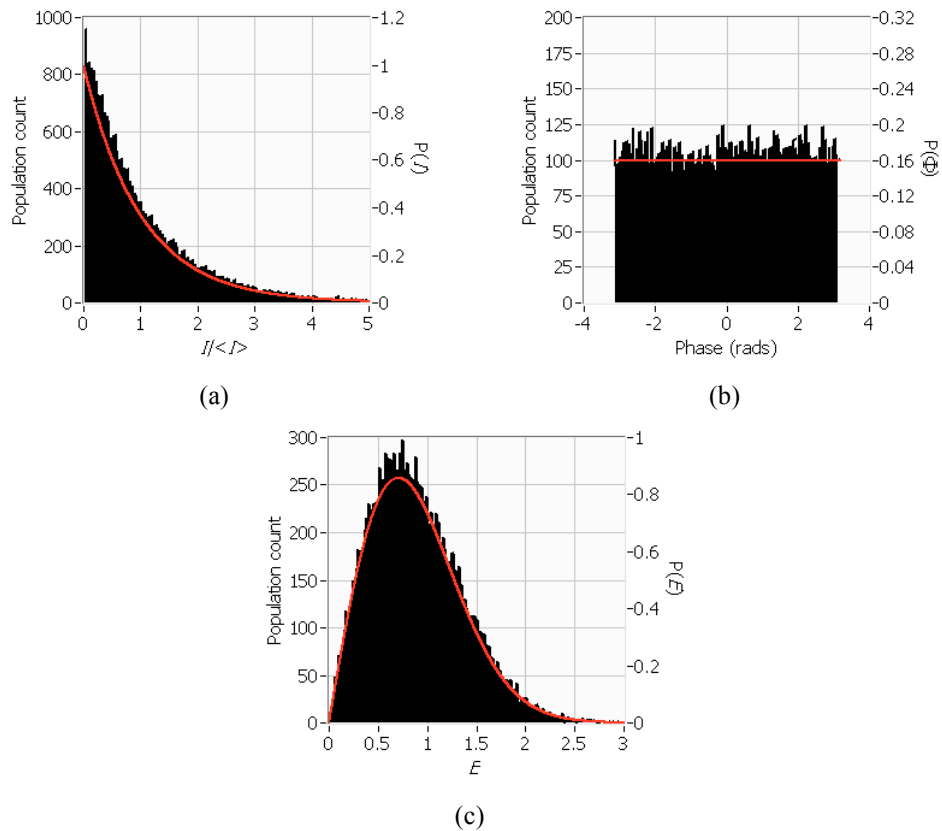


Figure 7.21- Statistical distribution of 25,000 simulated speckles (black) together with the expected probability density functions (red). (a) Intensity distribution; (b) Phase distribution; (c) Amplitude distribution

7.2.2 Modelling a speckle pattern

Figure 7.22 illustrates the relation between the process of physical scattering to the model of a speckle pattern in the simulation. An optically rough surface tilts about an axis which is perpendicular to and intersects the optical axis. The incident laser beam has a Gaussian intensity profile. The scattered beam, in reality, produces a speckle pattern like that identified by the real speckle pattern. The real speckle pattern is a profile taken from an image of a speckle pattern. As in Section 7.1.2, the model simplifies the continuous profile that

would be created by a real speckle pattern by splitting it up into discrete regions or speckles. An example of a discretised version of the real speckle pattern is illustrated by the simulated speckle pattern. The speckle pattern is collected by a receiving aperture whether that is in the form of a lens or a photodetector and the intensity is measured.

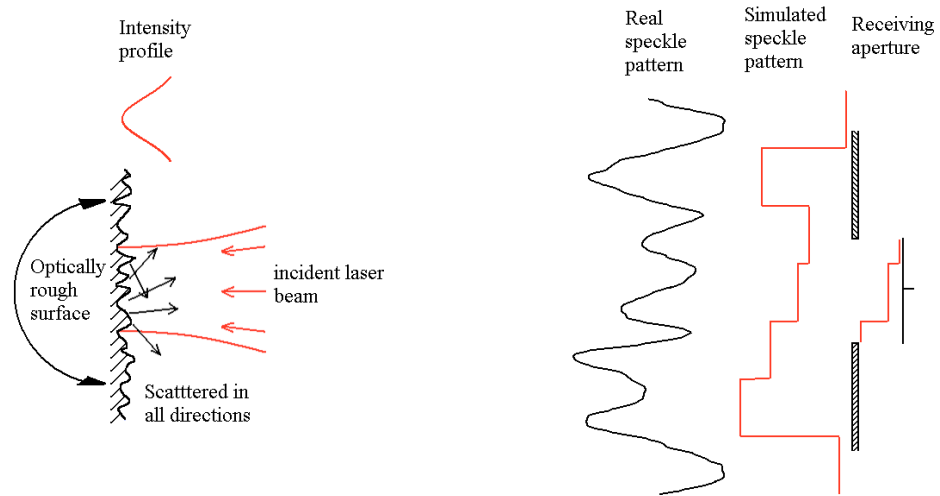


Figure 7.22 – Modelling the speckle pattern

7.2.2.1 Speckle size

The simulated speckles must also be of an appropriate size, as discussed previously in Section 7.1.2.1. The intensity and phase of each speckle is uniform across its extent. The speckles maintain a regular shape and size with a constant amplitude and phase across their extent. Their shape is square and the size of each simulated speckle is calculated using the average speckle size, as shown by equation (3.24).

7.2.2.2 The detector size

As in Section 7.1.2.2, the detector is square and its width depends on the vibrometer configuration under scrutiny. When the vibrometer has no focussing lens the detector size is taken directly as the physical dimension of the photodetector. When the vibrometer has a lens, the detector dimension is taken as the width of the beam emerging from the lens. The number of speckles in the aperture, M , depends on the speckle size at that standoff distance and the physical dimension of the aperture.

7.2.2.3 Simulating the Doppler signal

The simulation takes user inputted optical parameters, (beam diameter; receiving aperture width; standoff distance), measurement parameters (number of points per oscillation; number of oscillations) and target parameters (vibration frequency; angular displacement amplitude). Using these parameters the simulation determines the dimensions of a matrix of simulated speckles to be created. The matrix is sufficient in size to accommodate the whole number of speckles expected in the size of the receiving aperture and the speckle translation distance for the whole cycle of the surface motion. In the same manner as that shown in Section 7.1.2 and as illustrated in Figure 7.6, the speckle positions are disrupted in their presentation to the receiving aperture. The irregular positioning of the speckles disrupts the otherwise regular presentation of the simulated speckles to the receiving aperture. As the receiving aperture translates across the simulated speckle pattern matrix the resultant phase and amplitude of the Doppler signal change. The Doppler signal characteristic are again calculated using equation (7.2), equation (7.5) and equation (7.8). The simulated speckle noise is found from the change in the

resultant phase over time in accordance with $\frac{1}{2k} \frac{d\Phi_{res}(t)}{dt}$ as discussed in Section 7.1.2.3.

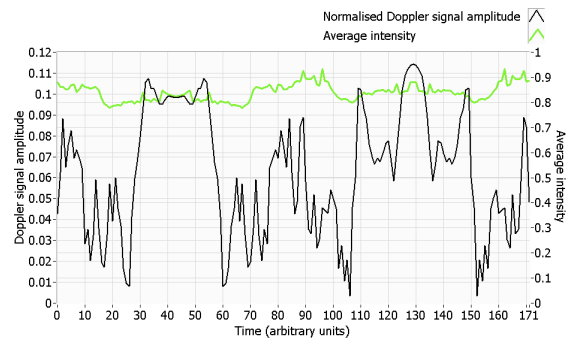
7.2.3 Simulating speckle dynamics

When a surface tilts about an axis which is perpendicular to and intersects the optical axis, the speckles at the detector exhibit translation with negligible evolution. Evolution would exist because the profile of the beam transits from an elliptical shape through to circular and therefore would modify the surface scattering. However the angular motion is generally less than a few degrees and the change to the scattering elements being illuminated is negligible. This is confirmed in chapter 6 and it is, therefore, reasonable to assume the speckle translation is the dominant speckle motion. A speckle translates by an amount $4\theta z_S$ in a plane a distance z_S away when the surface tilts through an angle 2θ [7.2] as seen in Section 4.1.2.

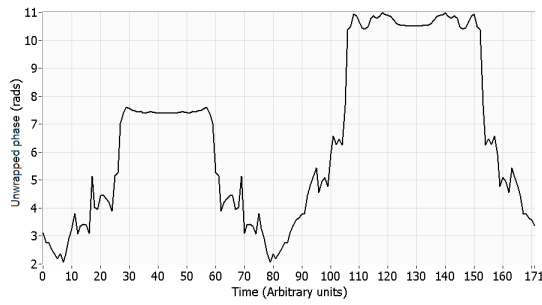
7.2.4 Tilt sensitivity using the simulator

Estimations of tilt sensitivity from the simulator are made using the same configurations as those for the experimental estimations discussed in Chapter 5. The target surface vibration parameters and the measurement parameters are kept constant throughout the simulations. The optical parameters vary depending on the particular vibrometer configuration being investigated. The two configurations being investigated vary the beam diameter from 100 μm to 600 μm , the standoff distance from 600mm to 700mm and the receiving aperture from 12mm to 1mm respectively. The surface tilts by 0.78° rms which causes the speckles to translate about 45mm and 54mm at the receiving apertures for the different configurations respectively. Figures 7.23 (a) to (d)

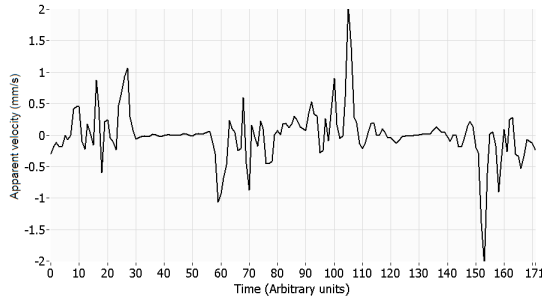
show examples of the temporal data produced by the simulation for one period of oscillation of the surface. Figures 7.23 (a) and (b) show the sequence of changes in Doppler signal amplitude and phase as a result of the speckle motion. The target is modelled to move in a sinusoidal form, which causes the speckles to translate back and forth over the receiving aperture. As discussed in Section 7.1.4, the periodic motion causes the sequence of amplitude and phase changes to appear to reflect and change sign about instances in time when the surface and hence speckles are stationary. Figure 7.23 (c) shows the resulting apparent velocity over the period of oscillation caused by the changes in phase shown in Figure 7.23 (b). In a similar fashion to that shown in Section 7.1.4, the most significant changes in phase, evident by the larger speckle noise peaks in Figure 7.23 (c), occur simultaneously with rapid changes in Doppler signal amplitude from a low level. These large speckle noise peaks occur most often around periods in time where the surface speed is highest, shown in Figure 7.23 (d). It is also evident that these peaks due to speckle noise are not as a consequence of low light amplitude. Figure 7.23 (a) also presents a trace of the average light intensity providing an indication of the quality of the simulated light signal level. At the time instances around these peaks the average light intensity is not significantly altered. This shows that speckle noise is not a signal quality issue and the more rapid changes in phase and low Doppler signal amplitude are more likely due to an unfavourable collection of speckles. This indicates that irrespective of the average light levels received, which can be increased with higher laser power or by applying treatments to the surface, speckle noise will still be a significant problem.



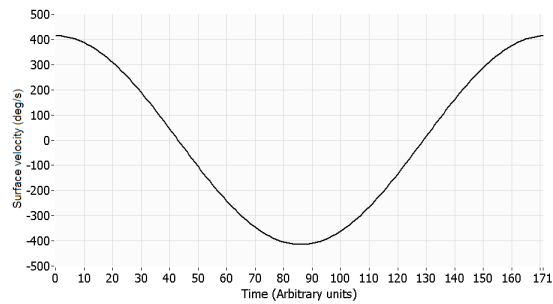
(a)



(b)



(c)



(d)

Figure 7.23 – (a) Doppler signal amplitude and the average intensity for one whole cycle, (b) Unwrapped phase of the Doppler signal for one whole cycle, (c) Apparent velocity for one whole cycle, (d) Tilt surface velocity for one whole cycle

The simulator is used to estimate tilt sensitivity, for comparison with experimental data presented in Chapter 5. The optical parameters, measurement parameters and target parameters for the simulation are matched to the experimental arrangement. The resulting data is analysed in the same manner as the experimental data. The estimations of tilt sensitivity are shown in Figure 7.24 and Table 7.7. The data points of the tilt sensitivity, for the simulator, are made from averages of 50 simulations allowing a statistical comparison. The temporal speckle noise data are produced for direct comparison with experimental data. The appropriate frequency bandwidth is chosen, the data are Fourier transformed and the ‘picket fence’ effect is compensated for. The peak values of the first 50 orders of the vibration frequency are found and an average is calculated for each order. Standard deviations are also calculated but not shown in Figure 7.24 for clarity of presentation.

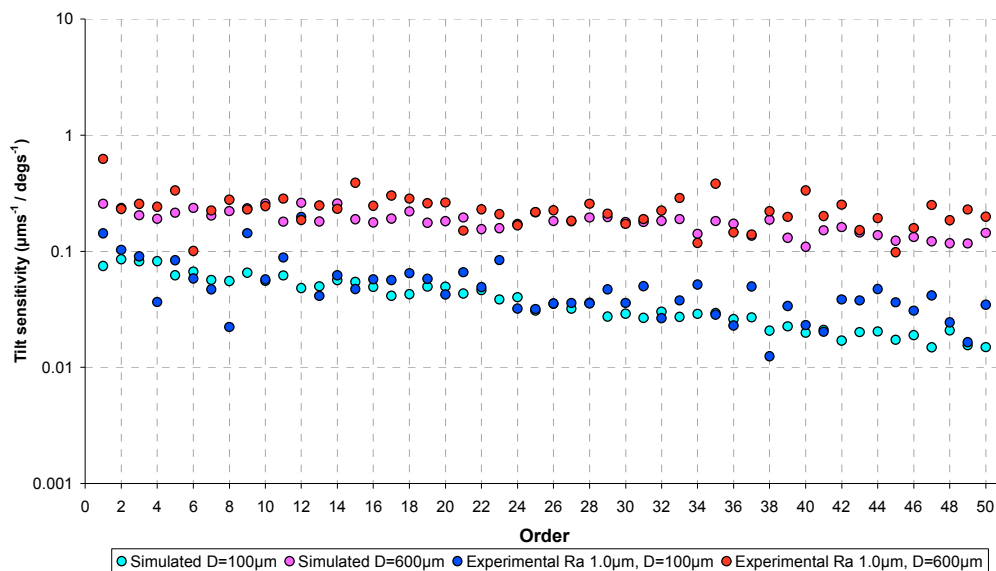


Figure 7.24 – Comparison of simulated estimates to experimental estimates of speckle noise

Table 7.7 shows a simplified comparison of the data in Figure 7.24. The values are presented in two ways, one showing the tilt sensitivity (per order) from the mean of the first 10 orders (likely to be of interest to the vibration engineer) the second showing the total rms for the first 50 orders. The estimations of tilt sensitivity produced by the simulations presented in Table 7.7 show good agreement with the estimations of tilt sensitivity produced by the experiments. The experimental values are taken from the surface with Ra 1.0 μm , which is expected to produce a fully developed speckle pattern.

<i>Tilt sensitivity: apparent velocity per unit angular velocity ($\mu\text{ms}^{-1} / \text{degs}^{-1}$)</i>		
<i>Surface finish</i>	Simulation	Experimentation
$D = 600\mu\text{m}$		
<i>Mean level by order (orders 1-10)</i>	0.22	0.28
<i>Standard deviation (orders 1-10)</i>	0.17	0.16
<i>Total level across 50 orders</i>	1.3	1.7
$D = 100\mu\text{m}$		
<i>Mean level by order (orders 1-10)</i>	0.069	0.078
<i>Standard deviation (orders 1-10)</i>	0.053	0.064
<i>Total level across 50 orders</i>	0.31	0.44

Table 7.6 – Speckle noise estimations, comparing those produced by the simulation with those produced through experimentation

Experimental estimations predict tilt sensitivity harmonics to be around 0.28 $\mu\text{m/s}$ per deg/s and the simulator estimates tilt sensitivity to be 0.22 $\mu\text{m/s}$ per deg/s for 600 μm beam over the first 10 orders. The total rms level for 600 μm beam diameter has been predicted at 1.7 $\mu\text{m/s}$ per deg/s by the experimental evaluations and 1.3 $\mu\text{m/s}$ per deg/s by the simulator. For 100 μm beam, the experimental predictions estimate the harmonic levels to be around 0.078 $\mu\text{m/s}$ per deg/s and the simulation predicts 0.069 $\mu\text{m/s}$ per deg/s over the first 10 orders. The total rms level for 100 μm beam diameter has been predicted as 0.38 $\mu\text{m/s}$ per deg/s by the experimental evaluations and 0.27 $\mu\text{m/s}$ per deg/s by the simulator. The simulator predicts marginally lower values but shows good consistency with the experimental results. The simulator shows consistency for the different beam diameters predicting lower tilt sensitivity levels for the smaller beam configuration falling in line with results observed in the experiments. Tilt sensitivity reduces as the vibration order increases and illustrates a spectral roll off which is comparable to the experimental.

7.3 Understanding gained from the simulations

The simulations have confirmed that when a surface tilts, speckle translation needs only to be considered in the motion of speckles. When a surface moves transverse to the optical axis of the beam, speckles evolve and translate. The simulations showed a novel approach to modelling speckle evolution. This was successful and verified with the experimental results detailed in Chapter 5. The rate of speckle decorrelation, when modelling speckle evolution, can be considered from the width of the beam (in the direction of the surface motion) relative to the surface motion. Modelling speckle evolution requires changing a summation of a population of phasors. A simple interpolation routine was investigated but it was found that this introduced artefacts into the speckle

noise data. This was evident by sudden changes in the Doppler signal at instances of transition from the predefined speckles. The Gaussian profile of the beam should be considered in a speckle evolution routine. This provides more appropriate transition times when exchanging phasors in the summation. The rate of speckle translation (for the life of a correlated speckle and when the beam is focussed on the surface) can simply be equated to that of the surface motion. The simulations have shown that speckles can be modelled in a simple way. They can be made the same size, which is in accordance with the expected size from statistics, and can be considered as square entities. This shows that the variations in size and shape of speckles in a real speckle pattern are insignificant when simulating pseudo-vibration. The transition across speckle entities is performed using a routine which integrates over a region of a speckle pattern. For the transverse sensitivity simulator the speckle pattern also evolves at a rate which is in accordance with the statistics detailed in Chapter 4 and allows partial phasor exchanges. These factors generate speckle transitions which concentrate on the fundamental mechanisms of speckle dynamics and have shown good agreement with experimental data.

The simulations have shown their ability to predict pseudo-vibration sensitivities for different sized laser beam spots and these compare well with experimental results. The difference in transverse sensitivity, modelled by the simulation, for the different beam spot sizes is consistent with that found by experimentation showing a difference by a factor of about 4 over the first 10 orders. The estimations of tilt sensitivity have predicted a difference by a factor of approximately 3.2 (for the first 10 orders) for the two beam spot sizes investigated. This is consistent with experimentation which estimates the same factor as approximately 3.6.

The simulator (for transverse sensitivity) has shown that the number of speckles collected in the aperture of the vibrometer does not make a difference to transverse sensitivity because speckle evolution, generally, is the dominant speckle motion. The simulator has demonstrated that if speckle translation is the dominant speckle behaviour (within the confines of the vibrometer aperture) then an increased aperture can reduce transverse sensitivity.

The simulations modelled the speckle intensity using the expected statistical distributions shown in Chapter 3. The dynamics of the speckles, in the simulations, have been modelled using the statistics, based on intensity, detailed in Chapter 4 and experimentally investigated in Chapter 6. Modelling the speckle dynamics

The simulators have shown that large changes in speckle noise are driven by large changes in phase which often occur simultaneously with large changes in the Doppler signal amplitude from a low level. It has been demonstrated that low Doppler signal amplitude is more often as a result of the summation of speckles on the photodetector rather than low mean light levels.

8 Conclusions and recommendations for further work

8.1 Introduction

This thesis has addressed the uncertainty in laser vibrometry due to the phenomenon known as speckle noise. Speckle noise is generated from the motion of laser speckle on the photodetector of a laser vibrometer. This motion can take on two forms, translation or evolution, but is more generally a combination of the two. The speckle motion phase-modulates the Doppler signal ultimately adding what is termed ‘speckle noise’ to the vibrometer output signal. Speckle noise occupies a broad frequency range. When target motions are periodic (as is often the case in vibration measurements) speckle noise is pseudo-random. This causes noise components at frequencies generally of interest to the vibration engineer (fundamental target motion frequency and many harmonics) and has historically been termed ‘pseudo-vibration’. Pseudo vibration can be indistinguishable from genuine surface vibrations, which necessitates careful data interpretation by the vibration engineer. Until now little was known quantitatively about the uncertainty due to pseudo-vibration.

The surface motions of greatest interest are transverse (translation oscillation in a direction perpendicular to the laser beam direction), tilt (angular oscillation around an axis in a direction perpendicular to the laser beam direction) and rotation (continuous motion around an axis perpendicular to the laser beam direction). Pseudo-vibration is known to originate from motions of optically

rough surfaces. This thesis has shown that noise is present in the vibrometer output, even in measurements from optically smooth surfaces where the term speckle noise becomes inappropriate. Pseudo-vibration, historically, was solely associated with speckle noise, but this thesis has extended the definition of pseudo-vibration to encompass noise generated from all surfaces (including optically smooth surfaces). Users of piezo-electric accelerometers will be familiar with the term ‘transverse sensitivity’ which is enshrined in standards and the equivalent terminology for laser vibrometers has been developed in this thesis. Collectively, the sensitivities to all the motion types (transverse, tilt and rotation) for any surface roughness or treatment are now referred to as ‘pseudo-vibration sensitivities’.

The early part of this thesis described speckle noise, from a user’s perspective, identifying how it generates uncertainty in measurements with a laser vibrometer. Chapter 2 presented the novel measurement of dynamic backlash using two laser rotational vibrometers. Despite the inherent speckle noise content, exacerbated by the differential technique, the measurement was made successfully. Understanding the fundamentals of the formation and the behaviour of speckles in response to the particular surface motions was investigated using published literature.

Pseudo-vibration sensitivities have been quantified by experimentation. Specially designed experimental rigs were produced (isolating specific target surface motions: transverse, tilt and rotation) and procedures developed to measure pseudo-vibration. The first of two methods to calculate pseudo-vibration sensitivities included an independent simultaneous measurement of genuine velocity. This was subtracted from the measured velocity to produce an apparent velocity, dominated by noise, from which pseudo-vibration sensitivities are calculated. The second method was developed for situations

where the measurement of genuine velocity cannot be obtained. In this case, two laser vibrometer measurements are made simultaneously using identical instruments. The laser beams have identical alignment and are positioned as close together as possible without overlap. Subtraction of their outputs cancels common components such as genuine vibration and, for rotor measurements on smoother surfaces, shaft out-of-roundness and leaves only uncorrelated noise components. As a result of the subtraction, the resulting signal takes an rms level that is $\sqrt{2}$ times either of the individual rms levels. Scaling then produces the apparent velocity from which pseudo-vibration sensitivities are calculated. The processing techniques and appropriate methods for presentation were developed. Pseudo-vibration was normalised by the amplitude of the surface vibration velocity to give transverse and tilt sensitivities, and the rotation velocity to give rotation sensitivity. The pseudo-vibration sensitivities are presented as a map showing the spectral shape of the noise, as the mean and standard deviation of each harmonic peak in the map, and as a mean level per order and a total rms level across a defined bandwidth. A variety of surface finishes were used ranging from optically rough surfaces (Ra 1.0 μm) to smooth mirror-like surfaces (Ra 11nm) and also a surface treated with retro-reflective tape. Two laser beam spot diameters (90/100 μm and 520/600 μm) from commercial laser vibrometers were used. The effect of changes in vibration velocity amplitude and changes in vibration displacement amplitude were also investigated. The prime novelty in this investigation was the quantification of the pseudo-vibration sensitivities, which are immediately useful as a resource to the vibration engineer.

After developing the methods and quantifying the pseudo-vibration sensitivities, the thesis continued by explaining more about the mechanism generating speckle noise. Actual speckle patterns and their behaviours for particular surface motions were observed and analysed. Relationships between

the motions of the speckles (based on intensity) and the pseudo-vibration sensitivities were also investigated.

Numerical simulations of pseudo-vibrations were developed and transverse sensitivity and tilt sensitivity were quantified. The simulations modelled the formation of speckles and their dynamic behaviour in a simple way, using statistics of fully developed speckle patterns. The motions of the speckles were modelled to replicate those expected and observed in the experimental study. Reflecting the experimental study, two laser beam spot diameters (100 μm and 600 μm) were investigated in the simulations. Novelty in the simulations included modelling of the sinusoidal motion of speckles, the modelling of speckle evolution in the context of laser vibrometry and the development of partial speckle transition steps without the need to sub-divide speckles into arrays. The same processing techniques, developed for the experimental study, were employed in the simulations. The simulated pseudo-vibration sensitivities were verified by the experimental investigation.

8.2 Transverse surface motion and transverse sensitivity

Speckle evolution is generally the dominant speckle motion generating speckle noise. Speckle translation is apparent but generally less significant. The magnitude and direction of speckle translation can change by altering the focal point relative to the surface, but speckle evolution generally remains the dominant mechanism. Pseudo-vibration sensitivity has been shown to be directly proportional to the amplitude of surface vibration velocity (for a fixed displacement amplitude) but it increases with decreasing surface vibration displacement. The laser beam spot diameter has the greatest effect on the transverse sensitivity. Larger beam spot diameters lower the transverse sensitivity. The spectral shape of transverse sensitivity is generally flat with a

marginal roll-off across 50 orders. Transverse sensitivity has been quantified as approximately 0.01% (per order for the first 10 orders) for a 600 μm beam spot diameter and for 100 μm beam spot diameter at about 0.03% (per order for the first 10 orders). In the range of surfaces investigated this difference varies by a factor of about 0.8 to 4. This also represents a marked superiority of the laser vibrometer over an accelerometer for transverse sensitivity which is often quoted as in the region of a few percent (<4-5%).

If the amplitude of the surface vibration displacement is less than the beam spot diameter, however, lower orders of the transverse sensitivity increase and the spectral roll-off also increases. A reduction in surface displacement amplitude by a factor of 8 has been shown to increase the transverse sensitivity (over the first 10 orders) by a factor of 2. Surface finish does not make a great deal of difference to the transverse sensitivity. Measurements from optically smoother surfaces (Ra 75nm) creating partially developed speckle patterns show similar transverse sensitivity to fully developed speckle patterns (Ra 1.0 μm and retro-reflective tape). However, for a smaller beam, optically smooth surfaces (Ra 11nm) have been shown to reduce transverse sensitivity by a factor of 3 to 4, in comparison to optically rougher surfaces. Increasing the beam diameter (specifically in the direction of the surface motion) has been shown to reduce transverse sensitivity. The method employed introduced an aperture in the laser beam path, which caused a reduction in sensitivity by $\frac{1}{2}$. The simulations of pseudo-vibration from a transverse surface motion have shown that speckles and their behaviour can be modelled in a simple way, agreeing well with experimental results. Simulations have shown that, because speckle evolution is dominant, any change to the size of the photodetector or number of speckles collected will make no difference to transverse sensitivity. Only when speckle translation is comparable to the photodetector size is

transverse sensitivity increased, but this is unlikely in general application with transverse surface motion.

8.3 Tilt surface motion and tilt sensitivity

Speckles predominantly translate with negligible evolution. The laser beam spot diameter has the greatest effect on the transverse sensitivity. Smaller beam spot diameters lower the transverse sensitivity. The spectral shape of tilt sensitivity is reasonably flat but less so for smaller beam spot diameters. The small beam diameter increases the size of the speckles. This causes slower phase changes which reduces speckle noise levels particularly at higher orders. Surface finish makes no significant difference to the tilt sensitivity. Retro-reflective tape has shown a modified speckle effect (based on intensity) to other optically rough surfaces, with more emphasis on the speckles in the central region of the Airy disc. Ultimately the mechanism generating speckle noise is unchanged and, therefore, this has resulted in little effect on the tilt sensitivity. Tilt sensitivity has been quantified as $0.1 \mu\text{ms}^{-1} / \text{degs}^{-1}$ (per order for the first 10 orders) for $100\mu\text{m}$ beam spot diameter, $1/3^{\text{rd}}$ of the tilt sensitivity from using a beam spot diameter of $600\mu\text{m}$ which has been quantified as $0.3 \mu\text{ms}^{-1} / \text{degs}^{-1}$ (per order for the first 10 orders). Simulations of tilt sensitivity have showed good agreement with experimental results. They have confirmed that speckle translation is the dominant speckle behaviour and tilt sensitivity can be estimated by modelling this speckle motion.

8.4 Rotation and rotation sensitivity

Speckle translation has been observed as the dominant regime, consistently with the larger beam and with small shaft diameters and when focussing on the

rotation axis with the small beam. However, qualitative observations have shown a significant evolution when the shaft diameter is increased and the smaller beam is focussed on the surface.

The laser beam spot diameter has the greatest effect on the rotation sensitivity. Smaller beam spot diameters lower the rotation sensitivity. Spectral shapes are generally flat but do have a marginal roll-off as the order increases. Shaft out-of-roundness has been shown to be a source of uncertainty in measurements of rotation sensitivity. This has been shown to affect lower orders of the spectrum of pseudo-vibration. The mean rotation sensitivity is therefore calculated from higher orders (41-50) which are not influenced by shaft out-of-roundness, utilising the flat spectral shape.

Rotation sensitivity increases with increasing shaft diameter, but is not directly proportional to it. Increasing the shaft diameter from 15mm to 110mm (whilst focussing the beam on the surface) has shown an increase in rotation sensitivity by a factor of approximately 2. For a 15mm diameter shaft, rotation sensitivity has been quantified at approximately $0.5 \mu\text{ms}^{-1} / \text{rads}^{-1}$ and for a 110mm diameter shaft rotation sensitivity has been quantified at approximately $1.0 \mu\text{ms}^{-1} / \text{rads}^{-1}$. Focussing the laser beam to near to the rotation axis of the shaft, rather than on its surface, has shown a reduction in rotation sensitivity, with a greater effect observed with measurements from larger shaft diameters. Focussing the smaller beam on the rotation axis of a 110mm diameter shaft presents a great advantage over using a larger beam focussed on the surface of the same shaft with an estimated reduction in rotation sensitivity by a factor of approximately 5. This reduction is likely to continue to increase as the shaft diameter increases further.

Surface finish affects rotation sensitivity and, generally, measurements on optically smoother surfaces show lower rotation sensitivity. An optically smooth surface (Ra 11nm) has shown a reduction by a factor of over 5 to that from a surface with Ra 1.0 μ m or to more than 7 of that from retro-reflective tape.

Rotation sensitivity in a measurement using a beam spot diameter of 90 μ m has been quantified up at to 0.6 μ ms⁻¹ / rads⁻¹ which is less than ½ of that from a 520 μ m beam spot diameter which has been quantified at as much as 1.4 μ ms⁻¹ / rads⁻¹.

The principles used in the single beam measurements can readily be employed to quantify rotation sensitivity for parallel beam vibrometer arrangements. Measurements of rotation sensitivity were only possible on surfaces with retro-reflective tape. Rotation sensitivity for a torsional measurement using beam spot diameters of 520 μ m has been quantified as 0.016 degs⁻¹ / rads⁻¹ per order.

Table 8.1 provides a quick reference summarising the pseudo-vibration sensitivities, observed methods which modify the magnitude and their associated factors. This table is immediately useful to the vibration engineer.

<i>Pseudo-vibration sensitivity</i>	<i>D = 100μm</i>	<i>D = 600μm (factor of D = 100μm)</i>	Observations and effect on pseudo-vibration sensitivity
<i>Transverse sensitivity</i>	0.03 %	3	Smooth surface (Ra 11nm) – 1/3 1mm aperture – 1/2
<i>Tilt sensitivity</i>	0.1 μms ⁻¹ / degs ⁻¹	1/3	-
<i>Rotation sensitivity</i>	0.6 μms ⁻¹ / rads ⁻¹	2 1/3	Smooth surface (Ra 11nm) – 1/7 Shaft diameter – 2 Focus to rotation axis instead of surface (110mm shaft diameter) – 3/5
<i>Parallel beam Rotation sensitivity</i>	-	0.016 degs ⁻¹ / rads ⁻¹	-

Table 8.1 - Quick reference for pseudo-vibration sensitivities

8.5 Recommendations for further work

This thesis has tackled important issues in laser vibrometry. The following subsections highlight areas of research to take this work forward. Chapter 6 analysed dynamic speckle based on intensity and this work can be taken further to improve understanding of the fundamental mechanisms generating speckle noise. The procedures and techniques to quantify pseudo-vibration can easily be extended to other configurations (parallel beam vibrometers and scanning laser vibrometers). The pseudo-vibration sensitivities, presented in this thesis, are immediately useful, but an estimate of noise levels alongside a measurement would also be of great benefit to the vibration engineer. This study can be extended towards formulation of Standards having developed successful techniques and drawn out key issues.

8.5.1 Wavefront analysis of dynamic speckle

Chapter 6 observed speckle patterns and dynamic speckle using the intensity of the speckle field and the changes that occur as the surfaces move. Speckle noise is primarily due to phase changes in the region being measured by the photodetector. Therefore observation of the phase field would be more appropriate but this is far more challenging to measure. A Shack-Hartmann sensor may be able to do this. It uses a lens array and sensor array to quantify variations in wavefront by measuring displacements of focussed regions of the field. The lens array focuses regions of the field onto an array of sensors. If the wavefront is flat a spot is found in the centre of the sensor array. Angular variation in the wavefront at the lens causes the focus to deviate from the centre of the sensor array. Processing the data from the Shack-Hartmann sensor provides a discretised view of the wavefront field. It would be interesting to see whether this could provide a detailed view of the phase distribution of a speckle pattern. The size of the lenses would have to be less than the size of a speckle. This can be achieved by locating the sensor at a sufficient distance from the surface generating the speckle pattern. Using similar methods and tools adopted in Chapter 6, this could also provide valuable information about the mechanism generating speckle noise never before observed.

8.5.2 Pseudo-vibration sensitivities for parallel beam vibrometers

This thesis has concentrated on the pseudo-vibration sensitivities using a single beam laser vibrometer. It has also calculated the rotation sensitivity for a parallel beam laser vibrometer making a torsional vibration measurement, which is the most appropriate pseudo-vibration sensitivity of concern for a vibrometer with this configuration. This is because parallel beam laser vibrometers are generally used to measure torsional oscillation in rotating

shafts. However, parallel beam laser vibrometers can be used to measure any angular motion. Pseudo-vibration is present in measurements using parallel beam laser vibrometers and further work is required to measure in-plane rotation sensitivity (continuous motion around an axis parallel with the laser beam direction) and tilt sensitivity (angular oscillation around an axis perpendicular to the laser beam direction).

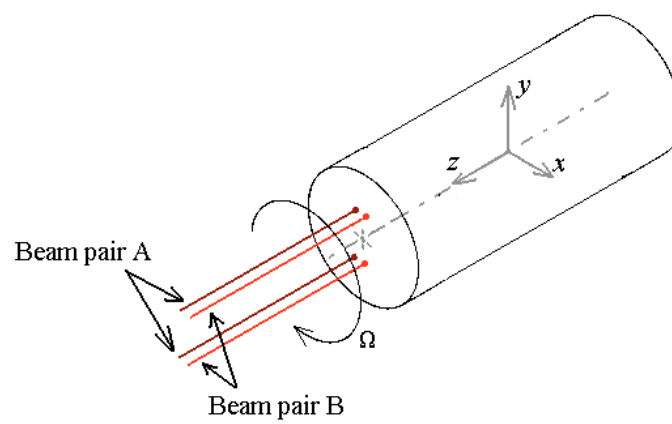


Figure 8.1 – Set-up for measurement of in-plane rotation sensitivity using parallel beam laser vibrometer

Figure 8.1 shows the set-up proposed to measure in-plane rotation sensitivity using parallel beam laser vibrometers. In-plane rotation sensitivity is applicable when a pitch or yaw measurement is required from the end of a shaft. In this case the pairs of beams are positioned centrally on the end of the shaft surface, aligned parallel and equidistant from the rotation axis of the shaft. Figure 8.2 shows the set-up to measure tilt sensitivity using parallel beam laser vibrometers. Tilt sensitivity is applicable in an angular measurement on a tilting surface. The pair of beams are generally positioned either side of the rotation axis. An important note is that, unlike all other pseudo-vibration sensitivities, tilt sensitivity (for parallel beam vibrometers) is coupled with the same motion it is intended to measure.

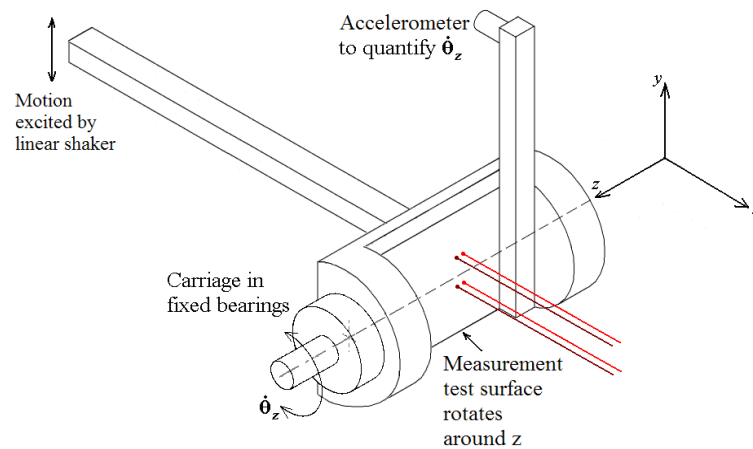


Figure 8.2 – Set-up for measurement of tilt sensitivity using parallel beam laser vibrometer

The procedures, outlined in this thesis (most appropriately the second method, using the difference in measured velocity from two laser vibrometers to calculate the apparent velocity), can be applied to quantify in-plane rotation sensitivity and tilt sensitivity.

8.5.3 Continuous scanning laser vibrometers

Scanning laser vibrometers can be used in a continuous scan mode to measure the vibration characteristics of a surface producing a continuous time resolved velocity measurement. However, the scanning of the surface will also cause speckle noise (and pseudo-vibration if the scan is periodic). Continuous scans are in the plane of the surface with the beam nominally perpendicular. Therefore, it is likely the speckle motions will be similar to that exhibited from a transverse surface motion. However, typical scan distances over the surface are likely to be much greater than the beam spot diameter and many more speckle decorrelations occur in the scan period than occur in the procedure for calculation of the transverse sensitivity presented in this thesis. When

comparing to transverse sensitivity (for laser vibrometers), this increased number of speckle decorrelation per period is likely to increase the spectral bandwidth and also increase the pseudo-vibration sensitivity. Pseudo-vibration will appear at the same frequency as the scan rate of the vibrometer and will also occupy many harmonics of that scan frequency. Scan frequency can be controlled so that it does not coincide with genuine vibration frequencies. It must be noted that the techniques used to scan the laser beam can also cause uncertainty at scan frequencies but this is not as a consequence of speckle noise. Scanning techniques involve the mechanical actuation of optical components. Either through slight laser beam misalignment with the optics or inherent design, Doppler shift of the laser beam occurs at the optics causing additional velocity components at scan frequencies. This is a topic of current research and would have to be accounted for or overcome in quantifying in-plane scanning sensitivity. One procedure to overcome this would be to move the surface rather than scan the beam and then either of the two experimental methods, described in this thesis, to quantify pseudo-vibration sensitivities could be employed. Scan distances would have to be taken into consideration as it has been shown that transverse sensitivity is not directly proportional to the displacement amplitude. As the scan distance increases, more speckle transitions would occur and the in-plane scanning sensitivity would increase.

Continuous scanning laser vibrometers can be used to track surface motions, for example scanning a turbine blade as it rotates. This can be done at a point or with a scan path across the surface. For tracking a point on the surface, pseudo-vibration is insignificant and the uncertainty that remains is due to Doppler shifts in the optical components. However, if the laser beam is scanned on a path across the surface as the blade rotates then pseudo-vibration can be a source of uncertainty especially if multiples of scan frequency coincide with rotation frequency. Components of pseudo-vibration and the

uncertainty due to the optical scan equipment as well as genuine vibrations (which often coincide with rotation frequencies) will all occur at the same frequencies. Evaluation of in-plane scanning sensitivity can address this issue by providing typical values associated with the scan distances required.

8.5.4 In-situ estimate of noise

Modification to a laser vibrometer's optical configuration to provide an in-situ estimate of speckle noise would provide an invaluable aid in data interpretation to the vibration engineer. By incorporating multiple photodetectors (at least two) which interrogate uncorrelated regions of the speckle field such an estimate can be made. The demodulated signals from these photodetectors will contain the same vibration velocity but uncorrelated noise components. Subtracting two of these signals will result in an estimate of RMS noise which is $\sqrt{2}$ of the RMS noise on either of the signals. This provides an estimate of the uncorrelated noise level in either demodulated signal. The resulting signal is not suitable for subtraction from either of the demodulated signals to leave genuine velocity, but the noise level estimate would indicate the level of noise in a measurement.

It is important for the speckle noise to be uncorrelated. For this to occur the photodetectors must be separated enough so they do not measure the same region of a speckle pattern and positioned so they are not coincident with the direction of speckle translation. Speckle size increases with stand-off distance and speckle translations can be in any direction in the plane of the photodetector. Therefore the separation distance and position of the photodetectors should be adaptable to compensate for this change and preclude measurements with correlated noise. The ramifications of introducing additional components and electronic hardware will increase manufacturing costs of the vibrometer.

However, incorporating an in-situ estimate of noise levels (and effectively pseudo-vibration sensitivities) is a feature that is not available in instruments that compete with laser vibrometers, such as accelerometers.

8.5.5 Standardising pseudo-vibration sensitivity for commercial laser vibrometers

It is common-place for transverse sensitivity to be quoted for accelerometers and International Standards are well established for manufacturers of accelerometers to produce such information [8.1]. It would be appropriate to make it standard practice for all laser vibrometer manufacturers to supply equivalent pseudo-vibration sensitivities with their instruments. As of yet, no equivalent International Standard is available or in development for laser vibrometers. Single beam translational laser vibrometers would require 3 pseudo-vibration sensitivities: transverse sensitivity; tilt sensitivity and rotation sensitivity. Parallel beam vibrometers can also be used in single beam mode and therefore would require the same pseudo-vibration sensitivities for single beam plus 3 more for their parallel beam mode (in-plane sensitivity, tilt sensitivity and rotation sensitivity).

This thesis has developed the procedures, processing techniques and methods of presentation to successfully quantify pseudo-vibration sensitivities. The methods employed could be further developed so manufacturers can provide equivalent information for their commercial laser vibrometers in a standardised way. This thesis has raised the key parameters to be considered in the measurement of pseudo-vibration sensitivity and these would need to be standardised. The design of the pseudo-vibration rig and tolerances on genuine velocities would have to be standardised. For transverse sensitivity and tilt sensitivity, displacement amplitude and surface flatness would need to be

standardised. The location of the laser beams focus position relative to the surface. For rotation sensitivity, it would be preferable to have a low shaft out-of-roundness (less than approximately 10 μ m) so lower orders can be used to quantify rotation sensitivity (despite the techniques that have been developed to minimise its effects in the rotation sensitivity). The location of the focal point of the laser beam relative to the rotation axis needs to be considered. For all pseudo-vibration sensitivities, parameters such as standoff distance, range of surface roughness, surface treatments, vibration frequencies and number of independent measurements should be standardised. In the processing and calculation of pseudo-vibration sensitivities the bandwidth and orders used to quantify mean sensitivity should be standardised.

The information offered by an International Standard on pseudo-vibration sensitivities would be useful to manufacturers and users. It would provide a greater understanding of the capabilities of the instrumentation and further means for comparison and promotion of the product in the commercial market. The customer would be able to make a more informed decision on the purchase of the equipment necessary to meet their needs. With a greater understanding of the capabilities of the laser vibrometer, the user can better assess the viability of data collection and its subsequent interpretation.

Appendix A

Algorithm overview

1. User inputted parameters are used to calculate the speckle size; the speckle translation distance and the total number of phasors to be created.
 - a. The speckle size is calculated using Equation (3.24)
 - b. The speckle translation distance is calculated using X_T in Section 4.2.1.
 - c. Total number of phasors is calculated from the sampling parameters ensuring at least one phasor is exchanged during the minimum surface displacement increment.
 - d. Size of the speckle matrix is calculated from the above parameters which specify the size of the speckle matrix in terms of time and space.
2. Using the parameters calculated in step 1. a triple nested loop generates the speckle matrix. Each phasor takes the form of an element shown by Equation (3.1).
3. A displacement function is generated for the convolution routine.
4. Speckle dynamics - evolution: Using Equation (7.6) the set of phasors is convolved with the displacement function which models the evolution.
5. Speckle dynamics - translation: The speckle translation is modelled by translating the photodetector across the evolving speckle pattern matrix using the speckle translation distance. At this point the speckle area

factor (calculated using Equation (7.8)) is also applied for every speckle.

6. Calculating the Doppler signal: The Doppler signal amplitude and phase are calculated by summing the speckles incident on the photodetector. These can also be calculated using Equations (7.2) to (7.5).
7. The apparent velocity is calculated from the derivative of the Doppler signal phase shown by Equation (2.2)
8. The Doppler signal amplitude; average intensity; Doppler signal phase; apparent velocity and surface velocity are output by the simulator.
9. Sensitivity is calculated from the spectrum of Apparent velocity as detailed in Section 5.2.1.

References

- [1.1.] Rothberg, S. J. (1994). Laser Speckle Studies for Vibration and Torque Measurement. Engineering and Applied Science. Southampton, University of Southampton.
- [1.2.] Pedrotti, F. L, Pedrotti, L. S (1996) Introduciton to Optics, 2nd edition. Prentice-Hall International.
- [1.3.] Gordon, J. D. R. E. I. (1962). "The granularity of scattered optical maser light." Proc I.R.E 50: 2367-2368.
- [1.4.] Oliver, B. M. (1963). "Sparkling spots and random diffraction." Proc IEEE 51: 220-221.
- [1.5.] Born, M. and E. Wolf (1970). Principles of Optics, Electromagnetic Theory of Propagation Interference and Diffraction of Light, Pergamon Press.
- [1.6.] Dainty, J. C. (1984). Laser Speckle and Related Phenomena. Laser Speckle and Related Phenomena. J. C. Dainty, Springer-Verlag. 9: 1-7

- [1.7.] Gabor, D. (1970). "Laser Speckle and Its Elimination." IBM Journal of Research and Development: 509-514.
- [1.8.] Fujii, H., T. Asakura, et al. (1976). "Measurement of surface roughness properties by means of laser speckle techniques." Optics Communications 16(1): 68.
- [1.9.] Ohtsubo, J. and T. Asakura (1978). "Measurement of surface roughness properties using speckle patterns with non-gaussian statistics." Ibid. 25(3): 315.
- [1.10.] Ohtsubo, J., H. Fujii, et al. (1975). "Surface Roughness Measurement by Using Speckle." Journal of Applied Physics 14: 293-298.
- [1.11.] Dainty, J. C. (1984). Recent Developments. Laser Speckle and Related Phenomena. J. C. Dainty, Springer-Verlag. 9: 321-339.
- [1.12.] Dainty, J. C. (1984). Stellar Speckle Interferometry. Laser Speckle and Related Phenomena. J. C. Dainty, Springer-Verlag. 9: 255-315.
- [1.13.] Tullis, I. D. C. (2001). The Laser Torquemeter and Implications of Speckle Decorrelation on Torque Measurement. Wolfson School of Mechanical & Manufacturing Engineering. Loughborough, Loughborough University.
- [1.14.] Halliwell N.A (1996). "The laser torsional vibrometer: a step forward in rotating machinery diagnostics" Journal of Sound and vibration 190(3): 399-418.

- [1.15.] Agnostinell G, Paone N, Cristalli C & Torcianti B (2008) On-line diagnostics of washing machines design: sources for the optimization of the measurement set-up. 8th international conference on vibration measurements by laser techniques: Advances and Applications.
- [1.16.] Halkon B & Rothberg, S.J (2004) “Automatic post-processing of laser vibrometry data for rotor vibration measurements” 8th International conference on vibrations in rotating machinery 215-230.
- [1.17.] Sumali H & Allen, M.S (2008) “Apparent non-linear effect of the microscope on the laser Doppler vibrometer” 8th International conference on vibration measurements by laser techniques: Advances and Applications.
- [1.18.] Aranchuk V, Lal A.K, Hess C.F, Sabatier J.M, Burgett R.D, Aranchuk I & Mayo W.T. (2006) Speckle noise in a continuously scanning multi-beam laser Doppler vibrometer for acoustic landmine detection” Proc SPIE 6217.
- [1.19.] Scalise L, Melis M. De, Morbiducci U, Segers P & Tomasini E. (2008) From cardiac to respiratory rate, from cardiac sounds to pulse velocity:a non contact, unified approach for monitoring of vital signs by means of optical vibrocardiography 8th international conference on vibration measurements by laser techniques: Advances and Applications.
- [1.20.] Felver B, King D, Lea S, Price G & Walmsley A (2008) Scanning laser vibrometry and Luminol Photomicrography to map cavitation activity

around ultrasonic scalars. 8th international conference on vibration measurements by laser techniques: Advances and Applications.

- [1.21.] Castellini P, Martarelli M & Tomasini E (2006) Laser Doppler vibrometry: Development of advanced solutions answering to technology's needs.
- [1.22.] Sracic M.W & Allen, M.S Experimental investigation on the effect of speckles noise on continuous scan laser Doppler vibrometer measurements.
- [1.23.] Rothberg S. J. , Baker J. R. et al (1989). "Laser Vibrometry: Pseudo-Vibrations." Journal of Sound and Vibration 135(3): 516-522.
- [1.24.] Rothberg S.J , Halkon B. J. (2004) Laser vibrometry meets laser speckle. Proc 6th International Conference on Vibration Measurements by Laser Techniques: Advances and Applications pg 280-291 Rothberg S.J, Halkon.
- [2.1.] Cristalli C, Torcianti B, Vass J, (2006). "A new method for filtering speckle noise in vibration signals measured by Laser Doppler Vibrometry for on-line quality control", Proc 7th International Conference on Vibration Measurements by Laser Techniques: Advances and Applications Vol. 6345.
- [2.2.] Streaun R F, Mitchell L D and Barker A J, Global noise characteristics of laser Doppler vibrometer – I Theory (1998). Optics and Lasers in Engineering 30, pg 127-139.

- [2.3.] Streaun R F, Mitchell L D and Barker A J, Global noise characteristics of laser Doppler vibrometer – II Experiments using beam dynamics (1998). *Optics and Lasers in Engineering* 30, pg 141-150.
- [2.4.] Rothberg S. J. , Baker J. R. et al (1989). “Laser Vibrometry: Pseudo-Vibrations.” *Journal of Sound and Vibration* 135(3): 516-522
- [2.5.] Denman M, Halliwell N, Rothberg S J. (1996). Speckle Noise reduction in Laser Vibrometry: experimental and numerical optimisation. Proc 2nd International Conference on Vibration Measurement by Laser Techniques: Advances and Applications. Vol 2868 pg 12-21.
- [2.6.] Rothberg S.J , Halkon B. J. (2004) Laser vibrometry meets laser speckle. Proc 6th International Conference on Vibration Measurements by Laser Techniques: Advances and Applications pg 280-291.
- [2.7.] Halkon, B. J (2004). “Laser Doppler Vibrometry for vibration measurements on rotating structures”. Wolfson School of Mechanical & Manufacturing Engineering. Loughborough, Loughborough University
- [2.8.] Bell, J. R (2001). “Application of Laser Doppler Velocimetry to rotor vibration measurement”. Wolfson School of Mechanical & Manufacturing Engineering. Loughborough, Loughborough University
- [2.9.] J. Stein & C. Wang, (1996) *Automatic Detection of Clearance in Mechanical Systems: Experimental Validation*, Mechanical Systems and Signal Processing, 1996 **10**(4), 395-412

- [3.1]. Dainty, J. C. (1984). Laser Speckle and Related Phenomena. Laser Speckle and Related Phenomena. Ed. J. C. Dainty, Springer-Verlag. 9: 1-7.
- [3.2]. Jakeman E. Ridley, K.D book (2006). "Modelling Fluctuations in Scattered Waves", Taylor & Francis
- [3.3]. Goodman J. W. (2008) "Speckle with a finite number of steps" Optical society of America 47(4) A111-A118
- [3.4]. A Papoulis. (1965) "Probability, random Variables and Stochastic Processes", Mcgraw Hill, New York
- [3.5]. Middleton, D. (1958) Introduction to Statistical Communication Theory", McGraw-Hill, New York
- [3.6]. Rothberg, S. J. (1994). Laser Speckle Studies for Vibration and Torque Measurement. Engineering and Applied Science. Southampton, University of Southampton.
- [3.7]. Tullis, I. D. C. (2001). The Laser Torquemeter and Implications of Speckle Decorrelation on Torque Measurement. Wolfson School of Mechanical & Manufacturing Engineering. Loughborough, Loughborough University.
- [3.8]. Goodman, J. W. (1984). Statistical Properties of Laser Speckle Patterns. Laser Speckle and Related Phenomena. J. C. Dainty, Springer-Verlag. 9: 9-74.

- [3.9]. Goodman, J. W. (1976). "Some fundamental properties of speckle." *Journal of Optical Society of America* 66(11): 1145-1150.
- [3.10]. McKechnie, T. S. (1974-75). *Statistics of coherent light speckle produced by stationary and moving apertures*. London, Imperial College of Science and Technology.
- [3.11]. Fujii H. Asakura, T. and Shindo, Y. (1976). "Measurements of Surface Roughness properties by means of laser speckle techniques" *Optics Communications* 16(1) 68-72
- [3.12]. Ohtsubo, J. and Asakura, T. (1978) "Measurement of surface roughness properties using speckle patterns with non gaussian statistics" *Optics Communications* 25(3) 315-319
- [3.13]. Asakura, T. and N. Takai (1981). "Dynamic Laser Speckles and their Application to Velocity Measurements of the Diffuse Object." *Journal of Applied Physics* 25: 179-194.
- [3.14]. Goldfischer, L. I. (1965). *Autocorrelation Function and Power Spectral Density of Laser-Produced Speckle Patterns*". *Journal of the Optical Society of America* 55(3): 247-253
- [4.1]. Takai, N. Sutanto, Asakura, T. (1980) "Dynamic statistical properties of laser speckle due to longitudinal motion of a diffuse object under gaussian beam illumination" *J Opt., Soc. Am* 70(7) 827-834
- [4.2]. N. Takai, Sutanto, and T. Asakura, (1980). "Laser speckles produced by the longitudinal motion of a diffuse object under Gaussian beam illumination," *Jpn. J. Appl. Phys.* 19, L75-L78

- [4.3]. Rothberg S. J. , Baker J. R. et al (1989). "Laser vibrometry: Pseudo-Vibrations." *Journal of Sound and Vibration* 135(3): 516-522
- [4.4]. Asakura, T. and N. Takai (1981). "Dynamic Laser Speckles and their Application to Velocity Measurements of the Diffuse Object." *Journal of Applied Physics* 25: 179-194.
- [4.5]. Rothberg, S. J. (1994). *Laser Speckle Studies for Vibration and Torque Measurement. Engineering and Applied Science. Southampton, University of Southampton.*
- [4.6]. Iwai, Takai. N et al (1981) "The autocorrelation function of the speckle intensity fluctuation integrated spatially by a detecting aperture of finite size" *Optica Acta* 25(10) 1425-1437
- [4.7]. Tullis I.D.C, Halliwell N.A et al (1998) "Spatially integrated speckle intensity: maximum resistance to decorrelation caused by in-plane target displacement" *Journal of Applied Optics* 37(30) 7062-7069
- [4.8]. Tullis, I. D. C. (2001). *The Laser Torquemeter and Implications of Speckle Decorrelation on Torque Measurement. Wolfson School of Mechanical & Manufacturing Engineering. Loughborough, Loughborough University.*
- [4.9]. Nakamura T and Asakura T (1993) "Statistical properties of dynamic speckles produced by a curved surface" *Optics Communications* 98 331-339

- [4.10]. Takai N. Iwai T. et al (1981) “An Effect of Curvature of Rotating Diffuse Objects on the Dynamics of Speckles Produced in the Diffraction Field” *Journal of Applied Phys B* 26 185-192
- [4.11]. Nakamura T. and Asakuar T. (1993) “Statistical properties of integrated dynamic speckles produced by a rotating spheroidal object” *Journal of Optics (Paris)* 24(3) 135-140
- [4.12]. Takai N. Iwai T. et al (1983) “Correlation distance of dynamic speckles” *Journal o Applied Optics* 22(1) 170-177
- [4.13]. Jakeman E.(1975) “The effect of wavefront curvature on the coherence properties of laser light scattered by target centres in uniform motion” *J. Phys. A: Math. Gen.* **8** L23-L28
- [4.14]. Takai N. Iwai T. et al (1983) “Correlation distance of dynamic speckles” *Journal o Applied Optics* 22(1) 170-177
- [4.15]. Jakeman E.(1975) “The effect of wavefront curvature on the coherence properties of laser light scattered by target centres in uniform motion” *J. Phys. A: Math. Gen.* **8** L23-L28
- [4.16]. Jakobsen M.L and Hanson S.G (2008) “Speckle dynamics for intensity-modulated illumination” *Journal of Applied Optics* 47(20) 3674-3680
- [4.17]. Rothberg S. J. (2006). Numerical simulation of speckle noise in laser vibrometry. *Applied Optics* Vol 45(19) 4523-4533
- [5.1]. BS ISO 16063-31:2009 Methods for the calibration of vibration and shock transducers: Testing of transverse vibration sensitivity

- [5.2]. Gade S and Herlufsen H 1987 Use of Weighting Functions in DFT/FFT Analysis (Part II) Appendix F: Picket Fence Effect Brüel and Kjær Technical Review 43 28-35
- [5.3]. Bell, J. R (2001). “Application of Laser Doppler Velocimetry to rotor vibration measurement”. Wolfson School of Mechanical & Manufacturing Engineering. Loughborough, Loughborough University
- [5.4]. LE Drain, The Laser Doppler Technique, Wiley, 222-225, 1980
- [7.1]. Rothberg S. J. (2006). Numerical simulation of speckle noise in laser Vibrometry. Applied Optics Vol 45(19) 4523-4533
- [7.2]. Rothberg S. J. , Baker J. R. et al (1989). “Laser Vibrometry: Pseudo-Vibrations.” Journal of Sound and Vibration 135(3): 516-522
- [8.1]. BS ISO 16063-31:2009 Methods for the calibration of vibration and shock transducers: Testing of transverse vibration sensitivity